

On the Role of Spin States in Organic Semiconductor Devices

Dissertation zur Erlangung des
naturwissenschaftlichen Doktorgrades
der Julius-Maximilians-Universität Würzburg



vorgelegt von

Stefan Kilian Väh

aus Würzburg

Würzburg 2016

Eingereicht am: 30.06.2016
bei der Fakultät für Physik und Astronomie

1. Gutachter: Prof. Dr. Vladimir Dyakonov
2. Gutachter: Prof. Dr. Jean Geurts
der Dissertation.

1. Prüfer: Prof. Dr. Vladimir Dyakonov
2. Prüfer: Prof. Dr. Jean Geurts
3. Prüfer: Prof. Dr. Giorgio Sangiovanni
im Promotionskolloquium.

Tag des Promotionskolloquiums: 07.12.2016

Doktorurkunde ausgehändigt am:

Contents

1. Introduction	1
2. Organic Photovoltaics	5
2.1. Organic Semiconductors	5
2.2. The Emergence of Organic Photovoltaics	7
2.3. Fundamental Processes in Organic Bulk Heterojunction Solar Cells	9
2.4. j-V-Characteristics and Solar Cell Parameters	14
2.5. Morphology of Bulk Heterojunction Solar Cells	16
3. Electron Paramagnetic Resonance	19
3.1. The Electron Spin	19
3.2. The Spin Hamiltonian	20
3.2.1. The Electron Zeeman Interaction	21
3.2.2. The Electron-Exchange Interaction	22
3.2.3. The Zero Field Interaction	23
3.2.4. Distance Dependency of Interactions	25
3.3. Electron Paramagnetic Resonance Theory	27
3.4. Optically Detected Magnetic Resonance Theory	31
3.4.1. Triplet-Triplet Annihilation	32
3.4.2. Spin-Dependent Recombination Model	33
3.5. Electrically Detected Magnetic Resonance Theory	35
3.5.1. Spin-Dependent Recombination	35
3.5.2. Spin-Dependent Transport	36
3.5.3. Detection Modes	36
4. Experimental Section	39
4.1. Materials	39
4.1.1. Donor-Materials	39
4.1.2. Acceptor-Materials	41
4.2. Sample Preparation	43

Contents

4.3. The X-Band EPR Spectrometer	48
4.3.1. Continuous Wave EPR	50
4.3.2. Photoluminescence Detected Magnetic Resonance	51
4.3.3. Electrically Detected Magnetic Resonance	52
4.3.4. Electroluminescence Detected Magnetic Resonance	53
5. Detection of Residual Iodine in PTB7:PCBM Blends due to the Additive DIO	55
5.1. Introduction	55
5.2. Experimental Details	56
5.3. Results & Discussion	57
5.3.1. Solar Cell Performance	57
5.3.2. XPS Measurements	58
5.3.3. Light Induced EPR Measurements	60
5.3.4. UPS- and CELIV Measurements	62
5.4. Conclusion	64
6. Triplet Exciton Formation in p-DTS(FBTTh₂)₂:PC₇₀BM Based Small-Molecule Solar Cells	65
6.1. Introduction	65
6.2. Experimental Details	68
6.3. Results & Discussion	69
6.3.1. Solar Cell Characteristics and Morphology	70
6.3.2. Identification of Zero Field Splitting Parameters	72
6.3.3. Triplet Excitons in p-DTS(FBTTh ₂) ₂ :PC ₇₀ BM Blends	74
6.3.4. Molecular Orientation of p-DTS(FBTTh ₂) ₂ Molecules	77
6.4. Conclusion	80
7. Influence of Galvinoxyl-Doping on Charge Separation	81
7.1. Introduction	81
7.2. Experimental Details	83
7.3. Results & Discussion	83
7.3.1. Galvinoxyl Doping Concentration Dependency	83
7.3.2. Temperature Dependency	85
7.4. Conclusion	87
8. Quantifying Spin-Dependent Recombination	89
8.1. Introduction	89
8.2. Experimental Details	91

8.3. Results & Discussion	93
8.3.1. EDMR Signal Genesis	94
8.3.2. OTRACE-EDMR	98
8.4. Conclusion	102
9. The Role of Spin States in Thermally Activated Delayed Fluorescence	
OLEDs	103
9.1. Introduction	103
9.2. Experimental Details	106
9.3. Results & Discussion	107
9.3.1. Exciplex Emission	107
9.3.2. PLDMR-measurements	108
9.3.3. EDMR-measurements	111
9.3.4. ELDMR-measurements	112
9.4. Conclusion	116
10. Summary	119
Bibliography	124
A. Publications and Conference Contributions	153
B. Danksagung	157

1. Introduction

“Nature bears long with those who wrong her. She is patient under abuse. But when abuse has gone too far, when the time of reckoning finally comes, she is equally slow to be appeased and to turn away her wrath.”

Nathaniel H. Egleston, 1882 [1]

Although this citation from the late 19th century originally addresses deforestation, it is easily applicable to the anthropogenic greenhouse effect and the consequential climate change. The time to stop the trend of increasing global temperature is rapidly running out. Finally, after more than one century, more and more policymakers are coming to the same conclusion.

Two political milestones will influence the energy supply of the Federal Republic of Germany until the middle of the 21st century. At first, the Energy Roadmap 2050 presented by the European Commission in 2011 at an European basis [2]. This strategic paper contains several elements that basically points down to the goal that emissions of greenhouse gases should be reduced by over 80% by 2050. Therefore, the European energy production has to be as carbon-free as possible. Furthermore, the decision of the German government in 2011 to shut down all remaining nuclear power plants by 2022 [3], which was triggered by the nuclear accident in Fukushima, Japan. In the end, it all boils down to the fact that renewable energies have to take over the major part in European energy production. Considering that, a lot of effort has to be spend in acquiring established capabilities and in the development of new technologies, further broadening the mix of renewable forms of energy.

In Figure 1.1, the gross electricity generation of the Federal Republic of Germany is shown for the years 2012 to 2015. Here, it is evident that the main part of the power production is still taken over by carbon based energy sources, like coal or petroleum products. Moreover, the fraction of nuclear energy which is still at 14.1% in 2015 will completely disappear until 2022. Here, the main challenge is to fill this gap by renewable energy sources rather than carbon based energy carriers.

The renewable energy sources, elevated in Figure 1.1, were steadily increasing up to 30% in 2015. Hence, at a first glance this development looks quite promising. At a second glance, however, most of the marked renewable sources stay rather constant over

1. Introduction

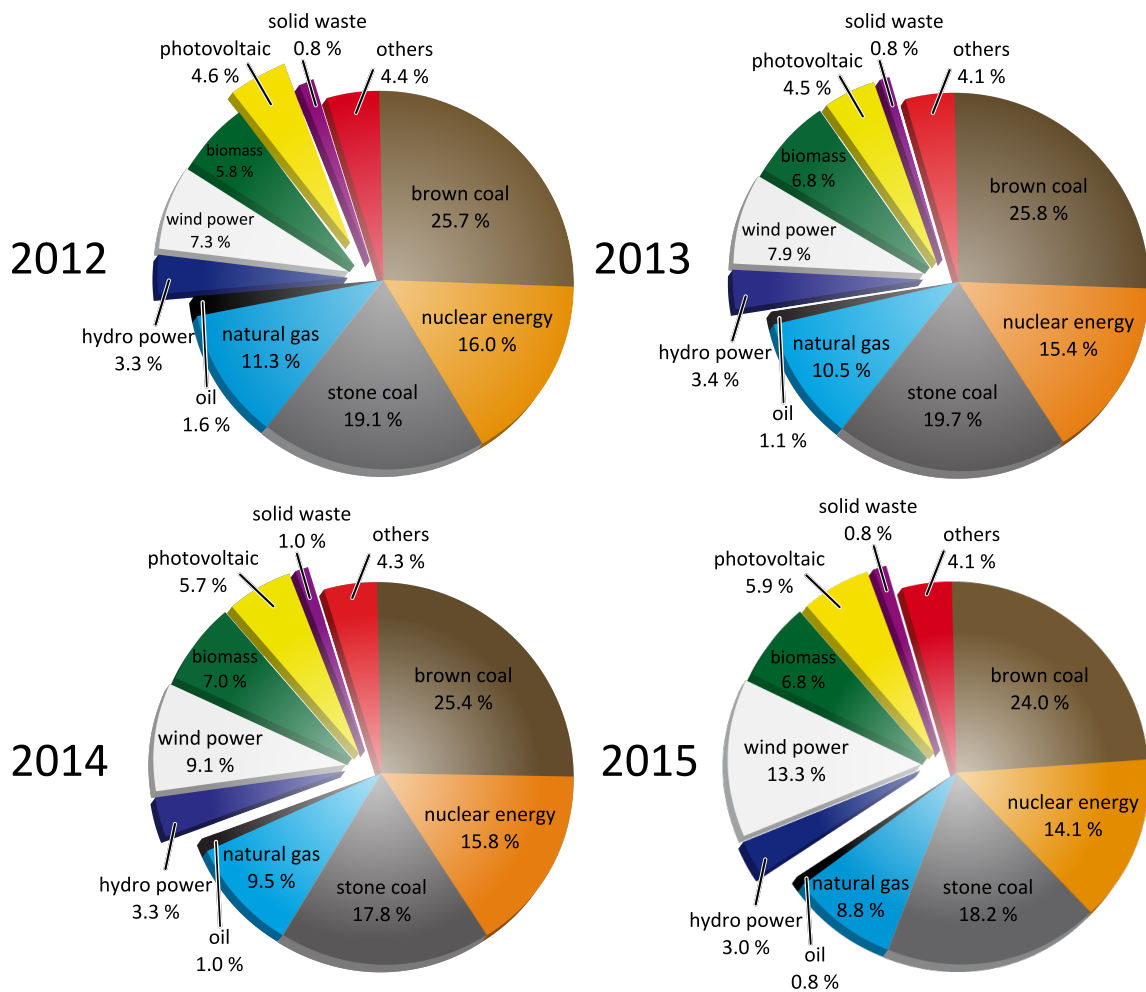


Figure 1.1.: Pie charts of the gross electricity generation of the Federal Republic of Germany in the years 2012 to 2015. The fractions assigned to renewable energies are elevated. They increase from 21.8% to 30.0% over the presented period of time. Data provided by the German Statistical Federal Agency which are partly estimated.

time, like hydro power, biomass, or solid waste. The energy source which is mainly responsible for the steady increase of renewable energies is rather wind power than photovoltaics. This, in turn, is quite surprising considering the extremely high amount of energy provided by the sun. Furthermore, despite of nuclear energy all other presented energy sources in Figure 1.1 were basically produced by solar energy. Therefore, it is remarkable that the direct conversion of solar energy to electricity is as low as 5.9% in 2015. The problem with solar irradiation is its quite low energy density per area. In order to improve the output of a solar power plant either the covered area or the efficiency of the used solar modules have to be increased. Nowadays, the most commonly used solar cells are based on silicon. As this is an established technology for many decades, the power conversion efficiency is at its maximum. Therefore, the only way to improve the output power of a solar power plant is to increase the covered area.

However, the production costs of silicon based solar cells are relatively high, since they are produced out of molten mass. Therefore, economic considerations limit the introduction of very large power plants or the complete coverage with roof top installations. As a consequence, reducing the costs of solar cells is another issue that has to be addressed in order to further increase the application of photovoltaic installations. Further drawbacks of silicon based solar modules are their unfavorable appearance and shape which constrict their application fields significantly.

One technology that circumvents these drawbacks are solar cells based on organic semiconductors. Due to their high absorption coefficient, a very thin film is sufficient to absorb all incident solar irradiation, which also allows for the usage of flexible substrates. Moreover, this type of solar cells can be processed out of solutions at room temperature which introduces the possibility to fabricate solar modules by a roll-to-roll process. This, in turn, will reduce the production costs of organic solar cells drastically. Furthermore, the tuneability of color and shape opens wide application fields, like semitransparent solar cells incorporated into glass panels or facade installations. The power conversion efficiency, however, still needs improvement. Whereas the efficiencies exceed the 10% threshold on a lab scale [4], they are still too low in up-scaled modules. Consequently, organic solar cell research is not finished yet but has to be intensified in order to add this very promising class of solar cells to the mix of renewable energy sources.

The first proof of charge transfer in a material system suitable for organic photovoltaics is based on a measurement which used the electron spin as a probe [5]. This work paved the way for the application of spectroscopic methods based on electron paramagnetic resonance in organic semiconducting materials. The conversion of sunlight into electricity in organic solar cells is not as simple as in inorganic semiconductor devices. There are several intermediate steps between light absorption and free charge carrier generation. The low spin relaxation times of organic materials makes the electron spin an ideal probe for these intermediate energetic states. However, advanced detection techniques had to be developed in order to increase the sensitivity, like optically detected magnetic resonance or electrically detected magnetic resonance. With these techniques at hand, the fundamental processes in organic semiconductors became accessible and could be investigated with great accuracy.

This work starts with an overview of organic semiconductors, the historical development of organic solar cells and the explanation of the fundamental processes involved in charge carrier generation. Afterwards, a theoretical description of the used measurement technique electron paramagnetic resonance and its extensions is given, which is followed by the explanation of the experimental details. Subsequently, four

1. Introduction

result chapters address spin-dependent processes and investigations in organic photovoltaic devices. Finally, the last result chapter investigates the generation of light in novel thermally activated delayed fluorescence organic light emitting diodes.

2. Organic Photovoltaics

In this chapter, an overview of the properties of organic semiconductors is given with a focus on organic photovoltaics. After clarifying the basic physics of organic semiconductors, a brief digression in the history of organic solar cells is given. Subsequently, the basic processes from light absorption to charge carrier generation are highlighted. Finally, the characterization of solar cell devices is addressed together with the very important property of morphology.

2.1. Organic Semiconductors

Although organic semiconductors aroused more and more interest of the scientific community over the last three decades, their first discovery dates back to the middle of the 20th century. In a study of halogen doped organic materials Akamatu et al. observed a conductivity in the dark [6]. In 1977 Shirakawa et al. discovered that a semiconducting polymer could have a "remarkably high conductivity at room temperature", after exposure to a halogen vapour [7]. This discovery is seen as a breakthrough towards conducting polymers and was rewarded with the nobel prize in 2000 for Hideki Shirakawa, Alan G. MacDiarmid and Alan J. Heeger. Since then, the ongoing development of organic semiconductors led to a manifold of optoelectronic devices like organic light-emitting diodes (OLEDs), organic field-effect transistors (OFETs) or organic solar cells.

The backbone of conjugated polymers consists of carbon atoms with alternating single and double bonds, which is depicted in Figure 2.1 (top). Carbon in its ground state possesses the configuration $1s^2 2s^2 2p^2$. The $2s^2 2p^2$ orbitals can hybridize in order to bond with other atoms. Thereby, they form an energetically lower configuration. Depending on the binding partners they hybridize in sp^3 -, sp^2 - or sp -configuration. In conjugated polymers, the carbon atoms hybridize in the sp^2 -configuration. This leads to the formation of three equivalent orbitals that are situated in-plane with a maximum spatial separation of 120° . They form three σ -bonds with the two neighboring carbon atoms and one hydrogen atom. However, the remaining p_z -orbital stands perpendicular to the sp^2 -plane. The overlap of two neighboring p_z -orbitals results in a π -bond. If

2. Organic Photovoltaics

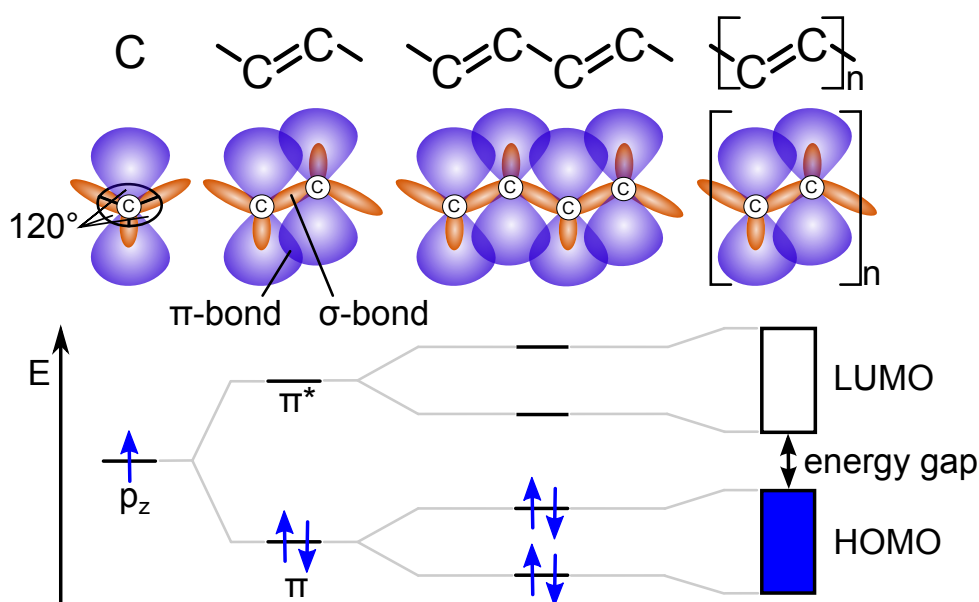


Figure 2.1.: Top: Conjugated polymers are based on alternating single and double bonds. Middle: The sp^2 orbitals form σ -bonds in a plane with a maximum spatial distance of 120° . The p_z orbitals form π -bonds, located above and beneath the σ -plane. Bottom: The p_z orbitals split energetically into bonding and antibonding states. An increasing number of participating carbon atoms lead to π -bands, named as HOMO and LUMO.

there are many π -bonds next to each other they will form a π -band where delocalized electrons can move freely above and below the sp^2 -plane. Whereas the strongly localized electrons forming the σ -bonds have no contribution to the conductivity of organic semiconductors, the main contribution stems from the delocalized π -electrons.

A π -bond splits the p_z -orbitals into binding and antibinding states. While the number of participating π -bonds increases the quantity of energetically marginally different binding and antibinding states will increase as well. If the number of atoms is large enough it will result in a band like structure, as illustrated in Figure 2.1 (bottom). Here, the band lower in energy is denoted as highest occupied molecular orbital (HOMO) and the band higher in energy as lowest unoccupied molecular orbital (LUMO). This can be seen as equivalent to the valence- and conduction band in comparison to inorganic semiconductors. The reason for the energy gap between HOMO and LUMO is the Peierls distortion [8, 9]. This theorem was introduced by Rudolf Peierls and is valid for a one dimensional system with an incompletely filled band. If the distance between the atoms differs, which is the case for alternating double and single bonds, it will open a gap at the fermi level. This leads to a separation of the HOMO- and LUMO level of around 1 to 3 eV, which results in semiconducting properties.

Polymers consist of a distributed number of monomers. In an ideal system, the delocalized π -electrons extend over the whole length of the polymer chain. Nevertheless,

the real extent always depends on tilts and twists of the polymer. This length is called conjugation length. Another mechanism distorting the π -electron system are errors in the molecular structure, resulting in trap states. Therefore, the conjugation lengths are randomly distributed which is the reason for the broad and featureless absorption and emission of organic semiconductors. Furthermore, the randomly distributed location of the polymer chains is also obstructive for charge transport from one chain to another. Here, crystalline phases are advantageous meaning the polymer chains orient themselves in an ordered way. Hence, the morphology, defined as the nanoscopic structure of a blend is of crucial importance for the operation of organic devices. The term morphology embraces the crystallinity and in particular the distribution of pure or enriched phases of one material.

2.2. The Emergence of Organic Photovoltaics

A decent conductivity together with a band gap that lies in the range of the visible light made organic semiconductors a reasonable candidate for photovoltaic applications. One main advantage compared to inorganic semiconductors is the very high absorption coefficient. This is why a very thin layer of 100 nm to 200 nm is sufficient for enough light absorption in order to convert the photonic energy into electricity. The first organic solar cells consisted of a thin layer of only one organic semiconductor. However, they showed poor power conversion efficiencies of far below 1% [10]. This is due to the very high exciton binding energies in organic materials, which is between 0.5 eV and 1 eV. Therefore, they are assigned as Frenkel excitons. The strong coulombic interaction is due to the relatively low dielectric constant of organic materials, which usually lies between three and four. Their splitting is very unlikely, because their binding energy exceeds by far the thermal energy at room temperature (≈ 26 meV). Furthermore, the lifetime and with that the diffusion length of the excitons is substantially limited. Hence, it is quite unlikely that they could be separated at the contacts. In the end, most of the excitons will recombine either radiatively, sending out a photon or non radiatively, via a multi-phonon relaxation process.

In 1986, Tang introduced a new type of organic device which was a huge step forward towards the development of efficient organic solar cells [11]. In this approach two organic single layers have to be put on top of each other forming a stacked bilayer system. This architecture is called planar heterojunction and is shown on the left hand side of Figure 2.2. If the second organic material has a higher electron affinity, the excitons will be split at the interface leaving the hole on the first material while the electron transfers to the second. This exciton splitting is energetically favorable, because the electron

2. Organic Photovoltaics

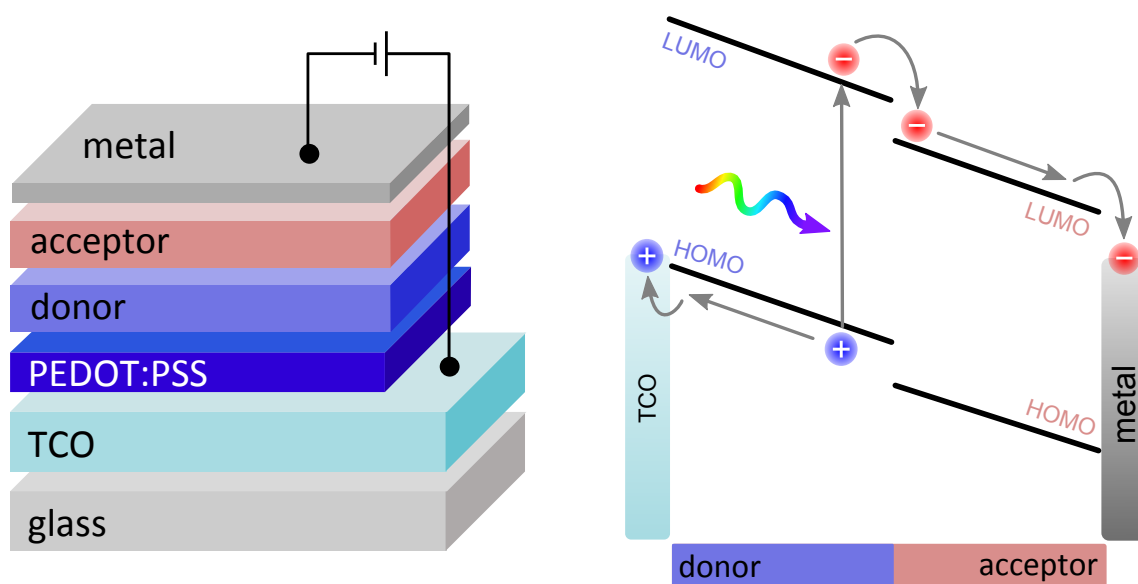


Figure 2.2.: Left: Structure of a planar heterojunction solar cell. Right: Energy diagram and charge carrier generation in the donor- and acceptor single layers.

moves to a state much lower in energy, which is sketched on the right hand side of Figure 2.2. Most of the light absorption happens in the so called donor material due to a better overlap of the absorption with the solar spectrum. It will provide the electron to the more electronegative material, which is in turn called acceptor. The introduction of bilayer solar cells yielded in an improvement of power conversion efficiencies to approximately 1%. Nevertheless, as thicknesses of the photoactive area are in the order of 100 nm and the diffusion length of excitons is around 10 nm, there are still a lot of excitonic losses in this kind of solar cells.

The problem of rather short diffusion lengths of excitons was solved by an intermixing of donor- and acceptor materials. Thereby, the amount of interfaces throughout the whole photoactive layer was vastly increased. This is either done by mixing two soluble organic materials in solution or by co-evaporating both constituents in high vacuum. The resulting device is called bulk heterojunction (BHJ) solar cell and is sketched on the left hand side of Figure 2.3. This approach was first reported in 1995 by Yu et al. However, an efficiency value of only <1% was reached by mixing the conjugated polymer poly[2-methoxy-5-(2'-ethyl-hexyloxy)-1,4-phenylenevinylene] (MEH-PPV) with the soluble fullerene derivative [6,6]-phenyl-C₆₁butyric acid methyl ester (PC₆₀BM) [12]. This BHJ solar cell has the big advantage that as long as the intermixing is fine enough all excitons will reach an interface and get split, as shown on the right hand side of Figure 2.3. However, if the intermixing is too fine there will be a lack of percolation pathways to the contacts. That implies the transport path of the charge carriers will be blocked by the wrong material at some point. This will result in severe extraction and recombination

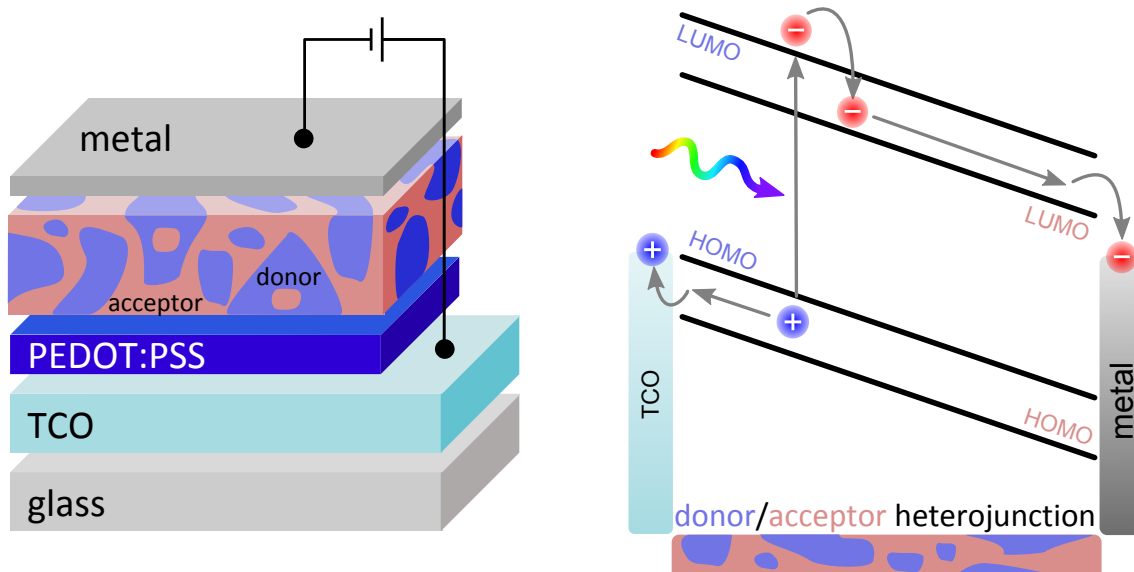


Figure 2.3.: Left: Architecture and right: Energy diagram of an intermixed donor-acceptor bulk heterojunction solar cell, showing that excitons are split and contribute to charge carrier generation over the whole photoactive layer.

problems. Again, the morphology of the photoactive layer plays a crucial role in the performance of organic solar cells. Therefore, different attempts were evolved in order to optimize the phase separation and crystallinity of the enriched phases. Parameters to influence the morphology are the choice of solvent [13], thermal treatments after solution processing [14] or the addition of a certain percentage of a selective solvent into the host solution [15]. Together with further improvements and developments of new organic molecules these preparation methods lead to an improvement of power conversion efficiencies up to 11 % [16].

2.3. Fundamental Processes in Organic Bulk Heterojunction Solar Cells

In the following, the fundamental processes needed to convert photons into electric energy are discussed from light absorption over exciton splitting to charge transport and extraction. They are basically the same for BHJ solar cells (Figure 2.3) and planar heterojunction solar cells (Figure 2.2). However, due to simplicity and the fact that mainly BHJ solar cells were used in this work, the discussion will focus on these devices.

Light Absorption and Exciton Diffusion

The spectrum of electromagnetic waves originating from the sun has a specific shape at the time it reaches the surface of the earth. The initial black body radiation is attenuated by the sun's chromosphere and more severely by the atmosphere of the earth. In particular, the strong absorption of different molecules like water or carbon dioxide leads to its distinctive shape which is shown in Figure 2.4. The use of organic materials in order to absorb sunlight is very efficient due to their very high absorption coefficient in the order of 10^7 m^{-1} in the relevant spectral range [17, 18]. An exemplary absorption spectrum for this is shown in Figure 2.4 for the material system PTB7:PC₇₀BM (see chapter 4.1 for molecular structures).

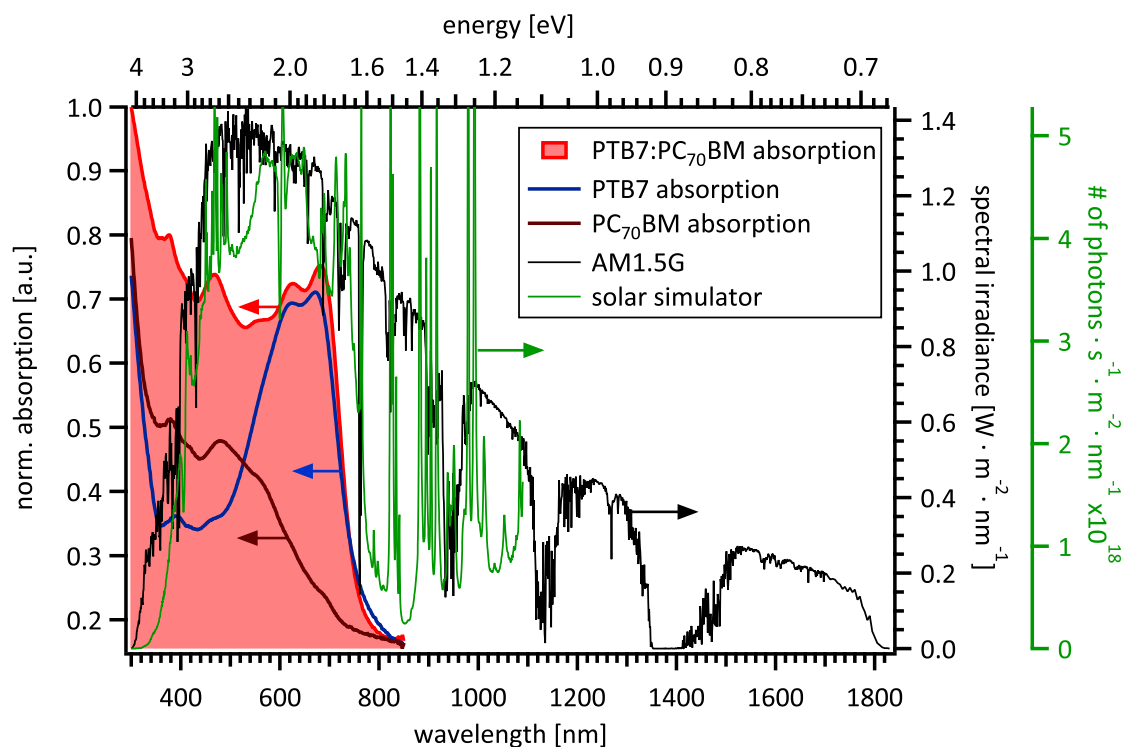


Figure 2.4.: Normalized absorption for the material system PTB7:PC₇₀BM, together with the corresponding pristine materials (colored lines, left axis). In comparison, an extraction of the AM1.5G spectrum is shown (black line, black right axis), revealing a decent spectral overlap between absorption and the solar spectrum. Data from the AM1.5G spectrum provided by the American Society for Testing and Materials. The spectrum of the solar simulator is presented in green (green right axis).

In a BHJ solar cell both organic compounds, the donor and acceptor, absorb light. However, the donor usually absorbs more relevant photons than the acceptor. Therefore, the following operational principles are explained after excitation of the donor phase. An absorbed photon creates an exciton. This possesses a singlet spin state, since the ground state of an organic material is also in singlet configuration. Subsequently,

the created exciton could reach an interface within its lifetime [19, 20], transferring the electron to the acceptor phase in a very fast process in the order of femtoseconds [5, 21]. As long as the electron is still in the range of the coulombic interaction it will occupy an intermediate state, called charge transfer state. Alternatively, the exciton could recombine again. This process happens either radiatively, visible as photoluminescence or non radiatively via a multi-phonon process. Thereby, the energy is converted into heat and is not usable anymore for the energy conversion process. The third possibility for the exciton is to flip one spin, forming an exciton with triplet multiplicity. This process, called inter system crossing is very inefficient for organic polymers but nevertheless possible. The resulting triplet exciton may not recombine easily due to the spin forbidden transition to the singlet ground state. Furthermore, its lower energy compared to the LUMO level of the acceptor makes it highly unlikely that it gets split at an interface. Therefore, it will possess a much longer lifetime than its singlet counterpart. All previously discussed processes are depicted in Figure 2.5.

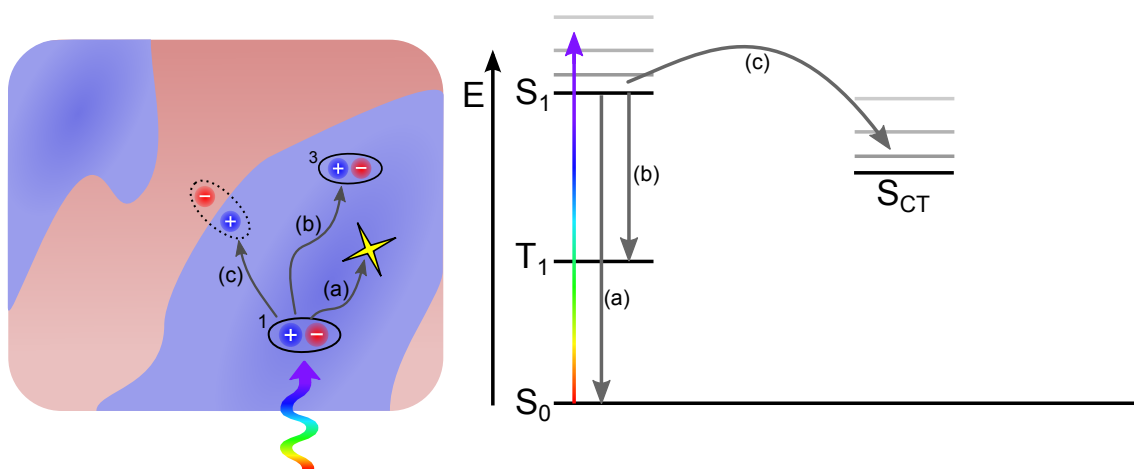


Figure 2.5.: Left: Sketch of the processes taking place in a BHJ solar cell. After light absorption in the donor phase (blue) a singlet exciton is formed that will either recombine again (a), change via inter system crossing its spin state forming a triplet exciton (b) or will reach within its lifetime an interface forming a singlet charge transfer complex (c). Right: Jablonski diagram of the processes shown on the left hand side with S_0 : singlet groundstate, S_1 : singlet excited state, T_1 triplet excited state and S_{CT} : singlet charge transfer state.

Charge Transfer States

The formation of a charge transfer complex can be seen as an intermediate step between a bound exciton and non-interacting charge carriers [22, 23, 24]. In literature, this state is often also referred to as charge transfer state, charge transfer exciton or polaron pair [24, 25, 26]. Nevertheless, this process has to be energetically favorable,

2. Organic Photovoltaics

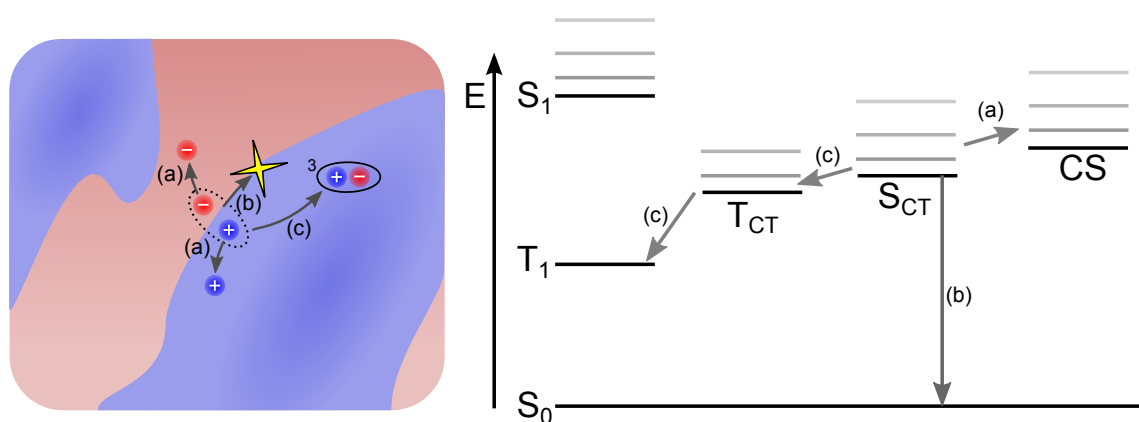


Figure 2.6.: Left: Sketch of the processes taking place after the formation of a singlet charge transfer state. It will either split into free charge carriers (a), recombine radiatively or non radiatively (b) or change its spin state forming firstly a triplet charge transfer state and subsequently a triplet excited state (c). Right: Jablonski diagram of the processes shown on the left hand side with S_0 : singlet ground state, S_1 : singlet excited state, T_1 triplet excited state, S_{CT} : singlet charge transfer state, T_{CT} : triplet charge transfer state and CS: charge separated state.

meaning that the energy of the charge transfer complex has to be lower than the exciton binding energy. However, if the exciton gets separated at an interface the two opposite charges will still be Coulomb bound to each other until they overcome their binding energy. If they succeed they will be "free", meaning all interactions can be neglected due to their spatial distance, which is sketched in Figure 2.6(a). Nevertheless, if they are not able to overcome their binding energy, they will recombine either radiatively, showing CT-photoluminescence, or non-radiatively [27, 28, 29, 30, 31]. This kind of loss mechanism is called geminate recombination because the participating charge carriers stem from the same excitation, which is shown in Figure 2.6(b). The charge transfer state formed by a singlet exciton possess the same multiplicity due to spin conservation. However, the energetic difference between singlet and triplet charge transfer state is very small. Therefore, the singlet charge transfer state possesses a certain probability to change its spin state, leading to a triplet charge transfer state [32, 33]. If the triplet excited state possess a lower energy than the charge transfer state the electron could transfer back to the donor phase, forming a triplet exciton. This process is called electron back transfer [34] and is depicted in Figure 2.6(c). Here, it is also conceivable that the triplet exciton is formed directly via the singlet charge transfer state. Although there are examples where the electron back transfer happens via a geminate process [35] it is more likely that it occurs via a non-geminate recombination process, further discussed in the following.

Charge Carrier Transport and Recombination

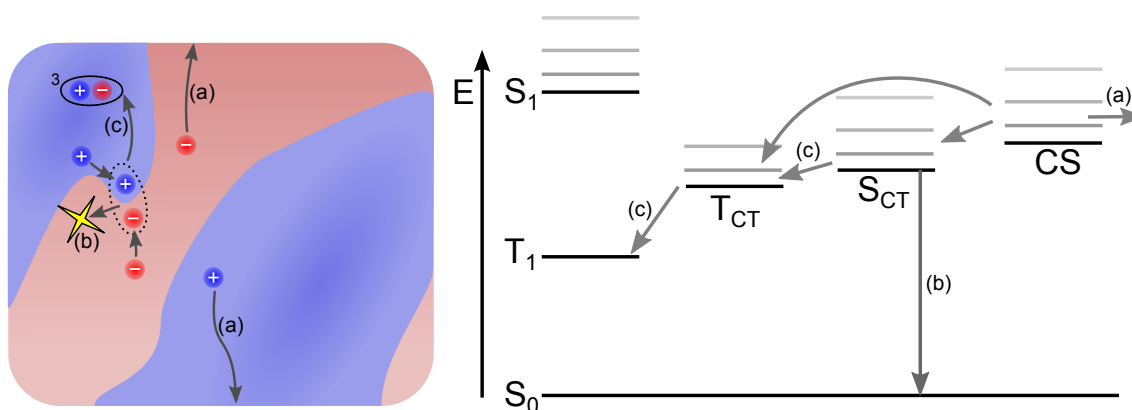


Figure 2.7.: Left: Sketch of the possible processes after formation of two free charge carriers. In the ideal case they are transported to their corresponding contacts and will be extracted (a). If they find a new counterpart they will form a charge transfer complex again. This may either recombine (b) or relax into a triplet excited state (c). Right: Jablonski diagram of the processes shown on the left hand side with S_0 : singlet groundstate, S_1 : singlet excited state, T_1 : triplet excited state, S_{CT} : singlet charge transfer state, T_{CT} : triplet charge transfer state and CS: charge separated state

Charge carriers in organic semiconductors behave like polarons. These quasi particles are described as the carrier itself together with a distortion of its surrounding crystal lattice [36, 37]. They can also be delineated as free charge carriers with an increased effective mass [38].

If two separated polarons are formed via absorption, exciton diffusion and charge transfer state dissociation, they have to reach their corresponding electrodes in order to create photocurrent. In contrast to inorganic semiconductors, where the charge carriers can move almost freely in the valence- and conduction band, polarons in organic semiconductors move rather by a hopping process via localized states. This is due to the lack of a long-range order in the organic compounds. As a consequence, the charge carrier mobility in organic semiconductors ($\approx 10^{-3} \text{ cm}^2/\text{Vs}$) is many orders of magnitude lower than in their inorganic counterpart ($\approx 10^3 \text{ cm}^2/\text{Vs}$). The charge carriers move only in their respective phase, therefore percolation pathways are needed for the polarons to reach their corresponding electrodes. The morphology of the active layer is again of crucial importance, not only for efficient exciton dissociation but also for charge transport. The charge carrier transport is indicated in Figure 2.7 (a).

If the hole in the donor and the electron in the acceptor rich phase reach the anode and cathode, respectively, they will finally be extracted. Problems occur when a charge carrier reaches the wrong electrode. This issue can be circumvented by introducing selective hole- and electron blocking layers between the active layer and the contacts

2. Organic Photovoltaics

[39, 40]. Another problem is the velocity of charge extraction. If the polarons are extracted too slow, a space charge region will pile up, further hindering an efficient charge extraction [41].

On their way to the electrodes, polarons with opposite charges could meet at an interface between donor and acceptor phase and be captured by the Coulombic force. As a result, they will form a charge transfer state again and recombine radiatively or non-radiatively. This process is called non-geminate recombination because the participating charge carriers stem from different excitations, which is shown in Figure 2.7 (b).

The spins of the initially free charge carriers are uncorrelated, therefore the probability for the charge transfer state to be in singlet or triplet multiplicity is 1:3. Like in the geminate case, charge transfer states may again form triplet excitons via electron back transfer as shown in Figure 2.7 (c). Due to the increased occupation of triplet charge transfer states it is likely that the electron back transfer is increased compared to the geminate case.

2.4. j-V-Characteristics and Solar Cell Parameters

The underlying mechanism of all kinds of solar cells is the photoelectric effect, discovered as early as 1887 by Heinrich Hertz [42]. In 1905 Einstein described this phenomenon as the absorption of light quanta [43], for which he was rewarded with the nobel price in 1921.

The characterization of a solar cell is done by measuring the current response for an externally applied voltage. Normalizing the current with the active area of the cell leads to the characteristic j-V curve of a device, exemplary shown in Figure 2.8. Here, measuring in the dark results in a typical diode like behavior. After blocking the current to a certain voltage it becomes conductive. Measuring the solar cell under illumination leads to a shift to negative current densities. There are several points of particular interest in the illuminated j-V curve. If no external voltage is applied, the current coming from the solar cell is called short circuit density (j_{sc}), marked in Figure 2.8(b). In this case, the internal electric field is only due to the difference in work functions of the corresponding electrodes. By applying a negative voltage to the device, the driving force for the charge carriers increases, leading to an enhanced extraction (Figure 2.8(a)). Another characteristic point is the open circuit voltage (V_{oc}). Here, no charge carriers are extracted from the device, i.e. all generated charges recombine again as illustrated in Figure 2.8(c). Applying an external voltage larger than the open circuit voltage leads to an injection of charge carriers at the corresponding electrodes and a high conductance,

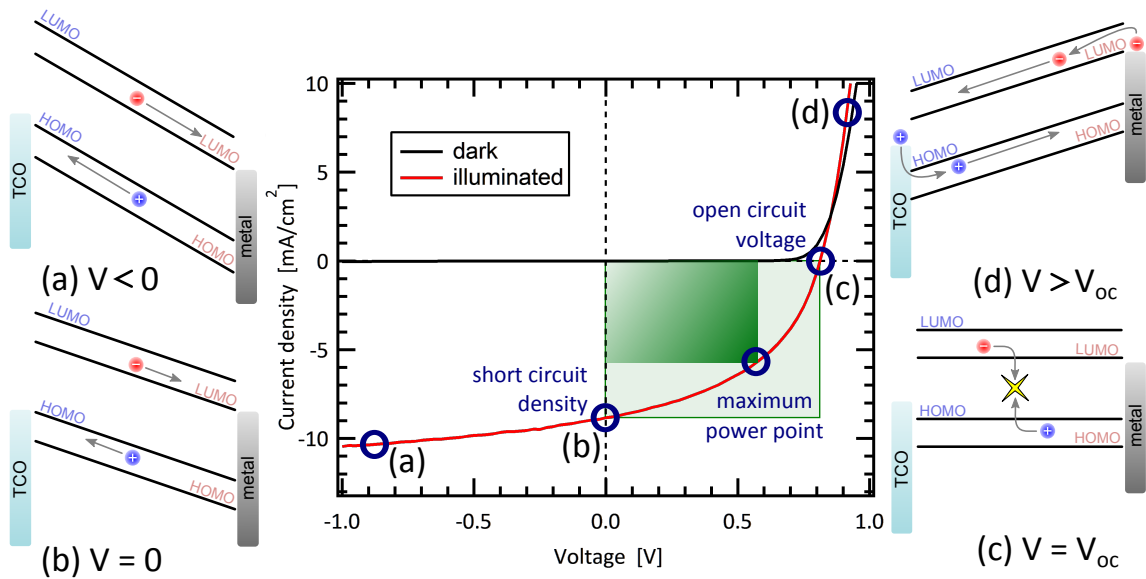


Figure 2.8.: Middle: *j*-*V* characteristics for a bulk heterojunction solar cell in the dark (black) and under simulated AM1.5G illumination (red). The characteristic points of the *j*-*V* curves, j_{sc} , V_{oc} and the maximum power point are highlighted. For four different points of the illuminated *j*-*V* curve the energetics of the LUMO and HOMO bands for the donor and acceptor are shown (left and right). (a) for negative voltages, (b) for no applied voltage, (c) for $V=V_{oc}$ and (d) for applied voltages exceeding V_{oc} . The *j*-*V* curve is exemplary shown for the material system p-DTS(FBTTh₂)₂:PC₇₀BM (see molecular structures in chapter 4.1).

limited by the series resistance of the device (Figure 2.8(d)). Another very important point of interest is the maximum power point (*mpp*). The electrical power is defined as the product of voltage and current. Therefore, the maximal power that is obtainable from a solar cell is given at the maximum power point, illustrated by the dark green rectangle in Figure 2.8.

The parameter that describes the ability of a solar cell to convert sun light into electricity is the power conversion efficiency η . In general, it is defined as the ratio between the maximal electrical power, given at the maximum power point P_{mpp} and the radiant power with which the solar cell is illuminated P_{illu} .

$$\eta = \frac{P_{mpp}}{P_{illu}} \quad (2.1)$$

Another parameter has to be considered in order to determine the maximum power point, the so called fill factor *FF*. This parameter is defined as the ratio between the theoretically possible electric power, the product of V_{oc} and j_{sc} (illustrated by the light green rectangle in Figure 2.8) and the actual maximum power point.

$$FF = \frac{P_{mpp}}{V_{oc} \cdot j_{sc}} \quad (2.2)$$

2. Organic Photovoltaics

In other words, the fill factor describes how rectangular the shape of the j-V-curve behaves between j_{sc} and V_{oc} . As a consequence, the power conversion efficiency η (2.1) can be rewritten to yield:

$$\eta = \frac{P_{mpp}}{P_{illu}} = \frac{V_{mpp} \cdot j_{mpp}}{P_{illu}} = \frac{V_{oc} \cdot j_{sc} \cdot FF}{P_{illu}}. \quad (2.3)$$

The maximal theoretical power conversion efficiency for a single junction device was calculated by Shockley and Queisser in 1961 for an inorganic p-n junction, yielding a η_{max} of 33 % [44].

Furthermore, a common measurement routine is needed in order to compare efficiency values for solar cells measured at different laboratories. These standard conditions are a constant device temperature of 25 °C together with a simulated AM1.5G reference spectrum with an irradiance power of 100 mW cm⁻² [45], which is shown in Figure 2.4 for the used solar simulator. The AM1.5G spectrum, also presented in Figure 2.4, is defined as the solar spectrum after passing through 1.5 times the air mass (AM). This means the solar radiation hits the atmosphere at an angle of 48°, which corresponds to mid-latitudes. The global (G) reference spectrum is defined by the direct and diffuse solar irradiance averaged over one year.

2.5. Morphology of Bulk Heterojunction Solar Cells

As already mentioned previously the morphology of the donor:acceptor blend, i.e. the composition of the active layer on a molecular level, is of crucial importance for the performance of an organic solar cell. Despite the fact that an intermixing of both materials is needed in order to separate primary formed excitons, it is also a drawback concerning recombination and percolation pathways. Therefore, the ideal morphology which is most suitable for charge carrier generation as well as charge carrier transport has to be found [46, 47, 48, 49]. Unfortunately, this is different for every organic blend system and a lot of effort has to be spent in advance to identify the ideal preparation conditions. Firstly, the best working ratio between donor- and acceptor material has to be found [13, 15, 50, 51]. The choice of solvent is another crucial parameter for the film formation when performing solution processing. Besides the most commonly used chlorobenzene, many other organic solvents could be used. This results in a changed formation of the active layers due to different drying speeds and altered solubility of the single components [13].

One method to improve the morphology is by thermal treatment subsequently to the film formation. This process is mainly used for the donor material poly (3-hexylthiophene)

2.5. Morphology of Bulk Heterojunction Solar Cells

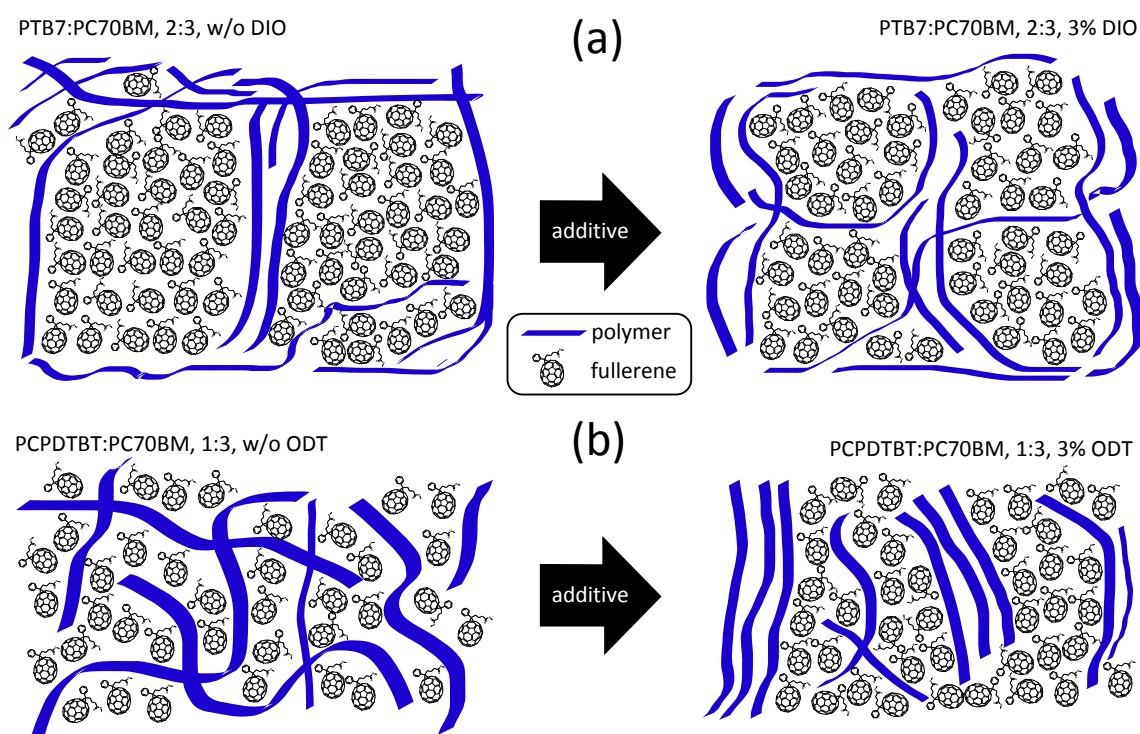


Figure 2.9.: The influence of processing additives on the film formation schematically shown for (a) PTB7:PC₇₀BM without the addition of DIO (left) and with 3 % by volume DIO (right). The size of fullerene rich phases gets reduced in order to reach a more ideal morphology. (b) Adding 3 % ODT to the material system PCPDTBT:PC₇₀BM leads to larger areas of fullerene rich phases (right) compared to a fine intermixing when prepared without additives (left). Modified from [52, 53].

(P3HT) blended with [6,6]-phenyl-C₆₁-butyric acid methyl ester (PC₆₀BM) [14, 54]. Both materials are more detailed explained in the next chapter. In this example, the efficiency of such a solar cell can be improved up to 3-4 % by heating the film for 10 minutes at 130 °C. This improvement is believed to result from better light absorption as well as enhanced transport properties due to a higher degree of phase separation and the formation of crystalline P3HT phases [46, 55, 56].

Another method to alter the morphology is the use of solvent additives [57]. The most used are 1,8-octanedithiol (ODT) or 1,8-diiodooctane (DIO), which are small molecules that possess a high boiling point of 332 °C and 270 °C, respectively. These materials are added to the host solution and act as a co-solvent. They are selective solvents for the most commonly used acceptor materials PC₆₀BM and PC₇₀BM. This leads to an improved capability for the fullerenes to move during film formation. With this method, the morphology of the active layer can be changed significantly, depending only on the amount of processing additive. One of the most famous examples for the use of additives is poly[[4,8-bis[(2-ethylhexyl)oxy]benzo[1,2-b:4,5-b']dithiophene-2,6-diyl][3-fluoro-2-[(2-ethylhexyl)carbonyl]thieno[3,4-b]thiophenediyl]] (PTB7) mixed with

2. Organic Photovoltaics

PC₇₀BM. Both materials will be further discussed in the next chapter. Thereby, the addition of 3 % by volume DIO to the initial blend solution leads to a an increase of device efficiency from 3.9% to 7.4 % [51]. By altering the solar cell layout this could be boosted up to 9.2 % [58, 59]. The use of additives results in a changed size of fullerene aggregates leading to a more ideal size of donor and acceptor rich phases. For PTB7:PC₇₀BM the size of the fullerene aggregates is reduced by the use of additives, as shown in Figure 2.9 (a). On the other hand, additives may also increase the phase separation. This was shown as early as 2007 by Peet et al. [15] for the material system poly[2,6-(4,4-bis-(2-ethylhexyl)-4H-cyclopenta[2,1-b;3,4-b']-dithiophene)-alt-4,7-(2,1,3-benzothiadiazole)] (PCPDTBT) blended with PC₇₀BM. This material system is seen as the first synthesized low bandgap polymer [60]. In this case, the efficiency improves from 2.8 % without the use of additives to 5.5 % by adding 3 % by volume ODT to the host solution. Here, the increase of donor- and acceptor rich phases, schematically shown in Figure 2.9 (b), leads again to a more ideal morphology which in turn results in improved exciton splitting efficiency, charge carrier mobility and lifetime [61, 62, 63].

All in all, the nanoscopic composition of the active layer, especially the size and crystallinity of donor and acceptor rich phases is most important for the best performance of organic BHJ solar cells. Almost every important step during the process of light conversion to electricity is affected by the morphology of the photoactive materials.

3. Electron Paramagnetic Resonance

3.1. The Electron Spin

All experiments presented in this work are using the electron spin to probe spin-dependent processes in organic semiconductors. The electron spin is an intrinsic form of angular momentum, i.e. it exists even when the electron holds no kinetic energy. It possesses all properties of a classical angular momentum despite the fact that it arises from a rotating mass. Furthermore, it is not explainable by classical mechanics only by quantum mechanics. In 1922 Stern and Gerlach discovered the presence of this type of angular momentum by the deflection of a silver atom beam in an inhomogeneous magnetic field [64]. A spin is carried by elementary particles as well as nuclei. Nevertheless, this work will only focus on the electron spin. In its simplest form, a free electron, like any other fermion, possesses a spin of $\frac{1}{2}$. This forms a doublet spin state. Applying an external magnetic field to a free electron leads to a precession of the spin either parallel or antiparallel to the magnetic field vector. This behavior is depicted on the left hand side of Figure 3.1.

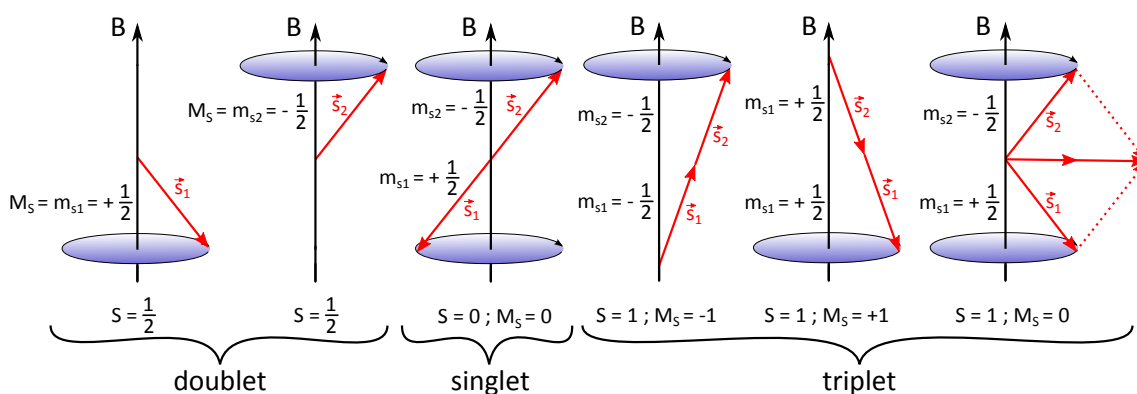


Figure 3.1.: Orientation and rotation of spins in an external magnetic field. A non-interacting spin is either in parallel or antiparallel configuration possessing doublet multiplicity. The combination of two spins leads to either a singlet multiplicity or three possible triplet configurations.

3. Electron Paramagnetic Resonance

Bringing two initially free spins close to each other will lead to an interaction between them. The different kind of couplings will be explained in the next section. In short, they will combine their single spins to form either a singlet- or a triplet state, featuring a total spin of $S = 0$ or $S = 1$, respectively. This process is shown on the right hand side of Figure 3.1. The quantity of possible spin states in a specific spin configuration is called multiplicity and given by the value $2S + 1$. This leads to the magnetic spin quantum number M_S , which ranges from $-S$ to S :

$$M_S = -S, -S + 1, \dots, S - 1, S \quad (3.1)$$

3.2. The Spin Hamiltonian

The total spin hamiltonian for a spin system with more than one electron ($S > \frac{1}{2}$) can be expressed as [65, 66, 67]:

$$\begin{aligned} \mathcal{H} = \sum_i \mathcal{H}_{EZI}(i) + \sum_i \mathcal{H}_{ZFI}(i) + \sum_i \sum_j \mathcal{H}_{EEI}(i, j) + \sum_i \sum_k \mathcal{H}_{HFI}(i, k) & \left\{ \text{electron spin} \right. \\ & \left. + \sum_k \mathcal{H}_{NZI}(i) + \sum_k \mathcal{H}_{NQI}(i) \right\} \text{nuclear spin} \end{aligned} \quad (3.2)$$

consisting of the single terms

- \mathcal{H}_{EZI} : Electron Zeeman Interaction of electron spin i
- \mathcal{H}_{ZFI} : Zero-Field Interaction of electron spin i
- \mathcal{H}_{EEI} : Electron-Exchange Interaction between electron spin i and j
- \mathcal{H}_{HFI} : Hyperfine Interaction between electron spin i and nuclear spin k
- \mathcal{H}_{NZI} : Nuclear Zeeman Interaction of nuclear spin k
- \mathcal{H}_{NQI} : Nuclear Quadrupole Interaction of nuclear spin k

In the materials studied in this work only a fraction of the occurring nuclei possess a spin $I > 0$, namely nitrogen ($I_N = 1$) and fluorine ($I_F = \frac{1}{2}$). Furthermore, the interactions between the electron spin and the nuclear spins are averaged out in the vicinity of different nuclei, which would only lead to a linewidth broadening. The nuclear quadrupole interaction \mathcal{H}_{NQI} is just relevant for nuclear spins $I > \frac{1}{2}$. For that reasons, all terms consisting of a nucleus spin, which is the hyperfine interaction \mathcal{H}_{HFI} , the nuclear Zeeman interaction \mathcal{H}_{NZI} and the nuclear quadrupole interaction \mathcal{H}_{NQI} are negligible for the investigated material systems.

The terms of crucial importance in order to explain the presented results are the properties of an electron spin in an external magnetic field \mathcal{H}_{EZI} , the interaction between two electron spins \mathcal{H}_{EEI} and the behavior of a spin state at zero magnetic field \mathcal{H}_{ZFI} . They will be discussed in more detail in the following sections.

3.2.1. The Electron Zeeman Interaction

For the first time, Pieter Zeeman discovered as early as 1897 the effect that optical spectra are split by applying an external magnetic field [68]. For this, he was rewarded with the nobel prize in 1902 together with Hendrik Antoon Lorentz. Consequently, the splitting of spin states in an external magnetic field is called Zeeman splitting and is described by the corresponding term \mathcal{H}_{EZI} in the spin hamiltonian (3.2). It is defined as

$$\mathcal{H}_{EZI} = \mathbf{g} \cdot \mu_B \cdot \hat{\mathbf{S}} \cdot \vec{\mathbf{B}} \quad (3.3)$$

with the g-tensor \mathbf{g} , the Bohr magneton μ_B , the spin operator $\hat{\mathbf{S}}$, which consist of the Pauli matrices and the external magnetic field $\vec{\mathbf{B}}$. While the number of eigenstates is given by the multiplicity $2S + 1$ of a spin system, the eigenenergies yield

$$E_{|S, M_S\rangle} = M_S \cdot \mathbf{g} \cdot \mu_B \cdot \vec{\mathbf{B}} \quad (3.4)$$

with M_S defined as the projection of the spin S on the external magnetic field, summarized in Figure 3.1.

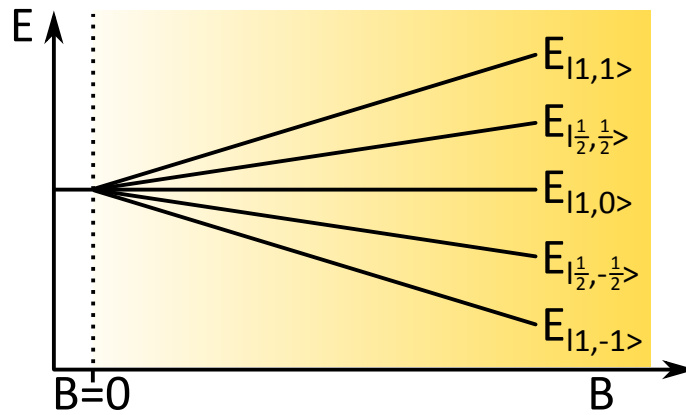


Figure 3.2.: Zeeman splitting for doublet and triplet multiplicity with the eigenenergies $E_{|S, M_S\rangle}$. At zero magnetic field the states are degenerate.

The energetic splitting of the eigenstates in an external magnetic field is depicted in Figure 3.2. The slope of the eigenstates with increasing magnetic field is only dependent on the spin state M_S and the g-tensor \mathbf{g} . The g-tensor is isotropic and yields to be

3. Electron Paramagnetic Resonance

$g=2.002319\dots$ for a free electron. However, deviations from this value exists for a spin in a host material caused by its atomic surroundings. This is due to a superposition of the external magnetic field with small local fields originating from the orbital momentum (spin-orbit coupling) or the crystal field. These deviations differ for different directions of the magnetic field, which yields a 3x3 matrix for the g-tensor. Nevertheless, it is diagonalizable and can be fully described by its three diagonal components g_{xx} , g_{yy} and g_{zz} . As the environment in every material is different, the g-tensor is a characteristic fingerprint for each material.

3.2.2. The Electron-Exchange Interaction

Considering the combination of two spin carrying particles, in this case fermions, will end up either in a singlet or triplet multiplicity (see Figure 3.1). Either a symmetric function for a triplet state or an antisymmetric function for a singlet state is formed. With that, the spatial wavefunction has to be symmetric in singlet and antisymmetric in triplet configuration. Combining the spatial wavefunction with the spin function will define the overall wavefunction, forming the atomic orbitals. If two electrons occupy the same spatial orbital, the Pauli principle will impose the spin state to be a singlet, because the total wavefunction has to be antisymmetric.

The electron exchange interaction is represented in the spin hamiltonian by the term \mathcal{H}_{EEI} [65, 69]:

$$\mathcal{H}_{EEI} = \hat{\mathbf{S}}_1^T \mathbf{J} \hat{\mathbf{S}}_2 = \begin{pmatrix} S_{1x} & S_{1y} & S_{1z} \end{pmatrix} \begin{pmatrix} J_{xx} & J_{xy} & J_{xz} \\ J_{yx} & J_{yy} & J_{yz} \\ J_{zx} & J_{zy} & J_{zz} \end{pmatrix} \begin{pmatrix} S_{2x} \\ S_{2y} \\ S_{2z} \end{pmatrix} \quad (3.5)$$

Here, $\hat{\mathbf{S}}_1$ and $\hat{\mathbf{S}}_2$ represent the spin operators of the two interacting spins and \mathbf{J} is a 3x3 matrix describing the exchange interaction. The origin for \mathbf{J} is the quantum mechanically postulated indistinguishability of identical particles. The underlying mechanisms are the overlap of the wavefunctions, the electric, coulombic interaction between the two partizipating particles as well as the Pauli principle. The strength of the magnetic interaction which is caused by their magnetic momenta is by far weaker than the exchange interaction and will be discussed in the next section. By considering only the isotropic part of the exchange operator \mathbf{J} , equation 3.5 simplifies to [65]

$$(\mathcal{H}_{EEI})_{iso} = J_0 \hat{\mathbf{S}}_1^T \hat{\mathbf{S}}_2 \quad (3.6)$$

where $J_0 = \frac{1}{3} tr(\mathbf{J})$ is the isotropic electron-exchange coupling constant. Whether the singlet or the triplet state possess the lower energy is dependent on the sign of J_0 . For

two hydrogen atoms $J_0 > 0$, which means that the bonding state is in singlet configuration and lies lower in energy. For the materials investigated in this work, however, the triplet state is energetically lower than the singlet state, i.e. $J_0 < 0$. The splitting between singlet- and triplet state caused by the exchange interaction is depicted in Figure 3.3. Unfortunately, several definitions are used for J_0 in literature ranging from $-2J_0$ to $2J_0$. In this work the definition used in [65, 67] was used.

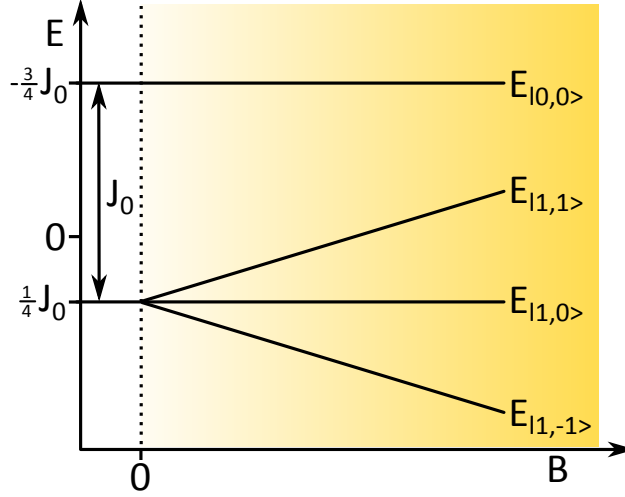


Figure 3.3.: Energetics for two interacting spins forming either singlet or triplet configuration. They are split by the isotropic exchange interaction J_0 .

3.2.3. The Zero Field Interaction

The term of the zero field interaction \mathcal{H}_{ZFI} has to be added to the spin hamiltonian (3.2) for spin systems with more than one spin, i.e. the total spin $S \geq 1$ [65]:

$$\mathcal{H}_{ZFI} = \hat{\mathbf{S}}^T \mathbf{D} \hat{\mathbf{S}} = \begin{pmatrix} S_x & S_y & S_z \end{pmatrix} \begin{pmatrix} D_{xx} & D_{xy} & D_{xz} \\ D_{yx} & D_{yy} & D_{yz} \\ D_{zx} & D_{zy} & D_{zz} \end{pmatrix} \begin{pmatrix} S_x \\ S_y \\ S_z \end{pmatrix} \quad (3.7)$$

It describes the magnetic interaction of two spins in close vicinity. The magnetic momentum of one spin will influence the local magnetic field of the other spin and vice versa. This impact leads to an energetic splitting of the spin sublevels even if no external magnetic field is applied. Therefore, the degeneracy at $B = 0$ is lifted, as shown in Figure 3.2 and 3.3. \mathbf{D} is defined as a second order tensor to account for its spatial dependency which makes it anisotropic. However, it can be diagonalized in its eigenframe:

3. Electron Paramagnetic Resonance

$$\mathbf{D} = \begin{pmatrix} D_{xx} & 0 & 0 \\ 0 & D_{yy} & 0 \\ 0 & 0 & D_{zz} \end{pmatrix} = \begin{pmatrix} \frac{1}{3}D - E & 0 & 0 \\ 0 & \frac{1}{3}D + E & 0 \\ 0 & 0 & -\frac{2}{3}D \end{pmatrix} \quad (3.8)$$

Thereby, the tensor \mathbf{D} is completely describable by the parameters D and E . While D accounts for the deviation of an isotropic electron distribution, E represents its rhombicity. The influence of both parameters on the energetics at zero field is illustrated in Figure 3.4.

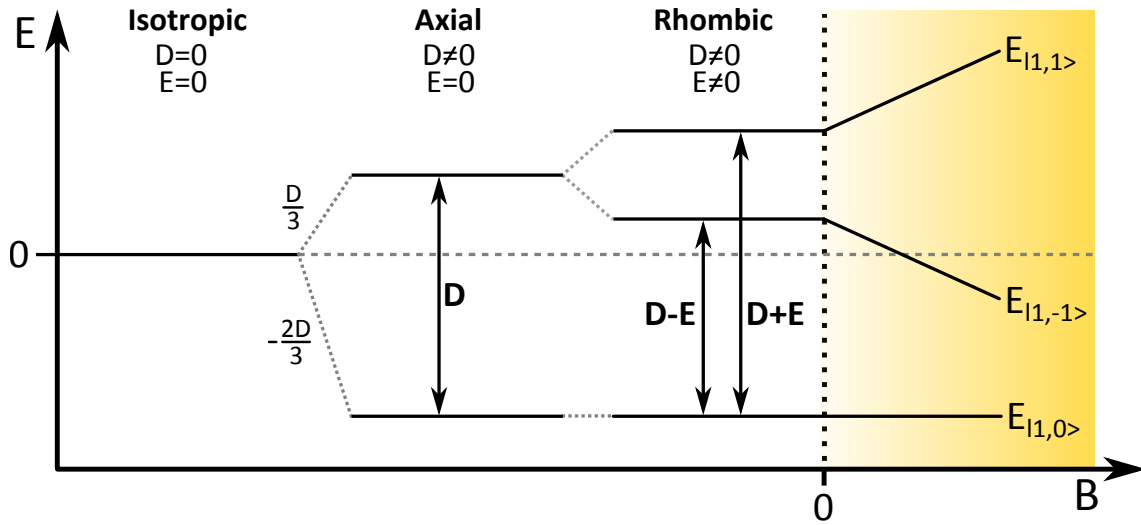


Figure 3.4.: Zero field splitting for a spin system with $S = 1$. The degeneracy is repealed by the parameters D and E , depending on the symmetry of the present wavefunction. Modified from [70].

The symmetry dependency of \mathbf{D} makes it an ideal probe to connect the wavefunction of two coupled spins with the molecular structure of the surrounding crystal. Therefore, the angle between externally applied magnetic field and the orientation of the wavefunction has to be changed. This leads to an angular dependence of D and E :

$$D = D_0 \cdot \left(\cos^2\theta - \frac{1}{3} \right) \quad (3.9)$$

$$E = E_0 \cdot \sin^2\theta \cdot \cos(2\phi) \quad (3.10)$$

With θ being the polar- and ϕ the azimuthal angle between $\vec{\mathbf{B}}$ and the crystal axis \vec{c} of a molecule. As a result, the magnetic separation of the transitions between the $\Delta M_s = 1$ sublevels is obtainable:

$$\Delta B = \frac{1}{\mu_B g} (D_0 \cdot (3 \cos^2\theta - 1) + 3 E_0 \sin^2\theta \cos(2\phi)) \quad (3.11)$$

3.2.4. Distance Dependency of Interactions

The previously introduced electron-exchange interaction \mathcal{H}_{EEI} and zero field interaction \mathcal{H}_{ZFI} are strongly dependent on the distance between the coupled particles. Therefore, the strength of the present interactions and its influence on the measurement signal has to be considered. The zero field interaction weakens with increasing distance between the two present spins according to [65]:

$$D = \frac{3\mu_0}{16\pi h} \frac{g_1 g_2 \mu_B^2}{r_{12}^3} (1 - 3 \cos^2 \theta) \quad (3.12)$$

Here, D is the zero field splitting parameter, μ_0 the permeability constant, g_1 and g_2 the g-factors of spin 1 and spin 2, r_{12} is the distance between spin 1 and 2 and θ is the angle between the spin vector \mathbf{r} and the direction of the external magnetic field \hat{e}_B , which is defined to be 0° . For the derivation of equation 3.12 the point magnetic dipole approximation was used, i.e. both spins have no extent, so $E = 0$.

For the electron-exchange interaction, the situation becomes more difficult. There are a lot more parameters involved in the emergence of the correct \mathbf{J} . The underlying principle, however, is that the overall wave function has to be antisymmetric when two electrons are exchanged. Therefore, the exchange interaction decreases exponentially with increasing distance due to the overlap of orbital wave functions [71, 72, 73]:

$$J = J_0 \cdot e^{-\beta r_{12}} \quad (3.13)$$

Here, J_0 is the maximum electronic coupling, β the decay coefficient of the electronic coupling and r_{12} the distance between the two coupled spins. Unfortunately, the exact determination of J is too complex for an explicit calculation [74, 71]. However, an upper limit for J in isolating solids was proposed by Jeschke [71] to be $J_0 = 4.05 \cdot 10^{11}$ MHz and $\beta = 18 \text{ nm}^{-1}$. Efimova [73] estimated J_0 to be in the range of $2.24 \cdot 10^{11} \leq J_0 \leq 2.24 \cdot 10^{13}$ MHz and Moser [72] found $\beta \approx 14 \text{ nm}^{-1}$. These upper and lower limits for the exchange interaction together with the distance dependency of the zero field interaction are calculated in Figure 3.5.

3. Electron Paramagnetic Resonance

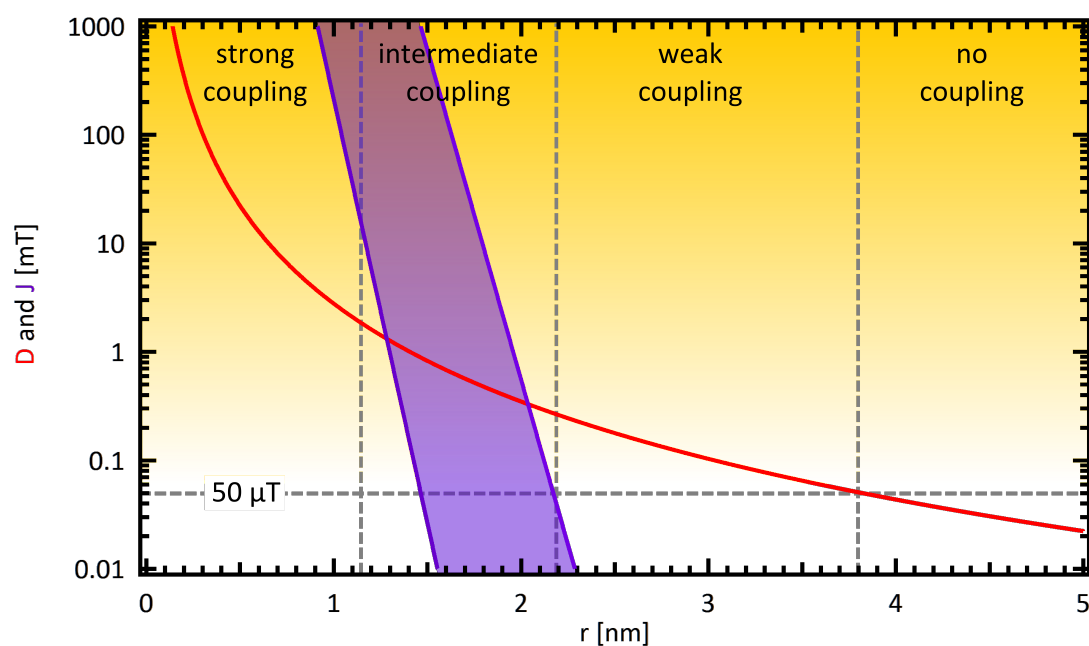


Figure 3.5.: The Electron-Exchange Interaction J (purple) as well as the zero field interaction D (red) in dependence of the distance between two interacting spins. For D the point magnetic dipole approximation was used and for J a maximum and minimum estimation was taken from literature [73, 72, 71]. With increasing distance one can distinguish between four coupling regimes. The earth magnetic field of approximately $50 \mu\text{T}$ is shown for comparison. Modified from [73, 75].

3.3. Electron Paramagnetic Resonance Theory

Not only was the alignment of spins by an external magnetic field discussed in the previous chapter, but also several crucial interactions. Now, the basic principles are highlighted how microwaves are able to manipulate the aligned spins. These underlying mechanisms of electron paramagnetic resonance technique are summarized based on the considerations in [65, 76, 77].

From a classical point of view, a particle with the mass m , the charge q and the angular momentum \vec{l} will result in a magnetic momentum of $\vec{\mu} = \frac{q\vec{l}}{2m}$. According to the corresponding principle, this leads to a magnetic angular momentum for a single electron spin (see section 3.1):

$$\mu_B = \frac{e\hbar}{2m_e} \quad (3.14)$$

Here, μ_B is defined as Bohr magneton, e the elementary charge, \hbar the Planck constant and m_e the electron mass. The improved sensitivity of EPR in comparison with its analogon NMR is due to the 1836 times larger mass of a proton compared to an electron. However, a single electron does not behave like a charged particle so the corresponding principle is not strictly applicable. Therefore, the angular momentum of the electron spin yields

$$\vec{\mu} = -g \cdot \mu_B \cdot \vec{S} \quad (3.15)$$

with the total spin \vec{S} and the g-factor g (see chapter 3.2.2). Applying an external magnetic field B_0 in z-direction of the laboratory reference frame results in a splitting of energy states (compare equation 3.4 in section 3.2.1) with the energy difference:

$$\Delta E = |\vec{\mu}| B_0 = g\mu_B B_0 \quad (3.16)$$

Thereby, the angular frequency of a transition between two sublevels is

$$\omega_0 = \frac{g_z \mu_B B_0}{\hbar} \quad (3.17)$$

where ω_0 is defined as the Larmor frequency and g_z is the z-component of the g factor. This transition is schematically shown in Figure 3.6.

In the laboratory the frequency ν ($= \omega/2\pi$) is often used instead of the angular frequency ω . This yields for magnetic fields, accessible with electro magnets, frequencies in the range up to 42 GHz. In this work, microwaves with the frequency of $\nu \approx 9.4$ GHz (X-band range) were used. Combined with a g-factor of ≈ 2 this yields a resonant magnetic field $B_0 \approx 337$ mT.

3. Electron Paramagnetic Resonance

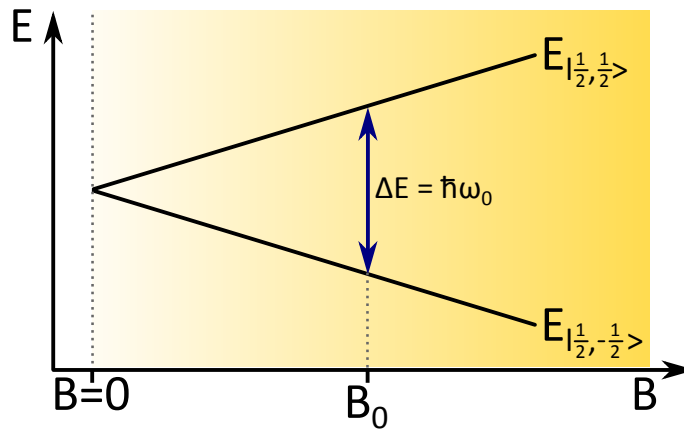


Figure 3.6.: Zeeman splitting for a doublet spin system with eigenenergies $E_{|s,m_s\rangle}$ and its corresponding transition at the magnetic field B_0 , yielding in an energy splitting of $\Delta E = \hbar\omega_0$.

In principle it is possible to measure even single spins with EPR related methods. In this work, however, an ensemble of many spins was investigated. Therefore, the previous considerations have to be extended by the macroscopic magnetization of a sample.

Only the difference between spins aligned parallel and antiparallel to the external magnetic field contribute to the total magnetization. This population difference is strongly dependent on the temperature and is defined by the Boltzmann distribution. In the high temperature approximation ($\Delta E \ll k_B T$), the polarization ϵ of a sample can be introduced:

$$\epsilon = \frac{\Delta E}{k_B T} = \frac{g\mu_B B_0}{k_B T} \quad (3.18)$$

Hence, the polarization of the transition is proportional to the applied magnetic field and inverse proportional to the temperature. The high temperature approximation is valid even at cryogenic temperatures of liquid helium for microwaves in X-band. However, it could become invalid with increasing Larmor frequencies at high magnetic fields. With the polarization ϵ , the magnetization in thermal equilibrium is defined by the sum of the magnetic momenta of the single spins, normalized on the sample volume V :

$$\vec{M}_0 = \frac{1}{V} \sum_{i=1}^N \vec{\mu}_i = \frac{\epsilon N g \mu_B}{2} \hat{e}_z \quad (3.19)$$

with \hat{e}_z as a unit vector in z-direction and N the total number of spins.

3.3. Electron Paramagnetic Resonance Theory

The magnetization vector \vec{M}_0 is not fixed in space when exposed to an external magnetic field, though, but moves according to the equation of motion:

$$\frac{d\vec{M}}{dt} = \vec{M} \times \frac{-g\mu_B}{\hbar} \vec{B}(t) \quad (3.20)$$

For a static magnetic field aligned in z-direction, the magnetization \vec{M} precesses with the Larmor frequency ω_0 around the external magnetic field \vec{B} , if $M_x, M_y \neq 0$. This process is depicted in Figure 3.7 a).

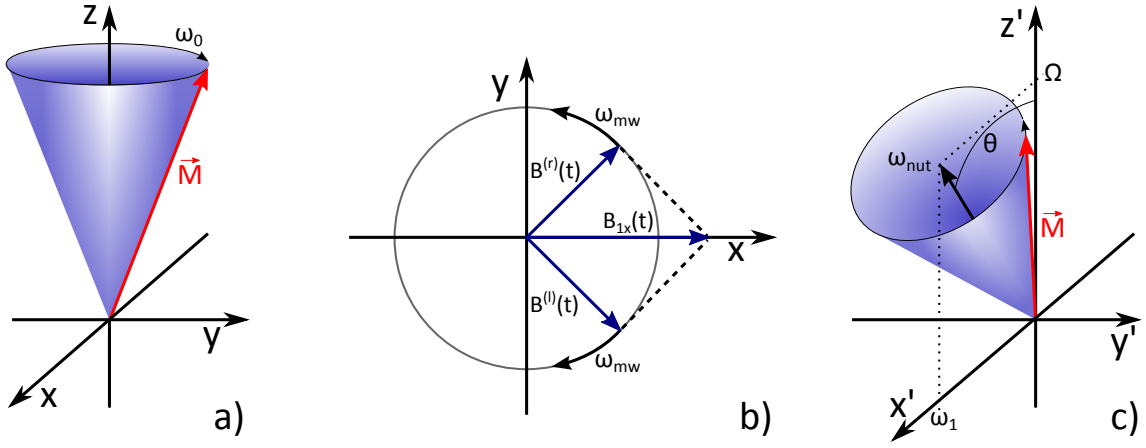


Figure 3.7.: a) Precession of the magnetization vector with the Larmor frequency ω_0 around the applied magnetic field B_0 in z-direction. b) Decomposition of a linearly polarized field in x-direction $B_{1x}(t)$ into two oppositely rotating fields $B^{(r)}(t)$ and $B^{(l)}(t)$. c) Magnetization vector in a coordinate system rotating with ω_{mw} . The additional alternating magnetic field in x-direction leads to the nutation frequency ω_{nut} .

In order to deflect the magnetization vector from the z-direction an additional magnetic field has to be applied. Equation 3.20 shows that any field, which is not in z-direction leads to a deflection of \vec{M} . However, if the frequency of the applied field differs from the Larmor frequency, the effect on the magnetization vector will average out over time. Due to the cross product in equation 3.20, a field in x- or y-direction has the largest effect on the magnetization. Therefore, a linearly polarized field in x-direction is introduced to the system:

$$B_{1x}(t) = 2 \cdot B_1 \cdot \cos(\omega_{mw} t) ; B_{1y}(t) = 0 ; B_{1z}(t) = 0 \quad (3.21)$$

with the amplitude $2B_1$ and the frequency ω_{mw} of the microwave field.

With this, equation 3.20 is analytically not solvable but decomposition into two oppositely rotating fields with equal magnitude yields (compare Figure 3.7 b)):

$$B_{1x}^{(r)}(t) = B_1 \cdot \cos(\omega_{mw} t) ; B_{1y}^{(r)}(t) = B_1 \cdot \sin(\omega_{mw} t) ; B_{1z}^{(r)}(t) = 0 \quad (3.22)$$

3. Electron Paramagnetic Resonance

$$B_{1x}^{(l)}(t) = B_1 \cdot \cos(\omega_{mw} t) ; B_{1y}^{(l)}(t) = -B_1 \cdot \sin(\omega_{mw} t) ; B_{1l}^{(r)}(t) = 0 \quad (3.23)$$

Only the right-handed rotating field follows the precession of the magnetization vector. The left-handed field rotates in opposite direction. Therefore, it has no relevant influence on \vec{M} . Considering only the right-handed microwave field and transferring the laboratory frame into a coordinate system which rotates with the microwave frequency ω_{mw} , equation 3.20 can be solved:

$$\frac{dM_x}{dt} = -(\omega_0 - \omega_{mw})M_y ; \frac{dM_y}{dt} = (\omega_0 - \omega_{mw})M_x - \omega_1 M_z ; \frac{dM_z}{dt} = \omega_1 M_y \quad (3.24)$$

Here, equation 3.7 was used together with the equivalent for the alternating magnetic field $\omega_1 = \frac{g_x \mu_B B_1}{\hbar}$. In the rotating coordinate system, the magnetization vector precesses only with the difference between the Larmor- and the microwave frequency in z-direction:

$$\Omega = \omega_0 - \omega_{mw} \quad (3.25)$$

The alternating magnetic field in x-direction leads to an additional precession around the x-axis with the frequency ω_1 . The resulting superimposed frequency of the magnetization vector will be the nutation frequency ω_{nut} , which is:

$$\omega_{nut} = \sqrt{\Omega^2 + \omega_1^2} \quad (3.26)$$

As depicted in Figure 3.7 c), the magnetization vector will be shifted from the z-direction by the angle θ :

$$\theta = \arctan\left(\frac{\omega_1}{\Omega}\right) \quad (3.27)$$

In case of a resonant microwave frequency ($\omega_{mw} = \omega_0$), Ω will be 0 and $\theta = 90^\circ$. On the other hand, if the offset from the resonance frequency is very large ($\Omega \gg \omega_1$), θ will be ≈ 0 . This means that the magnetization vector is not relevantly affected and remains on its thermodynamic equilibrium position.

However, equations 3.24 can not be the final solution. In fact, the magnetization vector that was once deflected would precess in this position forever without returning to its equilibrium state. Therefore, time constants have to be included whereby the system could relax back to its initial state. Here, the z-direction relaxes via spontaneous transitions between the two levels, while the x- and y-direction relaxes via spin conserving processes. As a result, two different relaxation times are obtained, which are

included in general applicable equations of motion valid for a two level system. They are called Bloch equations:

$$\frac{dM_x}{dt} = -\Omega M_y - \frac{M_x}{T_2} ; \quad \frac{dM_y}{dt} = \Omega M_x - \omega_1 M_z - \frac{M_y}{T_2} ; \quad \frac{dM_z}{dt} = \omega_1 M_y - \frac{M_z - M_0}{T_1} \quad (3.28)$$

Thereby, T_1 is the spin-lattice-relaxation time and T_2 the spin-spin-relaxation time. The relaxation mechanisms are also due to alternating magnetic fields. T_1 is mainly caused by phonon coupling or the relaxation of nuclear spins in x- and y-direction. T_2 is additionally influenced by flip-flop transitions where both spins change their state. Here, the alternating magnetic fields have to be in z-direction. In solid states T_1 is usually longer than T_2 .

In a standard EPR experiment the observable is the quantity of absorbed microwaves by an ensemble of spins, i.e. the magnetization (compare equation 3.19). Unfortunately, the detection of electromagnetic waves in the microwave regime is technically very challenging. Therefore, a large amount of spins is needed in order to get a sufficiently signal to noise ratio. However, organic devices possess only a little amount of active material due to the very thin active layer. Fortunately, other detection methods are available where the problem of microwave detection is circumvented. These are explained in the following sections.

3.4. Optically Detected Magnetic Resonance Theory

Electromagnetic waves in the visible regime are easily detectable, for example by a simple silicon photo diode. This is exploited by detecting the luminescence of a sample, whose intensity changes under magnetic resonant conditions. This technique is called optically detected magnetic resonance (ODMR). Hence, ODMR shows a largely improved sensitivity, meaning that already a small number of spin carrying particles are detectable. While the large amount of non-interacting charge carriers, i.e. electrons and polarons are visible via conventional EPR, the relatively small quantity of strongly interacting particles like triplet excitons could be detected via ODMR (compare with Figure 3.5). Furthermore, it is possible to switch from large, bulky samples to thin films that are more realistic concerning real organic devices.

Nevertheless, this measurement technique is not a direct detection method. Hence, a detour has to be taken by detecting optical photons. This is only possible because transitions between spin sublevels are coupled to optical transitions via a system of

3. Electron Paramagnetic Resonance

rate equations. Three mechanisms are seen to be mainly responsible for the signal generation, namely triplet-triplet annihilation [78, 79, 32, 80, 81], spin dependent recombination [82, 32, 33] and ground state depletion [83, 84, 85]. The latter is the dominant mechanism in isolated defects embedded in a host material, like NV-centers in diamond or silicon-vacancies in silicon carbide. While the triplet-triplet annihilation and the triplet polaron quenching will be further discussed in the following, the ground state depletion will be disregarded because only organic semiconductors are subject to this work.

3.4.1. Triplet-Triplet Annihilation

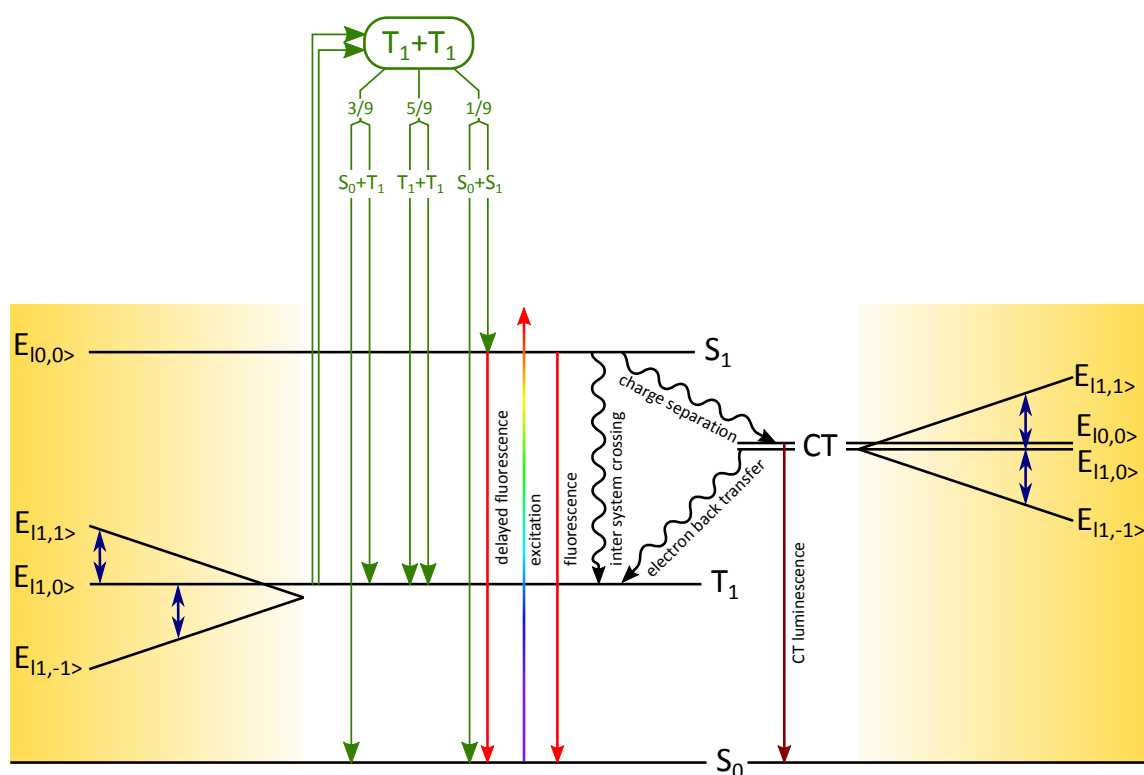


Figure 3.8.: Energetic scheme with possible transitions explaining the occurrence of the ODMR signal. In green the triplet-triplet annihilation process is shown with its decay possibilities and probabilities. The spin dependent recombination is illustrated on the right hand side with the corresponding population and depopulation mechanisms of the charge transfer state CT . Furthermore, S_0 is the ground state, S_1 the first excited singlet state and T_1 the first excited triplet state. Modified from [70].

The relaxation of a triplet exciton to the singlet ground state is spin forbidden. Therefore, it has to take place via non-radiative phonon scattering or, less probable, via phosphorescence. On this account, triplet excitons in organic semiconductors possess a much longer lifetime than their singlet counterparts. This long lifetime leads to a rela-

tively high population of excited triplet states in a cw-experiment, despite the very low intersystem crossing rate from an excited singlet state. If two triplet excitons meet, they will create a state with quintuplet multiplicity. This short living intermediate state possesses three different scattering channels. With the probability of $\frac{1}{9}$ the two excitons will decay into a singlet excited state S_1 and a singlet ground state S_0 . Furthermore, the scattering will end in a S_0 and a triplet excited state T_1 with the probability of $\frac{3}{9}$ or with the probability of $\frac{5}{9}$ back into two T_1 states. This process is depicted in Figure 3.8 (green). In other words, one scattering event will lead with 5.6 % ($\frac{1}{18}$) absolute probability to a S_1 state, which in turn possesses the possibility to recombine radiatively to the ground state S_0 . As this process stems from a long living triplet exciton decay channel, the lifetime is also longer than for the common singlet fluorescence. Therefore, it is called delayed fluorescence. This is seen as the main mechanism behind the occurrence of the ODMR signal in many organic semiconductors, because a change in population of triplet sublevels will couple to the scattering mechanism and has an influence on the delayed fluorescence [86, 87, 78, 88, 89, 90, 80].

Despite the fact that only 5.6 % of all scattering processes will have an effect on the ODMR signal, one has to keep in mind that only 22.2 % ($\frac{2}{9}$) will end in the singlet ground state and are lost for signal generation (disregarding ground state depletion). With the remaining probability of 72.2 % ($\frac{7}{9}$) this scattering leaves the original excited triplet states unchanged, which subsequently may scatter again.

3.4.2. Spin-Dependent Recombination Model

For the spin-dependent recombination model the distance dependency of different coupling interactions (chapter 3.2.4) has to be recalled. When a singlet exciton gets split, it will form a charge transfer (CT) state. Here, the electron is situated on the acceptor, while the polaron is placed on the donor. In addition to this geminate process, if two initially free charge carriers meet at an interface, they will form a charge transfer state as well. This could be in a singlet- or triplet configuration with probabilities of 25% or 75%, respectively. The morphology spatially separates the two spin carrying particles, which is why J - and D -coupling are weak. With respect to Figure 3.5 the CT state lies in the weak coupling regime and the corresponding energetic splitting is depicted on the right hand side of Figure 3.8 [91, 71].

A small J results in energetically almost degenerate $E_{|0,0\rangle}$ and $E_{|1,0\rangle}$ states, which facilitates inter system crossing between the two of them. The $E_{|0,0\rangle}$ state could be coupled radiatively to the ground state, yielding in a red shifted CT-luminescence or exciplex emission. Furthermore, from the CT-state an electron back transfer mechanism could take place, if the triplet excited state T_1 is lower in energy. Both transitions

3. *Electron Paramagnetic Resonance*

lead to a depopulation of the $E_{|1,0\rangle}$ state. Equalizing the population between the three triplet sublevels under magnetic resonant conditions results in a repopulation of $E_{|1,0\rangle}$. This has a great influence on the rates of CT-luminescence and electron back transfer. Due to the small zero field interaction the transitions $E_{|1,1\rangle} \rightarrow E_{|1,0\rangle}$ and $E_{|1,-1\rangle} \rightarrow E_{|1,0\rangle}$ will take place at the same magnetic field position.

3.5. Electrically Detected Magnetic Resonance Theory

Besides the sensitivity improving method of detecting photons, utilized in ODMR, electricity is also detectable with very high accuracy. This approach is called electrically detected magnetic resonance (EDMR). Here, the observable is neither the microwave absorption (like in common EPR) nor the change in luminescence (ODMR), but the change of current or voltage in a device due to magnetic resonant conditions.

3.5.1. Spin-Dependent Recombination

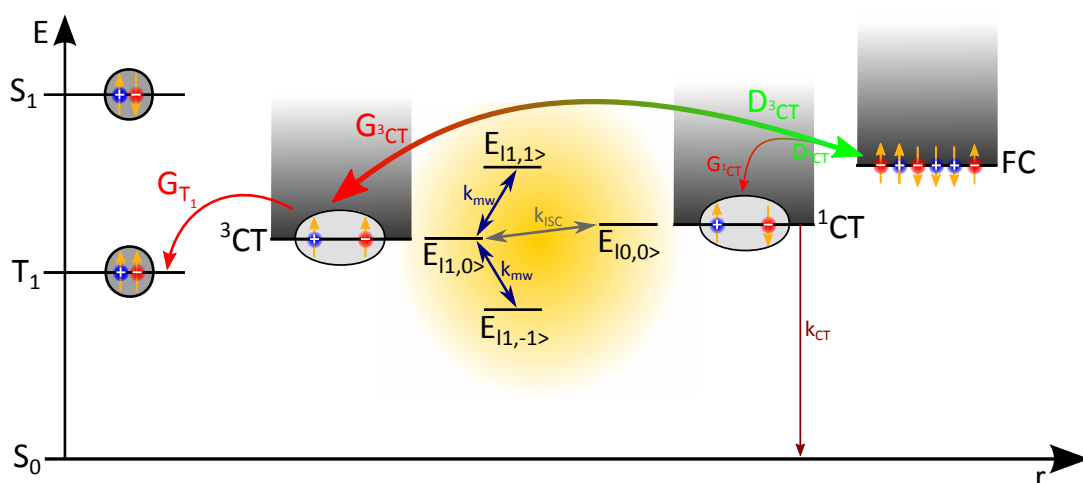


Figure 3.9.: Energetic scheme of the spin dependent recombination process. Two initially free charge carriers meet and form either a triplet (3CT , 75%) or singlet (1CT , 25%) charge transfer state with the rates $G_{{}^3CT}$ and $G_{{}^1CT}$, respectively. 3CT can recombine further into an excited triplet state T_1 with the rate G_{T_1} and 1CT to the ground state S_0 with the rate k_{CT} . Alternatively, both CT states can dissociate again into free charge carriers with the respective rates $D_{{}^3CT}$ and $D_{{}^1CT}$.

In 1972, an effect of spin resonant conditions on the current was observed for the first time in pure silicon [92]. In this work, a spin-dependent recombination mechanism was introduced mainly explained by the magnetization change due to the Boltzmann distribution. Nevertheless, neither the temperature dependency nor the signal strength were explainable by this model. In 1978, Kaplan, Solomon and Mott [93] suggested a different model that introduced the formation of an intermediate state prior to the actual recombination process. The main difference for this model is the demand that this state has to recombine or dissociate before the involved charge carriers may participate again on a different interaction. The underlying process of spin dependent recombination is very similar to aforementioned model explained for ODMR (see

3. Electron Paramagnetic Resonance

chapter 3.4.2) and is schematically shown in Figure 3.9. Here, two initially free charge carriers meet and form either a singlet or triplet charge transfer state with 25% or 75% probability, respectively. Afterwards, they either recombine to the ground- or excited triplet state or they dissociate again into non-interacting charges. The recombination process decreases the charge carrier density in the device, as a drain for free charge carriers is introduced. Therefore, spin resonant conditions influence the charge carrier density by the change of dissociation- or decay rates.

Most investigations concerning spin-dependent recombination were realized on either crystalline or amorphous silicon [94, 95, 96, 97, 98]. With the emergence of organic solar cells, however, this technique was also applied to organic semiconductors like PPV or polythiophene [99, 82], where similar effects were observed.

3.5.2. Spin-Dependent Transport

Besides the process of spin-dependent recombination, another spin-dependent effect is conceivable. Thereby, the spin dependent mechanism is the charge carrier transport. Organic semiconductors exhibit mainly a hopping like process via localized states. Each hopping step is described as a phonon activated tunneling event, as depicted on the left hand side of Figure 3.10. Thereby, two charge carriers located on the same state are not allowed to possess the same spin. Under spin resonant conditions, however, the Pauli exclusion is circumvented and the overall mobility should be enhanced. This spin-dependent transport is depicted on the right hand side of Figure 3.10. The device parameter, which is mainly affected, is the charge carrier mobility μ , as more pathways are accessible under resonant conditions.

3.5.3. Detection Modes

Keeping in mind the typical j-V-characteristic of an organic solar cell (compare Figure 2.8) the current density j changes from a blocking behavior ($V < 0$), over the, for solar cell application relevant fourth quadrant ($0 < V < V_{oc}$) to the injection regime ($V > V_{oc}$). Therefore, one could think about many points to measure the current in order to detect spin dependent effects. Unfortunately, a solar cell diode only follows the Ohmic law $\vec{j} = \sigma \cdot \vec{E}$ for high injection currents ($V > V_{oc}$) and the correct description of the j-V-curve becomes a lot more complicated. Derived from the Shockley equation [101] Waldauf [102] has found a more suitable expression for the j-V-characteristics of an organic solar cell:

$$j = j_0 \cdot \left(e^{-\frac{q(V-jR_s)}{nk_B T}} - 1 \right) + \frac{V - jR_s}{R_p} + j_{illu} \quad (3.29)$$

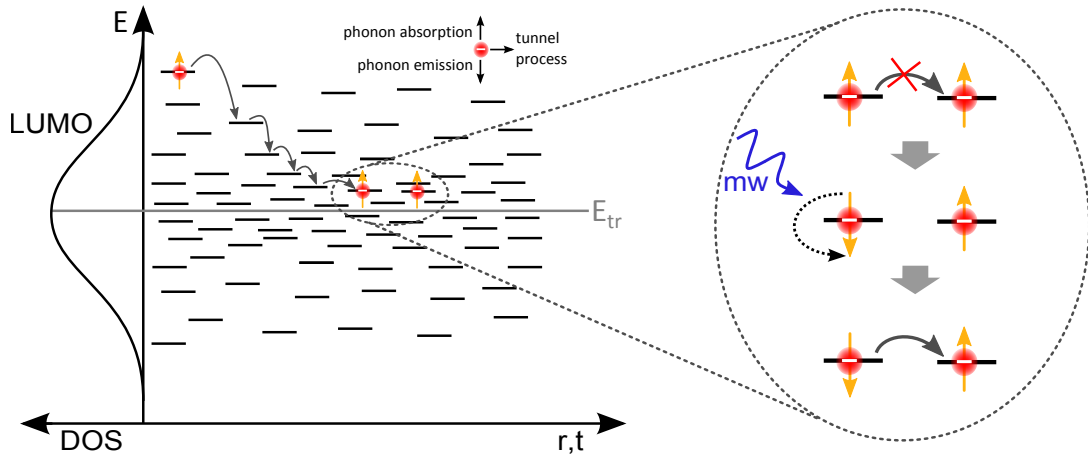


Figure 3.10.: Gaussian distribution of localized states around the transport energy E_{tr} after the Gaussian disorder model. A generated charge carrier relaxes due to a phonon assisted tunneling process (left). The occupancy of a single state by two identical particles is Pauli forbidden. Applying spin resonant conditions circumvents this prohibition (right). Modified from [100].

Here, j is the measured current density throughout the whole device, j_0 the reverse current, n the ideality factor, V the applied voltage $R_{s,p}$ the series and parallel resistance, respectively, and j_{illu} the generated current by illumination.

As a consequence, it becomes obvious that measuring the current is detrimental in order to distinguish between different origins of the spin dependent signal.

At V_{oc} , on the other hand, the generation of charge carriers is equal to the recombination, as no charges are extracted. With that, one may exclude any transport effects at this point. For an organic solar cell, the open circuit voltage could be derived to be [103, 104]:

$$V_{oc} = \frac{E_g}{q} - \frac{k_B T}{q} \cdot \ln \left(\frac{N_c^2}{np} \right) \quad (3.30)$$

At this, E_g is the effective band gap, N_c the effective density of states and n and p the charge carrier densities for electrons and holes, respectively. Assuming a constant N_c for a specific donor-acceptor blend, V_{oc} is only dependent on the charge carrier densities n and p . As these are only connected to generation (which is assumed to be constant for a given illumination intensity) and recombination, this working point of the diode seems to be ideal for the investigation of spin dependent recombination.

4. Experimental Section

In the previous chapter, a short overview was given concerning the underlying theory of the realized experiments. Now, the experimental details will be discussed, starting with the used materials, highlighting the sample preparation and closing with the description of the used experimental setups.

4.1. Materials

As already discussed in chapter 2.2, organic bulk heterojunction solar cells consist of two classes of organic semiconductors. The first group, the electron donors, have a higher LUMO in comparison to their counterpart, the electron acceptors. Furthermore, the donor materials should possess a high hole mobility, whereas the electron acceptor a high electron mobility. The mixing of both constituents in a certain ratio, will form the active layer of an organic bulk heterojunction solar cell. Almost all investigated materials in this work represent the most up to date available organic semiconductors for photovoltaic applications.

4.1.1. Donor-Materials

Donor materials in organic photovoltaics consist mainly of polymers, which are solution processable or small molecules, which are most often evaporated. Nonetheless, solvable small molecules emerged in the past years, unifying the advantages of solution processing together with the higher purity and negligible batch-to-batch variation of small molecules. Polymers, on the other hand, are dividable into different categories. Monomer based donors, like MDMO-PPV or P3HT were used in the first generation of bulk heterojunction solar cells. The vast increase in efficiencies over the last years was mainly due to the development of novel donor-acceptor copolymers, such as its most famous representative PTB7. More detailed descriptions of the used donor materials in this work will be given in the following.

4. Experimental Section

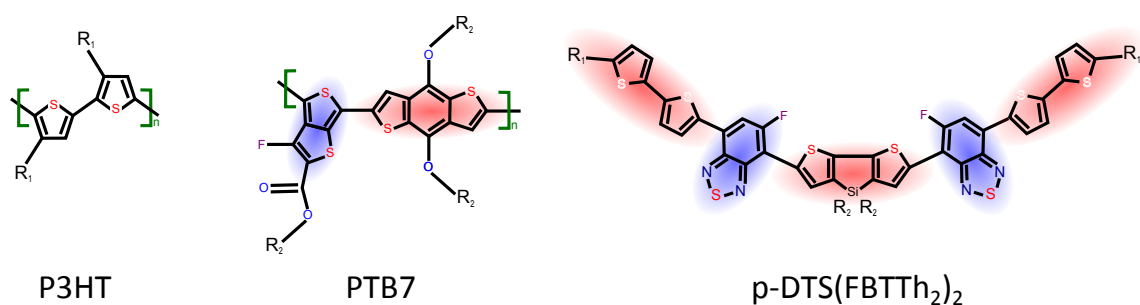


Figure 4.1.: Structural formulas of the organic donor materials used in this work P3HT, PTB7 and p-DTS(FBTTh₂)₂. The electron donating (red) and accepting (blue) regions are indicated. The full names are written in the main text. R₁ are hexyl- and R₂ ethylhexyl side chains.

P3HT

P3HT, short for poly(3-hexylthiophene), is the most extensively studied polymer for organic photovoltaics. It consists of a thiophene ring with an attached hexyl side chain for better solubility, as depicted in Figure 4.1. This polymer is able to form crystalline areas, even detectable by x-ray diffraction measurements [105], leading to improved transport properties [106]. Therefore, the device performances [14] are improved as well. For the enhancement in crystallinity, however, the position of the side chain is of crucial importance. A measure for this structural property is the regioregularity, which represents the percentage of side chains situated on the same atom of the thiophene ring. In this work, P3HT from Rieke metals was used with a regioregularity of $\geq 95\%$, called P200.

PTB7

The polymer PTB7 (poly[(4,8-bis-(2-ethylhexyloxy)-benzo(1,2-b:4,5-b')dithiophene)2,6-diylalt-(4-(2-ethylhexyl)-3-fluorothiopheno[3,4-b]thiophene)-2-carboxylate-2,6-diyl]) is one of the most famous and successful members of the class of donor-acceptor copolymers [51, 107, 108]. Its chemical structure is depicted in Figure 4.1. Not only consists this kind of polymers of one repeating monomeric unit, but of two or more [109, 110, 111]. They were developed with the goal to decrease the HOMO-LUMO gap, in order to increase light absorption and with that the short circuit current. Another aspect was a more ideal match with the LUMO of the acceptor, which would yield in an increased effective band gap and consequentially in a superior open circuit voltage [40, 112]. The last aspect to improve an organic semiconductor is a better $\pi - \pi$ -overlap of the molecular orbitals in order to facilitate charge transport over the polymeric backbone [113]. The name donor-acceptor (D-A) copolymer stems from the connection of an electron-rich and an electron-poor building block, forming the monomer of the D-A-copolymer.

It is assumed that this approach leads to a local dipole moment, which reduces the binding energy of the charge-transfer state in a polymer-fullerene blend [114, 115]. PTB7 consists of a combination of the electron-rich benzo[1,2-b:4,5-b']dithiophene (BDT) with the electron-poor thieno[3,4-b]thiophene (TT) building block. Both constituents are color coded in Figure 4.1. Whereas the BDT is responsible for an improved $\pi - \pi$ -overlap, the TT subunit reduces the HOMO-LUMO gap for enhanced light harvesting [113]. The PTB7 used in this work was purchased from 1-material.

p-DTS(FBTTh₂)₂

The synthesis of small molecules is more facile regarding purity, molecular weight and batch to batch variation compared to polymers. However, for a long time small molecules were only processable by vacuum deposition due to their lack of solubility. Solution processing has some advantages in comparison with evaporation techniques. The largest is the possibility of an efficient roll-to-roll process, where the active layer is deposited by a printing step. The aim for combining both benefits lead to the emergence of soluble small molecules [116, 117]. Until now, the power conversion efficiencies are comparable with the best performing polymer based solar cells [118, 119, 120]. One of the best performing soluble small molecules is p-DTS(FBTTh₂)₂. Its chemical formula is shown in Figure 4.1. Besides the steady advancement of the molecular structure [118, 121], other routes for pushing the solar cell performance were improvements of processing techniques [122, 123] and device layout [118, 119, 120]. For small molecules, an alternating D-A structure is not possible like in polymers. Therefore, p-DTS(FBTTh₂)₂ possesses a $D_1 - A - D_2 - A - D_1$ structure, which is color coded in Figure 4.1. Here, the central donating subunit D_2 consists of a bithiophene connected to a silicon atom with attached, aliphatic side chains for improved solubility (denoted R_2 in Figure 4.1). The following accepting parts are pyridyl[2,1,3]thiadiazole (PT) subunits with high electron affinity that leads to strong donor-acceptor interactions and a lower LUMO level. The purpose of the outer donating components D_1 is the extension of the π -conjugated system in order to reduce the HOMO-LUMO gap. The attached hexyl groups (R_1 in Figure 4.1) are again for an improved solubility [124, 121]. The p-DTS(FBTTh₂)₂ molecules used in this work were provided and synthesized by the group of Thuc-Quyen Nguyen from the University of California in Santa Barbara.

4.1.2. Acceptor-Materials

From the early days of organic solar cells until now, fullerene derivatives are by far the most commonly used acceptor material. They consist of carbon atoms and their most

4. Experimental Section

famous representative, the C_{60} , is spherically built by 12 pentagons and 20 hexagons. Basically, it looks very similar to a soccer ball. Its discovery in 1985 by Kroto and coworkers was rewarded with the nobel price in chemistry in 1996 [125]. A few years later, a new synthesis route made this molecule widely accessible for a variety of research and development applications [126, 127, 128, 129]. The intrinsic properties of fullerenes makes this class of materials an ideal acceptor for organic BHJ solar cells. A more detailed description of the used derivatives $PC_{60}BM$ and $PC_{70}BM$ is given in the following.

$PC_{60}BM$

As the solubility of C_{60} is quite poor, Hummelen developed a molecule consisting of a C_{60} -fullerene with an attached side chain. The resulting molecule was [6,6]-phenyl-C₆₁-butyric acid methyl ester, or shortly $PC_{60}BM$. It was first used in 1995 as a photodetector [130] and is depicted in Figure 4.2. Besides the increased solubility in organic solvents, $PC_{60}BM$ shows a high electron mobility of up to $2 \cdot 10^{-3} \text{ cm}^2 \text{ V}^{-1} \text{ s}^{-1}$, derived from space charge limited current (SCLC) measurements [131]. Furthermore, the exciton diffusion length was found to be in the order of 40 nm [132]. Nevertheless, the poor absorption, due to the high symmetry of the C_{60} -fullerene, reduces the $PC_{60}BM$ to an almost pure acceptor only taking a minor part in light absorption. Concerning the HOMO and LUMO levels of $PC_{60}BM$, no consensus can be found in literature. The values ranging from 3.7 eV to 4.5 eV for the LUMO and from 6.0 eV to 6.1 eV for the HOMO [133, 134, 135, 136]. With this, $PC_{60}BM$ possesses a sufficiently high electron affinity compared to the commonly used donor materials. Nevertheless, the loss in V_{oc} due to the LUMO offset is still a device performance limiting challenge.

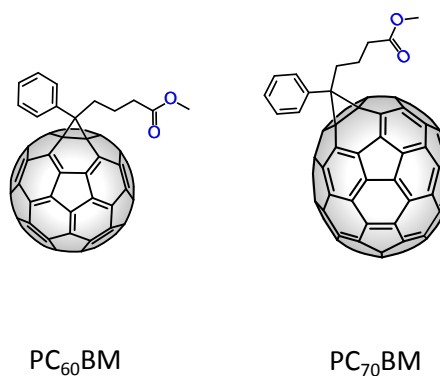


Figure 4.2.: Structural formulas of the organic acceptor materials $PC_{60}BM$ and $PC_{70}BM$ which were used in this work. The full names are given in the main text.

PC₇₀BM

The electron acceptor [6,6]-phenyl-C71 butyric acid methyl ester (PC₇₀BM) is very similar to PC₆₀BM concerning shape and nature, shown in Figure 4.2. However, the C₆₀-fullerene is replaced by a C₇₀-fullerene which yields a few property changes. First of all, the absorption is increased. This is due to the more asymmetric shape [137] and higher molecular weight compared to PC₆₀BM [135]. Therefore, PC₇₀BM is the best performing electron acceptor so far [137]. The electron mobility was found to be $1 \cdot 10^{-3} \text{ cm}^2 \text{ V}^{-1} \text{ s}^{-1}$ by SCLC measurements [138]. The LUMO level of PC₇₀BM differs only by a few meV compared to PC₆₀BM [60]. Nevertheless, it was shown that the electron has no preference to one of the two acceptor molecules within a charge transfer process in a donor acceptor blend [75]. Furthermore, the asymmetry of the C₇₀-fullerene causes the emergence of different isomers, depending on the position of the attached side chain. Synthesizing fullerenes will result in a mixture between different kinds. Here, mainly C₆₀ but only a small fraction of C₇₀ occurs. This results in a much higher price for PC₇₀BM compared to PC₆₀BM.

4.2. Sample Preparation

The custom-built samples were adapted to the requirements predefined by the used measurement methods. Nevertheless, all different samples have some preliminary steps in common. First of all, the material of interest has to be dissolved in an organic solvent, where chlorobenzene is most often used. This is done in a nitrogen filled glove-box, equipped with a microgram scale, diverse stir- and hotplates and a spin-coater. The special environment is needed in order to avoid exposure to humidity and oxygen as the used materials suffer from severe degradation. In the first step, a solution containing only the donor material is prepared. Depending on the solubility, different concentrations for the host solutions are used (p-DTS(FBTTh₂)₂: 21 mg/ml, PTB7: 8 mg/ml and P3HT: 30 mg/ml). In order to investigate pure materials, this solution can be used without further treatment. However, the actual solar cell blend is mostly more interesting. Therefore, the weighted acceptor material is solved in the host solution to get the best performing ratio between donor and acceptor (p-DTS(FBTTh₂)₂:PC₇₀BM, 1.5:1; PTB7:PC₇₀BM, 1:1.5; P3HT:PC₆₀BM, 1:0.8). Subsequently, the blends are further processed as described in the following.

4. Experimental Section

EPR-Samples

The samples for conventional EPR measurements feature the simplest design. For this, a standard X-band EPR tube with ≈ 2.8 mm inner diameter was taken and filled with a sufficient amount of material, normally ranging between $50 \mu\text{l}$ and $200 \mu\text{l}$. The more material the better, as the signal strength scales with the polarization, which is in turn dependent on the quantity of the investigated material (see chapter 3.3). Drying was achieved via a homemade pump system, where the EPR-tube gets evacuated to a rough vacuum of $\approx 10^{-2}$ mbar. During the drying process, a thick layer of the investigated material is deposited on the inner walls of the tube. After complete drying, the tube gets flushed at least six times with pure helium gas and is subsequently sealed under ≈ 20 mbar helium atmosphere with a blow torch. The use of helium as atmosphere of choice has two advantages. On the one hand, to avoid degradation as helium is not reactive at all. On the other hand, thermal coupling to the environment is needed for measurements at cryogenic temperatures, where helium stays gaseous in the whole accessible temperature range. The resulting sample tube is depicted in Figure 4.3. Usually, the inclosed material stays stable for a very long time without any detectable degradation effects.

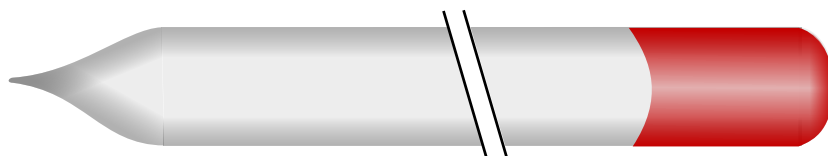


Figure 4.3.: Sketch of a typical EPR-sample. The standard X-band tube gets filled with the material of interest (shown in red), dried under rough vacuum and sealed by a blow torch with 20 mbar helium atmosphere.

PLDMR-Samples

In principle, it is possible to use the EPR samples for photoluminescence detected magnetic resonance (PLDMR) measurements as well. Nevertheless, the strong angular dependencies of the triplet excitons (see chapter 3.2.3), usually detected with PLDMR, may result in strange spectra that are not easily explainable. Therefore, the preparation method has to be altered. Thereby, a preferential orientation of the investigated molecules in the external magnetic field is obtained. Unfortunately, this leads to a more challenging preparation method.

If a powder-like PLDMR spectrum is desired, where all available angles are superimposed, a different kind of sample has to be prepared. For this, the EPR tube, filled with the solution of the investigated material, gets deep-frozen by liquid nitrogen. Subsequently, it is evacuated and flushed with helium. Closing the connection to the pump and unfreezing the solution leads to the recovery of the atmosphere due to the vapor pressure. This sequence is called a freeze-pump-thaw cycle which is repeated three times. Afterwards, the deep-frozen tube will be sealed again by a blow torch under ≈ 20 mbar helium atmosphere. Finally, thawing will result in a sealed, degassed solution. When measuring at cryogenic temperatures the solution freezes and the solved molecules orient in a random distribution.

As previously mentioned, only a small amount of material is needed in order to get a sufficient signal to noise ratio for PLDMR measurements. Way more crucial is the ability of a material to luminesce. Therefore, the sample can be designed in a more realistic fashion with respect to organic solar cells. Usually, a PLDMR sample is prepared as a thin film on a small slide of special quartz glass (herasil) which possesses almost no impurities of para- or ferromagnetic particles. Spin coating the film with a certain speed results in a film thickness of ≈ 100 nm, directly comparable to the thicknesses of real working devices. Subsequently, some effort has to be spent in order to make sure that the investigated material is only on one surface of the glass cuboid. Otherwise, the angular dependent measurements would be distorted. The glass piece is subsequently inserted into a standard EPR tube. The sealing, however, will be taken over by a special load lock system, shown in Figure 4.4. Here, a glass fiber is appended that allows direct excitation of the thin film on the herasil slide. If the EPR tube is turned by a certain angle, it will not influence the excitation source, i.e. the excitation is decoupled from rotation [70]. Another feature of the load lock system is its ability to evacuate the EPR tube and refill it with helium, which is very important for the investigation of environmental sensitive materials.

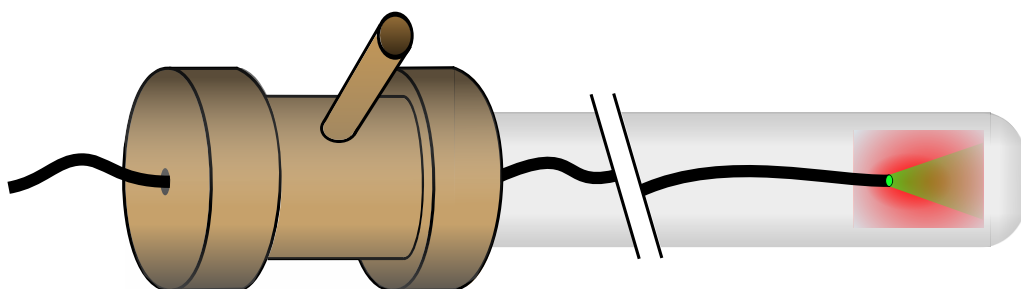


Figure 4.4.: Layout of the sample design for the angular dependent PLDMR measurements. The load-lock allows the insertion of a glass-fiber which decouples excitation of the investigated thin film (shown in green) from rotation. The inlet of the load-lock offers the possibility to evacuate- and fill the EPR tube with helium.

4. Experimental Section

EDMR-Samples

In order to detect current or voltage produced by an organic solar cell under magnetic resonance conditions, an actual working device has to be built. Realized on a standard lab-sized substrate with the dimensions 0.5" x 0.5", the fabrication is a routine process. However, the preparation becomes much more challenging for the application in the X-band resonator. The two main problems are the size and the usage of metal. Regarding the size, a standard EPR tube possesses an inner diameter of ≈ 2.8 mm. Nevertheless, special tubes are obtainable that are more accurately manufactured with an inner diameter of exactly 3 mm. Combining this with the thickness of the glass substrates, which is 1.1 mm, the solar cell has to be smaller than 2.8 mm in width. This constitutes the first boundary condition in size. The second problem is the use of metal in order to contact the solar cell. Electromagnetic waves are reflected by metal. Therefore, commonly used microwave resonators consist of metal or at least a metal coating on the inner walls because the reflection of electromagnetic waves results in a standing, resonant microwave. The introduction of a large amount of metal in the middle of the resonator would disturb the standing waves. Consequently, the quality of the resonator gets reduced drastically. Therefore, the corresponding contacts have to be lead out of the active part of the resonator, which means a distance of a few centimeters. This is accomplished via two 120 nm thick aluminum stripes forming the solar cell anode and cathode, respectively. The skin effect describes the exponential decay of current densities from the surface of metallic conductors by applying an alternating electric current. Using this, the penetration depth of microwaves with a frequency of 9.4 GHz results in 844 nm for aluminum. Accordingly, the transmitted microwave power is 86.7 % for 120 nm thick aluminium. The two introduced boundary conditions lead to a substrate size of 2.7 mm x 50 mm, as depicted in Figure 4.5. The cutting of the indium tin oxide (ITO) coated glass was outsourced to a specialized company (Weidner Glas), as the tolerances are very hard to accomplish.

On one end of the substrate, the actual solar cell was processed. As a first step, the ITO has to be structured in order to define the active area and to avoid electrical shorts. This was accomplished via acid treating after applying a protective capping layer by photo lithography. Subsequently, a thin layer of poly(3,4-ethylenedioxythiophene):poly(styrenesulfonate), shortly PEDOT:PSS, purchased from Heraeus (Clevios AL4083), was spin coated. It functions as a hole transport- and electron blocking layer. Moreover, the wetting ability of the organic solvent is increased. As PEDOT:PSS is water based, it has to be heated at 130°C for 10 minutes in a nitrogen filled glovebox in order to remove any residual humidity. Afterwards, the solution consisting of the active material blend was spin coated on top of PEDOT:PSS. Removing a small part of active material

on the very top of the substrate is needed in order to uncover the ITO bottom electrode. Further heat treatment may be applied if needed. Finally, the metal electrodes are thermally evaporated under high vacuum (base pressure $< 1 \cdot 10^{-6} \text{ mbar}$) with the help of a shadow mask, defining their appearance. Moreover, the active area can be varied between 1 and 6 mm^2 , in 1 mm^2 steps. Firstly, a 3 nm thin layer of calcium was evaporated with a rate of 0.2 – 0.3 $\text{\AA}/\text{s}$ and secondly 120 nm aluminum with 3 – 8 $\text{\AA}/\text{s}$. The resulting overall structure is depicted in Figure 4.5.

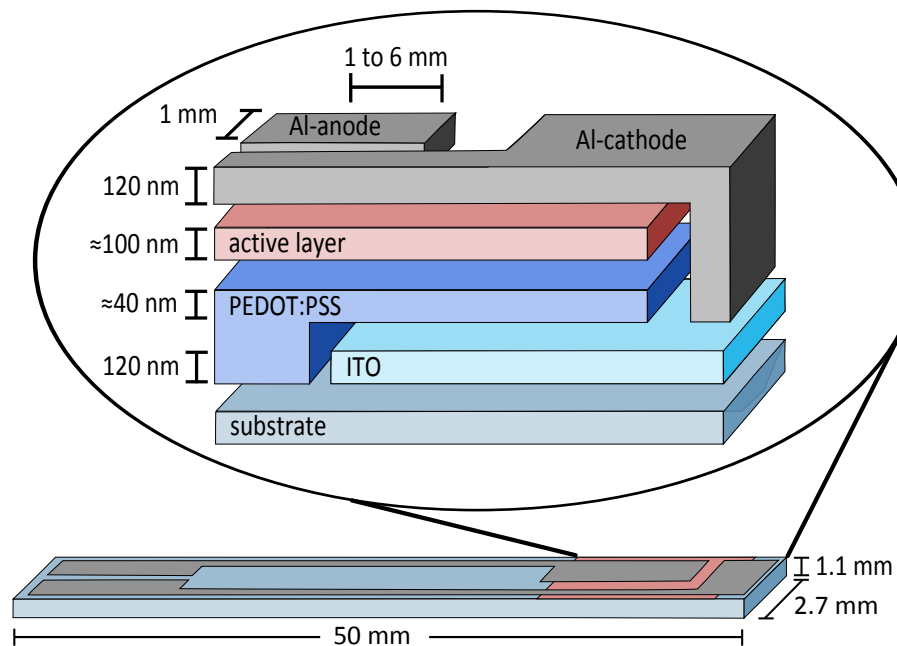


Figure 4.5.: Sketch of the processed organic solar cells suitable for EDMR measurements. On the bottom, the principle layout is shown, together with the dimensions of the substrate. On the top, a closer view on the single layers is given, forming the actual solar cell. The active area is defined by the overlap of ITO-cathode with the aluminum-anode, that can be varied from 1 to 6 mm^2 .

After solving the problem of solar cell dimensions, the contacting remains challenging. This was accomplished by the production of a special circuit board, consisting of two copper stripes which slide over the aluminum contact pads. In order to ensure sufficient contact between both metals, a metallic clamp was soldered to press the solar cell towards the circuit board. Once more, the main difficulty is the lack of space inside the EPR tube. However, with this solution it is possible to connect the solar cell inside a nitrogen filled glovebox, put it in an EPR tube and close the system from the environment with a homemade load-lock. This is additionally equipped with a LEMO connector which is connected with the contacting device by two coaxial wires. An additional inlet is applied in order to evacuate the system and refill it with helium atmosphere due to the previously discussed reasons. It is equipped with a valve (Femto) in order to

4. Experimental Section

prevent ambient conditions during transport. The whole system is depicted in Figure 4.6.

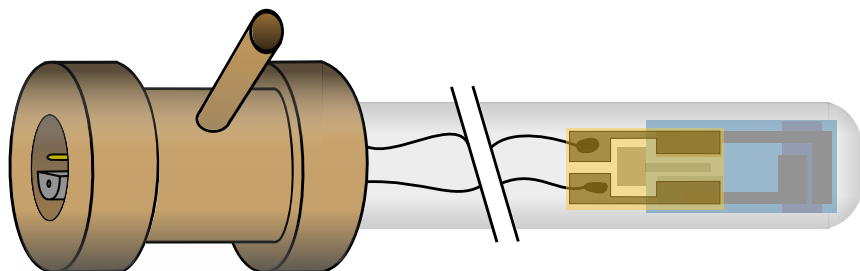


Figure 4.6.: Layout of the sample design for EDMR measurements. The organic solar cell is placed in a special X-band EPR tube with exactly 3 mm inner diameter. Contacting takes place at the end of the substrate, where the quality of the resonator is not affected too much from the metal clamps and wires. The anode and cathode are connected to a LEMO connector in the special designed load lock for EDMR measurements. The additional inlet is for atmosphere exchange purposes, similar to the PLDMR load lock.

4.3. The X-Band EPR Spectrometer

The base frame of all performed experiments is a self-modified X-band spectrometer (Bruker E200). It possesses some basic parts that are essential for all detection modes. The electromagnet consists of two large copper coils that generates fields from 0 up to ≈ 1.5 T. It has to be water-cooled to dissipate the emerging heat. In the center of the coils, the rectangular microwave cavity (Bruker ER4104OR) is situated, which operates in the TE_{102} mode. Furthermore, it is equipped with two optical accesses oriented in transmission with a loaded resonance frequency of 9.432 GHz. This yields 337 mT for a g -factor of 2.0023 (see equation 3.17), easily accessible by the electromagnet. The setup is also equipped with a helium-flow cryostat (Oxford Instruments ESR900), which makes it possible to adjust the temperature from 3.6 K to 300 K. Its stabilization is achieved by a temperature controller (Lakeshore 335) with a deviation from the setpoint of ± 10 mK. Almost all the time, detection is realized by a lock-in-amplifier (Signal Recovery 7230). On the one hand, this leads to a tremendous increase in signal-to-noise ratio by suppressing the non-resonant background and all frequencies which deviate from the modulation frequency. On the other hand, this phase sensitive measurement technique does not allow to draw conclusions concerning the sign of the signal. Last but not least, a vast variety of illumination sources is available. The standard illumination is realized by a white light LED (Luxeon Rebel ES). Moreover, several laser diodes are accessible in the blue (405 nm), red (650 nm) and infrared (785 nm) spectral

region, all in the output power range of ≈ 100 mW. Nevertheless, they possess a poor stability, concerning output power. Finally, a very stable, green (532 nm) DPSS laser is also available, which possesses an output power of 100 mW and is most often used for PLDMR measurements. The setup compiled for cwEPR measurements is depicted in Figure 4.7.

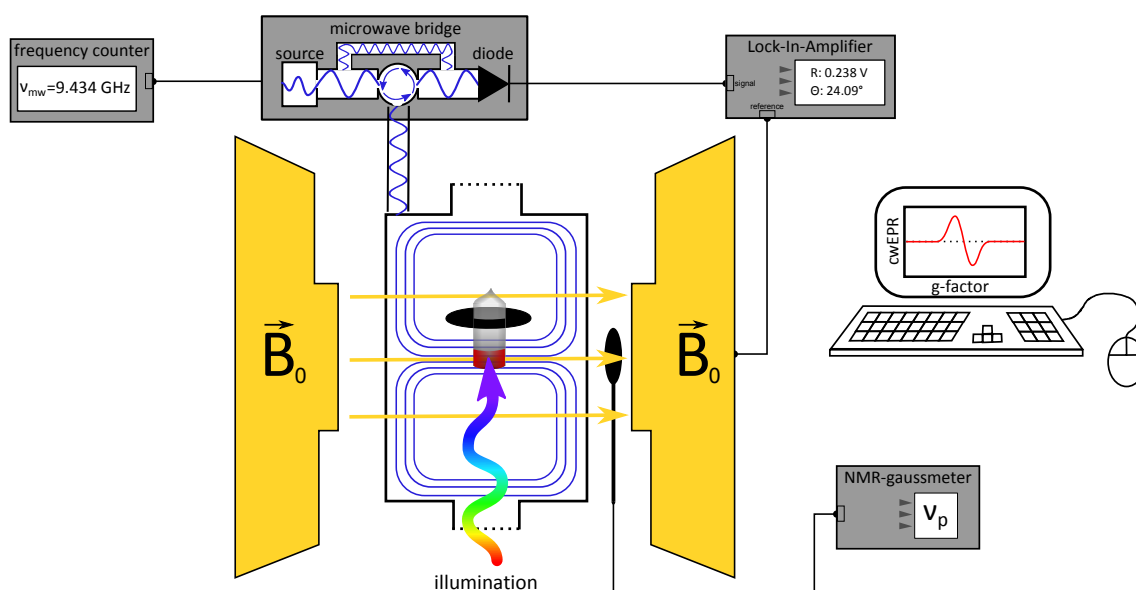


Figure 4.7.: Schematic picture of the cwEPR setup. The resonant cavity, operating in TE_{102} mode (blue) is placed inside two magnet coils (yellow), that provide a static magnetic field \vec{B}_0 . The microwaves are delivered by a microwave bridge, which also detects the reflected waves from the cavity, with a detection diode. Signal amplification is done with a lock-in-amplifier, where the modulated magnetic field acts as reference. The NMR-gaussmeter and a frequency counter provide the g-factor calibration.

g-Factor Calibration

Most of the times, it is of crucial importance that the correct value of the g-factor is obtained by EPR measurements, especially when comparing results measured at different experimental setups. Usually, special materials are added to the investigated molecules, like DPPH, which delivers high signals and whose g-factor is very well known. This is one way to connect the magnetic field with the corresponding g-factor. Another, more elegant method is utilized in this spectrometer. Here, the magnetic field together with the applied microwave frequency is measured with high accuracy. With this, one is able to calculate the exact g-factor according to equation 3.17.

The exact applied microwave frequency ν_{mw} is measured by a frequency counter (HP 5350B or Marconi EIP28b) with an accuracy of 7 significant digits. The determination of the exact magnetic field, however, is more difficult. Therefore, a high-precision

4. Experimental Section

NMR (nuclear magnetic resonance) gaussmeter (Bruker ER035M) is used, where the probe head is placed directly beside the cavity. The Larmor frequency ν_p of a proton is measured in close similarity to equation 3.17, replacing the gyromagnetic ratio for an electron $\gamma_e = g_e \frac{\mu_B}{\hbar}$ with the gyromagnetic ratio for a proton $\gamma_p = g_p \frac{\mu_n}{\hbar}$ in water or similar media. Both of them, the measured larmor frequency of the proton ν_p and the microwave frequency ν_{mw} yield the correct g-factor according to

$$g = g_e \frac{\gamma_p \nu_{mw}}{\gamma_e \nu_p} \quad (4.1)$$

with the g-factor for a free electron g_e .

All in all, only the two measured frequencies ν_p and ν_{mw} are needed in order to calibrate the EPR setup to correct g-values. As a consequence, the g-factor uncertainty, which lies in the order of 10^{-5} , is only due to technical limitations of the electromagnet.

4.3.1. Continuous Wave EPR

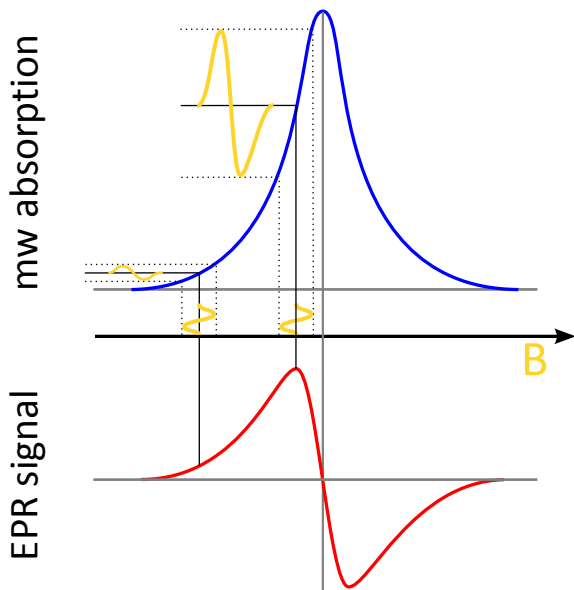


Figure 4.8.: EPR signal reconstruction resulting from the sine-modulated magnetic field. The microwave absorption peak (blue) is transformed to its first derivative (red). Modified from [75].

As already depicted in Figure 4.7, the reference signal for the lock-in-amplifier is an additional magnetic field. It is superimposed to the static magnetic field \vec{B}_0 and provided by two modulating coils which are placed inside the walls of the resonant cavity. Usually, a sine-modulation with a frequency of 100 kHz and an amplitude of 0.02 mT to 0.5 mT is used. The frequency originates from a frequency generator (Keithley 3390, not shown in Figure 4.7) which is synchronized with the lock-in-amplifier. The microwaves used for EPR measurements are generated and detected by the microwave bridge. Additionally, the detection signal is connected to the lock-in-amplifier in order to increase the signal to noise ratio.

The measurement signal is not a common absorption peak, but its first derivative. This is due to the sine modulation of the magnetic field. The signal reconstruction is shown in Figure 4.8.

4.3.2. Photoluminescence Detected Magnetic Resonance

For PLDMR measurements, a few changes have to be implemented in comparison to the EPR setup. The modified setup is depicted in Figure 4.9.

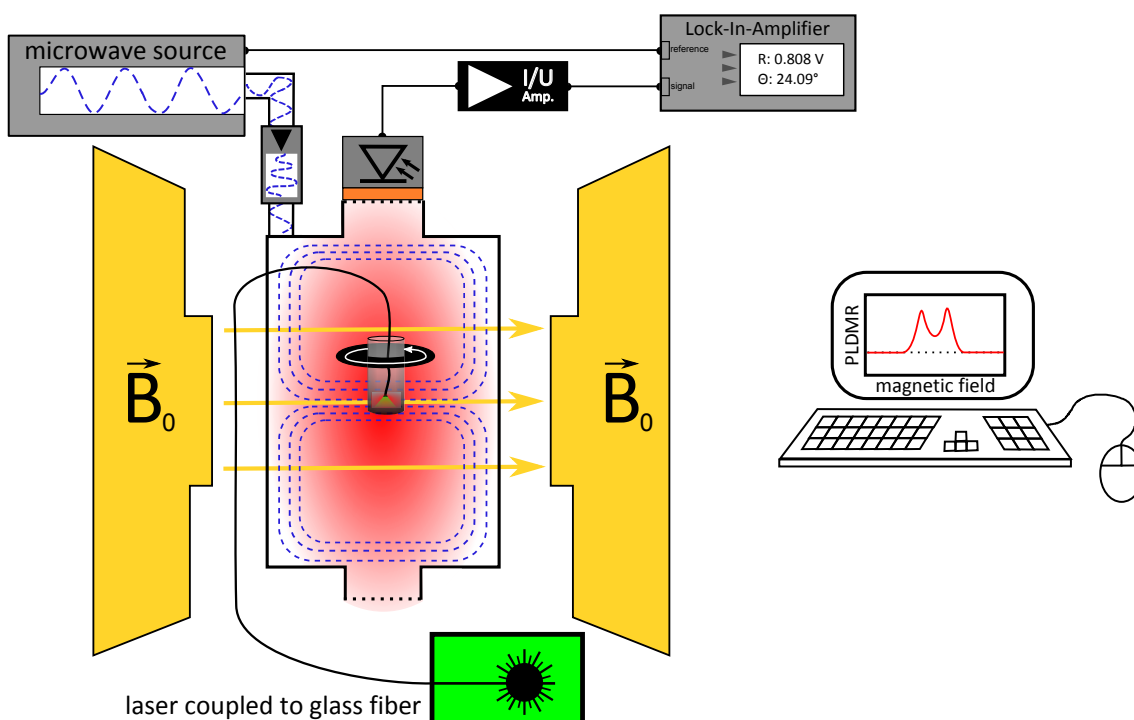


Figure 4.9.: Illustration of the PLDMR setup. Compared to the EPR setup, the microwave- and illumination source are replaced. The measurement signal consists of the luminescence (shown in red), detected via a silicon photo diode situated behind a longpass filter (orange) that separates excitation from luminescence. The microwaves are chopped in the kHz regime which acts as reference signal to the lock-in-amplifier.

First of all, the illumination source has to be a laser, because the excitation- and photoluminescence wavelengths must be separable. This is achieved by a long pass filter, adapted to the used laser. As an example, a 550 nm longpass filter is applied when illuminating with the 532 nm laser. This energetic separation is possible because the luminescence of the investigated materials is red shifted compared to the absorption. Detection of the luminescence takes place via a silicon photodiode which is situated behind the longpass filter. The measured photocurrent is converted and enhanced by a current/voltage amplifier (Femto DLPCA) and used as the observable for the lock-

4. Experimental Section

in-amplifier. The decoupling of excitation and rotation of the sample, also shown in Figure 4.9, was already discussed in section 4.2.

In addition to the changed illumination, the microwave source has to be replaced by a microwave synthesizer (Anritsu). On the one hand, this is due to the improved output power, which is additionally enhanced by a 2 W solid-state microwave amplifier (Microsemi). On the other hand, the bridge is incapable to chop the output power which is needed for amplitude modulation. Thereby, the microwaves follow a TTL (transistor-transistor-logic) signal, i.e. they are turned on and off in the kHz regime. The same TTL signal functions as the reference signal for the lock-in-amplifier. Therefore, the measured signal is the change of luminescence under applied microwaves, compared to switched off microwaves. Putting this value in relation to the overall signal of the luminescence PL, the PLDMR signal is the ratio $\Delta PL/PL$, expressed in %.

The main challenge in order to obtain reasonable PLDMR signals is the laser stability. If the illumination source is too instable, the noise will be added to the measurements, which makes it difficult to detect the usually low change of luminescence. Therefore, the 532 nm DPSS laser was the illumination source of choice for the materials shown in this work.

4.3.3. Electrically Detected Magnetic Resonance

The setup for electrically detected magnetic resonance (EDMR) is very similar to the one assembled for PLDMR. The main difference, however, is again a change of the observable. Whereas for EPR, the signal is the microwave absorption and for PLDMR the photoluminescence of the material, in EDMR the detected signal is electricity, i.e. current or voltage flowing through- or generated by an organic device. The corresponding setup is shown in Figure 4.10.

The investigation of the solar cell should be as close as possible to realistic working conditions. This means, that the measurement should preferably take place at room temperature, with illumination strength and spectrum as close to the one provided by the sun as possible. Therefore, a white light LED is chosen as illumination source with intensities on the sample below 100 mW/cm^2 .

Furthermore, the measurement mode is selectable between voltage- and current detection. For voltage detection, both electrodes of the cell simply have to be connected directly to the lock-in-amplifier. This measures the open circuit voltage of the solar cell (not shown in Figure 4.10). A little bit more complicated is current detection. Here, one electrode has to be connected to a source measuring unit (SMU - Keithley 237), where a specific voltage could be applied. The other electrode is connected to the current/voltage amplifier, which converts the current to the actual measurement

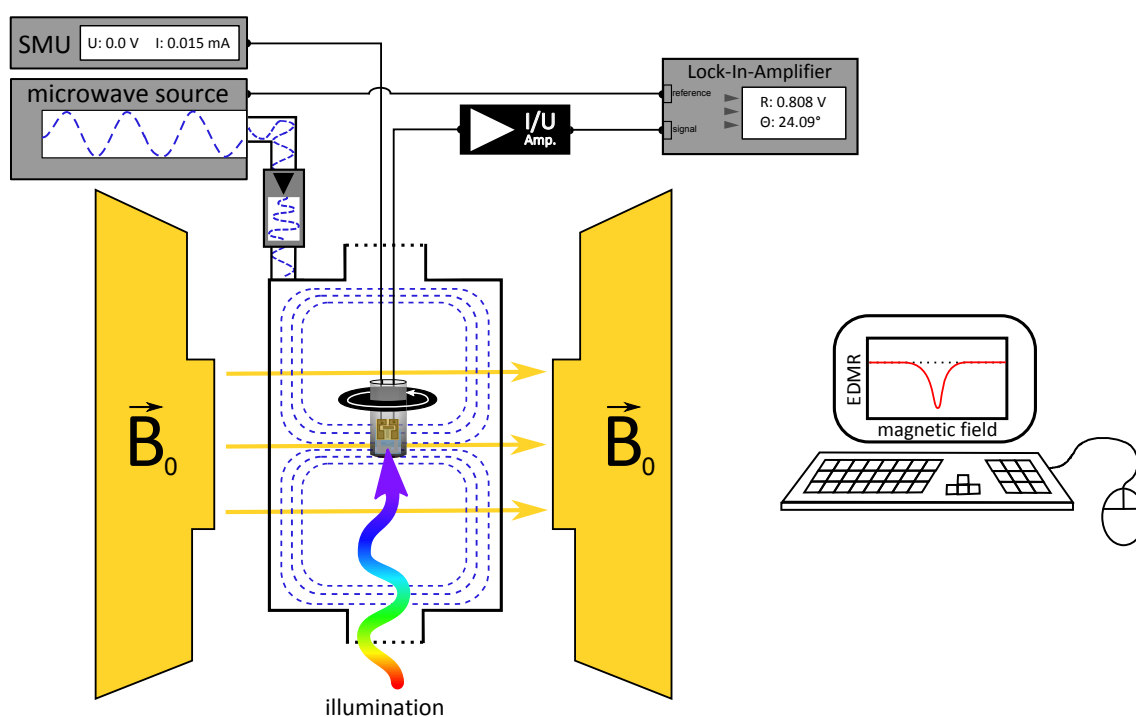


Figure 4.10.: Schematic picture of the EDMR setup. In comparison to the PLDMR setup, the observable has changed to electricity instead of photoluminescence. With the source measuring unit (SMU), every desired point of the j - V -characteristic can be chosen to detect the current flowing through the organic solar cell. The white light illumination with low intensity, together with room temperature operation yields realistic working conditions for organic solar cells.

signal. This is recorded by the lock-in-amplifier. Once again, the frequency of the TTL-modulated microwaves is the reference signal for the lock-in-amplifier. The circuitry follows the j - V -characteristic of the investigated solar cell, depending on the applied voltage (compare Figure 2.8).

All connecting cables have to be shielded properly. Moreover, the grounding of the shielding is very important for the signal-to-noise ratio of the measurement and is quite often very counterintuitive.

4.3.4. Electroluminescence Detected Magnetic Resonance

For electroluminescence detected magnetic resonance (ELDMR) measurements, the setups for EDMR and PLDMR have to be connected. Obviously, electricity is needed in order to generate electroluminescence. This electricity, however, is not the observable but the light generated by the device. Therefore, the SMU is needed in order to provide the current. In addition, the photodiode has to detect the light in front of the cavity. Naturally, the EDMR sample structure has to be used in order to generate electroluminescence.

4. Experimental Section

Similar to EDMR, one electrode is connected to the SMU, while the other is grounded manually. The current of the photodiode is converted and amplified by the current/voltage amplifier and acts as measurement signal for the lock-in-amplifier. Once again, the reference signal is the frequency of the TTL-modulated microwaves. The whole scheme of the ELDMR setup is shown in Figure 4.11.

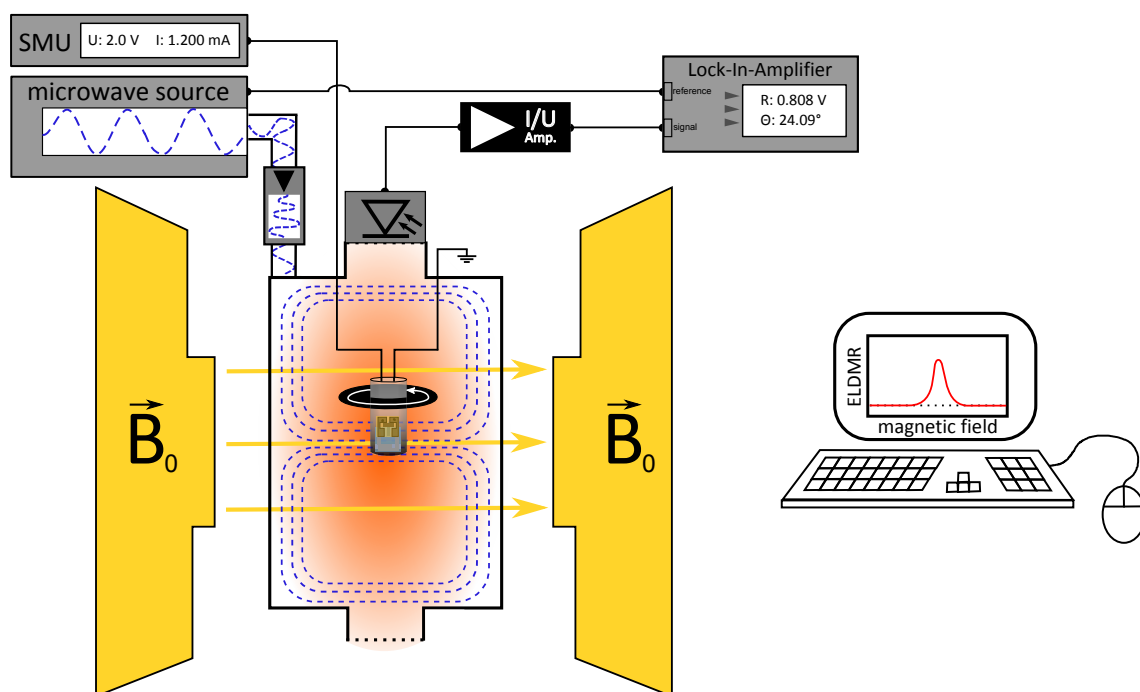


Figure 4.11.: Layout of the ELDMR setup. The setup is a connection between EDMR and PLDMR with the electroluminescence as observable. The source measuring unit (SMU) applies the desired driving current and the generated electroluminescence is detected by the photodiode.

The main problem for this detection method is the quite large distance between the device generating the light and the detector, situated at the optical access of the cavity. This demands the need of very high light intensities in cw operation and even though it is hardly above the detection limit of the photodiode. Another difficulty connected with the high current densities needed for sufficient light emission is the enhanced degradation of the devices during the measurement.

5. Detection of Residual Iodine in PTB7:PCBM Blends due to the Additive DIO¹

Abstract

The use of additives boosts the performance of highly efficient organic solar cells significantly. The morphology of the active layer is optimized by delaying the drying of the active layer and therefore, altering the size of polymer- and fullerene-rich phases. Peet et al. reported that additives consisting of alkanedihalides are removed during a high vacuum evaporation step [15, 139], indicating no further influence on device operation. For the material systems PTB7:PC₆₀BM and PTB7:PC₇₀BM prepared with the additive DIO, however, high vacuum drying is not sufficient to remove all residual iodine. Using light induced electron paramagnetic resonance (EPR) spectroscopy combined with X-ray photo electron spectroscopy (XPS) reveals that iodine is still detectable in the active layer after the preparation process with a surprisingly high concentration of $(7.3 \pm 2.1) \cdot 10^{19} \frac{1}{\text{cm}^3}$. While identifying a magnetic interaction of the photo generated charge carriers with the residual iodine a significant electronic doping effect could not be detected by ultraviolet photoelectron spectroscopy (UPS) and dark charge extraction by linearly increasing voltage (CELIV). However, an influence on the long-term stability is nonetheless possible.

5.1. Introduction

At present, most of the highest performing donor-acceptor copolymer material systems need to be processed together with an additional high boiling point solvent in order to achieve optimum PCE [15, 140, 141, 59, 122]. Those additives are selectively dissolving the acceptor molecules, leading to an altered size of polymer- and fullerene

¹The results of this chapter will be published in A4

5. Detection of Residual Iodine in PTB7:PCBM Blends due to the Additive DIO

rich phases in the active layer. Consequently, this gives better performance for a certain fraction of additives [51, 62, 53, 52, 122]. In most cases, the additives consist of an octanedihalide, whereby the commonly used additive for the material system PTB7:PC₇₀BM and for many other new low bandgap polymers is 1,8-diiodooctane (DIO). It was proposed that the reason for the enhanced PCE in PTB7:PC₇₀BM solar cells prepared with DIO is an intercalation of PC₇₀BM in PTB7 domains, leading to a reduction in size of fullerene and polymer rich regions [52, 142, 143, 144, 145]. For comparison see also chapter 2.5.

Peet et al. showed that additives consisting of alkane dithiols are removed under a rough vacuum step, using Fourier-transform infrared-, Raman- and X-ray photoelectron spectroscopy [15]. Subsequently, the same group reported that DIO is not present anymore in films made of poly(9,9-di-n-octylfluorine) (PFO) after a high vacuum drying step [139]. On the base of these first publications concerning the use of additives, it is consensus that additives get removed during the high vacuum drying step, which is necessary for metal evaporation. In this chapter, the detection of residual iodine in PTB7:PC₇₀BM blends is shown using XPS spectroscopy. This finding was confirmed by EPR experiments on three different blend systems consisting of pristine PTB7:PC₆₀BM, PTB7:PC₆₀BM with 1,8-octanedithiol (ODT) and PTB7:PC₆₀BM with DIO. Whereas a magnetic interaction is evident from the EPR results, a significant electronic contribution was neglected by measuring dark charge extraction by linear increasing voltage (CELIV) and ultraviolet photon spectroscopy (UPS).

5.2. Experimental Details

PTB7 was purchased from 1-Material, PC₆₀BM and PC₇₀BM from Solenne and DIO and ODT from Sigma Aldrich. All materials were used without further purification. PTB7 was dissolved in chlorobenzene with a concentration of 8 mg/ml. The blended PTB7:PCBM solution was prepared in a 2:3 mass ratio. For the samples with additives, 3 % by volume were added to the solution and stirred for at least 30 minutes. The whole sample preparation took place in a nitrogen glove box to avoid exposure to oxygen and humidity.

The organic bulk heterojunction solar cells were prepared by spin-coating a ≈ 40 nm thick PEDOT:PSS layer on top of an indium tin oxide (ITO) covered glass substrate. After annealing for 15 minutes at 130 °C in a nitrogen glove box, the blended solution was spin coated resulting in a film of around 100 nm thickness. Finally, the samples were transferred into an evaporation chamber where the top metal contacts (Ca/Al) were thermally evaporated on top of the active layer, resulting in an active area of around

3 mm². Subsequently, j-V sweeps were performed to determine the efficiency of the devices (compare with chapter 2.4). For charge extraction by linearly increasing voltage (CELIV) measurements, the devices were kept in the dark while applying a triangular voltage pulse. During the experiment an oscilloscope measured the induced current of the device [146, 147, 148, 149].

For XPS measurements, the same sample configuration was used like for the bulk heterojunction solar cells, although without the top metal electrodes. In XPS experiments, the samples are put in a high vacuum chamber and irradiated with X-rays. This measurement method is based on the photoelectric effect and is used to determine the atomic composition of a material. The high energy X-rays are absorbed while electrons situated in the atomic orbitals are emitted. By quantifying the kinetic energy of the emitted electrons (binding energy), the photoelectrons can be assigned to distinct atomic orbitals and elements. With this, the signal intensity at a specific binding energy is a measure for the atomic composition in the investigated sample. The change from X-rays to ultraviolet photons as irradiation source reveals the density of states of the valence band with very high accuracy. The reason for this is the small need of energy in order to release electrons situated near the HOMO level. Thus, the measurement technique is called ultraviolet photoelectron spectroscopy (UPS). All XPS and UPS measurements were done at the University of Tübingen in the group of Prof. Chassé.

The EPR samples were made according to chapter 4.2. In short, 100 μl of the prepared solutions were poured in a standard EPR quartz tube, evaporated under rough vacuum (end pressure 10^{-2} mbar) and sealed under 20 mbar helium atmosphere. All EPR experiments were performed at 30 K under the illumination of a white light LED or a 532 nm DPSS laser. The microwave power was highly attenuated by 35 dB in order to avoid disturbances from signal saturations. For further details see also chapter 4.3.1.

5.3. Results & Discussion

5.3.1. Solar Cell Performance

First of all, solar cells were made of the investigated blend solutions in order to get a confirmation of the quality of the materials and the prepared blends. The corresponding j-V-characteristics are shown in Figure 5.1. Here, the device without additives (blue) shows the highest V_{oc} , but due to the unoptimized fill factor and the poor j_{sc} the resulting power conversion efficiency is quite low. The respective values are listed in the table of Figure 5.1. Adding 3% by volume DIO to the blend leads to a vast increase in fill factor and j_{sc} , compared to the pristine blend. This results in the best solar cell

5. Detection of Residual Iodine in PTB7:PCBM Blends due to the Additive DIO

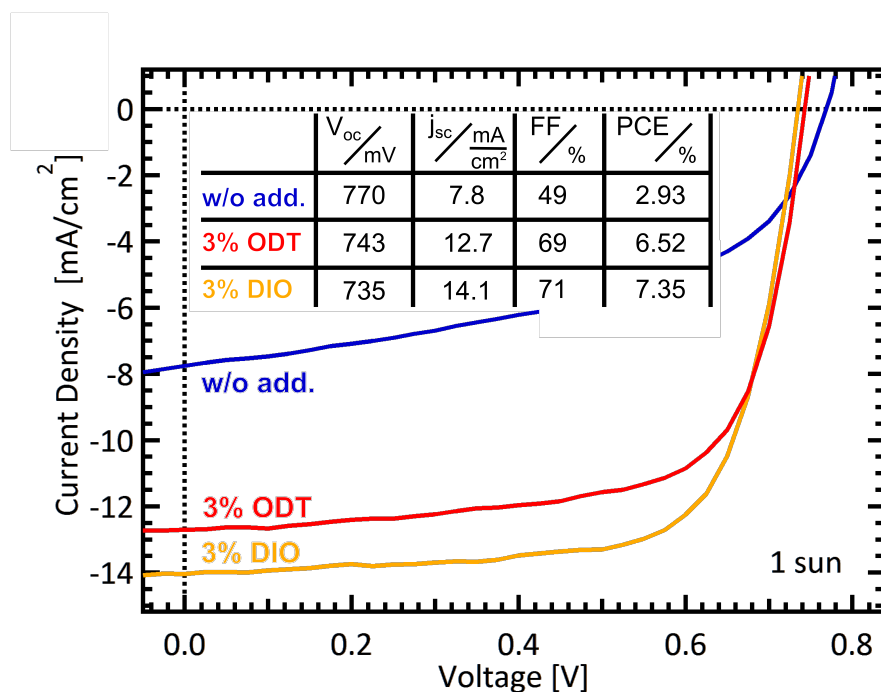


Figure 5.1: j-V-characteristics of three different organic solar cells made of the blends PTB7:PC₇₀BM (blue), PTB7:PC₇₀BM with 3% ODT (red) and PTB7:PC₇₀BM with 3% DIO (orange) under one sun illumination ($100 \frac{mW}{cm^2}$). The resulting solar cell parameters are listed in the table.

efficiency of 7.35%. Using ODT instead of DIO as an additive results in similar effects concerning V_{oc} and the fill factor. The slightly lower j_{sc} stems most probably from the not optimized morphology when using ODT. The determination of the exact amount of additives in order to obtain the most efficient solar cells was done for DIO, not for ODT [51].

5.3.2. XPS Measurements

In the next step, XPS measurements of the three investigated blends were performed with the results shown in Figure 5.2. All three samples showed a high signal coming from the 1s-shell of carbon with a binding energy of approximately 280 eV. Naturally, this results from the carbon backbone of all present materials. Furthermore, PTB7 monomers consist of sulfur and fluorine, which were clearly detectable as well. For sulfur, the signal stemmed from the 2p-orbital with a binding energy of ≈ 170 eV and for fluorine from the 1s-orbital with ≈ 690 eV. Oxygen, on the other hand, appears in PTB7 as well as PC₇₀BM which is why a clear signal was detected, coming from the 1s-shell with a binding energy of ≈ 520 eV (see also chapter 4.1 for further comparison). The sample prepared with 3% DIO, however, showed a weak but significant signal

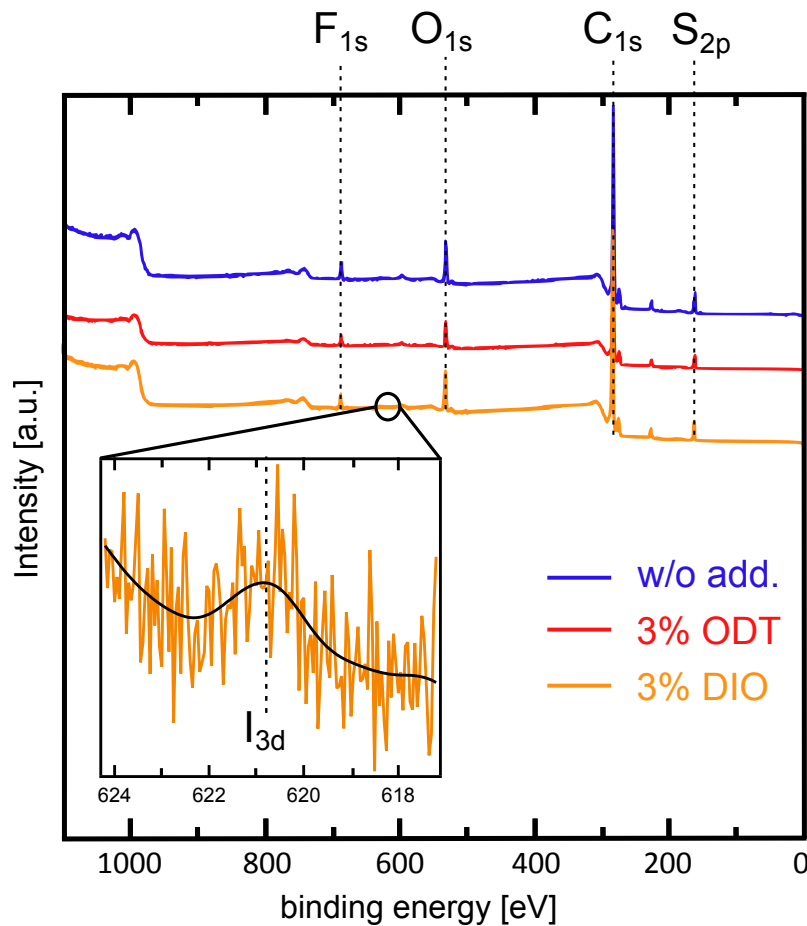


Figure 5.2.: XPS spectra of the three investigated blends PTB7:PC₇₀BM (blue), PTB7:PC₇₀BM with 3% ODT (red) and PTB7:PC₇₀BM with 3% DIO (orange). Dashed vertical lines indicate the existence of sulfur, carbon, oxygen and fluorine in all three samples. Inset: Zoom at the I_{3d} peak in the PTB7:PC₇₀BM blend processed with 3% DIO. The solid black line shows the smoothed data for better visualization.

stemming from the 3d-shell of iodine with a binding energy of 621 eV. Hence, a clear evidence for the presence of residual iodine in the blend prepared with 3% DIO was supplied. Nevertheless, the detection of residual sulfur for the blend with 3% ODT is not possible due to the occurrence of this element in the chemical structure of PTB7.

Not only does PTB7 include just one fluorine atom per monomer, it is also not present in any other investigated material. Therefore, the signal peaks were fitted and the signal height corresponds to the amount of elements present in the sample. Afterwards, the numbers were normalized to the fluorine peak for the quantitative analysis. The resulting relative signal intensities are listed in table 5.1, with good agreement with the expected values for the chemical composition. Comparing the amount of fluorine present in the sample PTB7:PC₇₀BM with 3% DIO with the amount of iodine reveals approximately a 4:1 ratio between these two elements. Therefore, one iodine atom is present for almost every fourth PTB7 monomer. Assuming a density of $1 \frac{g}{cm^3}$ for the

5. Detection of Residual Iodine in PTB7:PCBM Blends due to the Additive DIO

organic thin film yields an iodine concentration of $(7.3 \pm 2.1) \cdot 10^{19} \frac{1}{cm^3}$. The error originates from the vague fit of the iodine peak in Figure 5.2. Nevertheless, this value is a surprisingly high amount of residual iodine in the PTB7:PC₇₀BM blend prepared with DIO. However, the question if the iodine is still bound to the octane or if it reacts with a constituent of the blend remains open. Although slightly more sulfur was detected in the blend prepared with ODT, the quantity is not at all in a significant extent. Therefore, no statement can be made concerning residual sulfur when preparing a blend with ODT.

	F _{1s}	O _{1s}	C _{1s}	S _{2p}	I _{3d}
w/o add.	1	3.8	51.4	3.8	-
3% ODT	1	4.8	58.9	3.9	-
3% DIO	1	4.5	55.6	3.7	0.23

Table 5.1.: Atomic composition of the samples without additives, with 3% ODT and with 3% DIO, normalized on the fluorine signal as there is only one fluorine atom per PTB7 monomer.

5.3.3. Light Induced EPR Measurements

Additionally, the three different blends were investigated by means of electron paramagnetic resonance. The results are shown in Figure 5.3. The best performing solar cell blend is PTB7 mixed with PC₇₀BM. Unfortunately, the g-factors of both constituents are very similar. Therefore, they showed a highly overlapping EPR signal, visible in the upper part of Figure 5.3. Here, it is quite hard to distinguish between the signal coming from the polaron on PTB7 and the electron on PC₇₀BM [150, 151, 152, 153, 154]. On that account the acceptor material was changed from PC₇₀BM to PC₆₀BM. As already mentioned in chapter 4.1.2, the electronic properties of both materials are more or less identical [137, 131, 60, 135, 138, 75, 155]. The only reason for the improved performance of PC₇₀BM is the enhanced absorption cross section with the solar spectrum [137, 135]. In the lower part of Figure 5.3, the advantage of using PC₆₀BM instead of PC₇₀BM is clearly visible. Here, the signals coming from the polaron on PTB7 and the electron on PC₆₀BM are spectrally separated. The PTB7 signal possesses a higher g-factor ($g \approx 2.003$) which is why the signal occurs at lower magnetic fields. The electron on PC₆₀BM, on the other hand, has a lower g-factor near $g=2.000$ leading to a signal at higher magnetic fields [152, 154]. Both signal contributions are indicated by the dotted vertical lines in Figure 5.3.

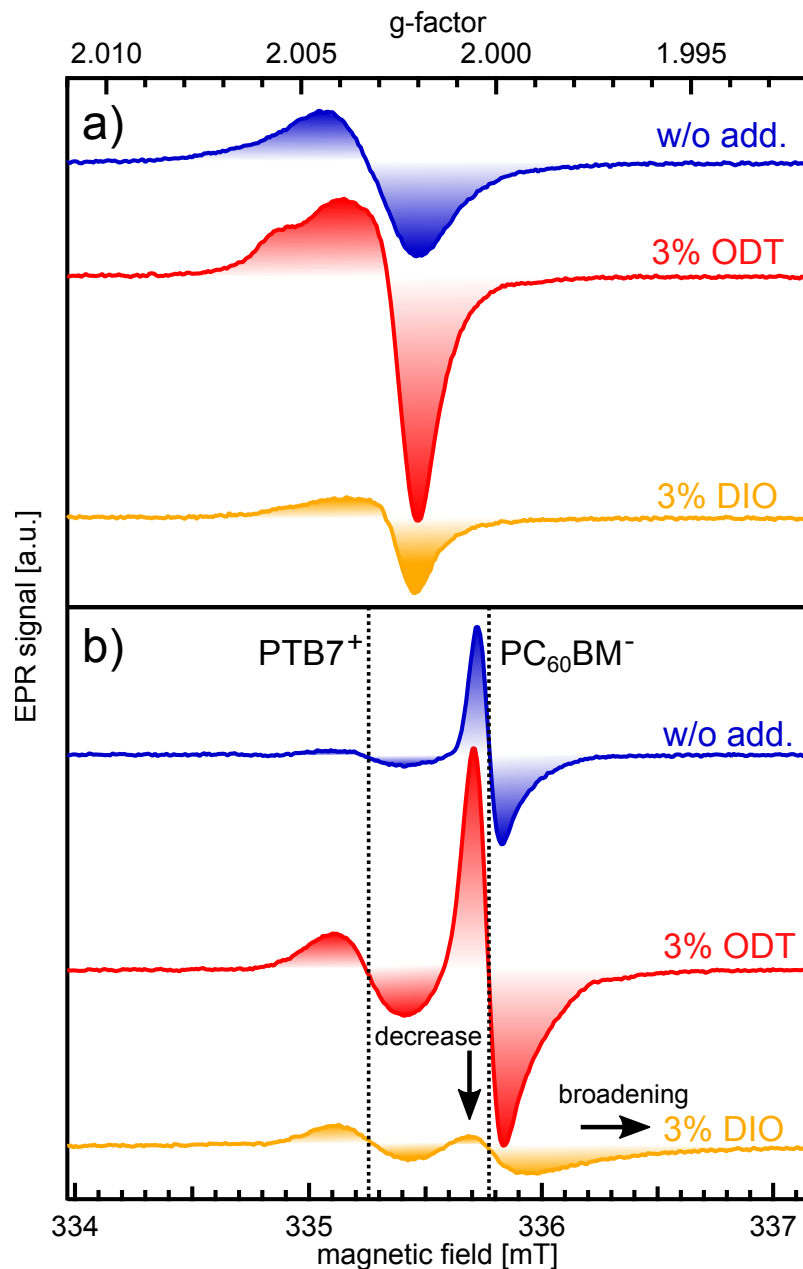


Figure 5.3.: a) EPR spectra of three different blends made of PTB7:PC₇₀BM (blue), PTB7:PC₇₀BM with 3% ODT (red) and PTB7:PC₇₀BM with 3% DIO (orange) under illumination with a white light LED. b) EPR spectra of the same blends replacing PC₇₀BM with PC₆₀BM. The dotted vertical lines indicate the position of the signal contributions of the two constituents PTB7⁺ and PC₆₀BM⁻. The spectra are vertically shifted for better visibility.

While there is no significant change in signal shape between the blend without additive and with 3% ODT, a clear deviation can be observed for the blend with 3% DIO. For this, the signals of both signatures show a line width broadening, while the overall signal strength of PCBM is decreased. This behavior is qualitatively the same for the PTB7:PC₇₀BM results. Previously, elemental iodine was used to dope polymers in

5. Detection of Residual Iodine in PTB7:PCBM Blends due to the Additive DIO

order to increase the EPR signal for g-factor determination [150, 151]. Therefore, the changing EPR signal due to the presence of iodine in the PTB7:PCBM films is consequential. The increase in linewidth of the two signal contributions can be ascribed to dipole-dipole interactions between two paramagnetic particles. In this case, it occurs probably between the electron- or polaron spin and the nuclear spin of the residual iodine ($I=\frac{5}{2}$). Recently, an EPR study on galvinoxyl doped P3HT:PC₆₀BM was published [156]. Here, the radical galvinoxyl possesses an intrinsic electron spin of $\frac{1}{2}$ and interacts with the electron spin and the CT-state. Furthermore, the EPR signals behave similar to the presented results for PTB7:PC₆₀BM with the addition of DIO. Especially, the same reduction of signal strength coming from the electron on PC₆₀BM with increasing amount of galvinoxyl was observed. Therefore, it was concluded that galvinoxyl stays mainly in the PC₆₀BM rich phase of the donor-acceptor blend [156]. Transferring this finding to the material system PTB7:PC₆₀BM hints towards the implication that the iodine stays preferably in the PC₆₀BM phase as well. This conclusion is in good agreement with the fact that DIO acts as selective solvent for fullerene derivatives. Unfortunately, conceivable residual sulfur in the blend prepared with ODT possesses no nuclear spin. Therefore, it is also not possible to detect this residual sulfur with EPR spectroscopy. All in all, the EPR measurements support the findings of the XPS study that a significant amount of iodine stays in the blend after film preparation.

However, the preparation method for organic solar cells and EPR samples is not entirely the same. The biggest difference is the lack of a high vacuum drying step, usually done in order to evaporate the metal contacts. Hence, it is possible that the residual iodine gets removed under high vacuum while it outlasts drying under rough vacuum. Therefore, a PTB7:PC₆₀BM with 3% DIO sample was prepared and measured via EPR. Afterwards, the sample tube was opened again in a nitrogen filled glovebox and put in a high vacuum ($<10^{-6}$ mbar) chamber for 18 hours. After that, the tube was sealed again and remeasured in order to compare both results before and after the high vacuum drying. The respective spectra are shown in Figure 5.4. If taking into account that the samples were measured on different days leading always to slightly altered results, the spectra are comparable within the accuracy of the measurement. This leads to the conclusion that even under high vacuum the iodine stays inside the film.

5.3.4. UPS- and CELIV Measurements

After clarifying the presence of residual iodine in the PTB7:PCBM films prepared with DIO its influence on electronic properties and solar cell operation remains an open question. Therefore, the density of states in close vicinity to the HOMO level was investigated by UPS measurements. This method is very similar to XPS. The X-rays as

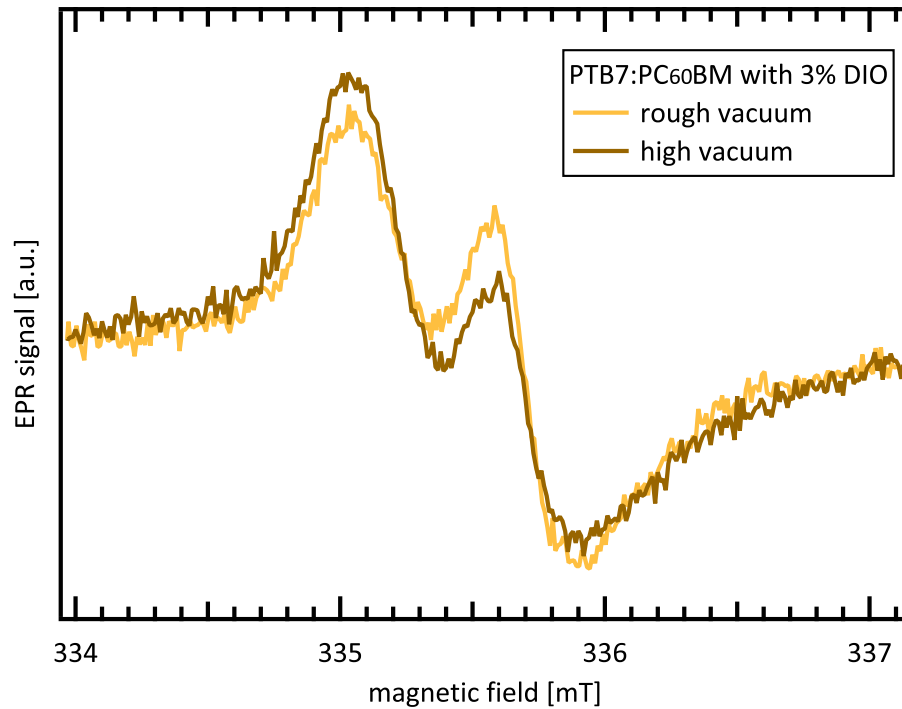


Figure 5.4.: EPR spectra of a PTB7:PC₆₀BM film prepared with 3% DIO. First measurement after preparation of a normal EPR sample under rough vacuum (light orange) and second measurement after a high vacuum drying step (dark orange).

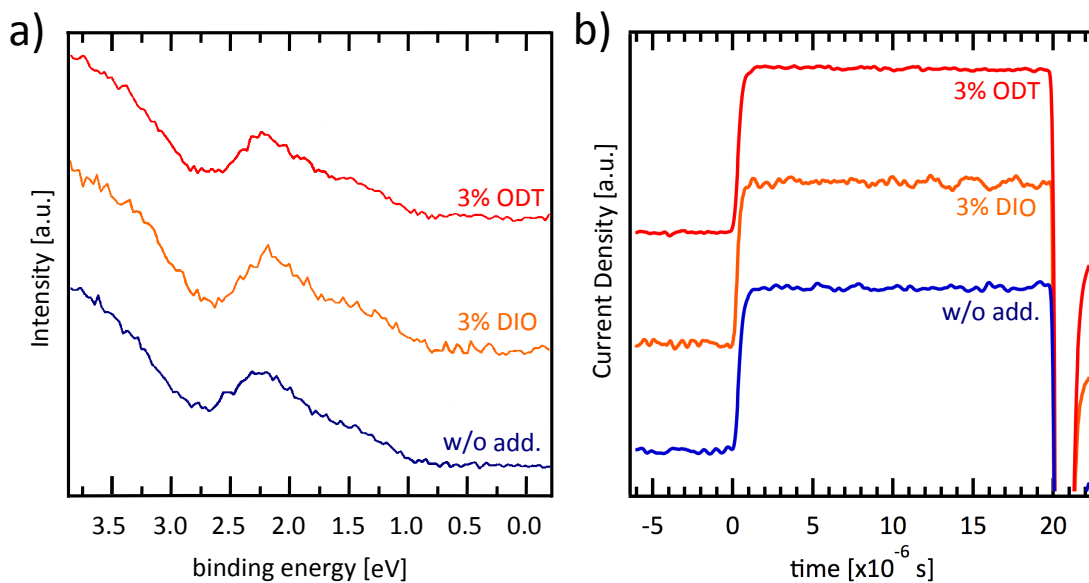


Figure 5.5.: a) UPS spectra of thin films consisting of PTB7:PC₇₀BM (blue), PTB7:PC₇₀BM with 3% ODT (red) and PTB7:PC₇₀BM with 3% DIO (orange). b) dark CELIV spectra from devices made of the investigated blends. No signal differences were detectable which means that iodine does not affect the electronic properties of the devices. The spectra are vertically shifted for better visibility.

5. Detection of Residual Iodine in PTB7:PCBM Blends due to the Additive DIO

excitation source, however, are replaced by ultraviolet photons leading to a higher accuracy for valence electrons. The measurements showed no significant difference between the three samples, though, as depicted in Figure 5.5 a). This means that iodine is not acting as a p-dopant in the material system PTB7:PC₇₀BM. Furthermore, also the dark CELIV results, shown in Figure 5.5 b) indicated no additional free charge carriers in the device prepared with DIO. Only a rectangular capacitive response of the solar cell was detected.

In previous studies, organic Schottky-junctions were doped with elemental iodine. Here, the film was exposed to iodine vapor for a short time which lead to a low doping concentration and subsequently to an improvement in photovoltage and photocurrent [157, 158, 159, 160, 161]. Comparing the presented result of residual iodine in the active layer of the PTB7:PCBM cells created with 3% DIO with the solar cell efficiencies shown in Figure 5.1 supports the assumption that iodine doping leads to an improved organic solar cell as well. However, the UPS- and CELIV results hint towards no impact of the residual iodine on the electronic properties of solar cells made of PTB7:PC₇₀BM. As already mentioned before, the slightly improved PCE for the devices prepared with DIO is more likely due to an optimization of device fabrication parameters which lead to an optimized morphology of the active layer. However, an influence on the long term device stability is still possible. Especially the degradation of metallic electrodes due to elemental iodine is conceivable.

5.4. Conclusion

XPS measurements revealed that iodine is still present in PTB7:PCBM solar cells prepared with the additive DIO yielding a surprisingly high concentration of $(7.3 \pm 2.1) \cdot 10^{19} \frac{1}{cm^3}$. Therefore, high vacuum drying is not always sufficient to remove residual additives. Additionally performed EPR measurements fully support these findings and revealed the indication that the iodine stays preferably in the fullerene phase. The iodine leads to a magnetic interaction of the photogenerated charge carriers in the device. However, we did not find evidence for an electronic doping effect changing the device properties. The degradation of metallic electrodes due to elemental iodine is nonetheless conceivable affecting long-term stability. All in all, based on the presented results the choice of additives in the preparation of organic solar cells becomes more important.

6. Triplet Exciton Formation in p-DTS(FBTTh₂)₂:PC₇₀BM Based Small-Molecule Solar Cells¹

Abstract

Triplet exciton formation in neat p-DTS(FBTTh₂)₂ and blends with PC₇₀BM, with and without the selective solvent additive 1,8-diiodooctane (DIO), was investigated by means of photoluminescence detected magnetic resonance (PLDMR) measurements. For all three material systems, a significant amount of long living but electrically inaccessible triplet excitons were detected, situated on the p-DTS(FBTTh₂)₂ molecules. The characteristic zero field splitting parameters for this state were identified to be $D = 42$ mT (1177 MHz) and $E = 5$ mT (140 MHz). However, no triplet excitons located on PC₇₀BM were detectable. Angular dependent PLDMR measurements were also performed to connect the extent of the excitonic wave function to the nanoscale morphology of the p-DTS(FBTTh₂)₂-molecules. A preferential orientation of the p-DTS(FBTTh₂)₂-molecules was found, revealing an edge-on alignment with respect to the substrate. Using electrically detected magnetic resonance (EDMR), the presence of these triplet excitons was confirmed even at room temperature, highlighting that triplet excitons form during solar cell operation. Of the three systems measured, the superior performing blend with DIO was found to have the largest triplet population. Despite prior predictions, no evidence was found that the formation of triplet excitons has a crucial impact on device performance in p-DTS(FBTTh₂)₂:PC₇₀BM based solar cells.

6.1. Introduction

The commonly used material combination for organic bulk heterojunction (BHJ) solar cells is a semiconducting polymer acting as electron donor and a fullerene derivative

¹The results of this chapter will be published in A5

6. Triplet Exciton Formation in *p*-DTS(FBTTh₂)₂:PC₇₀BM Based Small-Molecule Solar Cells

as electron acceptor. The challenges of polymer synthesis concerning purity, molecular weight and batch to batch variations lead to the emergence of solution processable small molecules where these drawbacks are not applicable [116, 117]. By now, the efficiencies of small molecule BHJ solar cells are comparable to their polymeric counterparts [162, 163].

One of the first successful soluble small molecules, *p*-DTS(FBTTh₂)₂, has become a benchmark system for this new class of materials. Prior studies highlight the steady progress in improving the molecular structure [121, 118], explaining the morphology [122], understanding basic processes [164, 165, 119], and describing routes for further increasing device efficiencies [123, 120, 118, 166]. While the fundamental processes have been vastly investigated for polymeric systems, there still exists a lack of fundamental investigations on soluble small molecule blends. In order to further improve these very promising materials, it is crucial to get a better understanding of charge generation processes, recombination dynamics, transport properties, and loss mechanisms.

Optical excitation of an organic semiconductor results in bound excitons rather than free charge carriers due to the small dielectric constant of $\epsilon \approx 3$ -4. Excitons initially possess singlet spin configuration, since optical excitation is a spin conserving process, and the ground state is a singlet state as well. However, there exists several processes by which singlet excitons are converted to the triplet spin state. In a pristine material, the most probable is inter system crossing (ISC). Here, singlet excitons change their spin state with a certain probability that is strongly dependent on spin-orbit coupling. Additionally, if the triplet state has less than half of the energy of the singlet state, the singlet exciton can split into two triplet excitons. This process is called singlet fission and is believed to be exploitable for improving the short circuit current in organic solar cells [167, 168]. In addition, with the introduction of an electron acceptor, the dissociation of the singlet excitons into charge carriers often happens on a much faster timescale than the aforementioned mechanisms [34]. Therefore, these triplet formation routes are typically negligible in donor-acceptor systems optimized for OPV.

The intermediate state preceding charge carrier dissociation or recombination is a charge transfer state (CTS). Here, the electron is situated on the acceptor material but is still weakly bound to the hole on the donor. As the spins of electron and hole interact with each other, the CTS can be in singlet- or triplet spin configuration, as well. However, the weak dipolar coupling leads to energetically almost degenerate states. Consequently, another formation mechanism for triplet excitons can occur succeeding the formation of a CTS. Here, a charge carrier pair may be transferred from a CTS to an excitonic triplet state in either the donor or acceptor material. This process is called elec-

tron back transfer (EBT). However, it is only possible if the triplet exciton state is lower in energy than the CTS. Hence, the occurrence of this process is dependent on the energetics of the investigated material system. Although EBT can occur from a geminate CTS [35], it will be more efficient via non-geminate recombination [169]. This is due to the unpolarized spins of initially free charge carriers, which leads to a 3:1 formation ratio between triplet- and singlet charge transfer states. However, it is still under discussion if the formation of the CTS follows this simple statistical approach [170, 171, 172]. All in all, the formation of triplet excitons is introduced as an additional loss mechanism due to the introduction of a drain for charge carriers [173, 169, 174].

The occurrence of triplet excitons in donor-acceptor blends was shown for a variety of material systems [175, 173, 169, 25, 176, 177, 34, 178]. Mostly, the proposed mechanism held responsible for triplet exciton formation is EBT [175, 173, 26, 169, 176, 34, 177]. Newly synthesized donor-materials possess a reduced bandgap which lowers the energy of the triplet exciton. This, in turn, increases the energetic driving force for triplet exciton formation from CT states. Furthermore, reducing the LUMO-LUMO and/or the HOMO-HOMO difference in OPV blend systems leads, on the one hand, to an increased open circuit voltage. On the other hand, however, the formation of triplet excitons on the donor or acceptor becomes energetically favorable [175, 176, 34, 179]. In the end, most of the previous works came to the conclusion that the population of triplet states leads to a reduction of device performance, since it is considered a major loss mechanism [25, 180, 35, 181, 173, 26, 34, 178, 175, 179, 182], or that triplet excitons act as a precursor for material degradation [176, 183]. However, some works also present routes for avoiding or attenuating triplet exciton formation, even when it is energetically favorable [184, 185, 186, 169, 35]. Unfortunately, just a few investigations take both energetics and morphology into account [187, 185].

The pervasive techniques for the investigation of triplet states are all-optical, such as transient absorption (TA) spectroscopy. Here, the difficulty is in the assignment of absorption peaks to different photo-excited species and the subsequent determination of lifetimes [173, 176, 175, 25, 182, 185, 180, 186, 169, 187]. The most direct and indubitable way to detect triplet states is the use of intrinsically spin-sensitive methods based on electron paramagnetic resonance (EPR). With these techniques, triplet states are clearly assignable to respective materials due to their characteristic Zeeman splitting (or g-factors) in externally applied magnetic fields. Only a few studies concerning triplet formation mechanisms have used these techniques, like photoluminescence and electrically detected magnetic resonance [181, 34, 178], transient electron spin resonance [35], or photoinduced absorption detected magnetic resonance [177].

6. Triplet Exciton Formation in *p*-DTS(FBTTh₂)₂:PC₇₀BM Based Small-Molecule Solar Cells

Despite energetic considerations, the orientation of molecules on the substrate is crucial for important device parameters like the ability to crystallize, light absorption, or charge transport. Therefore, the orientation of the molecules on a nanoscopic level is substantial for the improvement of organic solar cell materials. There exist only a few X-ray based methods to investigate the molecular orientation, for example grazing incidence wide angle X-ray spectroscopy (GIWAXS) [122]. Another method, however, is to exploit the orientation dependency of the wavefunction of the triplet excitons. This is done by using EPR based methods and changing the magnetic field direction with respect to the substrate surface, i.e. rotating the thin film in the magnetic field. With this, it is also possible to identify the orientation of the molecules on the substrate with high accuracy [188, 189, 190, 191, 192]. The advantage of these measurements compared to X-ray based techniques is the probing of photo- and electrically active molecules only, instead of the whole bulk. Furthermore, it is possible to clearly distinguish between crystalline and amorphous domains.

In this chapter, the formation mechanisms of triplet excitons in the material system *p*-DTS(FBTTh₂)₂:PC₇₀BM is studied using spin sensitive measurement techniques and relate our findings to device performance and thin film morphology, which is verified by PL quenching and angular dependent EPR-based measurements. In addition, this study is the first to measure triplet formation in real devices consisting of a BHJ blend of soluble small molecules.

6.2. Experimental Details

p-DTS(FBTTh₂)₂ was synthesized at the University of California in Santa Barbara and subsequently shipped to the University of Würzburg. PC₇₀BM was purchased from Solenne and 1,8-diiodooctane (DIO) from Sigma Aldrich. All materials were used without further purification. The pristine samples were prepared from a solution of *p*-DTS(FBTTh₂)₂ in chlorobenzene with a concentration of 21 mg/ml. For the blends, *p*-DTS(FBTTh₂)₂ and PC₇₀BM were mixed in a 3:2 ratio and dissolved in chlorobenzene with a final concentration of 35 mg/ml. For the samples with additives, 0.4 % by volume DIO was added to the solution.

For the BHJ devices indium tin oxid (ITO) covered glass substrates were used. First, a 40 nm thick PEDOT:PSS film was spin coated and annealed for 10 minutes at 130 °C inside a nitrogen glove box. Subsequently, the blended solution was spin coated, resulting in a film thickness of ≈100 nm. Finally, the samples were transferred into an evaporation chamber where the top metal contacts (Ca/Al) were thermally evaporated on top of the active layer. The *j*-*V*-characteristics were measured directly after the evap-

oration step inside the glovebox. The illumination source was a simulated AM1.5G spectrum.

The photoluminescence was measured at room temperature after excitation with a 405 nm diode laser under ambient conditions. It was fed into the monochromator via an Oriel liquid light guide with 5 mm diameter. The photon flux calibration was performed by a reference halogen lamp, mounted in an integrating sphere (labsphere LMS-100).

The PLDMR samples were prepared according to chapter 4.2. In short, the initial solutions were spin coated on 2.8 x 15 mm Herasil substrates, resulting in film thicknesses of ≈ 100 nm. The glass samples were placed into an EPR glass tube inside the glove box. They were isolated from ambient conditions with a homemade sealing system in order to prevent degradation due to oxygen and moisture. The thin film samples were illuminated with a glass fiber connected to a 532 nm DPSS laser, resulting in a cw illumination intensity of ≈ 60 mW.

For EDMR measurements, sample preparation took place as already discussed in chapter 4.2. Shortly, ITO covered glass substrates with 2.7 x 50 mm size were used and the solar cells were prepared after the aforementioned procedure. The devices were also placed in an EPR glass tube and electrically connected to a homemade sealing system. Afterwards, one electrode was connected to an external current-voltage source (Keithley) while the other was plugged to a current/voltage amplifier. For measuring the open circuit voltage directly, both electrodes were directly connected to the lock-in-amplifier.

The PLDMR and EDMR measurements were recorded by a modified X-Band spectrometer (Bruker E300), equipped with a continuous flow helium cryostat (Oxford ESR 900). Whereas all PLDMR measurements were performed at 5K, the EDMR spectra were recorded at room temperature. The PL was detected by a silicon photo diode placed in front of a microwave cavity with optical access (ER4104OR). The change of PL or photo current was detected via a Lock-In-Amplifier with the TTL modulated microwave as reference. For further information see also chapter 4.3.2 and 4.3.3.

6.3. Results & Discussion

In the following, the results obtained for the material system p-DTS(FBTTh₂)₂:PC₇₀BM are presented. At first, an overview on device performance and morphology is given. Subsequently, the zero field splitting parameters are obtained by a PLDMR experiment on a randomly distributed p-DTS(FBTTh₂)₂-sample. After this, PLDMR and EDMR techniques reveal the formation mechanisms of triplet excitons in this material sys-

tem. Finally, the orientation of molecules on the substrate is discussed using angular dependent PLDMR measurements.

6.3.1. Solar Cell Characteristics and Morphology

Three different material combinations were investigated, namely neat *p*-DTS(FBTTh₂)₂, *p*-DTS(FBTTh₂)₂ blended with PC₇₀BM in a 3:2 mass ratio and the same blend with the addition of 0.4 % by volume DIO. First of all, solar cells were prepared and the corresponding *j*-*V*-characteristics are shown in Figure 6.1 with the resulting solar cell parameters listed in the table inset. Here, it is evident that preparing a solar cell of only one organic material is not efficient concerning solar energy conversion. The pristine *p*-DTS(FBTTh₂)₂ shows almost no photovoltaic response, as shown in Figure 6.1 (blue). The low photocurrent of $5 \cdot 10^{-3}$ mA/cm² hints towards a very inefficient splitting of excitons, as is typical of most pristine organic semiconductors. Adding PC₇₀BM to the donor material leads to a splitting of excitons at the donor-acceptor interfaces and a decent power conversion efficiency (PCE) of ≈ 3 % (shown in orange). The best device, however, was achieved by adding a small amount of the processing additive DIO to the initial solution (red). Thereby, the morphology of the thin film is optimized. A much higher photocurrent and fill factor double the PCE to more than 7 %, which is in accordance to previously published values for this blend system [118, 122].

As previously reported, pristine *p*-DTS(FBTTh₂)₂ films show very high crystalline order on the substrate whereby the molecules orient in an edge-on orientation, as revealed by GIWAXS [122, 123]. Adding PC₇₀BM to the system results in a very fine intermixing of both materials when spin casting a thin film. On the one hand, the dissociation probability of excitons is enhanced, while on the other hand, charge transport properties are deteriorated and recombination is increased. The addition of 0.4 vol% DIO to the initial solution or thermal annealing leads to an increase of pure, crystalline *p*-DTS(FBTTh₂)₂ phases in the film. This, in turn, leads to an improved morphology as both CT dissociation and free carrier transport are enhanced. Hence, overall device performance is improved in spite of that the exciton dissociation efficiency is actually hampered [122, 164, 193].

In order to confirm these morphological differences, photoluminescence (PL) quenching studies were performed on the three investigated blend systems. In Figure 6.2 the corresponding calibrated photon fluxes of the PL are compared. Neat *p*-DTS(FBTTh₂)₂ showed the highest flux, as the singlet excitons mainly recombine radiatively. This is in accordance to the poor efficiency for the device made of pristine *p*-DTS(FBTTh₂)₂. Adding PC₇₀BM leads to a quenching of the PL by a factor of 550. Here, the singlet excitons are split efficiently, and the occurring free charges recombine mainly non-

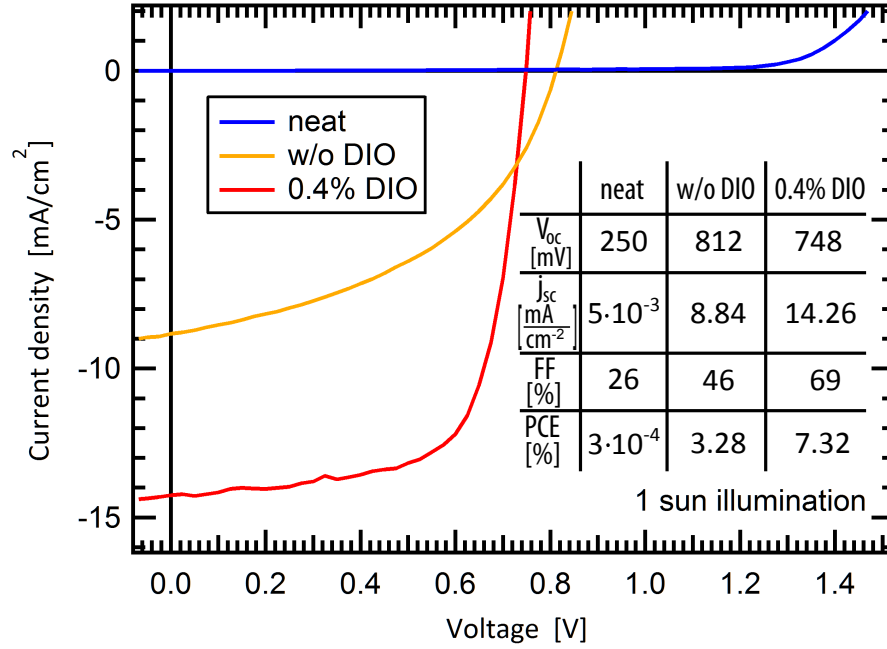


Figure 6.1: J-V-characteristics for the investigated material systems pristine p-DTS-(FBTTh₂)₂ (shown in blue), p-DTS(FBTTh₂)₂ blended with PC₇₀BM (orange) and p-DTS(FBTTh₂)₂:PC₇₀BM (red) with the addition of 0.4 % DIO. The corresponding solar cell parameters are listed in the table inset.

radiatively. In addition, radiative recombination via the charge transfer state is possible as well, introducing another recombination mechanism. Therefore, the presence of lower energy emission that stems from relaxed charge transfer states was confirmed, as has been reported previously [194, 195, 196]. This process is visible by the red-shifted part of the PL, indicated by the horizontal arrows in Figure 6.2. With the addition of DIO, the PL gets enhanced again by a factor of 54. This is due to an increasing contribution of singlet excitons that are not split efficiently at an interface and recombine radiatively in pure p-DTS(FBTTh₂)₂ phases. However, the blend with DIO yields the best performing solar cells which is in contradiction with the conclusions concerning exciton splitting. Nevertheless, the efficiency is also affected by recombination and transport properties which seem to be beneficial in this improved morphology [122, 164, 193]. The lack of pristine PC₇₀BM PL, which would have a maximum at ≈ 700 nm, supports the assessment that only rather small fullerene phases are formed. All in all, the morphological properties of p-DTS(FBTTh₂)₂-based material systems were confirmed via measurements of the PL photon fluxes.

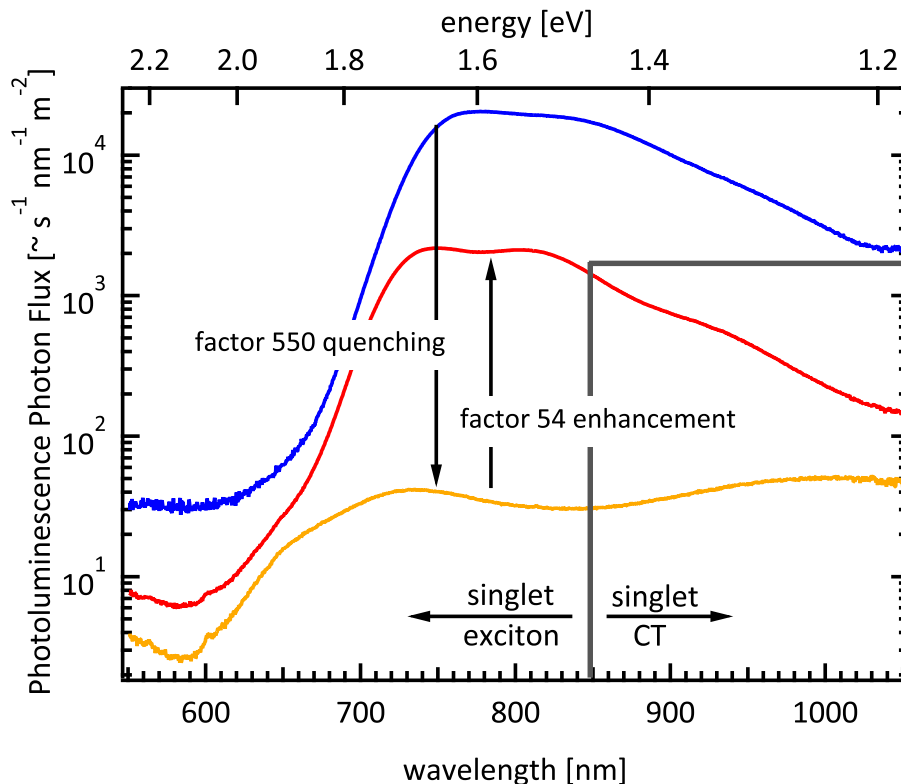


Figure 6.2.: Calibrated photoluminescence (PL) photon fluxes for thin films made of pristine p -DTS(FBTTh₂)₂ (blue), p -DTS(FBTTh₂)₂:PC₇₀BM (orange) and p -DTS-(FBTTh₂)₂:PC₇₀BM with the addition of 0.4 % DIO (red). The PL is quenched by a factor of 550 with the addition of PC₇₀BM. Adding 0.4 % DIO to the initial solution leads to a substantially enhanced PL. Two features are distinguishable, attributed to PL of singlet excitons and red-shifted emission of relaxed CT states, as indicated by the horizontal arrows.

6.3.2. Identification of Zero Field Splitting Parameters

The zero field splitting describes the energetic splitting of the Zeeman sublevels when no external magnetic field is applied. The exact theoretical description is presented in chapter 3.2.3. In short, the zero field splitting can be described by two parameters, namely D and E . They are directly connected to the extent of the triplet wavefunction, which is in turn strongly dependent on the distance between the two spin carrying particles. Therefore, the zero field splitting parameters are a characteristic fingerprint for each material. Furthermore, the zero field interaction is dependent on the angle between the externally applied magnetic field and the crystal axis. The most convenient way to determine D and E is to measure PLDMR on a randomly orientated sample. Here, a solution consisting of the investigated molecules was frozen, whereby the molecules orient randomly. The detailed sample preparation is described in chapter 4.2. This method yields a powder spectrum which can be simulated in order to deter-

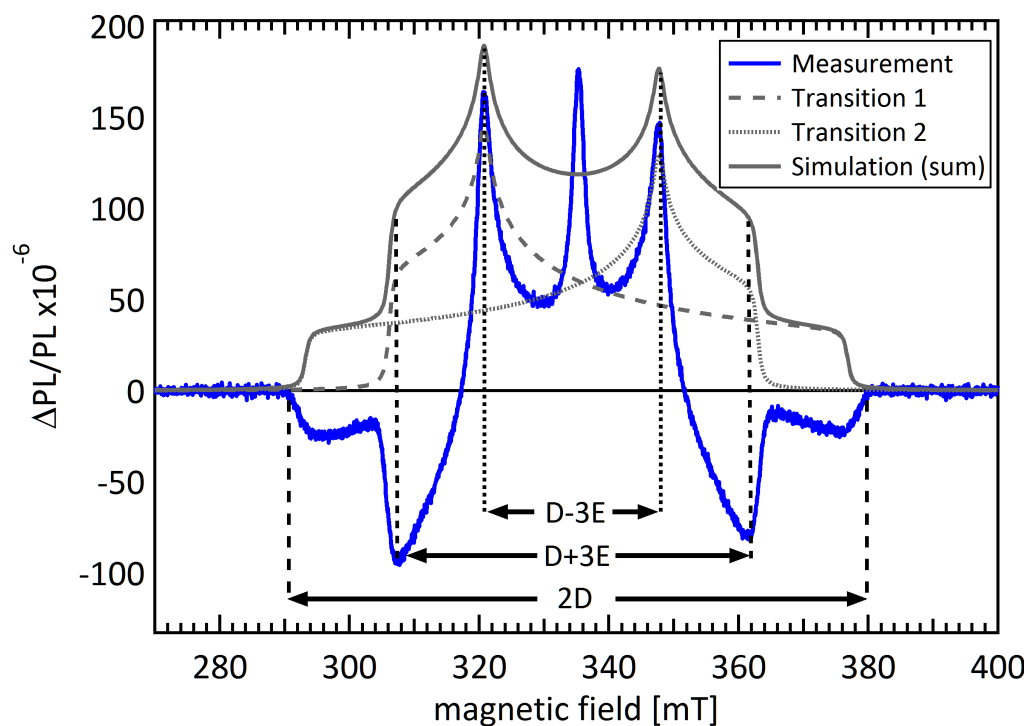


Figure 6.3.: PLDMR powder spectrum of pristine $p\text{-DTS}(\text{FBTTh}_2)_2$ molecules in a frozen chlorobenzene solution (blue). The simulated transitions between the single Zeeman sublevels are shown as dashed gray lines. The sum of both is depicted as solid gray line. The turning points of the spectrum are perfectly reproduced as indicated with horizontal arrows.

mine the respective D and E parameters. The result is shown in Figure 6.3. The signal (shown in blue) consists of two main components. First, a sharp central peak around 335 mT is observed, originating from weakly coupled spins with large distances. Second, a symmetric wing-like spectrum ranging from 290 mT to 380 mT is found, caused by localized triplet excitons on $p\text{-DTS}(\text{FBTTh}_2)_2$. The latter component has been simulated [66, 67, 197], whereas only the distinct turning points of the spectrum are necessary for the determination of the zero field splitting parameters and not the sign. The simulations for the single transitions are shown as dashed gray lines in Figure 6.3. Three distinct distances are apparent which can be assigned to the values $2D$, $D+3E$ and $D-3E$, as indicated in Figure 6.3. With these figures, the parameters $D = 42$ mT (1177 MHz) and $E = 5$ mT (140 MHz) can be straightforwardly calculated. As a consequence, D and E together with the distinct turning points constitute a characteristic fingerprint for the existence of triplet excitons on $p\text{-DTS}(\text{FBTTh}_2)_2$.

6.3.3. Triplet Excitons in *p*-DTS(FBTTh₂)₂:PC₇₀BM Blends

After the determination of the zero field splitting parameters *D* and *E* for the excitonic triplet state of *p*-DTS(FBTTh₂)₂, three spin coated thin film samples were investigated via PLDMR. The first one is pristine *p*-DTS(FBTTh₂)₂, the second one *p*-DTS(FBTTh₂)₂ blended with PC₇₀BM and last but not least *p*-DTS(FBTTh₂)₂:PC₇₀BM with the addition of 0.4 % DIO. In order to obtain more realistic conditions compared to solar cell operation, not a randomly oriented sample was chosen, but spin coated thin films on glass substrates (see also chapter 4.2). For reliable comparison, it was important to measure all samples at the same conditions, i.e. orientation with respect to the applied magnetic field, temperature and microwave power. Thus, the PLDMR signal strength can be correlated to the density of triplet excitons in the films. The resulting spectra are depicted in Figure 6.4. Here, the signal strengths for pristine *p*-DTS(FBTTh₂)₂ shows the highest triplet yield with a maximum relative PL change of 0.17 % at a magnetic field of ≈320 mT. Note, that the change of PL is normalized to the overall PL-signal. This accounts for variations in film thickness, collection efficiency of the photodiode or the altered radiative efficiency in the different blends (see also Figure 6.2). The very strong signal for pristine *p*-DTS(FBTTh₂)₂ can be explained by an efficient inter system crossing (ISC) of primary excited singlet excitons to long-living triplet excitons. The only recombination mechanisms for the singlet excitons are radiative- or non-radiative recombination together with the aforementioned ISC. This leads to a quite high triplet population in pristine materials.

Comparing the signal of *p*-DTS(FBTTh₂)₂:PC₇₀BM (orange curve in Figure 6.4) with pristine *p*-DTS(FBTTh₂)₂, the occurrence of a sharp central line at 335 mT is evident. This signal corresponds to a spatially extended triplet exciton, i.e. a CTS in a triplet spin state, which is populated via a mixing between singlet and triplet spin configuration [32, 23, 33]. The dipole–dipole interaction and with that the zero field splitting tensor **D** is highly dependent on the distance between the two spin carrying particles. Increasing this distance leads to a decreased zero field interaction and with that the symmetric line shape of the PLDMR signal merges to a central line. Remarkably, no CTS are detectable in pristine *p*-DTS(FBTTh₂)₂, which is in contrary to all other organic semiconductors studied so far [34, 183, 81, 70, 198]. As the CTS signal is visible in the randomly orientated sample (see Figure 6.3), this effect is explained by the very strong molecular order of the *p*-DTS(FBTTh₂)₂-molecules, preventing the singlet excitons to get split. This is in accordance with the very low j_{sc} for a device made of pristine *p*-DTS(FBTTh₂)₂, shown in Figure 2.8.

Furthermore, PC₇₀BM acts as an exciton quencher. Depending on domain size, singlet excitons get split, which in turn substantially reduces the probability of ISC. There-

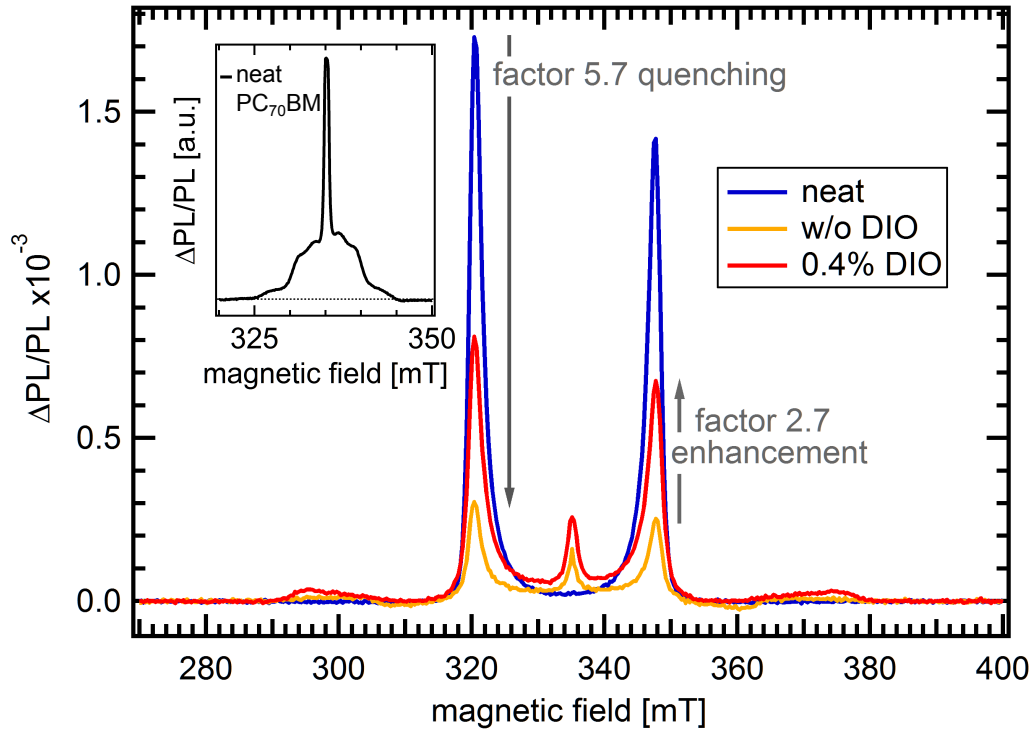


Figure 6.4.: PLDMR spectra of thin films made of pristine p-DTS(FBTTh₂)₂ (blue), p-DTS(FBTTh₂)₂:PC₇₀BM (orange) and p-DTS(FBTTh₂)₂:PC₇₀BM processed with 0.4 % DIO (red) measured at an angle of 90°. The PLDMR signal gets quenched by a factor of 5.7 with the addition of PC₇₀BM. Adding 0.4 % DIO to the initial solution leads to a partial recovery of the PLDMR signal with an enhancement by a factor of 2.7. The inset shows the PLDMR signal of pristine PC₇₀BM, which consists of a triplet signature with a width of 20 mT and a central peak.

fore, the PLDMR signal of p-DTS(FBTTh₂)₂:PC₇₀BM gets reduced by a factor of 5.7 in comparison to pristine p-DTS(FBTTh₂)₂, as indicated by the vertical arrow in Figure 6.4. However, the fact that there is a triplet population detectable after all hints towards another formation mechanism, which is the electron back transfer (EBT). The electron, which is already transferred to the PC₇₀BM phase during exciton dissociation, returns to the p-DTS(FBTTh₂)₂ phase again. This process is only favorable if the triplet state possesses a lower energy than the charge transfer state [173, 34]. A blend prepared without the addition of DIO leads to a very fine intermixed morphology, as discussed in section 6.3.1. Therefore, ISC is strongly suppressed because every singlet exciton will immediately find an interface where it gets split. As a result, the only possible formation mechanism for a p-DTS(FBTTh₂)₂:PC₇₀BM thin film is an EBT from the PC₇₀BM-phase to the excitonic triplet state of p-DTS(FBTTh₂)₂.

The PLDMR spectrum for the thin film made of p-DTS(FBTTh₂)₂:PC₇₀BM with 0.4 % DIO (red curve in Figure 6.4) possesses a signal strength in between the pristine sample

6. Triplet Exciton Formation in p -DTS(FBTTh₂)₂:PC₇₀BM Based Small-Molecule Solar Cells

and the blend without DIO. This is in contradiction to the morphological investigation presented in section 6.3.1. The EBT mechanism should be weakened due to the reduced interfacial area of interfaces between p -DTS(FBTTh₂)₂-molecules and PC₇₀BM. However, the formation of pure, crystalline p -DTS(FBTTh₂)₂-areas leads to enhanced lifetimes of singlet excitons, located in the donor-phases. This, in turn, leads to enhanced ISC, populating the excitonic triplet state not only via EBT, but also via ISC. The increased PL for the blend with 0.4 % DIO, as shown in Figure 6.2, supports the increased population of singlet excitons on p -DTS(FBTTh₂)₂ as well. The two occurring population mechanisms, ISC and EBT, are the reason for the enhanced triplet population in p -DTS(FBTTh₂)₂:PC₇₀BM solar cells processed with DIO. However, this is also the best performing device concerning solar conversion, as presented in Figure 6.1. This only leads to the conclusion that optimizing the morphology is by far more important for efficiency improvements than reducing losses via the triplet state, at least for this particular donor-acceptor blend.

The extent of the PLDMR signal of triplet excitons located on PC₇₀BM is ≈ 20 mT [199, 81, 200], as depicted in the inset of Figure 6.4 for pristine PC₇₀BM. Therefore, it is evident that no triplet excitons on PC₇₀BM are detectable. Consequently, the excitonic triplet state of PC₇₀BM has to possess a higher energy than the charge transfer state. Hence, it can not be populated via a back transfer process in this material system.

The transfer of these results to real working devices is not straightforward, because all PLDMR measurements were performed at 5 K. Therefore, the existence of triplet excitons at cryogenic temperatures may be valid, but an increase of temperature up to normal working conditions could also lead to an attenuation or even suppression of this effect. Nevertheless, it was already shown that the exciton diffusion length is not affected significantly by temperature [201]. To clarify this issue, solar cells were prepared which are suitable for EDMR measurements (for further details, see chapter 4.2). Thereby, it was possible to probe the occurrence of triplet excitons at room temperature. In this measurement, the illumination source was changed from the 532 nm DPPS laser to a white light LED with intensities below 1 sun. This yields realistic working conditions for organic solar cells. The results are depicted in Figure 6.5. Here, three different working points of the solar cell were investigated in order to further specify the relevance of triplet exciton formation. First of all, at open circuit voltage (V_{oc}), secondly at short circuit current (j_{sc}) and most importantly at the maximum power point (MPP). These points are indicated for the investigated device in the inset of Figure 6.5. For all three working points an EDMR signal is detectable and is clearly assignable to the excitonic triplet state of p -DTS(FBTTh₂)₂. This is highlighted by the same horizontal arrows as in Figure 6.3, showing the characteristic turning points of

the spectrum for triplet excitons situated on p-DTS(FBTTh₂)₂-molecules. As a consequence, it is evident that triplet excitonic states of p-DTS(FBTTh₂)₂ are populated even under realistic working conditions. Moreover, together with CT-states, they affect the photocurrent/photovoltage.

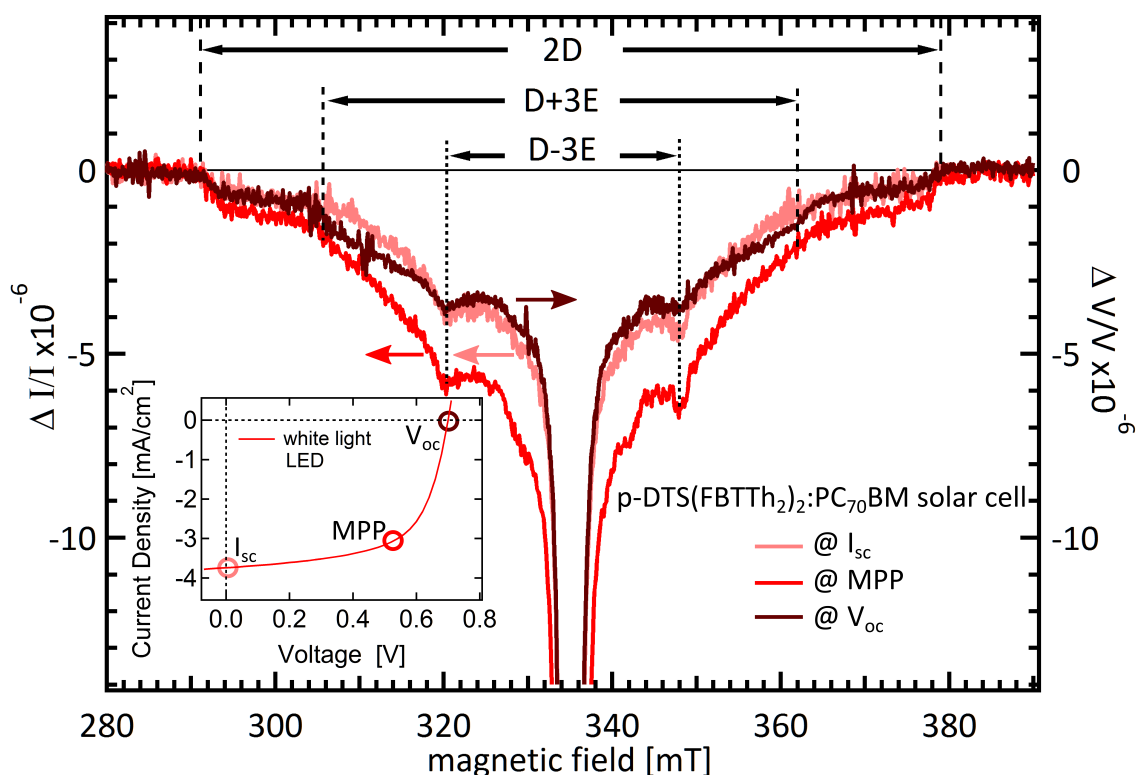


Figure 6.5.: EDMR measurements of a solar cell made of p-DTS(FBTTh₂)₂:PC₇₀BM with an optimized morphology by thermal annealing. The three spectra were recorded at different working positions of the device, as indicated in the inset. A clear signal from triplet excitons situated on the p-DTS(FBTTh₂)₂-molecules is visible, as marked by the three horizontal arrows showing the zero field splitting parameters of the triplet state on p-DTS(FBTTh₂)₂. The central peak is cut for better visibility and the colored arrows indicate the corresponding axis.

6.3.4. Molecular Orientation of p-DTS(FBTTh₂)₂ Molecules

Previous morphological studies on p-DTS(FBTTh₂)₂ films have shown that the molecules orient themselves on the substrate with a very high crystalline order. Furthermore, it was found that the side chains of the molecule stand on the substrate, defining the so-called edge-on configuration.

This kind of molecular orientation is depicted in Figure 6.6. Here, a coordinate system is introduced defining x, y and z as the principal axes of the p-DTS(FBTTh₂)₂-molecule, as depicted in Figure 6.6 a). Assuming edge-on configuration the molecules

6. Triplet Exciton Formation in p -DTS(FBTTh₂)₂:PC₇₀BM Based Small-Molecule Solar Cells

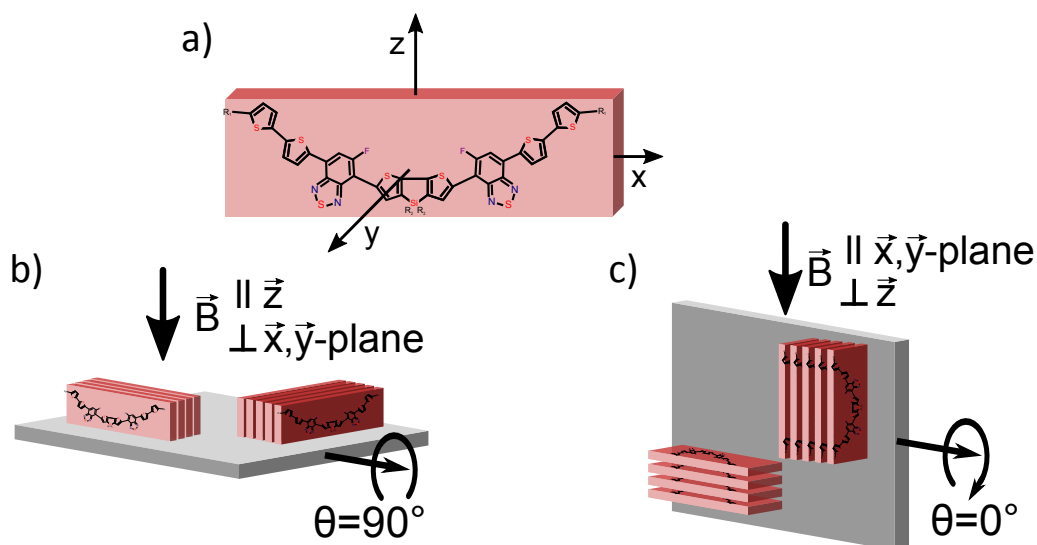


Figure 6.6.: a) Principal axes x , y and z describing the molecular orientation. b) Orientation of p -DTS(FBTTh₂)₂-molecules on the substrate surface for edge-on configuration. The external magnetic field is parallel to the z -axis, defining the rotation angle to be 90° . c) Rotating the sample to 0° yields the magnetic field to be parallel to the xy -plane of the molecule.

stand on the substrate surface with the z -axis being perpendicular to it. The orientation of the x - and y -axis, however, can be chosen randomly with the extreme positions depicted in Figure 6.6 b) and c). If an external magnetic field is applied to the substrate, the field is either parallel to the z -axis of the molecule (defined as 90° , Figure 6.6 b)) or in the xy -plane (corresponding to 0° , Figure 6.6 c)).

As already discussed theoretically in chapter 3.2.3, the extent of the triplet exciton wave function is connected to the position of the $\Delta m_s = 1$ transitions. This behavior is described in equation 3.11. Therefore, it is possible to probe the orientation of the triplet exciton carrying molecules if they orient themselves in an ordered way, unlike the molecules in a frozen solution, as shown in Figure 6.3. To prove the orientation, the angle between the crystal axes and the externally applied magnetic field is changed. This is realized by a goniometer which allows for rotating the sample tube in the microwave cavity (see also chapter 4.3.2). Measuring PLDMR spectra at different angles introduces a third parameter, which consequently results in the 3D-spectra shown in Figure 6.7. Here, the signal strength is displayed by the color coding, the external magnetic field correspond to the x -axis and the rotation angle is the ordinate. The angular resolved PLDMR spectra for the pristine p -DTS(FBTTh₂)₂-film, depicted in Figure 6.7a), show a very high dependency on the rotation angle. The dotted black lines in Figure 6.7a) represent the theoretical calculated signal pathways for p -DTS(FBTTh₂)₂-molecules with an edge-on orientation, according to Figure 6.6. Thereby, the Hamil-

tonian operator (see equation 3.7) was solved using the simulation software 'easypin' [66, 67, 197]. The precise accordance of the measurement signal with the theoretic calculation confirms the very high crystalline order of the p-DTS(FBTTh₂)₂-molecules on the substrate surface.

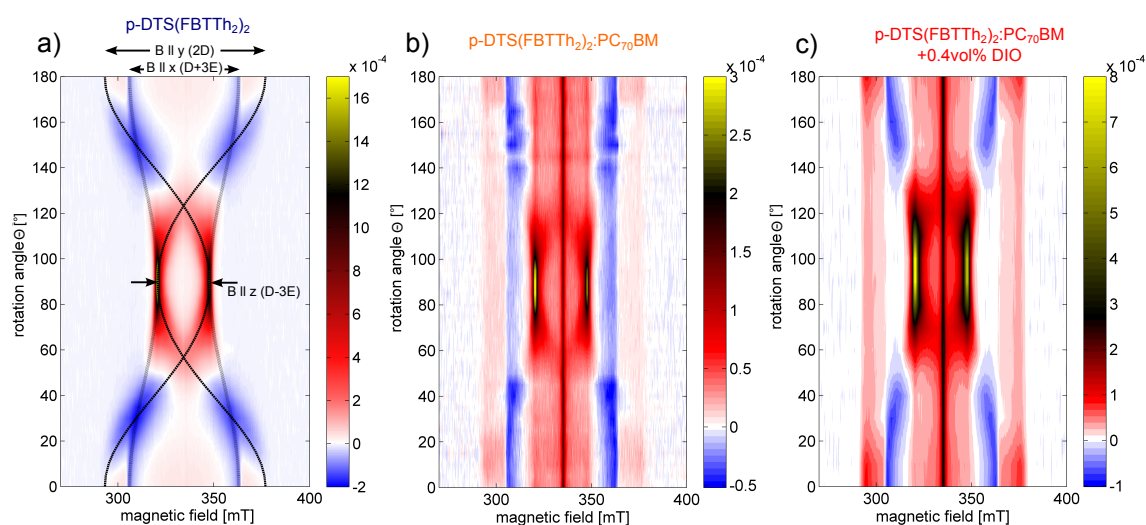


Figure 6.7.: Angular dependent PLDMR measurements of pristine p-DTS(FBTTh₂)₂ (a), p-DTS(FBTTh₂)₂:PC₇₀BM with 0.4 % DIO (b)) and p-DTS(FBTTh₂)₂:PC₇₀BM (c)). The black lines in a) are the theoretical calculated peak positions of the triplet signal with respect to the rotation angle Θ . The crystallinity and signal heights are decreasing from a) to c).

With the introduction of a second constituent, namely PC₇₀BM, the high molecular order is strongly suppressed. Figure 6.7 b) shows the near disappearance of the angular dependence of the PLDMR spectrum. Despite the stronger signal at a rotation angle of 90°, the spectra are almost identical for each rotation angle. This corresponds to a fine intermixing between p-DTS(FBTTh₂)₂- and PC₇₀BM. This behavior was also confirmed by the PL measurements, shown in Figure 6.2. The occurrence of the D-3E signal at a rotation angle of 90° is due to a still detectable preferred orientation of the p-DTS(FBTTh₂)₂-molecules. As a result, they are still oriented in an edge-on configuration with a certain probability but not nearly as crystalline as in the pristine p-DTS(FBTTh₂)₂-film.

Preparing a thin film from a solution with 0.4% added DIO yields an improved morphology with larger pure phases. Measuring angular dependent PLDMR on such a film results in the spectrum presented in Figure 6.7 c). Here, the extreme angular dependency of the PLDMR spectra for pristine p-DTS(FBTTh₂)₂ is attenuated as well. However, the disappearance of the negative triplet signal between $\approx 60^\circ$ and $\approx 120^\circ$ (shown in blue) hints towards a slightly higher overall crystallinity for the sample prepared with DIO compared to the sample made of p-DTS(FBTTh₂)₂:PC₇₀BM alone. This is again in

accordance with the morphological characterization made previously, in which larger areas of *p*-DTS(FBTTh₂)₂ were formed when adding DIO.

6.4. Conclusion

Three different material compositions were investigated consisting of pristine *p*-DTS(FBTTh₂)₂, *p*-DTS(FBTTh₂)₂:PC₇₀BM, and the same blend with the addition of 0.4 vol% DIO. First of all, the solar cell performance was verified together with the confirmation of morphological characteristics via measurements of the exciton quenching behavior using PL spectroscopy. Afterwards, the zero field splitting parameters $D = 42$ mT (1177 MHz) and $E = 5$ mT (140 MHz) of triplet excitons situated on *p*-DTS(FBTTh₂)₂-molecules were identified by measuring PLDMR on a randomly orientated sample. Switching to thin film samples yields more realistic working conditions concerning solar cell operation. Here, the triplet exciton formation mechanism for neat *p*-DTS(FBTTh₂)₂ was determined to be solely ISC. In addition, the formation mechanism for a fine intermixed blend is an EBT to the excitonic triplet state of *p*-DTS(FBTTh₂)₂. At last, the blend with the addition of DIO showed an indication for both mechanisms, ISC from larger *p*-DTS(FBTTh₂)₂-domains and EBT from interfaces to PC₇₀BM. However, no triplet excitons on PC₇₀BM were detectable, which rules out a back transfer to the acceptor molecule due to unfavorable energetics. Furthermore, the relative triplet yield was compared to device performance, showing no correlation at all. As a consequence, we showed that at least some OPV material systems exhibit a high open circuit voltage without suffering major losses to triplet excitons. This may suggest that well-working materials likely have a slow EBT rate, which allows them to maintain high performance despite the fact that EBT is energetically favorable. Additionally, the necessity of an optimized morphology for efficient exciton dissociation, charge generation, and charge transport is much more important for these material systems than optimizing them to reduce the population of triplet excitons. The relevance of these findings to operating devices was validated by EDMR measurements on a working device at room temperature under realistic illumination conditions.

Finally, the molecular orientation with respect to the substrate was investigated by angular dependent PLDMR measurements. Here, the strong tendency of *p*-DTS(FBTTh₂)₂ molecules to crystallize was confirmed together with the preferential edge-on orientation. All in all, this technique represents a versatile tool to simultaneously probe triplet exciton formation, molecular orientation, and crystallinity in one experiment.

7. Influence of Galvinoxyl-Doping on Charge Separation¹

Abstract

It was reported that organic solar cells doped with the free radical galvinoxyl show a strong increase in short circuit current and efficiency, respectively [202, 177]. Thereby, it was proposed that this enhancement stems from a resonant mechanism between the electron spin of galvinoxyl and the electron spin on PC₆₀BM. This, in turn, will lead to an equalization of spin sublevels of the charge transfer state. The effect was investigated by PLDMR spectroscopy on P3HT:PC₆₀BM thin films with different galvinoxyl doping concentrations, ruling out the formation of triplet excitons on both constituents. Moreover, the population of charge transfer states is indeed equalized when increasing the galvinoxyl concentration. Hence, an optimal doping level of 3.2 % by weight was estimated, in accordance to previously published values [202]. Furthermore, a temperature effect of the spin mechanism caused by galvinoxyl was excluded. All in all, the PLDMR measurements partly support the findings presented by Vardeny et al. [203, 204, 202, 205, 206, 177]. The strong increase of photocurrent, however, was not verified by the PLDMR measurements. As a consequence, the equalization of spin populations is not the only mechanism which is caused by galvinoxyl doping. The exact role of this molecule, however, remains puzzling.

7.1. Introduction

As already introduced in chapter 2.2, the high exciton binding energy in organic materials lead to the development of donor-acceptor systems. The most commonly used solar cell concept is the bulk heterojunction solar cell, where the donor consists of a polymer and the acceptor of a fullerene derivative. The probably most extensively studied material system is P3HT:PC₆₀BM, more detailed described in chapter 4.1. Thereby, the primary excited excitons need to be split at an interface between both constituents.

¹The results of this chapter are partly published in A1

7. Influence of Galvinoxyl-Doping on Charge Separation

This charge transfer process is a very important step between the absorption of light and the extraction of free charge carriers. The intermediate state, where the hole and electron are already spatially separated but nonetheless still coulombic bound, is called charge transfer (CT) state [24, 28, 195, 207]. This charge transfer exciton possesses a relatively long lifetime of a few microseconds [208]. Subsequently, the CT exciton may dissociate, forming free charge carriers that are extractable at the respective electrodes. More important, however, is the fact that the CT exciton may be in singlet or triplet configuration. With this, exciton dissociation and charge carrier recombination become spin dependent processes [208, 169].

To this day, organic solar cells struggle with limited power conversion efficiencies (PCE) compared to other, established photovoltaic technologies. Therefore, a lot of effort is spent in pushing the PCE further. For this, many different concepts were pursued, like improving device morphology [15, 209, 210], engineering new organic compounds [211, 212, 51, 213] or enhancing optical absorption [214]. One of the most severe factors which limits device performance is recombination. As this process is spin dependent, Vardeny et al. proposed the addition of a 'spin dopant' to donor-acceptor blends. It was suggested that this would modify the spin dependency in order to reduce geminate recombination in P3HT:PC₆₀BM blends [203, 206]. Furthermore, they concluded that this should have a detectable effect on device performance and, indeed, they presented P3HT:PC₆₀BM devices with increased PCE when manufactured with 2,6-Di-tert-butyl- α -(3,5-di-tert-butyl-4-oxo-2,5-cyclohexadien-1-ylidene)-p-tolyloxy (galvinoxyl, molecular structure depicted in Figure 7.1) [203, 204, 202, 205]. Recently, this concept was also shown for a different material system, namely PTB7:PC₆₀BM [177]. Galvinoxyl molecules possess an intrinsic electron spin of $\frac{1}{2}$, resulting in a resonant exchange interaction with other spin carrying particles [202]. Thereby, it was suggested that the geminate charge transfer state, which is in singlet configuration, gets transferred to the triplet state. Due to the longer lifetime of the triplet CT state, the splitting of the charge transfer exciton is facilitated. The responsible mechanism is supposed to be a spin-flip of the electron spin situated on PC₆₀BM through resonant conditions with the galvinoxyl spin [202]. Changing the acceptor from PC₆₀BM to PC₇₀BM and adding galvinoxyl, leads to a continuous decrease of PCE with increasing amount of galvinoxyl molecules [177]. Therefore, this mechanism is only visible in devices consisting of PC₆₀BM and galvinoxyl.

In accordance with this model, light induced electron paramagnetic resonance (EPR) was measured on P3HT:PC₆₀BM thin films with different galvinoxyl doping concentrations. Thereby, a preferred presence of galvinoxyl in the PC₆₀BM phase was ascertained [156]. Furthermore, the formation of triplet excitons on either constituent was ex-

cluded via photoluminescence detected magnetic resonance (PLDMR) measurements. Moreover, the singlet-triplet mixing of CT states due to galvinoxyl was confirmed by the same method.

7.2. Experimental Details

All samples were manufactured by the group of Prof. Jung-Keun Lee from the Chonbuk National University of Jeonju. The thin film samples were manufactured on PET foil by spin coating. P3HT was purchased from Rieke metals, PC₆₀BM from Nano-C and galvinoxyl from Sigma Aldrich and used without further purification. P3HT:PC₆₀BM solution was prepared in a 1:0.8 mass ratio, solved in 1,2-dichlorobenzene. For the galvinoxyl doped samples, a certain fraction of galvinoxyl powder was added to the initial solution in a weight percentage of 0.1, 1.0, 2.0, 4.0, 8.0 and 12.0 %. Spin coating yields film thicknesses of ≈ 220 nm. The samples, prepared in South Korea were shipped to the University of Würzburg excluding exposure to ambient atmosphere. Subsequently, the 2 cm x 2 cm sized PET thin films were cut inside a nitrogen filled glovebox into stripes with a width of 1 -2 mm. One of those was put inside a standard EPR tube, which was sealed under 20 mbar helium atmosphere.

The PLDMR measurements were performed as explained in chapter 4.3.2 with slight modifications. As no angular dependency was observed, the excitation by the fiber was disregarded and replaced by excitation via the optical entrance of the microwave cavity. The excitation source, however, was still the 532 nm DPSS laser. If not stated otherwise, the temperature adjusted by the cryostat was 5 K. For all measurements, the substrate surface was adjusted parallel to the external magnetic field and perpendicular to the laser excitation, respectively.

7.3. Results & Discussion

7.3.1. Galvinoxyl Doping Concentration Dependency

Galvinoxyl is a radical which carries an intrinsic spin of $\frac{1}{2}$. In combination with P3HT:PC₆₀BM, it is believed to cause a spin flip, most probable of an electron situated on PC₆₀BM [202, 177]. Therefore, it is conceivable that this molecule will also facilitate the population of triplet excitons. Here, the formation of excitons on PC₆₀BM is more likely but triplet excitons formed on P3HT are possible as well. To investigate this, PLDMR measurements were performed on samples with different galvinoxyl doping levels with the results shown in Figure 7.1 a).

7. Influence of Galvinoxyl-Doping on Charge Separation

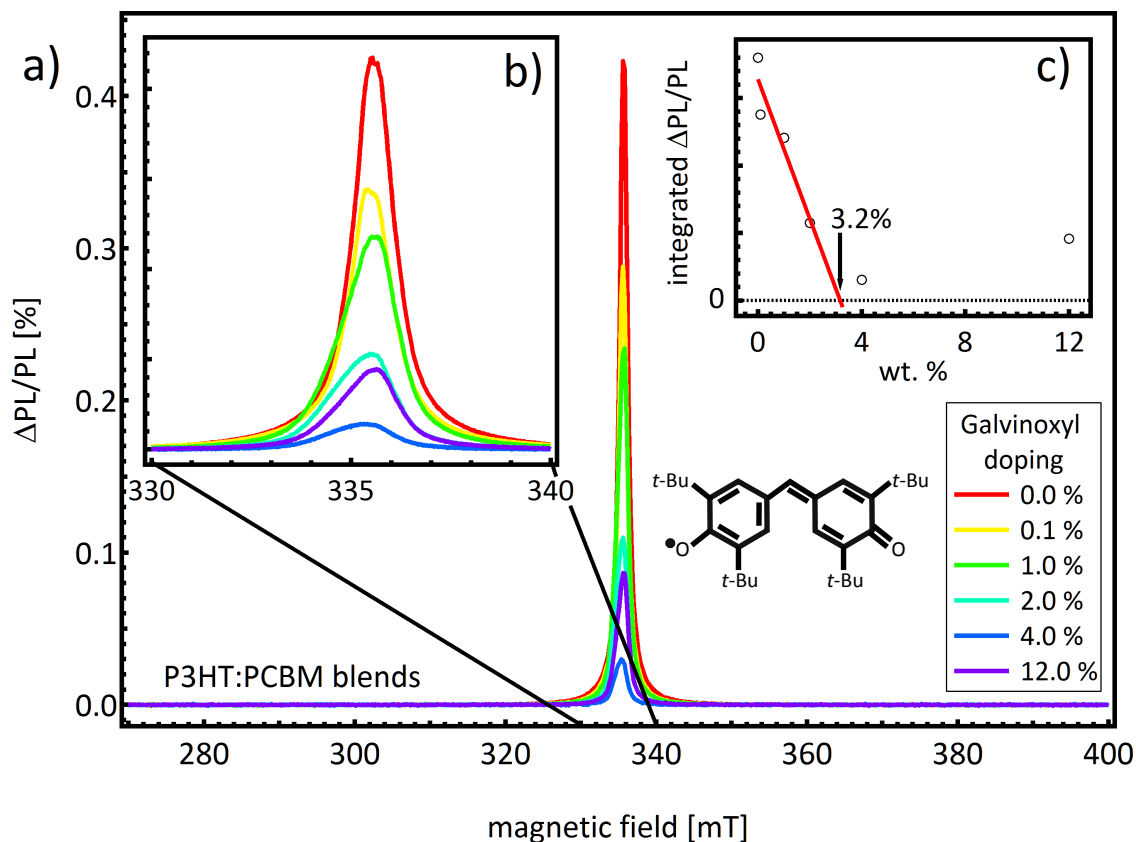


Figure 7.1.: a) PLDMR spectra for P3HT:PC₆₀BM blends with different galvinoxyl doping concentrations. The molecular structure of a galvinoxyl free radical is depicted in the picture, whereas *t*-Bu stands for *tert*-butyl. Neither triplet excitons on P3HT nor on PC₆₀BM are detectable. b) Central PLDMR peaks with higher resolution. The signal corresponds to a mixing of spin sublevels of the charge transfer state. c) The integrated PLDMR signals with respect to the corresponding doping concentration. A linear fit of the first four points (shown in red) indicate an optimal doping concentration of 3.2 %.

The clear absence of the characteristic triplet pattern (see also chapter 6), which ranges for P3HT usually from 280 mT to 390 mT [34], points directly to the conclusion that no triplet excitons are formed on P3HT. Furthermore, a PLDMR signal indicating triplets situated on PC₆₀BM is missing as well. As a consequence, the diffusion of primary excited singlet excitons to the donor-acceptor interfaces seem to be fast and independent of the galvinoxyl concentration. The only detectable change of photoluminescence (PL) is a sharp central peak at a *g*-factor of 2.002, also depicted in Figure 7.1 b) with a finer resolution. This kind of signal originates from a mixing between singlet and triplet charge transfer states, explicitly explained in chapter 3.4.2. Whereas the *S*₀ and *T*₀ sublevels of the CT state are almost degenerate, the *T*₁ and *T*₋₁ states are split apart when applying an external magnetic field (see chapter 3.2 for an exact theoretical description). At resonant conditions, microwaves enable spin flips between

the T_1 and T_{-1} states with the T_0 sublevel. Thereby, the population differences between these three states are equalized. This effect leads to a clear enhancement of the PL. The sign of the signal was confirmed by measuring the change of PL with an oscilloscope (not shown). The introduction of galvinoxyl molecules to the system seems to have a similar effect as the microwaves. Hence, the PLDMR signal decreases constantly with increasing galvinoxyl concentration until it reaches a minimum. Afterwards, it slowly recovers with further increasing doping level. This observation is in accordance with the working model introduced by Vardeny et al. [203, 204, 206, 202, 205]. Thereby, the galvinoxyl is supposed to cause a spin flip. As a consequence, galvinoxyl doping and irradiation with resonant microwaves are competitive processes. Hereby, the decreasing PLDMR signal with increasing galvinoxyl concentration is consistent. However, the recovering of the PLDMR signal when increasing the doping level up to 12 % is not explainable by spin flips. On the other hand, introducing 12 % by weight in a donor-acceptor system is a rather substantial fraction. Thus, it is possible that the galvinoxyl is not distributed uniformly through the thin film but accumulates to larger aggregates. Thereby, the ability to interact with electron spins on PC₆₀BM gets substantially suppressed. In Figure 7.1 c) the integrated PLDMR signals are shown for the respective galvinoxyl concentrations. Fitting the first four datapoints and extrapolating the fit to a vanishing signal intensity yields a doping concentration of 3.2 % by weight. As a result, adding ≈ 3 % galvinoxyl to the initial blend leads to an equalization of populations between the spin sublevels of the charge transfer state. This doping level is in surprisingly large accordance with the results shown for PCE improvements in P3HT:PC₆₀BM solar cells [202]. However, the huge increase of photocurrent in devices doped with galvinoxyl is hardly reconcilable with the presented PLDMR results. The maximum change of photoluminescence caused by resonant microwaves in the sample without added galvinoxyl lies beneath 1 %. The proposed gain in photocurrent due to spin flips of the charge transfer state is two orders of magnitude higher than the PLDMR signal. Therefore, it is unlikely that altering the spin populations is the only mechanism responsible for the vast increase in efficiency.

7.3.2. Temperature Dependency

So far, all PLDMR measurements were performed at cryogenic temperatures of 5 K. The results presented by Vardeny et al., however, were shown for room temperature experiments. Therefore, it is possible that the effect of galvinoxyl on the spin states of the charge transfer state increases significantly with increasing temperature. In order to investigate this temperature behavior, PLDMR measurements at different temperatures were performed on a P3HT:PC₆₀BM sample, doped with 0.1 weight percentage

7. Influence of Galvinoxyl-Doping on Charge Separation

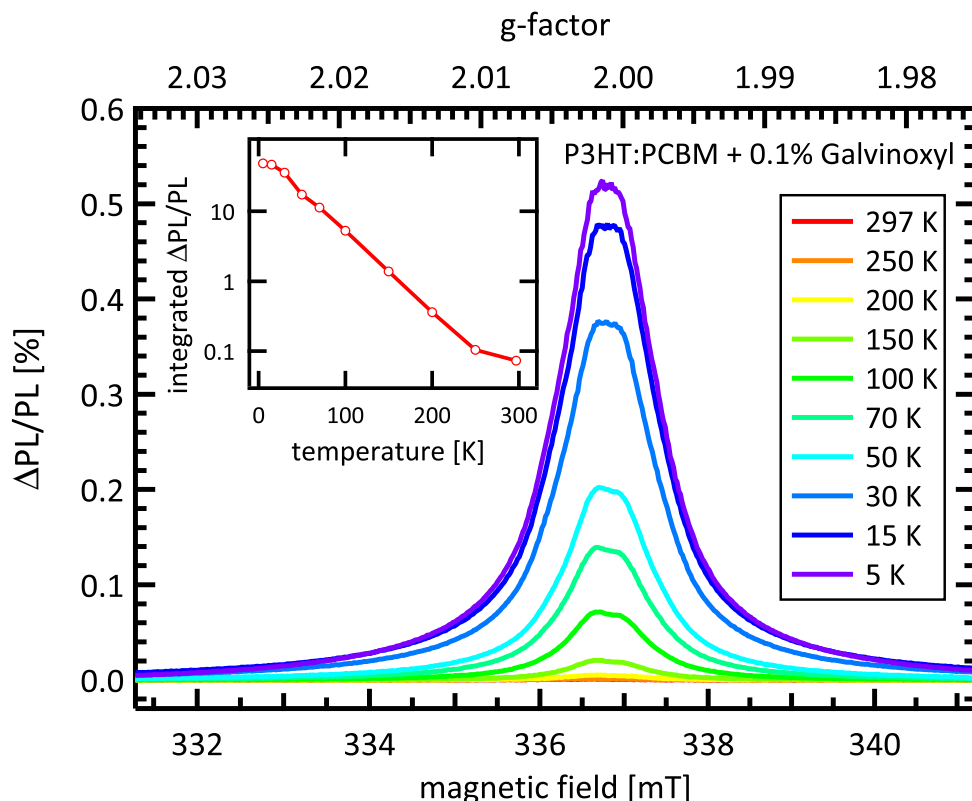


Figure 7.2.: PLDMR spectra for P3HT:PC₆₀BM with a galvinoxyl concentration of 0.1 % with changing temperature. The signal shape is not affected by temperature. Inset: integrated signal reveals exponential decrease of signal intensity with increasing temperature.

galvinoxyl. This material system was chosen because it showed the strongest PLDMR signal compared to the other doping concentrations at 5 K, as apparent in Figure 7.1. The PLDMR spectra with varying temperature are shown in Figure 7.2. Here, it is visible that the spectrum does not change its shape, only the signal intensity and linewidth broadening decrease. By integrating the spectra and plotting it logarithmically versus the corresponding temperature it is evident that the signal intensity falls off exponentially with increasing temperature, as depicted in the inset of Figure 7.2. This is in accordance with the signal dependency on the Boltzmann distribution, which was also derived in chapter 3.3. However, the signal intensity behaves as expected for magnetic resonance measurements. Therefore, the addition of galvinoxyl does not show any significant temperature effect on the PLDMR signal. Moreover, the spin dependent effect measurable with PLDMR becomes vanishingly small at room temperature. This is again in contradiction with the results obtained by Vardeny et al. [202], concluding that the photocurrent increase, caused by the doping with galvinoxyl, is not explainable by spin dependent processes alone.

7.4. Conclusion

PLDMR measurements on P3HT:PC₆₀BM thin films doped with different concentrations of the free radical galvinoxyl were performed. The measurements revealed that galvinoxyl is able to flip spins, altering the population of spin sublevels of the charge transfer state. Thereby, it is a competing process with the application of resonant microwaves, leading to a decrease in PLDMR signal intensity with increasing galvinoxyl concentration. An optimal doping level was found to be a weight percentage of 3.2 %, in accordance with the results published by Vardeny et al. [202]. However, it is very unlikely that spin effects of galvinoxyl is the main mechanism behind the vast increase in photocurrent that was published for this material system [202]. This was also supported by temperature dependent PLDMR measurements on P3HT:PC₆₀BM doped with 0.1 % galvinoxyl, which showed only a dependency on the Boltzmann distribution. All in all, the exact influence of galvinoxyl on an organic solar cell system remains puzzling. However, an influence on the morphology should not be excluded hastily but investigated more thoroughly.

8. Quantifying Spin-Dependent Recombination

Abstract

The influence of spins on recombination processes in organic solar cells is under heavy debate in the last years. Similar to OLED applications, the difference between singlet and triplet charge transfer states should have a major impact on non-geminate recombination. The method of choice for probing spin dependent processes in organic devices is EDMR. However, in continuous wave experiments all main processes occur at the same time. Furthermore, the explanation of the signal genesis remains challenging. Nevertheless, three distinguishable signal contributions were interpreted to stem from free charge carriers on both material constituents and one signal from a charge transfer state with small dipolar coupling.

The charge carrier extraction technique open circuit corrected transient charge extraction (OTRACE) temporally decouples the three main processes generation, recombination and extraction in organic solar cells [215]. Combining this with spin resonant conditions quantifies the fraction of spin dependent recombination in P3HT:PC₇₀BM solar cells to be $(0.012 \pm 0.009)\%$ at room temperature and $(0.052 \pm 0.031)\%$ at 200 K. Although these values constitute only lower limits, they are surprisingly small. As a consequence, the relevance of spin dependent recombination in organic solar cells has to be seriously reconsidered.

8.1. Introduction

In recent years, spin dependent processes in organic semiconductors attracted increasing attention in various application fields [216, 217, 169, 168]. Commercially available OLED devices consist of organic materials which are doped with a heavy atom in order to increase spin orbit coupling [218]. Here, the influence of spin statistics was figured out as early as 2000 and is vastly exploited nowadays, for example in OLED displays for telecommunication applications. Recently, a different approach was introduced by

8. Quantifying Spin-Dependent Recombination

Adachi et al. using thermal energy to convert triplet exciplexes into luminescent singlet exciplexes (see also chapter 9) [216]. In organic photovoltaics, however, the influence of spins on the performance is still under ongoing discussion. Hereby, recombination processes are in particular under suspicion to be strongly spin dependent [169]. For the geminate case, only singlet charge transfer excitons are formed subsequently to the creation of a singlet exciton. For the non-geminate case, however, uncorrelated spins form charge transfer states in a triplet to singlet ratio of 3:1. Both spin states possess diverse properties. The recombination to the singlet ground state is largely suppressed for the triplet CT state due to spin conservation rules, neglecting the possibility of an EBT. This results in a superior lifetime of triplet CT states compared to their singlet counterpart. The increased lifetime will, in turn, yield a higher probability for the triplet states to dissociate again into free charges, reducing the overall recombination. As a consequence, spins in organic semiconductors are a variable that could have serious influence on the functionality of organic devices.

Quite often the technique used to investigate spin dependent processes is the magnetic field effect. Here, an observable is monitored during the application of an externally applied magnetic field [219, 220, 168, 217]. The change of the observable, which is usually the current or luminescence, is connected to spin dependent processes occurring in the sample. However, this method has no possibility to distinguish between different overlapping contributions. Therefore, it can be seen as a first indication for spin dependent processes, but the exact assignment remains challenging. Another method to study triplet states is via the detour of lifetime determination. Thereby, transient photoinduced absorption measurements reveal long living states that are consequently assigned to triplet states [169, 173, 187, 185]. For an unequivocal proof of spin-dependent contributions, however, spin resonant measurement techniques have to be applied. As the sensitivity of conventional electron paramagnetic resonance measurements is limited, the more sensitive technique of electrically detected magnetic resonance (EDMR) is the method of choice concerning the investigation of spin dependent recombination in organic solar cells.

Continuous wave (cw) EDMR, on the other hand, has the drawback that fundamental processes like excitation, recombination and extraction happen at the same time. In order to investigate recombination alone, these processes have to be temporally separated. Therefore, the measurement technique open circuit corrected transient charge extraction (OTRACE) was combined with spin resonant conditions [215]. With this, it is possible to measure not only the temporally resolved charge carrier density but also the fraction of recombination which happens due to spin dependent processes (see next section for further details).

In this chapter, the composition of the cwEDMR signal is interpreted. Furthermore, the cwEDMR signals of various material systems are compared and finally, the fraction of spin-dependent recombination is exemplarily determined by the application of OTRACE measurements under spin-resonant conditions for the material system P3HT:PC₇₀BM.

8.2. Experimental Details

All organic solar cells, suitable for cwEDMR measurements were manufactured according to chapter 4.2. Shortly, ITO patterned substrates with the size of 2.7 mm x 50 mm were first spin coated with PEDOT:PSS. After subsequent heating at 130°C for 10 minutes in a nitrogen glove box, the active material was spin coated resulting in a film thickness of ≈ 100 nm. Finally, the top metal electrodes (Ca/Al) were thermally evaporated. The active layer consisted of a mixture of a donor- and an acceptor material in a blending ratio of 1:0.8 for P3HT:PC₆₀BM, 2:3 for PTB7:PC₇₀BM, 3:2 for p-DTS-(FBTTh₂)₂:PC₇₀BM, 1:4 for MDMO-PPV:PC₆₀BM and 1:4 for PCDTBT:PC₇₀BM. Except p-DTS(FBTTh₂)₂, which was synthesized at the University of California in Santa Barbara, all materials were commercially purchased and used without further purification.

The cwEDMR measurements were performed according to chapter 4.3.3. All presented spectra were recorded under open circuit conditions, meaning the change of the open circuit voltage V_{oc} is monitored with respect to spin resonant conditions. Thereby, both electrodes were directly connected to the lock-in-amplifier. Furthermore, the voltage was generated by illumination with a white light LED with intensities slightly below 1 sun. Moreover, the measurements were performed at room temperature, if not stated otherwise.

OTRACE

The charge carrier extraction technique OTRACE is a direct advancement of photo-CELIV [215]. Both methods are temporally separating excitation, recombination and extraction. In photo-CELIV, however, certain properties prevent this method to be ideal for the investigation of organic solar cells. First of all, a laser is used for exciting charge carriers. Despite of not being ideal for realistic working conditions, this is not a major drawback. After shutting off the laser, however, a voltage corresponding to the initial open circuit voltage is applied further on. Consequently, this leads to an injection of charge carriers, as flat band conditions are not fulfilled anymore. Therefore, the working point of the solar cell is shifted away from V_{oc} , yielding distorted results for the

8. Quantifying Spin-Dependent Recombination

charge carrier recombination dynamics. The photo-CELIV technique was firstly applied by Juska et al. investigating microcrystalline silicon [147], but also conjugated polymers [146] and organic solar cells [221].

OTRACE, on the other hand, circumvents these drawbacks. First of all, the laser illumination is replaced by a white light LED which yields more realistic working conditions. The major advantage, however, is the introduction of a second measurement, prior to the actual extraction pulse. Therefore, an open circuit voltage decay (OCVD) transient is recorded for the specific solar cell. Hereby, the open circuit voltage drops across a $G\Omega$ resistor and is monitored via an oscilloscope. Switching off the LED results in a characteristic decay of the open circuit voltage. Subsequently, this curve is digitalized and entered in an arbitrary waveform generator (AWG). Finally, the experiment can be performed according to Figure 8.1.

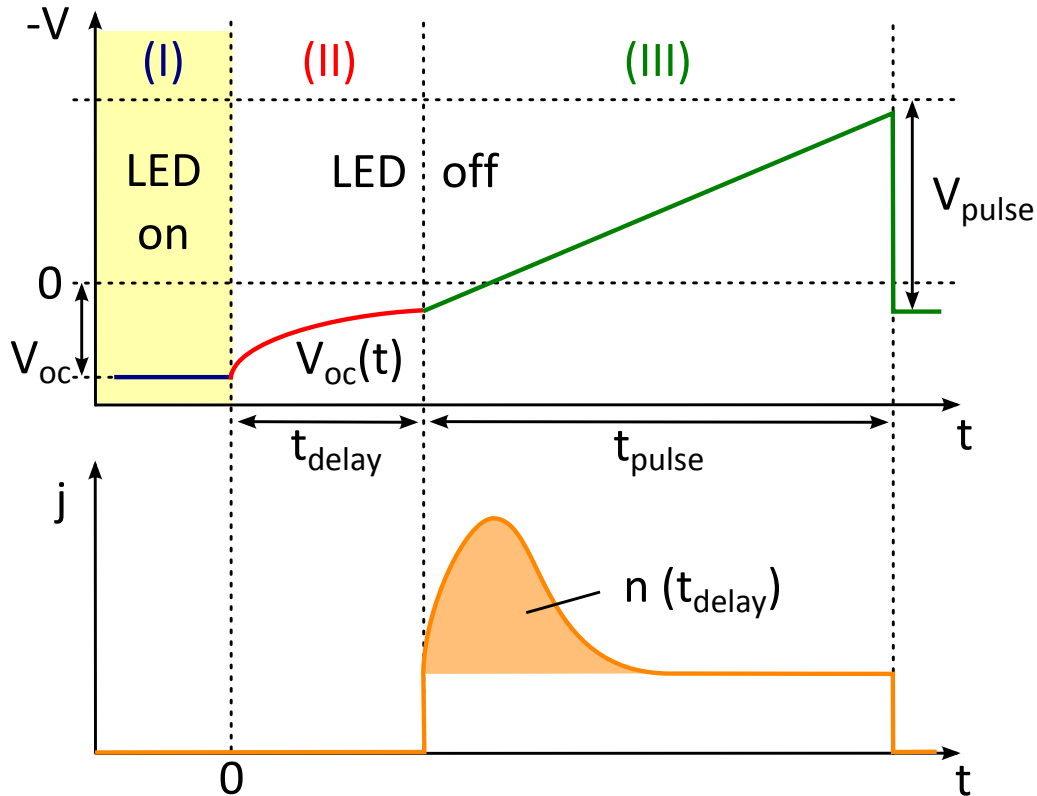


Figure 8.1.: Schematic OTRACE measurement sequence. The three basic mechanisms excitation (blue, I), recombination (red, II) and extraction (green, III) are temporally separated. The solar cell is kept at open circuit conditions during illumination and recombination by applying V_{oc} and the previously recorded OCVD transient. The triangular extraction pulse results in a capacitive, rectangular current response, together with a current signal originating from the remaining charge carriers in the device. With this, the charge carrier density $n(t_{delay})$ can be calculated.

In the beginning, the LED is illuminating the sample. At the same time, the solar cell is kept at V_{oc} . Consequently, no current is flowing through the device. When the LED

is switched off, the OCVD transient is applied simultaneously by the AWG in order to keep the solar cell at open circuit conditions. After a certain delay time, a triangular voltage pulse extracts all charge carriers that are still remaining in the device. On the one hand, this leads to a rectangular capacitive current response of the device and on the other hand, a current signal originating from the remaining charge carriers in the device is visible as an additional feature on top of the capacitive signal (filled orange area in Figure 8.1). Finally, the charge carrier concentration can be straightforwardly calculated. A distinction between electrons and holes, however, is not possible with this method. Nevertheless, in order to investigate recombination dynamics at realistic working conditions, OTRACE is the method of choice.

Setup for OTRACE-EDMR

Measuring OTRACE under spin resonant conditions leads to a rather complicated alteration of the EDMR setup, as depicted in Figure 8.2. First of all, the source measuring unit, used for applying a constant voltage to the solar cell in current detection mode, is replaced by an AWG. Furthermore, the commonly used Lock-In-amplifier is exchanged with an oscilloscope. Here, a high-performance computer, equipped with a transient recorder card was used which functioned as a storage oscilloscope with very high vertical resolution. The possibility to change between the $G\Omega$ resistor and the current-voltage amplifier was implemented manually. For future applications, however, an automatic switch would be beneficial. Moreover, the management of the magnetic coils implemented for rapid scan measurements, was realized by a self-developed control box. Last but not least, the LED has to be switched off as fast as possible to avoid distortions from the OCVD transient. This was implemented by a homemade switching box. All pulses were triggered by a pulse blaster card with ns accuracy.

8.3. Results & Discussion

The aim of this chapter is the quantification of spin dependent recombination processes in organic solar cells. Therefore, the occurrence of the cwEDMR signal has to be understood as good as possible. Due to the intention to investigate spin dependent recombination, all following experiments use the open circuit voltage as observable (see also chapter 3.5 for further explanation). Finally, an OTRACE experiment at magnetic resonant conditions will quantify the influence of spins on non-geminate recombination.

8. Quantifying Spin-Dependent Recombination

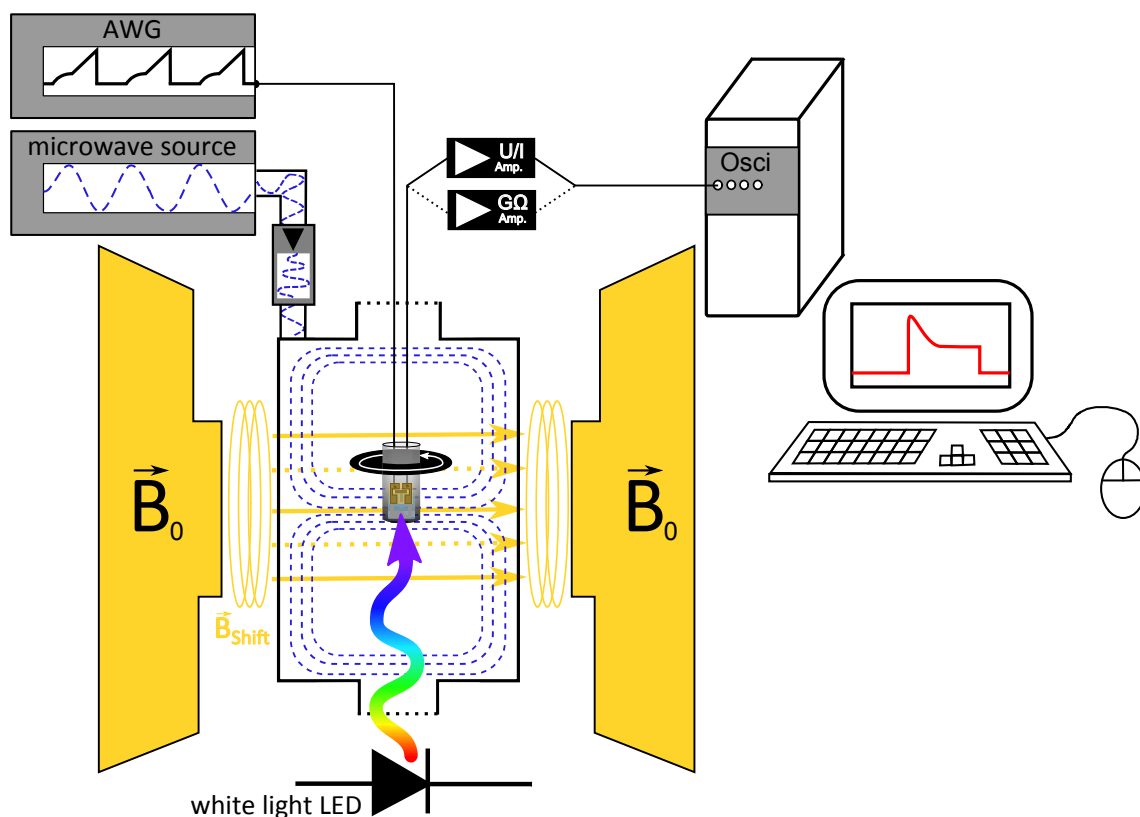


Figure 8.2.: Experimental setup for OTRACE-EDMR measurements. Implementing OTRACE into the EDMR setups leads to some substantial changes and extensions. Firstly, the SMU is replaced by an AWG, providing the OTRACE pulse sequence. Secondly, detection takes place via a digital storage oscilloscope, implemented in a high-performance computer. Here, either the OCVD transient is recorded via a GΩ amplifier (dotted connections) or the current through the device. Last but not least, the rapid scan coils have to be activated in order to shift the constant magnetic field. The illumination source is a white light LED to provide as realistic working conditions as possible.

8.3.1. EDMR Signal Genesis

Measuring cwEDMR at room temperature results in a characteristic peak at a g-factor of ≈ 2.0 , as depicted in Figure 8.3 for P3HT:PC₆₀BM. This signal corresponds to a $\Delta m_s = \pm 1$ transition, either for a free electron or for a triplet state without zero-field splitting. In the first case, the transitions take place between the $m_s = \frac{1}{2}$ and $m_s = -\frac{1}{2}$ Zeeman levels and in the latter between $m_s = \pm 1$ and $m_s = 0$. Usually, the zero field splitting introduces a magnetic separation between the two triplet transitions (see also chapter 6). If the distance between two spin carrying particles is high, the dipolar coupling will be so small that both transitions are not spectrally resolvable anymore. This behavior is theoretically described in chapter 3.2.4 and is depicted in Figure 3.5.

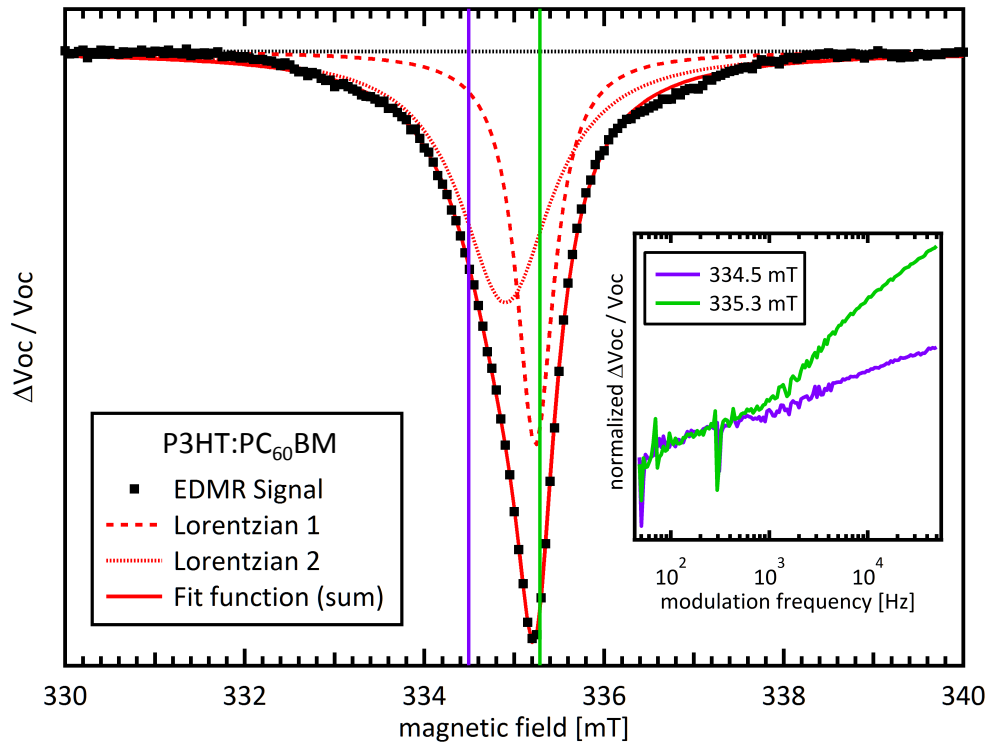


Figure 8.3.: Room temperature cwEDMR signal for a P3HT:PC₆₀BM solar cell (black squares). The fit function (solid red line) consists of two Lorentzian contributions (dotted and dashed red lines). Modulation frequency dependent measurements at two different magnetic field positions (indicated by the purple and green vertical lines) are depicted in the inset, revealing two different spin species.

By observing the cwEDMR more closely, it becomes evident that the signal is not describable by one contribution alone [181, 222, 223, 224]. Therefore, two Lorentzian peaks are needed in order to reproduce the measurement signal depicted by the red curves in Figure 8.3. The main contribution at 335.3 mT stems from the Lorentzian 1 (vertical green line), whereas at 334.5 mT, mainly from Lorentzian 2 (vertical purple line).

The change of the voltage due to spin resonant conditions is measured by switching the resonant microwaves on and off with a certain rate, as described in chapter 4.3.3. This rate is called modulation frequency and is a measure for the saturation behavior of a certain spin species. In order to investigate the two occurring signal contributions in the EDMR signal more precisely, the modulation frequency was increased, while the signal height at a specific magnetic field position was monitored. The results for the maximum peak position ($B=335.3$ mT) and at the shoulder of the signal ($B=334.5$ mT) are shown in the inset of Figure 8.3. Here, a clear deviation was observed for the two magnetic field positions, further proving that the EDMR peak consists of at least two different signal contributions. One interpretation would be a rather small zero-field

8. Quantifying Spin-Dependent Recombination

splitting, resulting in two signals that possess a small magnetic separation. However, the deviation of modulation frequency dependent measurements points towards more distinct signal contributions. Moreover, the widths of the single components are rather different, further hinting towards two independent processes. Another, better fitting explanation is that one signal stems from a triplet state with neglectable zero field splitting, while the other arises from a spin $\frac{1}{2}$ -particle. Comparing the signal positions with the g-factors of charge carriers in the actual materials, the second signal most probable arises from polarons on polymers (see also chapter 5).

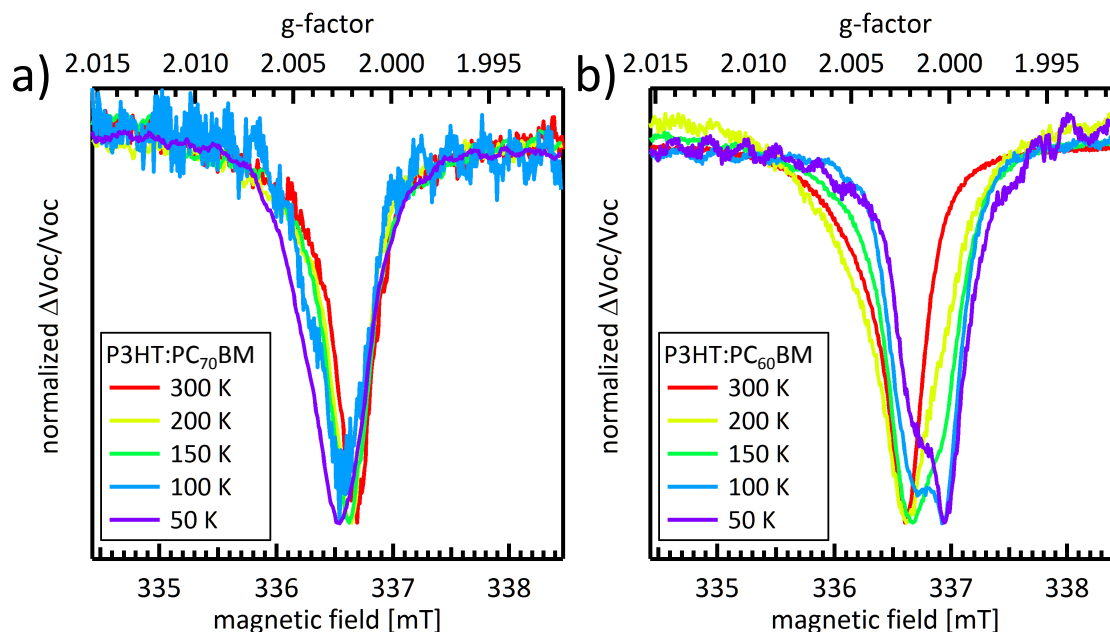


Figure 8.4.: Temperature dependent cwEDMR measurements for the material systems P3HT:PC₇₀BM (a) and P3HT:PC₆₀BM (b)). The signals are normalized for better comparison. For the sample consisting of PC₆₀BM, another signal contribution arises with decreasing temperature at g-factors around $g=2.00$. The same trend is visible for the device consisting of PC₇₀BM, with another signal arising at higher g-factors.

Performing temperature dependent cwEDMR measurements reveals a third contribution in the change of voltage due to spin resonant conditions. The results are depicted in Figure 8.4 for solar cells consisting of P3HT:PC₇₀BM (a) and P3HT:PC₆₀BM (b) [223]. For the sample with PC₇₀BM, the third contribution strengthens with lower temperatures and arises at higher g-factors. For the device consisting of PC₆₀BM, on the other hand, the third contribution appears at lower g-factors. These results are in great accordance with the corresponding g-factors of spins situated on PC₇₀BM and PC₆₀BM, respectively. As a conclusion, the cwEDMR signal is constituted of three contributions at low temperatures. Firstly, a charge transfer state with small zero field splitting, secondly a polaron on the polymer and thirdly an electron on the

fullerene. At room temperature, however, the signal coming from electron spins situated on fullerene molecules are not detectable.

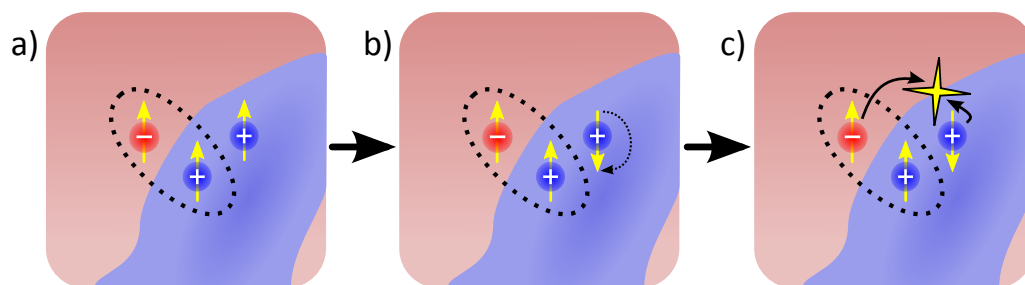


Figure 8.5.: Demonstrative picture of the processes responsible for the cwEDMR signal. A charge transfer state with a localized second polaron in close vicinity, where all spins (depicted as yellow arrows) possess parallel configuration (a)). Applying spin resonant conditions for the spin of the free polaron leads to a spin flip mechanism, indicated by the dashed arrow (b)). The polaron and electron in antiparallel configuration may recombine, as illustrated by the yellow star (c)).

A possible explanation for this is the introduction of a third particle in close vicinity of a charge transfer state [225, 226, 227]. The interaction of electron- and hole spins of the CT state forms a spin system which is either in singlet or triplet configuration. Their spatial separation, however, will lead to a rather low dipolar-coupling, resulting in a central line at a g -factor of ≈ 2.00 , as described theoretically in chapter 3.4.2. Imagining a third particle next to the CT state results in a more complicated situation, as illustrated in Figure 8.5. If the two spins of the CT state and the spin of the third particle are in parallel configuration, the recombination will be hindered (Figure 8.5 a)). Flipping the spin of the third particle (Figure 8.5 b)) at resonant conditions introduces the possibility to diffuse to the interface and subsequently recombining with the opposing particle (Figure 8.5 c)). The question if an intermediate step with a multiplicity of $\frac{3}{2}$ is formed prior to recombination or if the recombination happens without such an intermediate step is irrelevant for the explanation of the measurement signal. In Figure 8.5, this mechanism is shown for a third particle situated in the polymer phase. The same process, however, is also possible with an electron in the fullerene phase. Hence, the occurrence of three different signal contributions in the cwEDMR signal of P3HT:PC₆₀BM can be explained. Nevertheless, the strong temperature dependence of the fullerene signal remains puzzling. One conceivable explanation is the strong temperature dependence of the electron mobility. Whereas the electrons are mobile at room temperatures, they get more localized with decreasing temperature. Therefore, the fullerene signal appears only at cryogenic conditions, while the high trap density of polymers provides an additional room temperature signal.

8. Quantifying Spin-Dependent Recombination

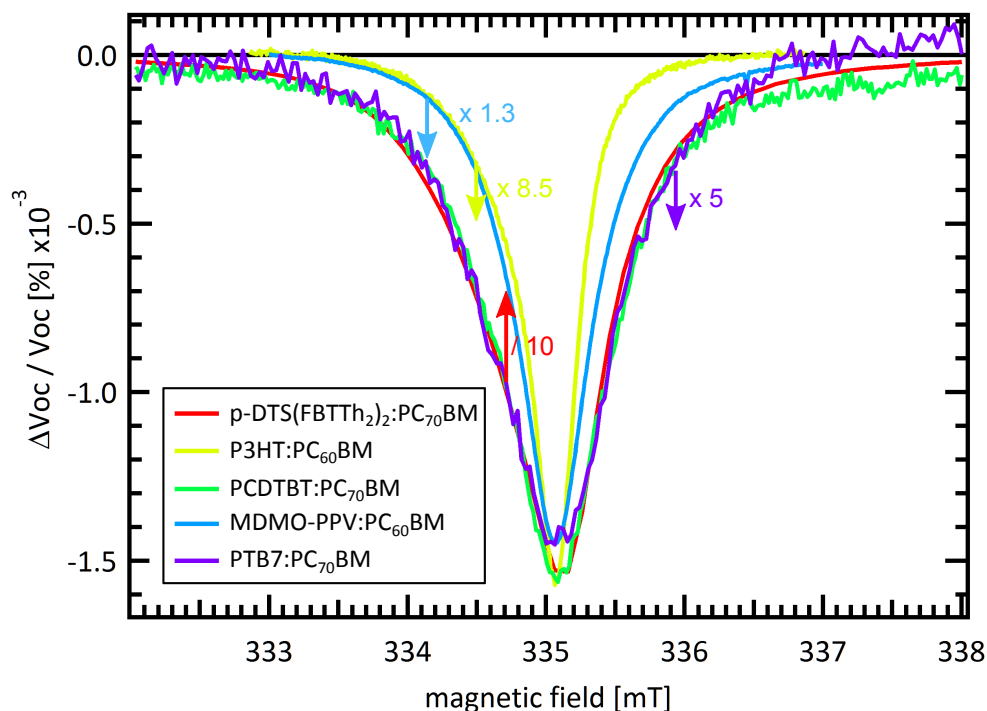


Figure 8.6.: Room temperature cwEDMR spectra of different organic solar cell material combinations. For better comparison, the signal of P3HT:PC₆₀BM was multiplied by a factor of 8.5, PTB7:PC₇₀BM by a factor of 5 and MDMO-PPVPC₆₀BM by a factor of 1.3, whereas the signal of p-DTS(FBTTh₂)₂:PC₇₀BM was divided by a factor of 10. All material combinations feature a similar signal structure and -height.

All previously shown results were obtained from the benchmark material system for organic photovoltaics, P3HT:PC₆₀BM. In Figure 8.6, the room temperature cwEDMR signals are shown for a variety of different material systems employed as active material in organic solar cells. For an improved visibility, the signals were scaled, to obtain similar signal heights. However, the signal intensities are not diverging by orders of magnitude. Moreover, the signal shapes are quite similar for all investigated material systems. Thereby, all peaks have to be reproduced by two signal contributions. As a consequence, the findings obtained for P3HT:PC₇₀BM are principally transferable to other organic solar cell material systems, as well.

8.3.2. OTRACE-EDMR

The quantification of spin-dependent recombination in organic solar cells was exemplary realized for P3HT:PCBM based solar cells, since this is the benchmark material system for organic solar cells. Aside from that, P3HT:PCBM devices yield very clear current traces when performing OTRACE measurements, which is beneficial in terms

of signal-to-noise ratio [215]. Furthermore, an electron back transfer mechanism is ruled out in solar cells consisting of a mixture of P3HT and fullerenes [34]. Therefore, only the spin-dependent recombination is probed by comparing an OTRACE signal at applied magnetic resonant conditions with an off-resonance OTRACE signal. Prior to the quantifying OTRACE experiment, a cwEDMR measurement is performed, in order to determine the resonant magnetic field position (see Figure 8.3 for comparison). Subsequently, the magnetic field is manually adjusted to the maximum peak position.

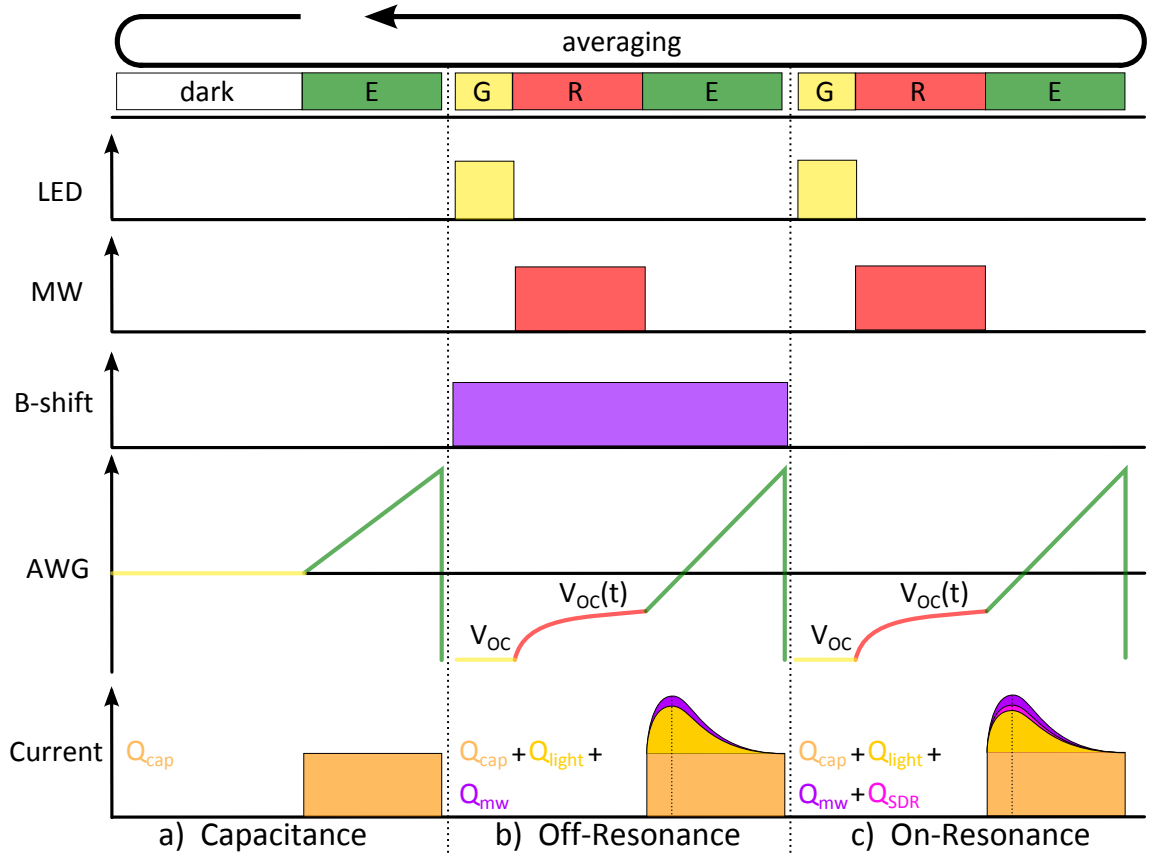


Figure 8.7.: Detection scheme used for OTRACE-EDMR measurements. The first sequence (a) probes only the capacitive response Q_{cap} of the investigated device by applying a triangular pulse without previous illumination. The second sequence (b) is an off-resonance measurement, realized by the shifted magnetic field. Here, a LED pulse creates charge carriers in the solar cell Q_{light} . The microwave pulse leads to a off-resonant increase in recombination and therefore, a decrease of charge carriers Q_{mw} . For the on-resonance sequence (c), the magnetic field shift is repealed, leading to an additional spin-dependent contribution of the recombination Q_{SDR} .

For further details concerning the OTRACE pulse, provided by the AWG, see also section 8.2. The OTRACE-EDMR experiments were realized by the detection scheme, depicted in Figure 8.7. Initially, a dark OTRACE signal is recorded in order to find the capacitive response of the investigated device (Figure 8.7 a)). The next sequence consists of an off-resonant OTRACE measurement, i.e. charge carriers are created by illumina-

8. Quantifying Spin-Dependent Recombination

nation, provided by a white LED. Moreover, a microwave pulse is applied during the recombination time. Last but not least, the magnetic field is shifted by two additional coils to an off-resonant magnetic field position. Here, a small displacement of ≈ 2 mT is already sufficient. Additionally to the capacitive response, this sequence leads to a light induced- and microwave induced contribution in the detected current transient. The whole second sequence is depicted in Figure 8.7 b). The last step of the detection scheme is the on-resonant OTRACE measurement, shown in Figure 8.7 c). Apart from the shifted magnetic field, all other pulses remain constant. Hence, the magnetic field position remains at the manually adjusted value for the peak maximum of the cwEDMR measurement. As a consequence, an additional contribution to the current transient appears, which is the fraction caused by spin-dependent recombination.

Though, the difference in the current transient due to spin-dependent recombination is very small. Therefore, the whole scheme has to be repeated many times in order to average the single current transients until the error is reduced significantly. This constitutes the main problem when performing OTRACE-EDMR measurements. Thereby, the solar cell has to be as stable as possible during the measurement time, which is another reason why P3HT:PC₇₀BM was chosen as the material system of choice. The presented detection scheme, on the other hand, is able to cushion minor instrumental- or sample drifts.

The OTRACE-EDMR results for a P3HT:PC₇₀BM solar cell are depicted in Figure 8.8. Here, it becomes obvious that the difference between on- and off-resonant measurement is extremely small, since no change in signal shape is visible to the eye. However, integrating the red-shaded area in Figure 8.8 a) yields a relevant difference in charge carrier density between on- and off resonance measurement. Thereby, the capacitive response was firstly subtracted from the overall signal, since only the light induced signal is of particular interest for recombination considerations. Subsequently, the difference between on- and off-resonance revealed the spin-dependent recombination part Q_{SDR} . With the dimensions of the active area, the number of charge carriers which were recombining due to spin resonant conditions can be straightforwardly calculated. For measurements performed at room temperature (see Figure 8.8 a)), this value yields $(3.7 \pm 2.6) \cdot 10^6$. Along with the total amount of light induced charge carriers $(3.0332 \pm 0.0049) \cdot 10^{10}$, the relative amount of charges that recombine due to spin-dependent processes gives $(0.012 \pm 0.009)\%$.

Reducing the temperature to 200 K and performing the same OTRACE-EDMR pulse sequence reveals an absolute number of recombined charge carriers due to spin-dependent processes of $(9.01 \pm 5.36) \cdot 10^6$. The measurement is depicted in Figure 8.8 b). The extraction time has to be considerably increased due to the attenuated transport

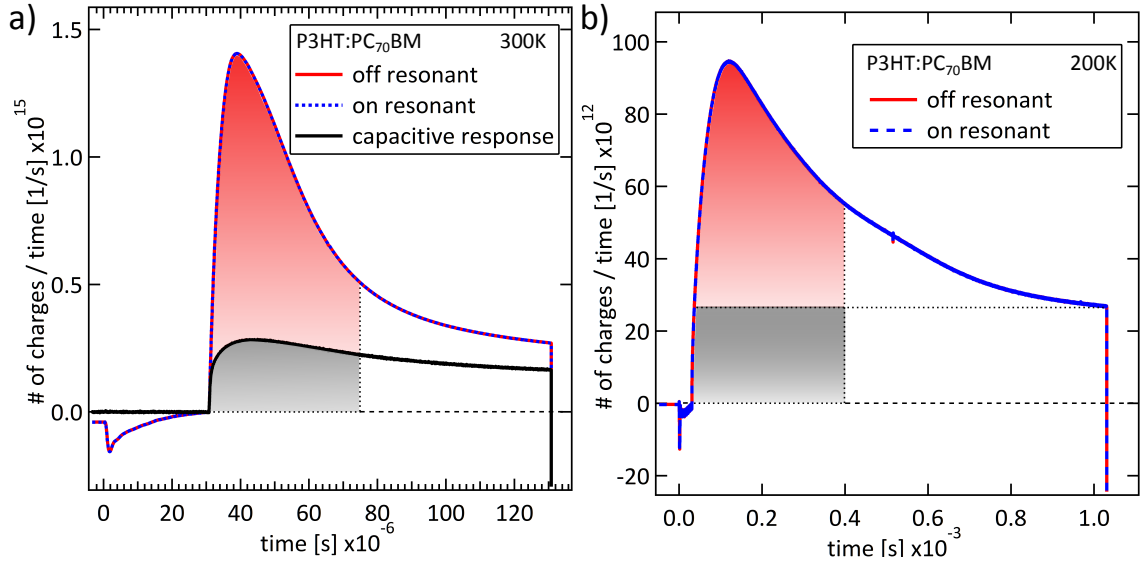


Figure 8.8.: On-resonant and off-resonant OTRACE-EDMR measurements of P3HT:PC₇₀BM at 300 K (a) and 200 K (b)). A difference is invisible for the eye but detectable by integrating the red-shaded area. Whereas the capacitive response is shown in black for the 300 K measurement, it is missing for 200 K and was estimated by the grey-shaded area. Note that the recombination time of 30 μ s and the peak voltage of the extraction pulse are constant. The huge difference in extraction time and signal height is only due to temperature dependent transport properties of organic materials.

properties of organic materials at low temperatures. However, the recombination time of 30 μ s and the extraction voltage were kept constant for both measurements. Unfortunately, a dark OTRACE measurement is missing for this temperature. Therefore, an estimation of the capacitive signal was performed, assuming a strict rectangular signal of the device. With this, the error estimation is ambiguous. Nonetheless, the relative change yields $(0.052 \pm 0.031)\%$, considering only the error of the light induced measurements. Comparing this value to the one obtained at room temperature yields an increase by a factor of ≈ 5 . This behavior is consequentially explainable with the Boltzmann distribution yielding a rise in signal strength when reducing the temperature. Nevertheless, the amount of recombined charge carriers due to spin dependent processes is surprisingly low. In some publications, spin dependent processes are considered as the main recombination mechanism in some organic photovoltaic systems [169, 187]. Although the previously presented fraction of spin dependent recombination is just a lower limit, the dependency on spins is orders of magnitude lower than expected.

8.4. Conclusion

Continuous wave EDMR signals of P3HT:PC₆₀BM were assigned to three components arising from different origins. At room temperature, only the contribution from transitions between triplet sublevels of a charge transfer state and the signal due to a polaron on P3HT are detectable. Reducing the temperature leads to the appearance of another contribution, attributed to a trapped electron on the fullerene. These findings were compared to different material systems, revealing the principal transferability of the results obtained for the benchmark material system P3HT:PC₇₀BM.

The OTRACE measurements technique temporally separates the three basic processes excitation, recombination and extraction in organic solar cells. Performing this under spin resonant conditions quantifies the fraction due to spin dependent recombination at room temperature to be $(0.012 \pm 0.009)\%$. Reducing the temperature to 200 K, increases the fraction by a factor of ≈ 5 to $(0.052 \pm 0.031)\%$. This is explainable by the influence of the Boltzmann distribution. Despite the fact that these values only constitute lower limits, they are orders of magnitude lower than expected. Therefore, the influence of spins on non-geminate recombination processes should be seriously reconsidered.

9. The Role of Spin States in Thermally Activated Delayed Fluorescence OLEDs¹

Abstract

Organic light emitting diodes (OLEDs) based on thermally activated delayed fluorescence (TADF) have high potential for economical and sustainable lighting applications. The efficiency of the TADF pathway is only partially governed by the spin statistics of injected electrons and holes, in which the intermediate exciplex state at the interface of two molecules is formed in the emissive singlet spin configuration with a probability of 25%. Rather, if the energetic separation between the singlet- and triplet exciplex spin configurations ΔE_{ST} is in the range of thermal energy, an efficient reverse intersystem crossing (RISC) from triplet- to singlet state may take place. For the investigation of the involvement of spins in exciplex emission, PLDMR and EDMR measurements suffer from severe limitations. However, ELDMR was found to be the most suitable tool for investigating the influence of spin states in electroluminescent devices and indubitably prove the involvement of spins in the emergence of TADF electroluminescence. Temperature dependent studies of bilayer devices revealed an energetic separation of the singlet and triplet exciplex state of THCA:Bphen and MTDATA:BPhen to be $\Delta E_{ST} = (20.7 \pm 1.2)$ meV and $\Delta E_{ST} = (58.2 \pm 4.5)$ meV, respectively. Finally, different scenarios were discussed explaining the reduced ΔE_{ST} for THCA:BPhen. An optimized separation distance is needed in order to reduce ΔE_{ST} , while maintaining sufficient interfacial recombination efficiency.

9.1. Introduction

The shift from organic solar cells to organic light emitting diodes (OLEDs) seems to be rather sudden. However, the basic mechanisms of solar cells and light emitting de-

¹The results of this chapter will be published in A6

9. The Role of Spin States in Thermally Activated Delayed Fluorescence OLEDs

vices are principally the same, with the only difference that they occur in the reverse order. Whereas solar cells are supposed to create electricity from light, LEDs shall create light from electricity. Furthermore, an ideal solar cell material is not only supposed to absorb and convert light, it also has to be as efficiently as possible when emitting light [228]. This foundation is based on the fact, that an emitted photon could be reabsorbed while non-radiatively recombined charge carriers are irrevocably lost. Unfortunately, an universal organic compound, suitable for application in lighting and solar conversion was not discovered, yet.

In OLEDs, the spins of the injected charge carriers are uncorrelated. Therefore, if they form an intermediate charge transfer state prior to recombination, they will have a singlet to triplet ratio of 1:3. Usually, only the singlet state recombines radiatively to the ground state, which is why OLEDs based on fluorescence are limited to a maximum internal quantum efficiency of 25%. However, the radiative efficiency can be increased if the triplet energy is used as well, i.e. by converting the triplet- to an emissive singlet state [229, 230, 218].

The most commonly used technique to access the triplet energy are phosphorescent materials containing a heavy metal atom like iridium or platinum. The strongly increased inter system crossing (ISC) rate yields internal quantum efficiencies up to 100 % [218].

Recently, another mechanism which enables the up-conversion of non-radiative triplet- to radiative singlet states in fluorescent materials was introduced [231, 232, 233, 216]. This mechanism is based on materials where the energy difference between the triplet- and the singlet state ΔE_{ST} is in the range of thermal energy at room temperature (≈ 26 meV). The thermal up-conversion process results in delayed fluorescence, since the triplet state possesses a longer lifetime. Consequently, light emitting devices exploiting this mechanism are referred to as thermally activated delayed fluorescence (TADF) OLEDs. An overview of the occurring processes is depicted in Figure 9.1.

TADF occurs in inter-molecular [231, 232] and intra-molecular material systems [233, 216, 234, 235, 236]. In both cases, the wavefunction overlap of the two particles forming the emissive state defines the energetic difference between the singlet and triplet states ΔE_{ST} , to which the most dominant parameter is the distance between the participating charge carriers (see also chapter 3.2.4). This value is defined by the electron-exchange interaction J , introduced in chapter 3.2.2. If this is small enough both spin configuration will be energetically nearly degenerate and can be interconverted by thermal energy and/or by spin-orbit or hyperfine interaction. Incidentally, a charge transfer state with a strong emissive transition to the ground state is often times called exciplex in literature.

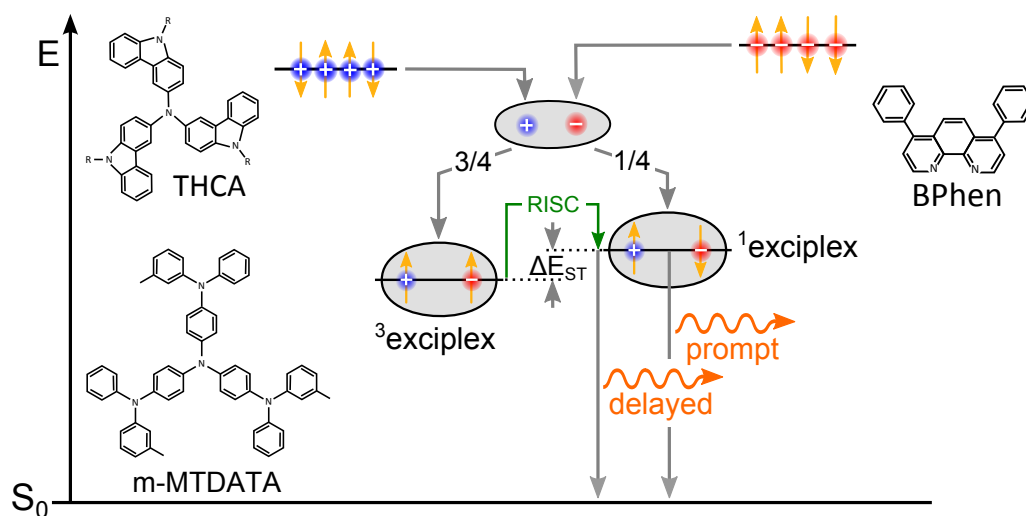


Figure 9.1.: Jablonski diagram of the occurring processes in TADF OLEDs. Electrons and holes form exciplexes, that possess a triplet to singlet ratio of 3:1. The singlet exciplexes recombine radiatively, whereby the luminescence occurs promptly. The triplet exciplexes can be converted via a thermally activated RISC process to the singlet state. This luminescence is delayed due to the longer lifetime of triplet states. Additionally, the molecular structures of the used materials are shown.

The reference donor-material for TADF OLEDs is 4,4,4-tris[3-methylphenyl-(phenyl)-aminotriphenylamine (m-MTDATA), which could be combined with different acceptor molecules in order to obtain exciplex emission [216, 237]. Moreover, the donor material tri(9-hexylcarbazol-3-yl)amine (THCA) together with different acceptors shows very promising properties in the development of white OLEDs [238, 239]. Both material systems possess large external quantum efficiency values, rendering them highly attractive for lighting applications [235, 238, 239, 240, 237, 241]. Whereas THCA forms glassy layers and is characterizable by non-planar structures [238], m-MTDATA possess a star-shaped, planar structure forming flat layers in the solid state [242]. The molecular structures of the investigated materials are depicted in Figure 9.1.

Generally, the dependence of recombination processes on the spin states follows from the magnetic field effect (MFE). In TADF materials and devices, MFE on electroluminescence (MEL), photoluminescence (MPL) and photocurrent (MPC) were also reported [243, 244, 174, 245]. Strong temperature dependence of MEL, MPL and MPC indicate a crucial role of the thermal activation in the generation of EL [244, 243, 174]. As pointed out in [244], however, it is difficult to distinguish between recombination pathways involving exciplex states formed at donor-acceptor interfaces and weakly bound polaron pairs formed otherwise, as both are magnetic field dependent. Moreover, the formation of (weakly) bound excited pair (or exciplex) states from injected charge carriers may depend on charge transport properties of device active layers, which are in-

9. The Role of Spin States in Thermally Activated Delayed Fluorescence OLEDs

trinsically temperature dependent, e.g. due to imbalanced mobilities. Hence, measuring the influence of a magnetic field on the EL at various temperatures is important, but alone does not allow to decipher the underlying spin-dependent recombination channel [246].

In this chapter, ELDMR, PLDMR and EDMR studies were performed on the material system tri(9-hexylcarbazol-3-yl)amine (THCA) together with 4,7-diphenyl-1,10-phenanthroline (Bphen). Thereby, the energy difference between the singlet and triplet exciplex state ΔE_{ST} was determined. Subsequently, this value was compared with the benchmark material 4,4,4-tris[3-methylphenyl(phenyl)-aminotriphenylamine (m-MT-DATA) and related to the molecular structure.

9.2. Experimental Details

THCA was synthesized at the Kaunas University of Technology (Lithuania). m-MT-DATA and BPhen were purchased from Aldrich. For the initial solutions, THCA, m-MT-DATA, or BPhen were dissolved in chlorobenzene with a concentration of 20 mg/ml.

Bilayer device were fabricated on indium tin oxide (ITO) covered glass substrates. First, poly(3,4-ethylenedioxythiophene):polystyrolsulfonate (PEDOT:PSS, 4083Ai) from Heraeus was spin coated, resulting in a ≈ 40 nm thick film, which was subsequently annealed for 10 minutes at 130°C in a nitrogen glovebox. Afterwards, the hole transport material was spin coated yielding a film thickness of ≈ 50 nm. In the next step, the samples were transferred into an evaporation chamber where 20 nm of the electron transport material BPhen was thermally evaporated on top of the hole transport layer. Finally, the top electrode (3 nm Ca / 120 nm Al) was evaporated, completing the device.

For the EDMR measurements, ITO covered glass substrates with 2.7 x 50 mm size were used and the OLEDs were prepared according to the aforementioned procedure. Subsequently, they were placed in an EPR glass tube and electrically connected to a homemade sealing system and then connected to an external source-measure unit (Keithley).

The ELDMR measurements were done in a modified X-Band spectrometer (Bruker E300) equipped with a continuous flow helium cryostat (Oxford ESR 900). The EL was detected by a silicon photodiode placed in front of a microwave cavity with optical access (ER4104OR). The change of EL was detected via a Lock-In-Amplifier with the TTL modulated microwave as reference.

The spectrally resolved photoluminescence (PL) was measured at room temperature by an Edinburgh Instruments FLS980 spectrometer. The steady-state EL spectra were recorded by biasing the completed device with an Agilent 4155C parameter analyzer in

constant current mode and coupling the emitted light via light guides to an Acton Spectra SP-2356 spectrometer (Princeton Instruments) or to a small SPM 002 spectrometer (Photon Control).

9.3. Results & Discussion

First, the presence of the TADF mechanism has to be shown for the used material combinations. Second, PLDMR and EDMR measurements were performed, leading to very vague results, though. Third, ELDMR was found as the method of choice for the investigation of TADF OLEDs, revealing the energetic separation of the singlet and triplet exciplex state ΔE_{ST} by temperature dependent measurements and unambiguously proving the involvement of spin states in the occurrence of TADF.

9.3.1. Exciplex Emission

At first, the occurrence of exciplex emission has to be verified for the investigated material systems. Therefore, different thin film samples were prepared, consisting of single layers of the pristine materials and stacked bilayers for the combination. On the one hand, the photoluminescence (PL) of the pristine materials was measured and on the other hand, the electroluminescence of the bilayer devices. In the latter, donor- and acceptor materials were processed subsequently, leading to two stacked layers with a well-defined recombination zone. The results for the used materials are shown in Figure 9.2.

BPhen possesses the largest HOMO-LUMO gap, which yields a PL peak at ≈ 380 nm. Here, singlet excitons are created via laser irradiation which immediately recombine again, emitting their energy as luminescence. The PL of pristine THCA peaks around 470 nm, leading to blue emission, which was already exploited in the development of a white OLED structure [238, 239]. Combining both materials in a bilayer structure, however, results in the disappearance of the direct band-to-band emission of the individual constituents, since no recombination partners are available when applying an external current. Moreover, electrons and holes have to travel through the bulk until they reach the interface to their counter-material. Here, they form exciplexes that possess a significantly lower energy than the singlet excitons. Therefore, the electroluminescent exciplex emission is heavily red-shifted, leading to a broad EL peak around 590 nm. The same principle applies for m-MTDATA:BPhen with an electroluminescence maximum around 560 nm.

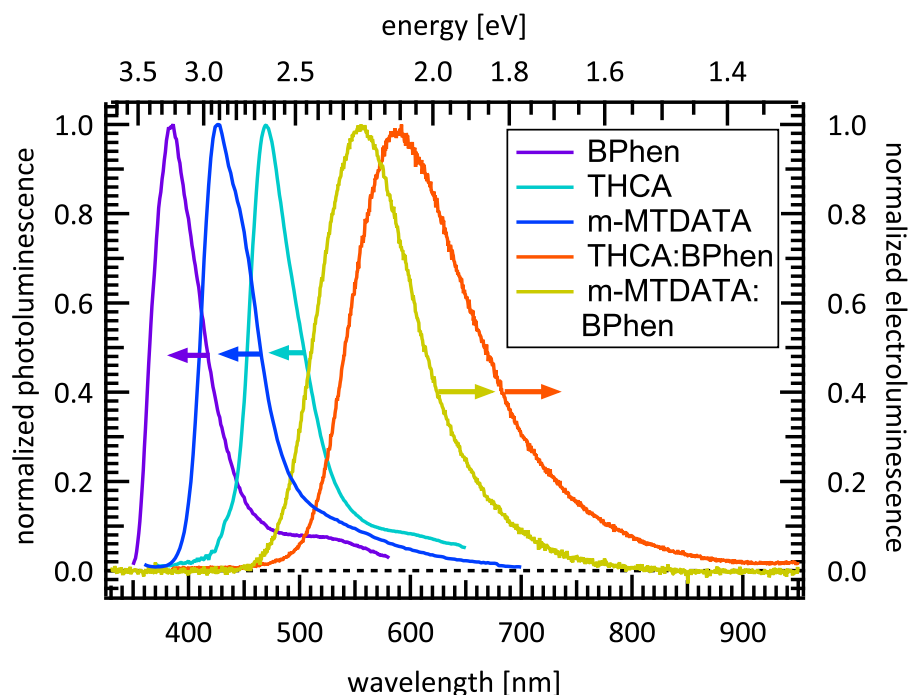


Figure 9.2.: Normalized photoluminescence spectra of pristine BPhen (purple) and -THCA (cyan). Forming a bilayer device and measuring electroluminescence yields exciplex emission with a substantial red-shift for m-MTDATA:BPhen (yellow) and THCA:BPhen (orange).

With this, the electroluminescent exciplex emission was confirmed when processing a bilayer device. Furthermore, the emission originating from singlet excitons of the pristine materials is strongly quenched. As a consequence, probing the EL of a bilayer device leads to the sheer investigation of the exciplex states.

9.3.2. PLDMR-measurements

In the next step, PLDMR measurements were performed on a blend, consisting of THCA and BPhen in a 1:1 mass ratio. Here, a 405 nm laser was used, together with a 450 nm longpass filter. The temperature dependent photoluminescence spectra are depicted in Figure 9.3.

In comparison to the previously shown PL spectra (see Figure 9.2) of the pristine materials, it becomes evident that the PL of the blend consists of at least two contributions. Especially at lower temperatures, the signal shows signatures of exciplex emission and PL of pristine THCA. Due to the aforementioned laser/longpass filter combination, a contribution of pristine BPhen emission is not detectable but nevertheless possible, as well. However, if present after all it is probably quite weak due to the low absorption at 405 nm, as implied in Figure 9.3. The multiple contributions are not sur-

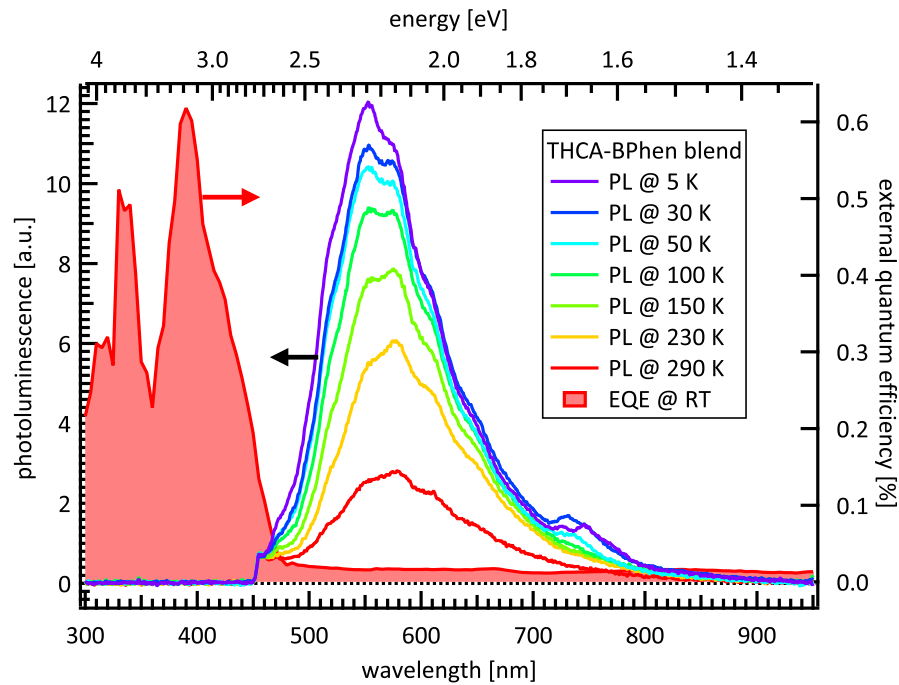


Figure 9.3.: a) Photoluminescence spectra for a THCA:BPhen blend at different temperatures. The signal consists of a contribution from exciplexes and a contribution originating from singlet emission of pristine THCA. b) EQE spectrum of a blend consisting of THCA:BPhen. Note the absence of an exciplex contribution.

prising at all, since laser illumination excites the pure phases, creating singlet excitons. These may either dissociate at an interface, forming exciplexes, or recombine radiatively. Since the dissociation probability decreases with decreasing temperature, the strengthening of the singlet PL with lowering temperature is consequential.

Furthermore, measuring the external quantum efficiency of a device consisting of a THCA:BPhen blend revealed the inability of the exciplex state to contribute to photocurrent, as presented in Figure 9.3 (filled red). As a consequence, the exciplex state has to possess an isolated energetic position, which means it is not able to dissociate again but has to recombine either radiatively or non-radiatively. Another explanation would be its inability to absorb light. However, this is unlikely, due to the strong oscillator strength of the emissive transition of the singlet exciplex state.

In the next step, temperature- and microwave power dependent PLDMR measurements were performed on the same sample. The results are depicted in Figure 9.4.

The temperature dependent PLDMR, shown in Figure 9.4 a) reveals the presence of two distinct signatures, where one is narrow while the other possesses a wider extent. They are reproducible by a double Gaussian fit beneath 150 K and with a single Gaussian fit above 100 K. Remarkably, both constituents show reversed temperature behaviors. Furthermore, measuring at a fixed temperature and decreasing the used mi-

9. The Role of Spin States in Thermally Activated Delayed Fluorescence OLEDs

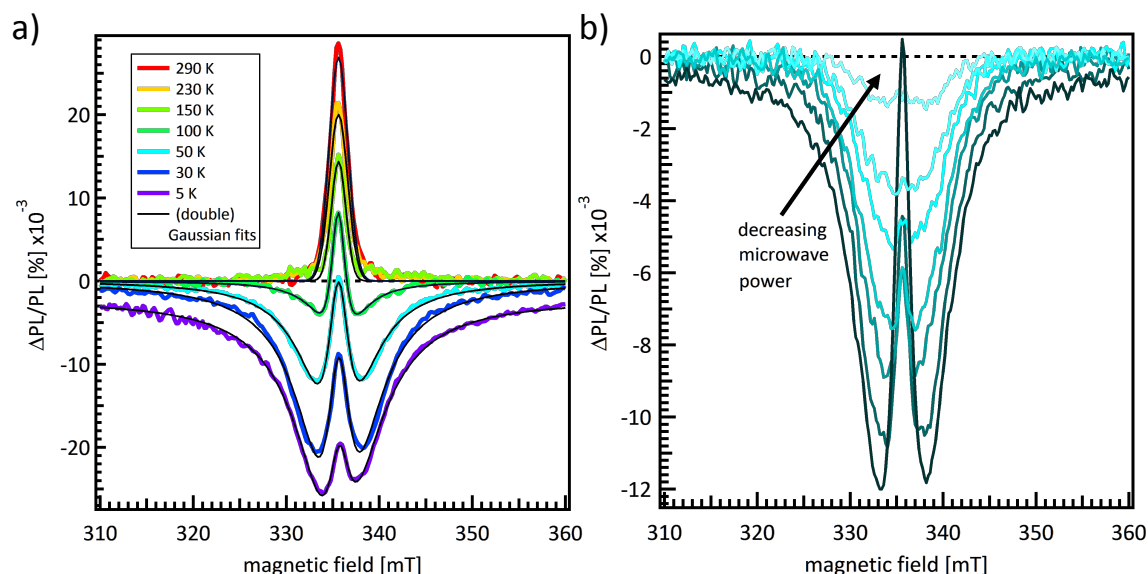


Figure 9.4.: a) temperature dependent PLDMR spectra of a THCA:BPhen blend at maximum microwave power. The signal consists of two contributions that show different temperature dependencies. Both signals are reproducible by Gaussian fits. Beneath 150K, a double Gaussian is needed in order to reproduce the measurement signals. b) microwave power dependent PLDMR spectra of the same blend at 50 K. The two signal contributions are clearly distinguishable by their different saturation behaviors and reversed temperature dependencies.

crowave power results again in a different saturation behavior for the two signal components, as depicted in Figure 9.4 b). With this, it becomes evident that the PLDMR signal of the THCA:BPhen blend is composed of at least two distinct signal contributions.

Unfortunately, the assignment proves to be difficult. However, the reversed temperature dependency and differing linewidths represent valuable indications. Accordingly, the broad signal could be assigned to localized triplet excitons, either on THCA or BPhen. The wider, yet unresolved extent could be due to undefined zero-field-splittings caused by distributed spin distances. Moreover, the signal strengthening at lower temperatures is characteristic for a signal originating from triplet-triplet-annihilation processes. The other signal, showing a smaller linewidth and a reversed temperature behavior, could stem from exciplexes. The expected wider distance would reduce the linewidth of the signal. As the spin mixing is a temperature activated process, the reversed temperature dependency is also consequential. However, an overlap of differently originating signals is highly conceivable as well, since in PLDMR, a narrow central signal is detectable for almost every material. Therefore, a direct observation of spin dependent processes solely occurring in the exciplex state is not possible with PLDMR. Moreover, the population path of the involved states is not at all representa-

tive for OLED application, since illumination created the excited species. Here, they are predominantly in the singlet state, in contrast to electrical excitation.

9.3.3. EDMR-measurements

In EDMR measurements, the current flowing through a device is the observable for spin resonant investigations. Hence, it is more suitable for studying OLEDs than PL-DMR, since the excitation occurs via electrical charge injection. For this purpose, THCA:BPhen bilayer devices were fabricated, where the interface between both materials defines the recombination zone. As a first step, the IV-characteristic was measured, which is depicted as black line in Figure 9.5 a). Here, the voltage has to be increased up to a certain threshold, where the device starts to emit light. The electroluminescence, measured at the same time, is shown as red curve in Figure 9.5 a). For the presented device, the threshold voltage was at ≈ 2.5 V. Before this value, no luminescence was detectable.

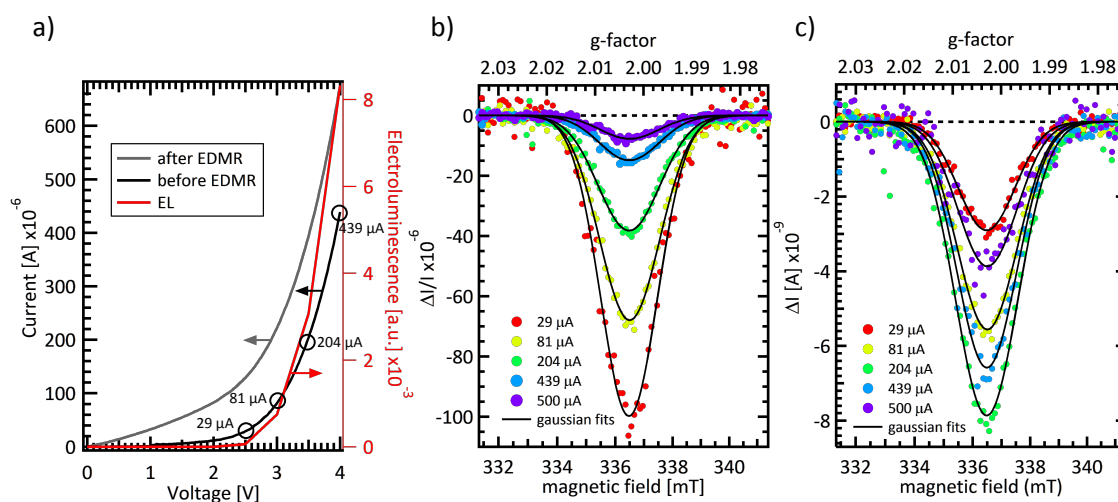


Figure 9.5.: a) IV-characteristic before (black) and after (gray) the EDMR measurements, together with the emerging electroluminescence (red) of the investigated THCA:BPhen bilayer device. Indicated are different working points above the threshold voltage. b) EDMR signals for the different working points of the device (colored dots) with gaussian fits (black). c) absolute change of current for the same measurements.

In the next step, EDMR measurements were performed. Interestingly, no signal was detectable for applied voltages below the threshold voltage. While applying 2.5 V to the device, a current of 29 μA was flowing. Using this current as input for the EDMR measurements, a spin dependent change of photocurrent occurs, as shown in Figure 9.5 b). As a consequence, the EDMR signal is due to a spin dependent process which occurs during exciplex emission, since neither EL nor EDMR is detectable beneath the threshold voltage. Increasing the voltage, and with this the current, leads to a decrease of

9. The Role of Spin States in Thermally Activated Delayed Fluorescence OLEDs

the EDMR signal. This behavior is counterintuitive, since more current should result in more exciplexes, which, in turn, should increase the EDMR signal. Moreover, the EDMR signal is normalized to the input signal, in this case the current. In Figure 9.5 c), only the change of current ΔI is shown for different measurement points, not the normalized signal. Here, ΔI is more or less the same for all investigated working points, that are indicated by the circles in Figure 9.5 a). With this it becomes obvious, that the normalization is responsible for the decreasing EDMR signal. Likely, the reason for the increased overall current is the severe degradation of the device due to the quite high applied current flows. Remeasuring the IV-characteristic after performing the EDMR measurements revealed a vastly altered IV-curve, depicted in gray in Figure 9.5 a). This proves the continuous degradation which takes place during the EDMR measurements.

As a result, EDMR is basically a suitable tool for measuring spin sensitive processes in OLEDs. However, the severe degradation during the measurement is a huge problem since it distorts the obtained outcomes. Furthermore, the possibility of manifold spin dependent contributions to the current which are superimposed with the interesting exciplex signal is not easy to exclude, as well.

9.3.4. ELDMR-measurements

The method of choice when probing spin dependent emission of TADF OLEDs is electroluminescence detected magnetic resonance (ELDMR), more detailed described in chapter 4.3.4. Here, the electroluminescence (EL) represents the observable of the measurement. Thereby, a change in the EL caused by spin-resonant conditions is monitored. The advantages of this technique are apparent. Firstly, the population of exciplexes takes place via injected charge carriers, which ensures the correct spin-statistics. Secondly, the observable is directly the property of the material system which is of particular interest. Furthermore, degradation of the devices is negligible, since leakage currents are not contributing to emission.

In Figure 9.6, the ELDMR signals of the material system THCA:BPhen are shown for different temperatures. They are reproducible by simple Gaussian fits. This allows for different interpretations. At first, the distance between the spin carrying particles is very large, i.e. the dipolar coupling between them is negligibly low (see also chapter 3.2.4). With this, the two $\Delta m_s = \pm 1$ transitions are at the same magnetic field position and possess a simple line width broadening, describing the overall line width. The second explanation comprises the existence of a very small dipolar coupling, leading to slightly shifted positions of the $\Delta m_s = \pm 1$ transitions. Together with slightly smaller line widths, the signal could be reproduced as well. However, with the lack of knowledge

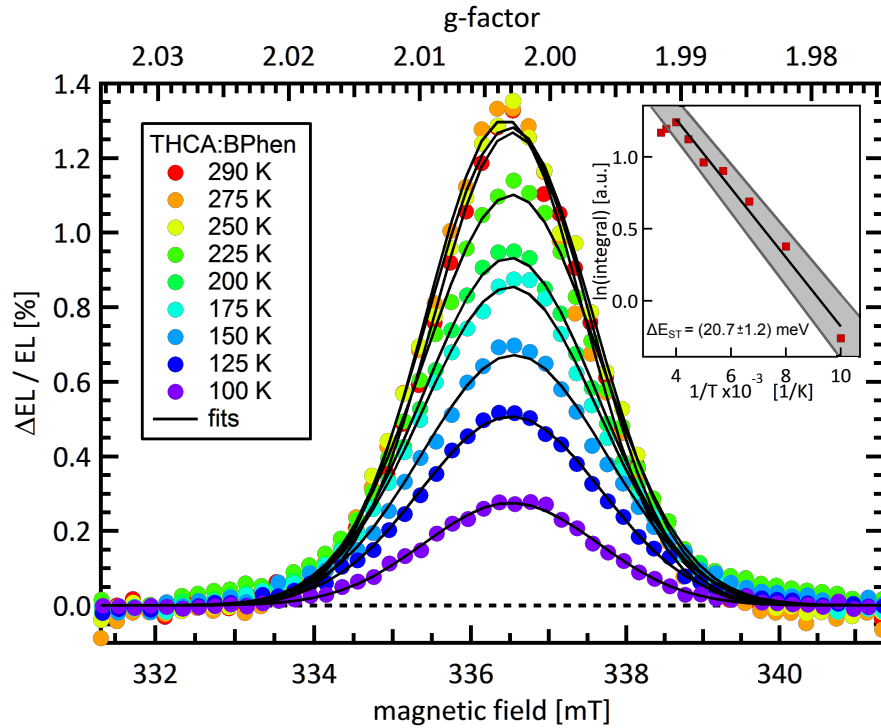


Figure 9.6.: Relative change of the electroluminescence of a THCA:BPhen OLED due to spin resonant conditions at different temperatures (colored dots). The signals are reproduced by Gaussian fits (black lines) which were weighted with the standard deviation of the respective measurements. Inset: Arrhenius plot of the integral of the Gaussian fits (red dots) together with a linear fit (black line) and the corresponding error margins (gray shaded area) in order to obtain the singlet-triplet splitting ΔE_{ST} . The first two data points are excluded from the fit.

about the exact linewidth of the signal and the limited resolution of the used spectrometer, the exact assignment remains concealed.

Nevertheless, the signal strength, which lies in the percent range, is extraordinarily large. In context to the peak position at a g-factor of 2.002, it reveals a very strong dependency of electron spins in the creation process of emission in TADF OLEDs. However, the decrease of signal strength with decreasing temperature is counterintuitive at a first glance. Considering only Boltzmann statistics, the intensity should increase with decreasing temperature as the polarization of the sample increases as well (compare with chapter 3.3). However, the exactly opposite trend is observable in Figure 9.6. While the signal stays rather constant until 250 K, it starts to decrease with decreasing temperature afterwards. This behavior is only explainable by the previously introduced mechanism of thermally activated fluorescence. Applying a magnetic field lifts the degeneracy of the three triplet states. Therefore, the $m_s = \pm 1$ -states become inaccessible for the reversed inter system crossing (RISC) process. Under spin resonant conditions, the populations between the triplet sub-states are equalized, which leads

9. The Role of Spin States in Thermally Activated Delayed Fluorescence OLEDs

to the observed increase in emission. However, in order to be efficient, the RISC mechanism needs additional thermal energy. Lowering this by decreasing the temperature, yields a decreasing influence of the spin resonant conditions, since the populations are equalized but can not be transferred to the emissive singlet state (see also Figure 9.1).

The temperature dependency is used for further evaluation of the presented data. Integrating the Gaussian fits in Figure 9.6 and plotting the logarithm of the obtained values versus the inversed temperature yields an Arrhenius plot as shown in the inset of Figure 9.6. Here, the temperature dependent data points were fitted with a linear function. The resulting slope of the fit reveals the energetic separation between the singlet and triplet exciplex state ΔE_{ST} , which is (20.7 ± 1.2) meV for the material system THCA:BPhen. The first two points were excluded, since they show no significant temperature dependency. This is due to the sufficient thermal energy for the RISC to be efficient for temperatures above 240 K, which corresponds to 20.7 meV. Compared to literature values for different material systems, the obtained value is quite low. However, the assignment of ΔE_{ST} with methods different than ELDMR is prone to failure, as discussed in the previous sections.

In the next step, the material system was changed from THCA:BPhen to m-MTDATA:BPhen in order to find differences in the energetic separation between triplet and singlet exciplex states.

In Figure 9.7, temperature dependent ELDMR spectra are shown for a bilayer device consisting of m-MTDATA:BPhen. Apparently, the signal strength at room temperature is slightly decreased in comparison to the material system THCA:BPhen. Moreover, the signal vanishes below 150 K, while for THCA:BPhen, a signal was still measurable at 100 K. These two observations already point towards a weaker RISC mechanism for the exciplex emission of m-MTDATA:BPhen. Evaluating the data in the previously discussed manner reveals an energetic singlet-triplet exciplex separation of (58.2 ± 4.5) meV, significantly higher than for THCA:BPhen. This result coincides perfectly with the earlier obtained observations.

The different values for ΔE_{ST} can be explained by two possible scenarios. Firstly, the morphology of the two components may play a crucial role. Whereas m-MTDATA possesses a more planar configuration, THCA is a star shaped molecule with three side arms, which can be viewed as a 3D system [238]. Therefore, m-MTDATA crystallizes in predominantly flat layers, which was also confirmed by excimer formation [237]. THCA thin films, on the other hand, can be characterized by non-planar layers [238], without the occurrence of excimer emission [239, 238, 240]. Atomic force microscopy measurements on thin films made of the respective donor-molecules show a significantly increased roughness for THCA ($R_a=0.73$ nm) compared to m-MTDATA ($R_a=0.26$ nm),

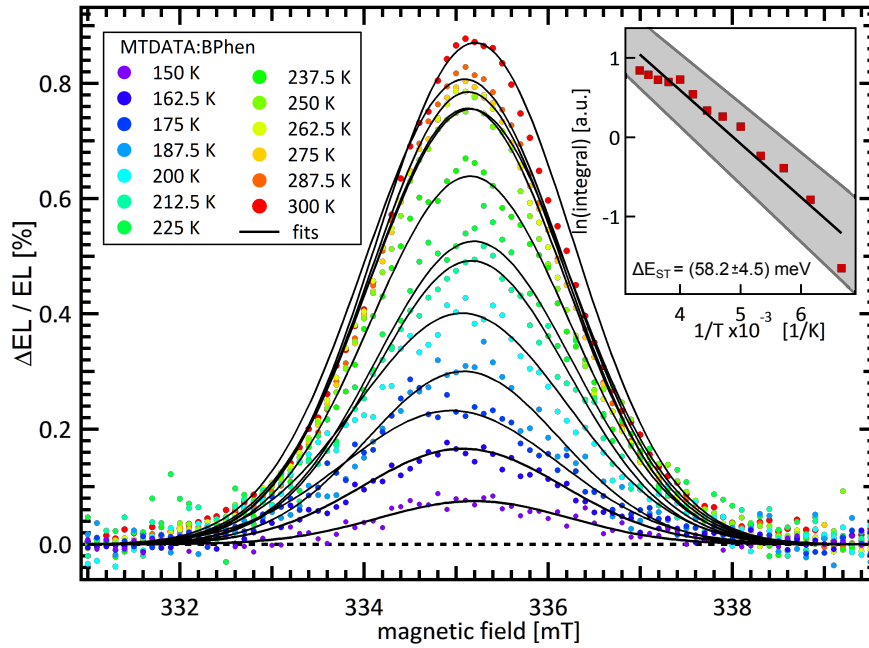


Figure 9.7.: ELDMR signal of a m-MTDATA:BPhen OLED at different temperatures (colored dots), together with Gaussian fits (black lines), weighted with the standard deviations of the single measurements. Inset: Arrhenius plot of the area of the Gaussian fits (red dots) together with a linear fit (black line) and the error margins (gray shaded area). From this the singlet-triplet splitting ΔE_{ST} was obtained.

as depicted in Figure 9.8. Consequently, the AFM data hint towards a different separation distance which would lead to a smaller exchange interaction between the two spin carrying particles, which consequentially yields a reduced ΔE_{ST} . Here, already a small increase in distance would result in a significantly increased exchange interaction, since their correlation is exponential (see also chapter 3.2.4).

Another explanation, yet harder to investigate, is the wavefunction alignment. The exchange interaction is in principle a measure for the strength of overlapping electron- and hole wavefunction, respectively. If the HOMO-wavefunction of the p-layer is orientated perpendicular to the LUMO-wavefunction of the n-layer, the overlap between both will be minimized, which, in turn, would also minimize ΔE_{ST} [247, 248]. Therefore, it is possible that the different crystallization of m-MTDATA and THCA yields a more ideal wavefunction overlap for the material system THCA:BPhen than for m-MTDATA:BPhen. All in all, the difference in activation energies can not be unequivocally elucidated with the presented measurements. However, for future improvement of TADF OLEDs, material systems with the lowest possible energy gap ΔE_{ST} need to be found, while maintaining high interfacial recombination efficiency. Consequently, the

9. The Role of Spin States in Thermally Activated Delayed Fluorescence OLEDs

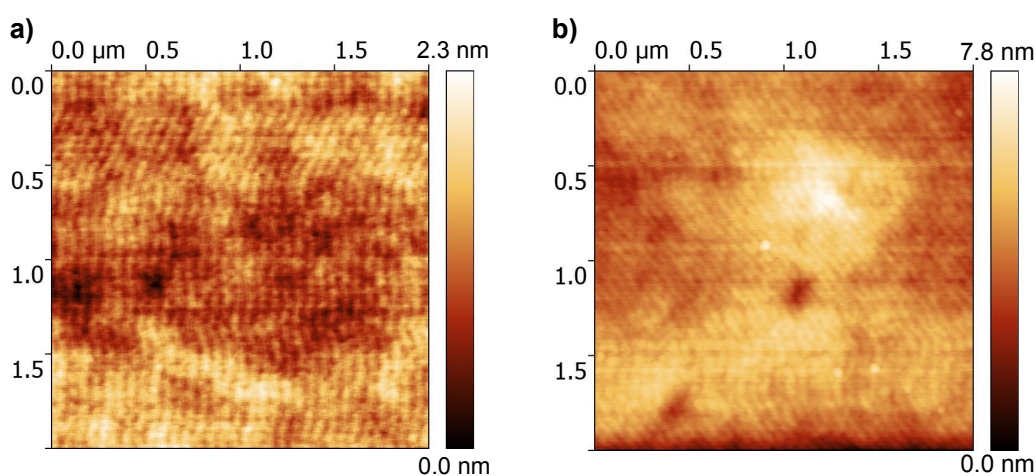


Figure 9.8.: Atomic force microscopy measurements for a) MTDATA- and b) THCA- molecules on an ITO/PEDOT:PSS substrate. THCA exhibits an increased surface roughness compared to MTDATA.

electron-hole distance, together with the wavefunction overlap define crucial parameters for future material synthesis and combinations.

9.4. Conclusion

In summary, resonant spin sensitive measurements based on electron paramagnetic resonance provide important insights on the role of spin states in two TADF donor-acceptor systems. In particular, the properties of TADF OLEDs based on the material systems THCA: BPhen and m-MTDATA: BPhen were investigated. At first, the occurrence of exciplex emission was confirmed by processing bilayer devices and measuring electroluminescence. Subsequently, different detection techniques were used in order to investigate the influence of spins on the emergence of delayed fluorescence. Here, PLDMR proved to be ineffective due to the unfavorable population of singlet excitons and the consequential overlap of different signal contributions. EDMR was ruled out, since it probes a convolution of all spin-dependent processes that occur in the device. Moreover, it was strongly influenced by degradation of the device. Finally, ELDMR was found to be the perfect tool to investigate spin-dependent processes in OLEDs without being affected by other thermally activated intermediate steps, e.g. charge carrier encounter and transport processes. With temperature dependent measurements, the energetic separation between singlet- and triplet exciplex state ΔE_{ST} was determined to be (20.7 ± 1.2) meV for the material system THCA: BPhen and (58.2 ± 4.5) meV for m-MTDATA: BPhen. Two possible scenarios for this difference are conceivable. Firstly, a larger distance between the two spin carrying particles forming the exciplex state and secondly, a more perpendicular alignment of the HOMO and LUMO wavefunctions of

the involved materials, minimizing the wavefunction overlap. Both effects would result in a decrease of the exchange interaction, which yields a reduced ΔE_{ST} . For future developments, material systems have to be found where ΔE_{ST} is as low as possible while the emissive recombination probability should stay as high as possible.

10. Summary

The present work addressed the influence of spins on fundamental processes in organic semiconductors. In most cases, the role of spins in the conversion of sun light into electricity was of particular interest. However, also the reversed process, an electric current creating luminescence, was investigated by means of spin sensitive measurements. In this work, many material systems were probed with a variety of innovative detection techniques based on electron paramagnetic resonance spectroscopy. More precisely, the observable could be customized which resulted in the experimental techniques photoluminescence detected magnetic resonance (PLDMR), electrically detected magnetic resonance (EDMR), and electroluminescence detected magnetic resonance (ELDMR). Besides the commonly used continuous wave EPR spectroscopy, this selection of measurement methods yielded an access to almost all intermediate steps occurring in organic semiconductors during the conversion of light into electricity and vice versa. Special attention was paid to the fact that all results were applicable to realistic working conditions of the investigated devices, i.e. room temperature application and realistic illumination conditions.

First of all, a short overview of the historic development of organic solar cells was given together with an explanation of the basic properties and fundamental processes of these devices, including the involved spin-states. Furthermore, solar cell characterization and the morphology of the active layer were discussed. The next chapter contained theoretic considerations concerning the effect of a magnetic field on spins together with several interaction mechanisms. Furthermore, the basic principle how microwaves influence aligned spins were discussed as well. Finally, different models were introduced which are able to explain the occurrence of the observed signals. Afterwards, the detailed description of the experimental niceties was discussed, i.e. highlighting the used materials, the sample preparation, and the different spectrometer designs.

The first result chapter addressed the influence of the processing additive diiodooctane (DIO) on the material system PTB7:PC₇₀BM, which was investigated by conventional electron paramagnetic resonance. This technique allows to distinguish between free charge carriers either located on the donor- or acceptor material. Together with X-

10. Summary

ray photoelectron spectroscopy the presence of iodine in the PTB7:PC₇₀BM-samples was shown even after a high vacuum drying step with a surprisingly high concentration of $(7.3 \pm 2.1) \cdot 10^{19} \frac{1}{\text{cm}^3}$. Furthermore, an indication that iodine stays preferably in the fullerene phase was revealed. Moreover, no evidence for an electronic doping effect was found. However, these results will have an impact on prospective choices of additives in the preparation of organic solar cells.

The formation of triplet excitons in the material system p-DTS(FBTTh₂)₂:PC₇₀BM was discussed in chapter 6. Here, the donor consisted of a soluble small molecule instead of a polymer. With the use of PLDMR, the triplet exciton formation mechanisms were revealed to be either an electron back transfer from the PC₇₀BM to the excitonic triplet state of the p-DTS(FBTTh₂)₂-molecules or an inter system crossing from the singlet excitonic state. The exact route, however, is strongly dependent on the morphology of the active layer. The detection of triplet excitons at room temperature via EDMR measurements proved the relevance of these findings to real operation conditions. Furthermore, the relative triplet yield of three different material compositions was compared to device performance, revealing no correlation at all. As a consequence, the formation of triplet excitons, despite appearing to be an energetically favorable process, cannot be considered as a major loss mechanism in this specific donor-acceptor blend. Finally, the molecular orientation with respect to the substrate was investigated by angular dependent PLDMR measurements. Here, the strong tendency of p-DTS-(FBTTh₂)₂-molecules to crystallize was confirmed together with the preferential edge-on orientation.

In chapter 7, the influence of the additive galvinoxyl on charge transfer states was investigated by means of PLDMR. Here, it was found that galvinoxyl is indeed able to flip spins as stated in literature. Therefore, it is a competing process with the applied magnetic resonant conditions. Measuring different doping concentrations, an optimum of 3.2 % was found for the material system P3HT:PC₆₀BM. However, the reported increase of the photocurrent which was attributed to spin flips caused by galvinoxyl could not be confirmed.

The quantification of spin-dependent processes in organic solar cells is not straightforward. However, combining EDMR measurements with the electric charge carrier extraction technique OTRACE revealed a surprisingly low fraction of spin-dependent charge carrier recombination of $(0.012 \pm 0.009)\%$ at room temperature and $(0.052 \pm 0.031)\%$ at 200 K for the material system P3HT:PC₇₀BM. Moreover, the genesis of the EDMR signal was interpreted to stem from a charge transfer state and localized charge carriers in the vicinity of an interface between donor- and acceptor material.

The last emphasis of this work concerned the role of spins in thermally activated delayed fluorescence OLEDs, as presented in chapter 9. Here, two different material systems that showed strong exciplex emission were investigated. After finding the most suitable detection technique, namely ELDMR, temperature dependent measurements revealed an energetic splitting ΔE_{ST} between the singlet- and triplet exciplex state to be (20.5 ± 1.2) meV for THCA:BPhen and (68.3 ± 5.4) meV for m-MTDATA:BPhen. These measurements were the first that unambiguously proved the involvement of spins in the occurrence of exciplex emission. Considering the possible causes for the different energetic splittings revealed new design rules for future material combinations and synthesis.

All in all, this work constitutes a significant contribution to further enlighten the exact role of spins in the application of organic semiconductor devices. Furthermore, it will have a direct impact on future material optimizations.

Zusammenfassung

Die vorliegende Arbeit behandelt den Einfluss der Elektronenspins auf grundlegende Prozesse in organischen Halbleitern. In den meisten Fällen wurde der Spineinfluss während der Umwandlung von Sonnenlicht in Elektrizität untersucht. Zusätzlich wurde in einer Studie der gegenteilige Prozess behandelt. Dabei wurde der Einfluss der Spins auf die Umwandlung von elektrischem Strom in Licht betrachtet. Es wurden viele verschiedene Materialsysteme verwendet, die mit einer Vielzahl an Methoden vermessen wurden, welche alle auf dem Prinzip der Elektronenspinresonanz beruhen. Dabei wurde stets die Messgröße variiert, was zu den verwendeten Messmethoden Photolumineszenz detektierte Magnetresonanz (PLDMR), elektrisch detektierte Magnetresonanz (EDMR) und Elektrolumineszenz detektierte Magnetresonanz (ELDMR) geführt hat. Zusammen mit der gewöhnlichen Elektronenspinresonanz Spektroskopie führt diese Auswahl an vielfältigen Messmethoden dazu, dass so gut wie alle Zwischenschritte bei der Umwandlung von Licht in Elektrizität als auch von Elektrizität in Licht untersucht werden können. Besonderes Augenmerk wurde darauf gelegt, dass alle Messungen auf realistische Bedingungen übertragbar sind, d.h. bei Raumtemperatur und unter normalen Beleuchtungsstärken und -wellenlängen.

Zu Beginn der Arbeit wurde ein kurzer Überblick über die historische Entwicklung von organischen Solarzellen gegeben, zusammen mit der Erläuterung von grundlegenden Prozessen in den untersuchten Bauteilen, stets auch hinsichtlich der vorkommenden Spinzustände. Desweiteren wurde die Solarzellencharakterisierung und die Morphologie der aktiven Schicht diskutiert. Das darauf folgende Kapitel behandelte die theoretische Beschreibung des Magnetfeldeffekts auf Spinzustände und diverse Wechselwirkungsmechanismen. Darüber hinaus wurde diskutiert, wie Mikrowellen die vom Magnetfeld ausgerichteten Spins beeinflussen können. Zu guter Letzt wurden verschiedene Modelle vorgestellt, mit deren Hilfe sich die erzielten Ergebnisse interpretieren lassen. Das nächste Kapitel beschreibt schließlich detailliert die experimentellen Feinheiten, wie verwendete Materialien, Probenherstellung und verschiedene Spektrometer Konfigurationen.

Das erste Ergebnis Kapitel beschreibt den Einfluss des Zusatzmittels 1,8-Dijodoktan auf das Materialsystem PTB7:PC₇₀BM. Dies wurde mit Hilfe von konventioneller Elektronenspinresonanz untersucht, welche es ermöglicht zwischen Elektronen auf dem Akzeptor- und Polaronen auf dem Donormaterial zu unterscheiden. Ergänzend dazu wurden Röntgenphotoelektronenspektroskopiemessungen durchgeführt, welche zu dem Ergebnis führten, dass Jod trotz Hochvakuumtrocknung mit der relativen hohen Konzentration von $(7.3 \pm 2.1) \cdot 10^{19} \frac{1}{\text{cm}^3}$ in dem Material verbleibt. Zudem bleibt Jod wahrschein-

lich bevorzugt in der Akzeptorphase. Es wurde außerdem kein elektronischer Dopingeffekt gefunden. Nichtsdestotrotz wird dieses Ergebnis einen Einfluss auf die zukünftige Wahl des Zusatzmittels haben.

Kapitel 6 handelt von der Entstehung von Triplett Exzitonen in dem Materialsystem p-DTS(FBTTh₂)₂:PC₇₀BM, wobei das Donormaterial aus löslichen kleinen Molekülen besteht, anstatt aus Polymeren. Mit Hilfe von PLDMR Messungen konnten die Entstehungsmechanismen Elektronenrücktransfer, sowie inter system crossing den verschiedenen Proben zugeordnet werden. Der genaue Mechanismus hängt jedoch stark von der Morphologie des untersuchten Materialsystems ab. Durch den Nachweis von Triplett Exzitonen bei Raumtemperatur konnte die Relevanz der Ergebnisse auch bei realen Bedingungen bestätigt werden. Vergleicht man das Triplett Vorkommen mit den Solarzelleneffizienzen konnte keine Korrelation erkannt werden. Daraus ergibt sich, dass Triplett Exzitonen für das untersuchte Materialsystem keine Effizienz limitierende Größe darstellen. Zum Abschluss wurde die Ausrichtung der Moleküle auf dem Substrat mit Hilfe von winkelabhängigen Messungen bestätigt.

Der Einfluss des Zusatzmittels Galvinoxyl auf die Funktionsweise von organischen Solarzellen wird in Kapitel 7 untersucht. Es wurden PLDMR durchgeführt, die gezeigt haben, dass Galvinoxyl in der Lage ist Spin Zustände zu verändern, wie von der Literatur vorhergesagt. Aufgrund dessen handelt es sich um einen konkurrierenden Prozess gegenüber den erzeugten Spin resonanten Bedingungen. Durch die Messung an verschiedenen Doping Konzentrationen konnte ein Optimum von 3.2 % für das Materialsystem P3HT:PC₆₀BM bestimmt werden. Trotzdem ist es unwahrscheinlich, dass der sehr große Anstieg des Photostroms in mit Galvinoxyl gedopten Solarzellen auf spinabhängige Prozesse zurückzuführen ist.

Die Quantifizierung von spinabhängigen Prozessen in organischen Solarzellen beinhaltet viele Schwierigkeiten. Durch die Kombination des EDMR Messprinzips mit der Ladungsträgerextraktionsmethode OTRACE war es jedoch möglich, einen spinabhängigen Rekombinationsanteil von $(0.012 \pm 0.009)\%$ bei Raumtemperatur und $(0.052 \pm 0.031)\%$ bei 200 K für das Materialsystem P3HT:PC₇₀BM zu bestimmen. Darüber hinaus wurde eine Interpretation eingeführt, die in der Lage ist, das Zustandekommen des EDMR Signals zu erklären.

Im letzten Ergebnisteil (Kapitel 9) wurde der Fokus darauf gelegt, wie Spins die Funktionsweise von organischen Leuchtdioden (OLEDs) beeinflussen, die auf thermisch aktivierter verzögerter Lumineszenz (TADF) basieren. Dabei wurden verschiedene Detektionsverfahren verwendet, wobei sich heraus gestellt hat, dass ELDMR das einzig verwendbare darstellt. Damit konnten durch temperaturabhängige Messungen der energetische Unterschied zwischen dem Singulett- und Triplett Exciplex Zustand ΔE_{ST}

10. Summary

bestimmt werden. Es ergaben sich (20.5 ± 1.2) meV für THCA:BPhen und (68.3 ± 5.4) meV für m-MTDATA:BPhen. Durch diese Messungen wurde zum ersten Mal zweifelsfrei der Einfluss von Spins in der Entstehung der Elektrolumineszenz von TADF OLEDs gezeigt. Aufgrund der Diskussion von möglichen Gründen, die für die verschiedenen Werte von ΔE_{ST} verantwortlich sind, konnten neue Vorgaben für zukünftige Materialkombinationen und -synthese gefunden werden.

Zusammenfassend lässt sich sagen, dass die vorliegende Arbeit einen bedeutenden Beitrag geliefert hat, um spinabhängige Prozesse in organischen Halbleitern aufzuklären. Darauf aufbauend werden Folgestudien vielleicht eines Tages sämtliche spinabhängigen Prozesse in diesen viel versprechenden Materialsystemen erklären können.

Bibliography

- [1] N. H. Egleston. What we owe to the trees. *Harper's New Monthly Magazine*, **46**, 383, 686 (1882).
- [2] Energy roadmap 2050. *Communication from the Commission to the European Parliament, the Council, the European Economic and Social Committee and the Committee of the Regions, Brussels*, **15**, 12 (2011).
- [3] B. der Bundesrepublik Deutschland. Der weg zur energie der zukunft. *Regierungserklärung von Bundeskanzlerin Dr. Angela Merkel zur Energiepolitik vor dem Deutschen Bundestag* (2011).
- [4] Heliatek sets new organic photovoltaic world record efficiency of 13.2%. www.Heliatek.com (2016). Press release.
- [5] N. Sariciftci, L. Smilowitz, A. Heeger and F. Wudl. Photoinduced electron transfer from a conducting polymer to buckminsterfullerene. *Science*, **258**, 5087, 1474 (1992). doi: [10.1126/science.258.5087.1474](https://doi.org/10.1126/science.258.5087.1474).
- [6] H. Akamatu, H. Inokuchi and Y. Matsunaga. Electrical conductivity of the perylene-bromine complex. *Nature*, **173**, 168 (1954). doi: [10.1038/173168a0](https://doi.org/10.1038/173168a0).
- [7] H. Shirakawa, E. J. Louis, A. G. MacDiarmid, C. K. Chiang and A. J. Heeger. Synthesis of electrically conducting organic polymers: halogen derivatives of polyacetylene, (ch). *Journal of the Chemical Society, Chemical Communications*, 578–580 (1977). doi: [10.1039/C39770000578](https://doi.org/10.1039/C39770000578).
- [8] R. E. Peierls. *Surprises in theoretical physics*. Princeton University Press (1979).
- [9] R. Hoffmann, C. Janiak and C. Kollmar. A chemical approach to the orbitals of organic polymers. *Macromolecules*, **24**, 13, 3725 (1991). doi: [10.1021/ma00013a001](https://doi.org/10.1021/ma00013a001).
- [10] G. Chamberlain. Organic solar cells: a review. *Solar cells*, **8**, 1, 47 (1983). doi: [10.1016/0379-6787\(83\)90039-X](https://doi.org/10.1016/0379-6787(83)90039-X).

Bibliography

- [11] C. W. Tang. Two-layer organic photovoltaic cell. *Applied Physics Letters*, **48**, 2, 183 (1986). doi: [10.1063/1.96937](https://doi.org/10.1063/1.96937).
- [12] G. Yu, J. Gao, J. C. Hummelen, F. Wudl and A. J. Heeger. Polymer photovoltaic cells: enhanced efficiencies via a network of internal donor-acceptor heterojunctions. *Science*, **270**, 5243, 1789 (1995). doi: [10.1126/science.270.5243.1789](https://doi.org/10.1126/science.270.5243.1789).
- [13] S. E. Shaheen, C. J. Brabec, N. S. Sariciftci, F. Padinger, T. Fromherz and J. C. Hummelen. 2.5% efficient organic plastic solar cells. *Applied Physics Letters*, **78**, 6, 841 (2001). doi: [10.1063/1.1345834](https://doi.org/10.1063/1.1345834).
- [14] F. Padinger, R. S. Rittberger, N. S. Sariciftci et al. Effects of postproduction treatment on plastic solar cells. *Advanced Functional Materials*, **13**, 1, 85 (2003). doi: [10.1002/adfm.200390011](https://doi.org/10.1002/adfm.200390011).
- [15] J. Peet, J. Y. Kim, N. E. Coates, W. L. Ma, D. Moses, A. J. Heeger and G. C. Bazan. Efficiency enhancement in low-bandgap polymer solar cells by processing with alkane dithiols. *Nature Materials*, **6**, 7, 497 (2007). doi: [10.1038/nmat1928](https://doi.org/10.1038/nmat1928).
- [16] M. A. Green, K. Emery, Y. Hishikawa, W. Warta and E. D. Dunlop. Solar cell efficiency tables (version 45). *Progress in photovoltaics: research and applications*, **23**, 1, 1 (2015). doi: [10.1002/pip.2573](https://doi.org/10.1002/pip.2573).
- [17] S. Martin, D. Bradley, P. Lane, H. Mellor and P. Burn. Linear and nonlinear optical properties of the conjugated polymers ppv and meh-ppv. *Physical Review B*, **59**, 23, 15133 (1999). doi: [10.1103/PhysRevB.59.15133](https://doi.org/10.1103/PhysRevB.59.15133).
- [18] H. Hoppe, N. Arnold, N. Sariciftci and D. Meissner. Modeling the optical absorption within conjugated polymer/fullerene-based bulk-heterojunction organic solar cells. *Solar energy materials and solar cells*, **80**, 1, 105 (2003). doi: [10.1016/S0927-0248\(03\)00137-5](https://doi.org/10.1016/S0927-0248(03)00137-5).
- [19] L. W. Barbour, R. D. Pensack, M. Hegadorn, S. Arzhantsev and J. B. Asbury. Excitation transport and charge separation in an organic photovoltaic material: Watching excitations diffuse to interfaces. *The Journal of Physical Chemistry C*, **112**, 10, 3926 (2008). doi: [10.1021/jp0759628](https://doi.org/10.1021/jp0759628).
- [20] E. Collini and G. D. Scholes. Coherent intrachain energy migration in a conjugated polymer at room temperature. *Science*, **323**, 5912, 369 (2009). doi: [10.1126/science.1164016](https://doi.org/10.1126/science.1164016).

- [21] I.-W. Hwang, D. Moses and A. J. Heeger. Photoinduced Carrier Generation in P3HT/PCBM Bulk Heterojunction Materials. *Journal of Physical Chemistry C*, **112**, 11, 4350 (2008). doi: [10.1021/jp075565x](https://doi.org/10.1021/jp075565x).
- [22] T. M. Clarke and J. R. Durrant. Charge Photogeneration in Organic Solar Cells. *Chemical Reviews*, **110**, 11, 6736 (2010). doi: [10.1021/cr900271s](https://doi.org/10.1021/cr900271s).
- [23] E. Frankevich, A. Lymarev, I. Sokolik, F. Karasz, S. Blumstengel, R. Baughman and H. Hörhold. Polaron-pair generation in poly (phenylene vinylenes). *Physical Review B*, **46**, 15, 9320 (1992). doi: [10.1103/PhysRevB.46.9320](https://doi.org/10.1103/PhysRevB.46.9320).
- [24] C. Deibel, T. Strobel and V. Dyakonov. Role of the Charge Transfer State in Organic Donor-Acceptor Solar Cells. *Advanced Materials*, **22**, 37, 4097 (2010). doi: [10.1002/adma.201000376](https://doi.org/10.1002/adma.201000376).
- [25] D. Veldman, S. C. J. Meskers and R. A. J. Janssen. The Energy of Charge-Transfer States in Electron Donor-Acceptor Blends: Insight into the Energy Losses in Organic Solar Cells. *Advanced Functional Materials*, **19**, 12, 1939 (2009). doi: [10.1002/adfm.200900090](https://doi.org/10.1002/adfm.200900090).
- [26] D. Veldman, Ö. İpek, S. C. J. Meskers, J. Sweelssen, M. M. Koetse, S. C. Veenstra, J. M. Kroon, S. S. v. Bavel, J. Loos and R. A. J. Janssen. Compositional and Electric Field Dependence of the Dissociation of Charge Transfer Excitons in Alternating Polyfluorene Copolymer/Fullerene Blends. *Journal of the American Chemical Society*, **130**, 24, 7721 (2008). doi: [10.1021/ja8012598](https://doi.org/10.1021/ja8012598).
- [27] K. Vandewal, A. Gadisa, W. D. Oosterbaan, S. Bertho, F. Banishoeib, I. Van Severen, L. Lutsen, T. J. Cleij, D. Vanderzande and J. V. Manca. The relation between open-circuit voltage and the onset of photocurrent generation by charge-transfer absorption in polymer: Fullerene bulk heterojunction solar cells. *Advanced Functional Materials*, **18**, 14, 2064 (2008). doi: [10.1002/adfm.200800056](https://doi.org/10.1002/adfm.200800056).
- [28] J. Benson-Smith, L. Goris, K. Vandewal, K. Haenen, J. Manca, D. Vanderzande, D. Bradley and J. Nelson. Formation of a Ground-State Charge-Transfer Complex in Polyfluorene//[6,6]-Phenyl-C61 Butyric Acid Methyl Ester (PCBM) Blend Films and Its Role in the Function of Polymer/PCBM Solar Cells. *Advanced Functional Materials*, **17**, 3, 451 (2007). doi: [10.1002/adfm.200600484](https://doi.org/10.1002/adfm.200600484).
- [29] M. A. Loi, S. Toffanin, M. Muccini, M. Forster, U. Scherf and M. Scharber. Charge transfer excitons in bulk heterojunctions of a polyfluorene copolymer and a

Bibliography

- fullerene derivative. *Advanced Functional Materials*, **17**, 13, 2111 (2007). doi: [10.1002/adfm.200601098](https://doi.org/10.1002/adfm.200601098).
- [30] K. Hasharoni, M. Keshavarz-K, A. Sastre, R. González, C. Bellavia-Lund, Y. Greenwald, T. Swager, F. Wudl and A. Heeger. Near ir photoluminescence in mixed films of conjugated polymers and fullerenes. *The Journal of Chemical Physics*, **107**, 7, 2308 (1997). doi: [10.1063/1.474607](https://doi.org/10.1063/1.474607).
- [31] A. C. Morteani, R. H. Friend and C. Silva. Exciton trapping at heterojunctions in polymer blends. *The Journal of chemical physics*, **122**, 24, 244906 (2005). doi: [10.1063/1.1924504](https://doi.org/10.1063/1.1924504).
- [32] V. Dyakonov, G. Rösler, M. Schwoerer and E. Frankevich. Evidence for triplet interchain polaron pairs and their transformations in polyphenylenevinylene. *Physical Review B*, **56**, 7, 3852 (1997). doi: [10.1103/PhysRevB.56.3852](https://doi.org/10.1103/PhysRevB.56.3852).
- [33] V. Dyakonov and E. Frankevich. On the role played by polaron pairs in photo-physical processes in semiconducting polymers. *Chemical Physics*, **227**, 1-2, 203 (1998). doi: [10.1016/S0301-0104\(97\)00305-4](https://doi.org/10.1016/S0301-0104(97)00305-4).
- [34] M. Liedtke, A. Sperlich, H. Kraus, A. Baumann, C. Deibel, M. J. M. Wirix, J. Loos, C. M. Cardona and V. Dyakonov. Triplet Exciton Generation in Bulk-Heterojunction Solar Cells Based on Endohedral Fullerenes. *Journal of the American Chemical Society*, **133**, 23, 9088 (2011). doi: [doi: 10.1021/ja2025432](https://doi.org/10.1021/ja2025432).
- [35] F. Kraffert, R. Steyrlleuthner, S. Albrecht, D. Neher, M. C. Scharber, R. Bittl and J. Behrends. Charge separation in pcptdtbt: Pcbm blends from an epr perspective. *The Journal of Physical Chemistry C*, **118**, 49, 28482 (2014). doi: [10.1021/jp509650v](https://doi.org/10.1021/jp509650v).
- [36] L. Landau. Uber die bewegung des elektrons im kristallgitter. *Phys. Zs. Sowjetunion*, **3**, 664 (1933).
- [37] S. Pekar. Research in electron theory of crystals (1963).
- [38] L. Landau and S. Pekar. Effective mass of the polaron. *Journal of Experimental and Theoretical Physics*, **18**, 419 (1948).
- [39] C. Waldauf, M. Morana, P. Denk, P. Schilinsky, K. Coakley, S. Choulis and C. Brabec. Highly efficient inverted organic photovoltaics using solution based titanium oxide as electron selective contact. *Applied Physics Letters*, **89**, 23, 233517 (2006). doi: [10.1063/1.2402890](https://doi.org/10.1063/1.2402890).

- [40] M. C. Scharber, D. Mühlbacher, M. Koppe, P. Denk, C. Waldauf, A. J. Heeger and C. J. Brabec. Design Rules for Donors in Bulk-Heterojunction Solar Cells—Towards 10% Energy-Conversion Efficiency. *Advanced Materials*, **18**, 6, 789 (2006). doi: [10.1002/adma.200501717](https://doi.org/10.1002/adma.200501717).
- [41] C. Deibel and V. Dyakonov. Polymer–fullerene bulk heterojunction solar cells. *Reports on Progress in Physics*, **73**, 9, 096401 (2010). doi: [10.1088/0034-4885/73/9/096401](https://doi.org/10.1088/0034-4885/73/9/096401).
- [42] H. Hertz. Ueber einen einfluss des ultravioletten lichtes auf die electriche entladung. *Annalen der Physik*, **267**, 8, 983 (1887).
- [43] A. Einstein. Über einem die erzeugung und verwandlung des lichtes betreffenden heuristischen gesichtspunkt. *Annalen der Physik*, **4** (1905). doi: [10.1002/andp.19053220607](https://doi.org/10.1002/andp.19053220607).
- [44] W. Shockley and H. J. Queisser. Detailed balance limit of efficiency of p-n junction solar cells. *Journal of applied physics*, **32**, 3, 510 (1961). doi: [10.1063/1.1736034](https://doi.org/10.1063/1.1736034).
- [45] V. Shrotriya, G. Li, Y. Yao, T. Moriarty, K. Emery and Y. Yang. Accurate measurement and characterization of organic solar cells. *Advanced Functional Materials*, **16**, 15, 2016 (2006). doi: [10.1002/adfm.200600489](https://doi.org/10.1002/adfm.200600489).
- [46] C. J. Brabec, M. Heeney, I. McCulloch and J. Nelson. Influence of blend microstructure on bulk heterojunction organic photovoltaic performance. *Chemical Society Reviews*, **40**, 3, 1185 (2011). doi: [10.1039/C0CS00045K](https://doi.org/10.1039/C0CS00045K).
- [47] H. Hoppe and N. S. Sariciftci. Morphology of polymer/fullerene bulk heterojunction solar cells. *Journal of Materials Chemistry*, **16**, 1, 45 (2006). doi: [10.1039/B510618B](https://doi.org/10.1039/B510618B).
- [48] L.-M. Chen, Z. Hong, G. Li and Y. Yang. Recent progress in polymer solar cells: manipulation of polymer: fullerene morphology and the formation of efficient inverted polymer solar cells. *Advanced Materials*, **21**, 14-15, 1434 (2009). doi: [10.1002/adma.200802854](https://doi.org/10.1002/adma.200802854).
- [49] A. J. Moulé and K. Meerholz. Morphology control in solution-processed bulk-heterojunction solar cell mixtures. *Advanced Functional Materials*, **19**, 19, 3028 (2009). doi: [10.1002/adfm.200900775](https://doi.org/10.1002/adfm.200900775).

Bibliography

- [50] S. Günes, H. Neugebauer and N. S. Sariciftci. Conjugated Polymer-Based Organic Solar Cells. *Chemical Reviews*, **107**, 4, 1324 (2007). doi: [10.1021/cr050149z](https://doi.org/10.1021/cr050149z).
- [51] Y. Liang, Z. Xu, J. Xia, S.-T. Tsai, Y. Wu, G. Li, C. Ray and L. Yu. For the Bright Future - Bulk Heterojunction Polymer Solar Cells with Power Conversion Efficiency of 7.4 percent. *Advanced Materials*, **22**, 20, E135 (2010). doi: [10.1002/adma.200903528](https://doi.org/10.1002/adma.200903528).
- [52] S. J. Lou, J. M. Szarko, T. Xu, L. Yu, T. J. Marks and L. X. Chen. Effects of additives on the morphology of solution phase aggregates formed by active layer components of high-efficiency organic solar cells. *Journal of the American Chemical Society*, **133**, 51, 20661 (2011). doi: [10.1021/ja2085564](https://doi.org/10.1021/ja2085564).
- [53] J. K. Lee, W. L. Ma, C. J. Brabec, J. Yuen, J. S. Moon, J. Y. Kim, K. Lee, G. C. Bazan and A. J. Heeger. Processing Additives for Improved Efficiency from Bulk Heterojunction Solar Cells. *Journal of the American Chemical Society*, **130**, 11, 3619 (2008). doi: [10.1021/ja710079w](https://doi.org/10.1021/ja710079w).
- [54] Y. Kim, S. A. Choulis, J. Nelson, D. D. Bradley, S. Cook and J. R. Durrant. Device annealing effect in organic solar cells with blends of regioregular poly (3-hexylthiophene) and soluble fullerene. *Applied Physics Letters*, **86**, 6, 3502 (2005). doi: [10.1063/1.1861123](https://doi.org/10.1063/1.1861123).
- [55] D. Chirvase, J. Parisi, J. C. Hummelen and V. Dyakonov. Influence of nanomorphology on the photovoltaic action of polymer–fullerene composites. *Nanotechnology*, **15**, 9, 1317 (2004). doi: [10.1088/0957-4484/15/9/035](https://doi.org/10.1088/0957-4484/15/9/035).
- [56] P. Vanlaeke, A. Swinnen, I. Haeldermans, G. Vanhoyland, T. Aernouts, D. Cheyns, C. Deibel, J. D’Haen, P. Heremans, J. Poortmans and J. Manca. P3HT/PCBM bulk heterojunction solar cells: Relation between morphology and electro-optical characteristics. *Solar Energy Materials and Solar Cells*, **90**, 14, 2150 (2006). doi: [10.1016/j.solmat.2006.02.010](https://doi.org/10.1016/j.solmat.2006.02.010).
- [57] H.-C. Liao, C.-C. Ho, C.-Y. Chang, M.-H. Jao, S. B. Darling and W.-F. Su. Additives for morphology control in high-efficiency organic solar cells. *Materials today*, **16**, 9, 326 (2013). doi: [10.1016/j.mattod.2013.08.013](https://doi.org/10.1016/j.mattod.2013.08.013).
- [58] Z. He, C. Zhong, X. Huang, W.-Y. Wong, H. Wu, L. Chen, S. Su and Y. Cao. Simultaneous enhancement of open-circuit voltage, short-circuit current density, and fill factor in polymer solar cells. *Advanced Materials*, **23**, 40, 4636 (2011). doi: [10.1002/adma.201103006](https://doi.org/10.1002/adma.201103006).

- [59] Z. He, C. Zhong, S. Su, M. Xu, H. Wu and Y. Cao. Enhanced power-conversion efficiency in polymer solar cells using an inverted device structure. *Nature Photonics*, **6**, 9, 591 (2012). doi: [10.1038/nphoton.2012.190](https://doi.org/10.1038/nphoton.2012.190).
- [60] D. Mühlbacher, M. Scharber, M. Morana, Z. Zhu, D. Waller, R. Gaudiana and C. Brabec. High photovoltaic performance of a low-bandgap polymer. *Advanced Materials*, **18**, 21, 2884 (2006). doi: [10.1002/adma.200600160](https://doi.org/10.1002/adma.200600160).
- [61] I.-W. Hwang, J. Young Kim, S. Cho, J. Yuen, N. Coates, K. Lee, M. Heeney, I. McCulloch, D. Moses and A. Heeger. Bulk heterojunction materials composed of poly (2, 5-bis (3-tetradecylthiophen-2-yl) thieno [3, 2-b] thiophene): Ultrafast electron transfer and carrier recombination. *The Journal of Physical Chemistry C*, **112**, 21, 7853 (2008). doi: [10.1021/jp711404c](https://doi.org/10.1021/jp711404c).
- [62] N. E. Coates, I.-W. Hwang, J. Peet, G. C. Bazan, D. Moses and A. J. Heeger. 1, 8-octanedithiol as a processing additive for bulk heterojunction materials: Enhanced photoconductive response. *Applied Physics Letters*, **93**, 7, 072105 (2008). doi: [10.1063/1.2969405](https://doi.org/10.1063/1.2969405).
- [63] S. Albrecht, W. Schindler, J. Kurpiers, J. Kniepert, J. C. Blakesley, I. Dumsch, S. Al-lard, K. Fostiropoulos, U. Scherf and D. Neher. On the field dependence of free charge carrier generation and recombination in blends of pcptdtb/pc70bm: Influence of solvent additives. *The Journal of Physical Chemistry Letters*, **3**, 5, 640 (2012). doi: [10.1021/jz3000849](https://doi.org/10.1021/jz3000849).
- [64] W. Gerlach and O. Stern. Der experimentelle nachweis des magnetischen moments des silberatoms. *Zeitschrift für Physik A Hadrons and Nuclei*, **8**, 1, 110 (1922). doi: [10.1007/BF01329580](https://doi.org/10.1007/BF01329580).
- [65] J. A. Weil and J. R. Bolton. *Electron Paramagnetic Resonance*. Elementary Theory and Practical Applications. Wiley-Interscience, 2nd edition (2008).
- [66] S. Stoll. Spectral simulations in solid-state electron paramagnetic resonance. Ph.D. thesis, ETH Zürich (2003). doi: [10.3929/ethz-a-004529758](https://doi.org/10.3929/ethz-a-004529758).
- [67] S. Stoll and A. Schweiger. EasySpin, a comprehensive software package for spectral simulation and analysis in EPR. *Journal of Magnetic Resonance*, **178**, 1, 42 (2006). doi: [10.1016/j.jmr.2005.08.013](https://doi.org/10.1016/j.jmr.2005.08.013).
- [68] P. Zeeman. Vii. doublets and triplets in the spectrum produced by external magnetic forces. *The London, Edinburgh, and Dublin Philosophical Magazine and Journal of Science*, **44**, 266, 55 (1897). doi: [10.1080/14786449708621028](https://doi.org/10.1080/14786449708621028).

Bibliography

- [69] J. H. Van Vleck. The theory of electric and magnetic susceptibilities (1932).
- [70] H. Kraus. Optically detected magnetic resonance on organic and inorganic carbon-based semiconductors. Ph.D. thesis, University of Würzburg (2014).
- [71] G. Jeschke. Determination of the nanostructure of polymer materials by electron paramagnetic resonance spectroscopy. *Macromolecular Rapid Communications*, **23**, 4, 227 (2002). doi: [10.1002/1521-3927\(20020301\)23:43.0.CO;2-D](https://doi.org/10.1002/1521-3927(20020301)23:43.0.CO;2-D).
- [72] C. C. Moser, J. M. Keske, K. Warncke, R. S. Farid and P. L. Dutton. Nature of biological electron transfer. *Nature*, **355**, 6363, 796 (1992). doi: [10.1038/355796a0](https://doi.org/10.1038/355796a0).
- [73] O. Efimova and P. J. Hore. Role of exchange and dipolar interactions in the radical pair model of the avian magnetic compass. *Biophysical Journal*, **94**, 5, 1565 (2008). doi: [10.1529/biophysj.107.119362](https://doi.org/10.1529/biophysj.107.119362).
- [74] R. Coffman and G. Buettner. A limit function for long-range ferromagnetic and antiferromagnetic superexchange. *Journal of Physical Chemistry*, **83**, 18, 2387 (1979). doi: [10.1021/j100481a017](https://doi.org/10.1021/j100481a017).
- [75] A. Sperlich. Electron paramagnetic resonance spectroscopy of conjugated polymers and fullerenes for organic photovoltaics. Ph.D. thesis, University of Würzburg (2013).
- [76] S. K. Misra. *Multifrequency electron paramagnetic resonance: theory and applications*. John Wiley & Sons (2011).
- [77] M. Brustolon. *Electron paramagnetic resonance: a practitioner's toolkit*. John Wiley & Sons (2009).
- [78] A. Suna. Kinematics of Exciton-Exciton Annihilation in Molecular Crystals. *Physical Review B*, **1**, 4, 1716 (1970). doi: [10.1103/PhysRevB.1.1716](https://doi.org/10.1103/PhysRevB.1.1716).
- [79] R. E. Merrifield. Magnetic effects on triplet exciton interactions. *Pure and Applied Chemistry*, **27**, 3, 481 (1971). doi: [10.1351/pac197127030481](https://doi.org/10.1351/pac197127030481).
- [80] J. Partee, E. Frankevich, B. Uhlhorn, J. Shinar, Y. Ding and T. Barton. Delayed fluorescence and triplet-triplet annihilation in Pi-conjugated polymers. *Physical Review Letters*, **82**, 18, 3673 (1999). doi: [10.1103/PhysRevLett.82.3673](https://doi.org/10.1103/PhysRevLett.82.3673).
- [81] D. Stich, F. Späth, H. Kraus, A. Sperlich, V. Dyakonov and T. Hertel. Triplet-triplet exciton dynamics in single-walled carbon nanotubes. *Nature Photonics*, **8**, 2, 139 (2014). doi: [10.1038/nphoton.2013.316](https://doi.org/10.1038/nphoton.2013.316).

- [82] V. Dyakonov, N. Gauss, G. Rösler, S. Karg, W. Rieß and M. Schwoerer. Electron spin resonance in ppv-photodiodes: detection via photoinduced current. *Chemical Physics*, **189**, 3, 687 (1994). doi: [10.1016/0301-0104\(94\)00340-8](https://doi.org/10.1016/0301-0104(94)00340-8).
- [83] A. Gruber. Scanning Confocal Optical Microscopy and Magnetic Resonance on Single Defect Centers. *Science*, **276**, 5321, 2012 (1997). doi: [10.1126/science.276.5321.2012](https://doi.org/10.1126/science.276.5321.2012).
- [84] N. Manson, J. Harrison and M. Sellars. Nitrogen-vacancy center in diamond: Model of the electronic structure and associated dynamics. *Physical Review B*, **74**, 10, 104303 (2006). doi: [10.1103/PhysRevB.74.104303](https://doi.org/10.1103/PhysRevB.74.104303).
- [85] D. Riedel, F. Fuchs, H. Kraus, S. Väh, A. Sperlich, V. Dyakonov, A. Soltamova, P. Baranov, V. Ilyin and G. Astakhov. Resonant Addressing and Manipulation of Silicon Vacancy Qubits in Silicon Carbide. *Physical Review Letters*, **109**, 22, 226402 (2012). doi: [10.1103/PhysRevLett.109.226402](https://doi.org/10.1103/PhysRevLett.109.226402).
- [86] R. Johnson, R. Merrifield, P. Avakian and R. Flippen. Effects of magnetic fields on the mutual annihilation of triplet excitons in molecular crystals. *Physical Review Letters*, **19**, 6, 285 (1967). doi: [10.1103/PhysRevLett.19.285](https://doi.org/10.1103/PhysRevLett.19.285).
- [87] R. Johnson and R. Merrifield. Effects of magnetic fields on the mutual annihilation of triplet excitons in anthracene crystals. *Physical Review B*, **1**, 2, 896 (1970). doi: [10.1103/PhysRevB.1.896](https://doi.org/10.1103/PhysRevB.1.896).
- [88] L. Hachani, A. Benfredj, S. Romdhane, M. Mejatty, J. Monge and H. Bouchriha. Fluorescence-detected magnetic resonance in organic systems: A pair-density matrix formalism approach. *Physical Review B*, **77**, 3, 035212 (2008). doi: [10.1103/PhysRevB.77.035212](https://doi.org/10.1103/PhysRevB.77.035212).
- [89] E. Frankevich, V. Lesin and A. Pristupa. Magnetic resonance of short-lived intermediate complexes in the reaction of quenching of triplet excitons by radicals. *Soviet Journal of Experimental and Theoretical Physics*, **48**, 208 (1978).
- [90] J. Piris, T. E. Dykstra, A. A. Bakulin, P. H. v. Loosdrecht, W. Knulst, M. T. Trinh, J. M. Schins and L. D. Siebbeles. Photogeneration and ultrafast dynamics of excitons and charges in p3ht/pcbm blends. *The Journal of Physical Chemistry C*, **113**, 32, 14500 (2009). doi: [10.1021/jp904229q](https://doi.org/10.1021/jp904229q).
- [91] K. A. McLauchlan and U. Steiner. Invited article: The spin-correlated radical pair as a reaction intermediate. *Molecular Physics*, **73**, 2, 241 (1991). doi: [10.1080/00268979100101181](https://doi.org/10.1080/00268979100101181).

Bibliography

- [92] D. J. Lepine. Spin-dependent recombination on silicon surface. *Physical Review B*, **6**, 2, 436 (1972). doi: [10.1103/PhysRevB.6.436](https://doi.org/10.1103/PhysRevB.6.436).
- [93] D. Kaplan, I. Solomon and N. Mott. Explanation of the large spin-dependent recombination effect in semiconductors. *Journal de Physique Lettres*, **39**, 4, 51 (1978). doi: [10.1051/jphyslet:0197800390405100](https://doi.org/10.1051/jphyslet:0197800390405100).
- [94] I. Solomon. Spin-dependent recombination in a silicon pn junction. *Solid State Communications*, **20**, 3, 215 (1976). doi: [10.1016/0038-1098\(76\)90179-4](https://doi.org/10.1016/0038-1098(76)90179-4).
- [95] B. Movaghar, B. Ries and L. Schweitzer. Theory of the resonant and non-resonant photoconductivity changes in amorphous silicon. *Philosophical Magazine B*, **41**, 2, 159 (1980). doi: [10.1080/13642818008245377](https://doi.org/10.1080/13642818008245377).
- [96] Z. Xiong and D. Miller. General expression for the electrically detected magnetic resonance signal from semiconductors. *Applied physics letters*, **63**, 3, 352 (1993). doi: [10.1063/1.110040](https://doi.org/10.1063/1.110040).
- [97] K. Lips, C. Lerner and W. Fuhs. Semiclassical model of electrically detected magnetic resonance in undoped a-si: H. *Journal of non-crystalline solids*, **198**, 267 (1996). doi: [10.1016/0022-3093\(95\)00713-X](https://doi.org/10.1016/0022-3093(95)00713-X).
- [98] A. Barabanov, V. Lvov and O. Tretyak. About the mechanisms of spin-dependent recombination in semiconductors. *physica status solidi (b)*, **207**, 2, 419 (1998). doi: [10.1002/\(SICI\)1521-3951\(199806\)207:2<419::AID-PSSB419>3.0.CO;2-G](https://doi.org/10.1002/(SICI)1521-3951(199806)207:2<419::AID-PSSB419>3.0.CO;2-G).
- [99] L. Swanson, J. Shinar, A. Brown, D. C. Bradley, R. Friend, P. Burn, A. Kraft and A. Holmes. Electroluminescence-detected magnetic-resonance study of poly-paraphenylenevinylene (ppv)-based light-emitting diodes. *Physical Review B*, **46**, 23, 15072 (1992). doi: [10.1103/PhysRevB.46.15072](https://doi.org/10.1103/PhysRevB.46.15072).
- [100] A. Wagenpfahl. Numerical simulations on limitations and optimization strategies of organic solar cells. Ph.D. thesis, University of Würzburg (2013).
- [101] F. Goucher, G. Pearson, M. Sparks, G. Teal and W. Shockley. Theory and experiment for a germanium p-n junction. *Physical Review*, **81**, 4, 637 (1951). doi: [10.1103/PhysRev.81.637.2](https://doi.org/10.1103/PhysRev.81.637.2).
- [102] C. Waldauf, P. Schilinsky, J. Hauch and C. J. Brabec. Material and device concepts for organic photovoltaics: towards competitive efficiencies. *Thin Solid Films*, **451**, 503 (2004). doi: [10.1016/j.tsf.2003.11.043](https://doi.org/10.1016/j.tsf.2003.11.043).

- [103] D. Cheyns, J. Poortmans, P. Heremans, C. Deibel, S. Verlaak, B. Rand and J. Ge-noe. Analytical model for the open-circuit voltage and its associated resistance in organic planar heterojunction solar cells. *Physical Review B*, **77**, 16, 165332 (2008). doi: [10.1103/PhysRevB.77.165332](https://doi.org/10.1103/PhysRevB.77.165332).
- [104] D. Rauh, A. Wagenpfahl, C. Deibel and V. Dyakonov. Relation of open circuit volt-age to charge carrier density in organic bulk heterojunction solar cells. *Applied Physics Letters*, **98**, 13, 133301 (2011). doi: [10.1063/1.3566979](https://doi.org/10.1063/1.3566979).
- [105] U. Zhokhavets, T. Erb, H. Hoppe, G. Gobsch and N. S. Sariciftci. Effect of an-nealing of poly (3-hexylthiophene)/fullerene bulk heterojunction composites on structural and optical properties. *Thin Solid Films*, **496**, 2, 679 (2006). doi: [10.1016/j.tsf.2005.09.093](https://doi.org/10.1016/j.tsf.2005.09.093).
- [106] C. R. McNeill, J. J. Halls, R. Wilson, G. L. Whiting, S. Berkebile, M. G. Ram-sey, R. H. Friend and N. C. Greenham. Efficient polythiophene/polyfluorene copolymer bulk heterojunction photovoltaic devices: device physics and an-nealing effects. *Advanced Functional Materials*, **18**, 16, 2309 (2008). doi: [10.1002/adfm.200800182](https://doi.org/10.1002/adfm.200800182).
- [107] Y. Liang, Y. Wu, D. Feng, S.-T. Tsai, H.-J. Son, G. Li and L. Yu. Development of new semiconducting polymers for high performance solar cells. *Journal of the American Chemical Society*, **131**, 1, 56 (2008). doi: [10.1021/ja808373p](https://doi.org/10.1021/ja808373p).
- [108] Y. Liang, D. Feng, Y. Wu, S.-T. Tsai, G. Li, C. Ray and L. Yu. Highly efficient so-lar cell polymers developed via fine-tuning of structural and electronic prop-erties. *Journal of the American Chemical Society*, **131**, 22, 7792 (2009). doi: [10.1021/ja901545q](https://doi.org/10.1021/ja901545q).
- [109] E. Bundgaard and F. Krebs. Low-band-gap conjugated polymers based on thio-phenes, benzothiadiazole, and benzobis (thiadiazole). *Macromolecules*, **39**, 8, 2823 (2006). doi: [10.1021/ma052683e](https://doi.org/10.1021/ma052683e).
- [110] E. Bundgaard and F. C. Krebs. Low band gap polymers for organic photo-voltaics. *Solar Energy Materials and Solar Cells*, **91**, 11, 954 (2007). doi: [10.1016/j.solmat.2007.01.015](https://doi.org/10.1016/j.solmat.2007.01.015).
- [111] A. J. Heeger. Semiconducting polymers: the third generation. *Chemical Society Reviews*, **39**, 7, 2354 (2010). doi: [10.1039/B914956M](https://doi.org/10.1039/B914956M).

Bibliography

- [112] L. Koster, E. Smits, V. Mihailetschi and P. Blom. Device model for the operation of polymer/fullerene bulk heterojunction solar cells. *Physical Review B*, **72**, 8, 085205 (2005). doi: [10.1103/PhysRevB.72.085205](https://doi.org/10.1103/PhysRevB.72.085205).
- [113] L. Lu and L. Yu. Understanding low bandgap polymer ptb7 and optimizing polymer solar cells based on it. *Advanced Materials*, **26**, 26, 4413 (2014). doi: [10.1002/adma.201400384](https://doi.org/10.1002/adma.201400384).
- [114] B. Giesecking, B. Jäck, E. Preis, S. Jung, M. Forster, U. Scherf, C. Deibel and V. Dyakonov. Excitation Dynamics in Low Band Gap Donor-Acceptor Copolymers and Blends. *Advanced Energy Materials*, n/a–n/a (2012). doi: [10.1002/aenm.201200304](https://doi.org/10.1002/aenm.201200304).
- [115] B. Giesecking. Excitation dynamics and charge carrier generation in organic semiconductors for photovoltaic applications. Ph.D. thesis, University of Würzburg (2013).
- [116] J. Roncali. Molecular bulk heterojunctions: an emerging approach to organic solar cells. *Accounts of chemical research*, **42**, 11, 1719 (2009). doi: [10.1021/ar900041b](https://doi.org/10.1021/ar900041b).
- [117] Y. Sun, G. C. Welch, W. L. Leong, C. J. Takacs, G. C. Bazan and A. J. Heeger. Solution-processed small-molecule solar cells with 6.7% efficiency. *Nature materials*, **11**, 1, 44 (2012). doi: [10.1038/nmat3160](https://doi.org/10.1038/nmat3160).
- [118] V. Gupta, A. K. K. Kyaw, D. H. Wang, S. Chand, G. C. Bazan and A. J. Heeger. Barium: An efficient cathode layer for bulk-heterojunction solar cells. *Scientific reports*, **3** (2013). doi: [10.1038/srep01965](https://doi.org/10.1038/srep01965).
- [119] A. K. K. Kyaw, D. H. Wang, V. Gupta, W. L. Leong, L. Ke, G. C. Bazan and A. J. Heeger. Intensity dependence of current–voltage characteristics and recombination in high-efficiency solution-processed small-molecule solar cells. *ACS nano*, **7**, 5, 4569 (2013). doi: [10.1021/nm401267s](https://doi.org/10.1021/nm401267s).
- [120] A. K. K. Kyaw, D. H. Wang, V. Gupta, J. Zhang, S. Chand, G. C. Bazan and A. J. Heeger. Efficient solution-processed small-molecule solar cells with inverted structure. *Advanced Materials*, **25**, 17, 2397 (2013). doi: [10.1002/adma.201300295](https://doi.org/10.1002/adma.201300295).
- [121] T. S. van der Poll, J. A. Love, T.-Q. Nguyen and G. C. Bazan. Non-basic high-performance molecules for solution-processed organic solar cells. *Advanced Materials*, **24**, 27, 3646 (2012). doi: [10.1002/adma.201201127](https://doi.org/10.1002/adma.201201127).

- [122] J. A. Love, C. M. Proctor, J. Liu, C. J. Takacs, A. Sharenko, T. S. van der Poll, A. J. Heeger, G. C. Bazan and T.-Q. Nguyen. Film morphology of high efficiency solution-processed small-molecule solar cells. *Advanced Functional Materials*, **23**, 40, 5019 (2013). doi: [10.1002/adfm.201300099](https://doi.org/10.1002/adfm.201300099).
- [123] L. A. Perez, K. W. Chou, J. A. Love, T. S. van der Poll, D.-M. Smilgies, T.-Q. Nguyen, E. J. Kramer, A. Amassian and G. C. Bazan. Solvent additive effects on small molecule crystallization in bulk heterojunction solar cells probed during spin casting. *Advanced Materials*, **25**, 44, 6380 (2013). doi: [10.1002/adma.201302389](https://doi.org/10.1002/adma.201302389).
- [124] J. E. Coughlin, Z. B. Henson, G. C. Welch and G. C. Bazan. Design and synthesis of molecular donors for solution-processed high-efficiency organic solar cells. *Accounts of chemical research*, **47**, 1, 257 (2013). doi: [10.1021/ar400136b](https://doi.org/10.1021/ar400136b).
- [125] H. W. Kroto, J. R. Heath, S. C. O'Brien, R. F. Curl, R. E. Smalley et al. C₆₀: buckminsterfullerene. *Nature*, **318**, 6042, 162 (1985). doi: [10.1038/318162a0](https://doi.org/10.1038/318162a0).
- [126] W. Krätschmer, L. D. Lamb, K. Fostiropoulos and D. R. Huffman. C₆₀: a new form of carbon. *Nature*, **347**, 6291, 354 (1990). doi: [10.1038/347354a0](https://doi.org/10.1038/347354a0).
- [127] R. Taylor, J. Hare, K. Ala'a and H. W. Kroto. Isolation, separation and characterisation of the fullerenes c₆₀ and c₇₀: the third form of carbon. *Journal of the Chemical Society, Chemical Communications*, , 20, 1423 (1990). doi: [10.1039/C39900001423](https://doi.org/10.1039/C39900001423).
- [128] H. Ajie, M. M. Alvarez, S. J. Anz, R. D. Beck, F. Diederich, K. Fostiropoulos, D. R. Huffman, W. Krätschmer, Y. Rubin et al. Characterization of the soluble all-carbon molecules c₆₀ and c₇₀. *Journal of Physical Chemistry*, **94**, 24, 8630 (1990). doi: [10.1021/j100387a004](https://doi.org/10.1021/j100387a004).
- [129] R. Haufler, J. Conceicao, L. Chibante, Y. Chai, N. Byrne, S. Flanagan, M. Haley, S. C. O'Brien, C. Pan et al. Efficient production of c₆₀ (buckminsterfullerene), c₆₀h₃₆, and the solvated buckide ion. *Journal of Physical Chemistry*, **94**, 24, 8634 (1990). doi: [10.1021/j100387a005](https://doi.org/10.1021/j100387a005).
- [130] J. C. Hummelen, B. W. Knight, F. LePeq, F. Wudl, J. Yao and C. L. Wilkins. Preparation and characterization of fulleroid and methanofullerene derivatives. *The Journal of Organic Chemistry*, **60**, 3, 532 (1995). doi: [10.1021/jo00108a012](https://doi.org/10.1021/jo00108a012).
- [131] V. D. Mihailetschi, J. K. van Duren, P. W. Blom, J. C. Hummelen, R. A. Janssen, J. M. Kroon, M. T. Rispens, W. J. H. Verhees and M. M. Wienk. Electron transport

Bibliography

- in a methanofullerene. *Advanced Functional Materials*, **13**, 1, 43 (2003). doi: [10.1002/adfm.200390004](https://doi.org/10.1002/adfm.200390004).
- [132] P. Peumans, A. Yakimov and S. R. Forrest. Small molecular weight organic thin-film photodetectors and solar cells. *Journal of Applied Physics*, **93**, 7, 3693 (2003). doi: [10.1063/1.1534621](https://doi.org/10.1063/1.1534621).
- [133] E. Meijer, D. De Leeuw, S. Setayesh, E. Van Veenendaal, B.-H. Huisman, P. Blom, J. Hummelen, U. Scherf and T. Klapwijk. Solution-processed ambipolar organic field-effect transistors and inverters. *Nature materials*, **2**, 10, 678 (2003). doi: [10.1038/nmat978](https://doi.org/10.1038/nmat978).
- [134] B. Thompson and J. Fréchet. Polymer–Fullerene Composite Solar Cells. *Angewandte Chemie International Edition*, **47**, 1, 58 (2008). doi: [10.1002/anie.200702506](https://doi.org/10.1002/anie.200702506).
- [135] C. J. Brabec, V. Dyakonov and U. Scherf. *Organic Photovoltaics*. Materials, Device Physics, and Manufacturing Technologies. Wiley VCH: Weinheim, Germany (2008).
- [136] C. J. Brabec, N. S. Sariciftci and J. C. Hummelen. Plastic solar cells. *Advanced Functional Materials*, **11**, 1, 15 (2001). ISSN 1616-3028. doi: [10.1002/1616-3028\(200102\)11:1<15::AID-ADFM15>3.0.CO;2-A](https://doi.org/10.1002/1616-3028(200102)11:1<15::AID-ADFM15>3.0.CO;2-A).
- [137] M. M. Wienk, J. M. Kroon, W. J. H. Verhees, J. Knol, J. C. Hummelen, P. A. van Hal and R. A. J. Janssen. Efficient Methano[70]fullerene/MDMO-PPV Bulk Heterojunction Photovoltaic Cells. *Angewandte Chemie International Edition*, **42**, 29, 3371 (2003). doi: [10.1002/anie.200351647](https://doi.org/10.1002/anie.200351647).
- [138] Y. He, J. You, L. Dou, C.-C. Chen, E. Richard, K. C. Cha, Y. Wu, G. Li and Y. Yang. High performance low band gap polymer solar cells with a non-conventional acceptor. *Chemical Communications*, **48**, 61, 7616 (2012). doi: [10.1039/C2CC33282E](https://doi.org/10.1039/C2CC33282E).
- [139] J. Peet, E. Brocker, Y. Xu and G. C. Bazan. Controlled β -phase formation in poly(9,9-di-n-octylfluorene) by processing with alkyl additives. *Advanced Materials*, **20**, 10, 1882 (2008). doi: [10.1002/adma.200702515](https://doi.org/10.1002/adma.200702515).
- [140] J. Peet, M. L. Senatore, A. J. Heeger and G. C. Bazan. Bulk heterojunction solar cells: The role of processing in the fabrication and optimization of plastic solar cells (adv. mater. 14–15/2009). *Advanced Materials*, **21**, 14-15 (2009). doi: [10.1002/adma.200802559](https://doi.org/10.1002/adma.200802559).

- [141] C. V. Hoven, X.-D. Dang, R. C. Coffin, J. Peet, T.-Q. Nguyen and G. C. Bazan. Improved performance of polymer bulk heterojunction solar cells through the reduction of phase separation via solvent additives. *Advanced Materials*, **22**, 8, E63 (2010). doi: [10.1002/adma.200903677](https://doi.org/10.1002/adma.200903677).
- [142] M. R. Hammond, R. J. Kline, A. A. Herzing, L. J. Richter, D. S. Germack, H.-W. Ro, C. L. Soles, D. A. Fischer, T. Xu, L. Yu, M. F. Toney and D. M. DeLongchamp. Molecular Order in High-Efficiency Polymer/Fullerene Bulk Heterojunction Solar Cells. *ACS Nano*, **5**, 10, 8248 (2011). doi: [doi: 10.1021/nn202951e](https://doi.org/10.1021/nn202951e).
- [143] B. A. Collins, J. R. Tumbleston, E. Gann, C. R. McNeill and H. Ade. Absolute Measurement of Domain Composition and Nanoscale Size Distribution Explains Performance in PTB7:PC 71BM Solar Cells. *Advanced Energy Materials*, **10** (2012). doi: [10.1002/aenm.201200377](https://doi.org/10.1002/aenm.201200377).
- [144] F. Liu, W. Zhao, J. R. Tumbleston, C. Wang, Y. Gu, D. Wang, A. L. Briseno, H. Ade and T. P. Russell. Understanding the morphology of ptb7:pcbm blends in organic photovoltaics. *Advanced Energy Materials*, **4**, 5 (2014). doi: [10.1002/aenm.201301377](https://doi.org/10.1002/aenm.201301377).
- [145] A. Foertig, J. Kniepert, M. Gluecker, T. Brenner, V. Dyakonov, D. Neher and C. Deibel. Nongeminate and geminate recombination in ptb7: Pcbm solar cells. *Advanced Functional Materials*, **24**, 9, 1306 (2014). doi: [10.1002/adfm.201302134](https://doi.org/10.1002/adfm.201302134).
- [146] G. Juška, K. Arlauskas, M. Viliūnas, K. Genevičius, R. Österbacka and H. Stubb. Charge transport in π -conjugated polymers from extraction current transients. *Physical Review B*, **62**, 24, R16235 (2000). doi: [10.1103/PhysRevB.62.R16235](https://doi.org/10.1103/PhysRevB.62.R16235).
- [147] G. Juška, K. Arlauskas, M. Viliūnas and J. Kočka. Extraction Current Transients: New Method of Study of Charge Transport in Microcrystalline Silicon. *Physical Review Letters*, **84**, 21, 4946 (2000). doi: [10.1103/PhysRevLett.84.4946](https://doi.org/10.1103/PhysRevLett.84.4946).
- [148] A. Baumann, T. J. Savenije, D. H. K. Murthy, M. Heeney, V. Dyakonov and C. Deibel. Influence of Phase Segregation on Recombination Dynamics in Organic Bulk-Heterojunction Solar Cells. *Advanced Functional Materials*, **21**, 9, 1687 (2011). doi: [10.1002/adfm.201002358](https://doi.org/10.1002/adfm.201002358).
- [149] A. Baumann. Charge Dynamics in Organic Bulk Heterojunction Solar Cells. Ph.D. thesis, University of Würzburg (2011).

Bibliography

- [150] J. D. Ceuster, E. Goovaerts, A. Bouwen, J. C. Hummelen and V. Dyakonov. High-frequency (95 GHz) electron paramagnetic resonance study of the photoinduced charge transfer in conjugated polymer-fullerene composites. *Physical Review B*, **64**, 19, 1 (2001). doi: [10.1103/PhysRevB.64.195206](https://doi.org/10.1103/PhysRevB.64.195206).
- [151] A. Aguirre, P. Gast, S. Orlinskii, I. Akimoto, E. J. J. Groenen, H. El Mkami, E. Goovaerts and S. Van Doorslaer. Multifrequency EPR analysis of the positive polaron in I2-doped poly(3-hexylthiophene) and in poly[2-methoxy-5-(3,7-dimethyloctyloxy)]-1,4-phenylenevinylene. *Physical Chemistry Chemical Physics*, **10**, 47, 7129 (2008). doi: [10.1039/b811419f](https://doi.org/10.1039/b811419f).
- [152] O. Poluektov, S. Filippone, N. Martín, A. Sperlich, C. Deibel and V. Dyakonov. Spin Signatures of Photogenerated Radical Anions in Polymer-[70]Fullerene Bulk Heterojunctions: High Frequency Pulsed EPR Spectroscopy. *Journal of Physical Chemistry B*, **114**, 14426 (2010). doi: [10.1021/jp1012347](https://doi.org/10.1021/jp1012347).
- [153] A. Sperlich, M. Liedtke, J. Kern, H. Kraus, C. Deibel, S. Filippone, J. L. Delgado and V. Dyakonov. Photoinduced C70 radical anions in polymer:fullerene blends. *physica status solidi (RRL)*, **5**, 3, 128 (2011). doi: [10.1002/pssr.201105030](https://doi.org/10.1002/pssr.201105030).
- [154] J. Niklas, K. L. Mardis, B. P. Banks, G. M. Grooms, A. Sperlich, V. Dyakonov, S. Beaupré, M. Leclerc, T. Xu, L. Yu et al. Highly-efficient charge separation and polaron delocalization in polymer–fullerene bulk-heterojunctions: a comparative multi-frequency epr and dft study. *Physical Chemistry Chemical Physics*, **15**, 24, 9562 (2013). doi: [10.1039/C3CP51477C](https://doi.org/10.1039/C3CP51477C).
- [155] P. H. Wöbkenberg, D. D. C. Bradley, D. Kronholm, J. C. Hummelen, D. M. de Leeuw, M. Cölle and T. D. Anthopoulos. High mobility n-channel organic field-effect transistors based on soluble C60 and C70 fullerene derivatives. *Synthetic Metals*, **158**, 11, 468 (2008). doi: [10.1016/j.synthmet.2008.03.016](https://doi.org/10.1016/j.synthmet.2008.03.016).
- [156] J. M. Cho, D. S. Kim, S. Bae, S.-J. Moon, W. S. Shin, D. H. Kim, S. H. Kim, A. Sperlich, S. Vöth, V. Dyakonov et al. Light-induced electron spin resonance study of galvinoxyl-doped p3ht/pcbm bulk heterojunctions. *Organic Electronics*, **27**, 119 (2015). doi: [10.1016/j.orgel.2015.08.032](https://doi.org/10.1016/j.orgel.2015.08.032).
- [157] T. Skotheim, J.-M. Yang, J. Otvos and M. Klein. Photovoltaic properties of auromerocyanine–tio2 sandwich cells. ii. properties of illuminated cells and effects of doping with electron acceptors. *The Journal of Chemical Physics*, **77**, 12, 6151 (1982). doi: [10.1063/1.443815](https://doi.org/10.1063/1.443815).

- [158] W. Nevin and G. Chamberlain. Photovoltaic properties of iodine-doped magnesium tetraphenylporphyrin sandwich cells. optimization of doping, and dark electrical properties. *Journal of applied physics*, **68**, 10, 5247 (1990). doi: [10.1063/1.347041](https://doi.org/10.1063/1.347041).
- [159] W. Nevin and G. Chamberlain. Photovoltaic properties of iodine-doped magnesium tetraphenylporphyrin sandwich cells. ii. properties of illuminated cells. *Journal of applied physics*, **69**, 8, 4324 (1991). doi: [10.1063/1.348407](https://doi.org/10.1063/1.348407).
- [160] G. Sharma, S. Sangodkar and M. Roy. Influence of iodine on the electrical and photoelectrical properties of zinc phthalocyanine thin film devices. *Materials Science and Engineering: B*, **41**, 2, 222 (1996). doi: [10.1016/S0921-5107\(96\)01673-X](https://doi.org/10.1016/S0921-5107(96)01673-X).
- [161] K. Takechi, T. Shiga, T. Motohiro, T. Akiyama, S. Yamada, H. Nakayama and K. Kohama. Solar cells using iodine-doped polythiophene–porphyrin polymer films. *Solar energy materials and solar cells*, **90**, 9, 1322 (2006). doi: [10.1016/j.solmat.2005.08.010](https://doi.org/10.1016/j.solmat.2005.08.010).
- [162] B. Kan, Q. Zhang, M. Li, X. Wan, W. Ni, G. Long, Y. Wang, X. Yang, H. Feng and Y. Chen. Solution-processed organic solar cells based on dialkylthiol-substituted benzodithiophene unit with efficiency near 10%. *Journal of the American Chemical Society*, **136**, 44, 15529 (2014). doi: [10.1021/ja509703k](https://doi.org/10.1021/ja509703k).
- [163] B. Kan, M. Li, Q. Zhang, F. Liu, X. Wan, Y. Wang, W. Ni, G. Long, X. Yang, H. Feng et al. A series of simple oligomer-like small molecules based on oligothiophenes for solution-processed solar cells with high efficiency. *Journal of the American Chemical Society*, **137**, 11, 3886 (2015). doi: [10.1021/jacs.5b00305](https://doi.org/10.1021/jacs.5b00305).
- [164] C. M. Proctor, S. Albrecht, M. Kuik, D. Neher and T.-Q. Nguyen. Overcoming geminate recombination and enhancing extraction in solution-processed small molecule solar cells. *Advanced Energy Materials*, **4**, 10 (2014). doi: [10.1002/aenm.201400230](https://doi.org/10.1002/aenm.201400230).
- [165] S. Gélinas, A. Rao, A. Kumar, S. L. Smith, A. W. Chin, J. Clark, T. S. van der Poll, G. C. Bazan and R. H. Friend. Ultrafast long-range charge separation in organic semiconductor photovoltaic diodes. *Science*, **343**, 6170, 512 (2014). doi: [10.1126/science.1246249](https://doi.org/10.1126/science.1246249).
- [166] D. H. Wang, A. K. K. Kyaw, V. Gupta, G. C. Bazan and A. J. Heeger. Enhanced efficiency parameters of solution-processable small-molecule solar cells depend-

Bibliography

- ing on its sheet resistance. *Advanced Energy Materials*, **3**, 9, 1161 (2013). doi: [10.1002/aenm.201300277](https://doi.org/10.1002/aenm.201300277).
- [167] A. Rao, M. W. B. Wilson, J. M. Hodgkiss, S. Albert-Seifried, H. Bässler and R. H. Friend. Exciton Fission and Charge Generation via Triplet Excitons in Pentacene/C60 Bilayers. *Journal of the American Chemical Society*, **132**, 36, 12698 (2010). doi: [doi: 10.1021/ja1042462](https://doi.org/10.1021/ja1042462).
- [168] D. N. Congreve, J. Lee, N. J. Thompson, E. Hontz, S. R. Yost, P. D. Reuswig, M. E. Bahlke, S. Reineke, T. Van Voorhis and M. A. Baldo. External quantum efficiency above 100% in a singlet-exciton-fission-based organic photovoltaic cell. *Science*, **340**, 6130, 334 (2013). doi: [10.1126/science.1232994](https://doi.org/10.1126/science.1232994).
- [169] A. Rao, P. C. Chow, S. Gélinas, C. W. Schlenker, C.-Z. Li, H.-L. Yip, A. K.-Y. Jen, D. S. Ginger and R. H. Friend. The role of spin in the kinetic control of recombination in organic photovoltaics. *Nature*, **500**, 7463, 435 (2013). doi: [10.1038/nature12339](https://doi.org/10.1038/nature12339).
- [170] Y. Cao, I. D. Parker, G. Yu, C. Zhang and A. J. Heeger. Improved quantum efficiency for electroluminescence in semiconducting polymers. *Nature*, **397**, 6718, 414 (1999). doi: [10.1038/17087](https://doi.org/10.1038/17087).
- [171] M. Segal, M. Baldo, R. Holmes, S. Forrest and Z. Soos. Excitonic singlet-triplet ratios in molecular and polymeric organic materials. *Physical Review B*, **68**, 7, 075211 (2003). doi: [10.1103/PhysRevB.68.075211](https://doi.org/10.1103/PhysRevB.68.075211).
- [172] M. Reufer, M. J. Walter, P. G. Lagoudakis, A. B. Hummel, J. S. Kolb, H. G. Roskos, U. Scherf and J. M. Lupton. Spin-conserving carrier recombination in conjugated polymers. *Nature Materials*, **4**, 4, 340 (2005). doi: [10.1038/nmat1354](https://doi.org/10.1038/nmat1354).
- [173] D. Veldman, T. Offermans, J. Sweelssen, M. M. Koetse, S. C. Meskers and R. A. Janssen. Triplet formation from the charge-separated state in blends of mdmop-pv with cyano-containing acceptor polymers. *Thin Solid Films*, **511**, 333 (2006). doi: [10.1016/j.tsf.2005.12.034](https://doi.org/10.1016/j.tsf.2005.12.034).
- [174] W. Chang, D. N. Congreve, E. Hontz, M. E. Bahlke, D. P. McMahon, S. Reineke, T. C. Wu, V. Bulović, T. Van Voorhis and M. A. Baldo. Spin-dependent charge transfer state design rules in organic photovoltaics. *Nature communications*, **6** (2015). doi: [10.1038/ncomms7415](https://doi.org/10.1038/ncomms7415).
- [175] H. Ohkita, S. Cook, Y. Astuti, W. Duffy, M. Heeney, S. Tierney, I. McCulloch, D. D. Bradley and J. R. Durrant. Radical ion pair mediated triplet formation in

- polymer–fullerene blend films. *Chemical communications*, , 37, 3939 (2006). doi: [10.1039/B608832E](https://doi.org/10.1039/B608832E).
- [176] S. Cook, H. Ohkita, J. R. Durrant, Y. Kim, J. J. Benson-Smith, J. Nelson and D. D. Bradley. Singlet exciton transfer and fullerene triplet formation in polymer–fullerene blend films. *Applied physics letters*, **89**, 10, 101128 (2006). doi: [10.1063/1.2338528](https://doi.org/10.1063/1.2338528).
- [177] T. Basel, U. Huynh, T. Zheng, T. Xu, L. Yu and Z. V. Vardeny. Optical, electrical, and magnetic studies of organic solar cells based on low bandgap copolymer with spin 1/2 radical additives. *Advanced Functional Materials*, **25**, 12, 1895 (2015). doi: [10.1002/adfm.201403191](https://doi.org/10.1002/adfm.201403191).
- [178] B. Z. Tedlla, F. Zhu, M. Cox, J. Drikkoningen, J. Manca, B. Koopmans and E. Goovaerts. Understanding triplet formation pathways in bulk heterojunction polymer: Fullerene photovoltaic devices. *Advanced Energy Materials*, **5**, 2 (2015). doi: [10.1002/aenm.201401109](https://doi.org/10.1002/aenm.201401109).
- [179] J. Niklas, S. Beaupré, M. Leclerc, T. Xu, L. Yu, A. Sperlich, V. Dyakonov and O. G. Poluektov. Photoinduced dynamics of charge separation: From photosynthesis to polymer–fullerene bulk heterojunctions. *The Journal of Physical Chemistry B*, **119**, 24, 7407 (2015). doi: [10.1021/jp511021v](https://doi.org/10.1021/jp511021v).
- [180] D. Di Nuzzo, G.-J. A. H. Wetzelaer, R. K. M. Bouwer, V. S. Gevaerts, S. C. J. Meskers, J. C. Hummelen, P. W. M. Blom and R. A. J. Janssen. Simultaneous Open-Circuit Voltage Enhancement and Short-Circuit Current Loss in Polymer: Fullerene Solar Cells Correlated by Reduced Quantum Efficiency for Photoinduced Electron Transfer. *Advanced Energy Materials*, n/a–n/a (2012). doi: [10.1002/aenm.201200426](https://doi.org/10.1002/aenm.201200426).
- [181] M. C. Scharber, N. A. Schultz and N. S. Sariciftci. Optical- and photocurrent-detected magnetic resonance studies on conjugated polymer/fullerene composites. *Physical Review B*, **67**, 8, 1 (2003). doi: [10.1103/PhysRevB.67.085202](https://doi.org/10.1103/PhysRevB.67.085202).
- [182] C. Dyer-Smith, L. X. Reynolds, A. Bruno, D. D. C. Bradley, S. A. Haque and J. Nelson. Triplet Formation in Fullerene Multi-Adduct Blends for Organic Solar Cells and Its Influence on Device Performance. *Advanced Functional Materials*, **20**, 16, 2701 (2010). doi: [10.1002/adfm.201000477](https://doi.org/10.1002/adfm.201000477).
- [183] A. Sperlich, H. Kraus, C. Deibel, H. Blok, J. Schmidt and V. Dyakonov. Reversible and Irreversible Interactions of Poly(3-hexylthiophene) with Oxygen Studied by

Bibliography

- Spin-Sensitive Methods. *Journal of Physical Chemistry B*, **115**, 46, 13513 (2011). doi: [doi: 10.1021/jp2077215](https://doi.org/10.1021/jp2077215).
- [184] E. T. Hoke, I. T. Sachs-Quintana, M. T. Lloyd, I. Kauvar, W. R. Mateker, A. M. Nardes, C. H. Peters, N. Kopidakis and M. D. McGehee. The Role of Electron Affinity in Determining Whether Fullerenes Catalyze or Inhibit Photooxidation of Polymers for Solar Cells. *Advanced Energy Materials*, n/a–n/a (2012). doi: [10.1002/aenm.201200169](https://doi.org/10.1002/aenm.201200169).
- [185] D. Di Nuzzo, A. Aguirre, M. Shahid, V. S. Gevaerts, S. C. J. Meskers and R. A. J. Janssen. Improved Film Morphology Reduces Charge Carrier Recombination into the Triplet Excited State in a Small Bandgap Polymer-Fullerene Photovoltaic Cell. *Advanced Materials*, **22**, 38, 4321 (2010). doi: [10.1002/adma.201001452](https://doi.org/10.1002/adma.201001452).
- [186] C. W. Schlenker, K.-S. Chen, H.-L. Yip, C.-Z. Li, L. R. Bradshaw, S. T. Ochsenbein, F. Ding, X. S. Li, D. R. Gamelin, A. K. Y. Jen and D. S. Ginger. Polymer Triplet Energy Levels Need Not Limit Photocurrent Collection in Organic Solar Cells. *Journal of the American Chemical Society*, 121116124820008 (2012). doi: [10.1021/ja306110b](https://doi.org/10.1021/ja306110b).
- [187] P. C. Chow, S. Gélinas, A. Rao and R. H. Friend. Quantitative bimolecular recombination in organic photovoltaics through triplet exciton formation. *Journal of the American Chemical Society*, **136**, 9, 3424 (2014). doi: [10.1021/ja410092n](https://doi.org/10.1021/ja410092n).
- [188] C. A. Hutchison Jr and B. W. Mangum. Paramagnetic resonance absorption in naphthalene in its phosphorescent state. *The Journal of Chemical Physics*, **34**, 3, 908 (1961). doi: [10.1063/1.1731693](https://doi.org/10.1063/1.1731693).
- [189] R. W. Brandon, R. E. Gerkin and C. A. Hutchison Jr. Paramagnetic resonance absorption in phenanthrene in its phosphorescent state. *The Journal of Chemical Physics*, **41**, 12, 3717 (1964). doi: [10.1063/1.1725804](https://doi.org/10.1063/1.1725804).
- [190] S. Cambre, J. De Ceuster, E. Goovaerts, A. Bouwen and H. Detert. Quantitative evaluation of the preferential orientation of para-phenylene vinylene pentamers in polystyrene films by optically detected magnetic resonance. *Applied Magnetic Resonance*, **31**, 343 (2007). doi: [10.1007/BF03166589](https://doi.org/10.1007/BF03166589).
- [191] T. Biskup, M. Sommer, S. Rein, D. L. Meyer, M. Kohlstädt, U. Würfel and S. Weber. Ordering of pcdtbt revealed by time-resolved electron paramagnetic resonance spectroscopy of its triplet excitons. *Angewandte Chemie International Edition* (2015). doi: [10.1002/anie.201502241](https://doi.org/10.1002/anie.201502241).

- [192] V. Dyakonov, H. Kraus, A. Sperlich, R. Magerle, M. Zerson and M. Dehnert. *Elementary Processes in Organic Photovoltaics—Interplay between microscopic structure and intermolecular charge transfer processes in polymer-fullerene bulk-heterojunctions*. Springer International Publishing (2016).
- [193] S. Mukherjee, C. M. Proctor, G. C. Bazan, T.-Q. Nguyen and H. Ade. Significance of average domain purity and mixed domains on the photovoltaic performance of high-efficiency solution-processed small-molecule bhj solar cells. *Advanced Energy Materials*, **5**, 21 (2015). doi: [10.1002/aenm.201500877](https://doi.org/10.1002/aenm.201500877).
- [194] K. Tvingstedt, K. Vandewal, A. Gadisa, F. Zhang, J. Manca and O. Inganäs. Electroluminescence from charge transfer states in polymer solar cells. *Journal of the American Chemical Society*, **131**, 33, 11819 (2009). doi: [10.1021/ja903100p](https://doi.org/10.1021/ja903100p).
- [195] K. Tvingstedt, K. Vandewal, F. Zhang and O. Inganäs. On the Dissociation Efficiency of Charge Transfer Excitons and Frenkel Excitons in Organic Solar Cells: A Luminescence Quenching Study. *Journal of Physical Chemistry C*, **114**, 49, 21824 (2010). doi: [10.1021/jp107587h](https://doi.org/10.1021/jp107587h).
- [196] N. A. Ran, M. Kuik, J. A. Love, C. M. Proctor, I. Nagao, G. C. Bazan and T.-Q. Nguyen. Understanding the charge-transfer state and singlet exciton emission from solution-processed small-molecule organic solar cells. *Advanced Materials*, **26**, 43, 7405 (2014). doi: [10.1002/adma.201402423](https://doi.org/10.1002/adma.201402423).
- [197] S. Stoll. Chapter six-cw-epr spectral simulations: Solid state. *Methods in enzymology*, **563**, 121 (2015). doi: [10.1016/bs.mie.2015.06.003](https://doi.org/10.1016/bs.mie.2015.06.003).
- [198] S. Väh. Winkelaufgelöste Photolumineszenz detektierte Magnetresonanz an organischen Halbleitern. Master's thesis, University of Würzburg (2011).
- [199] B. Z. Tedlla, F. Zhu, M. Cox, B. Koopmans and E. Goovaerts. Spin-dependent photophysics in polymers lightly doped with fullerene derivatives: Photoluminescence and electrically detected magnetic resonance. *Physical Review B*, **91**, 8, 085309 (2015). doi: [10.1103/PhysRevB.91.085309](https://doi.org/10.1103/PhysRevB.91.085309).
- [200] O. G. Poluektov, J. Niklas, K. L. Mardis, S. Beaupré, M. Leclerc, C. Villegas, S. Erten-Ela, J. L. Delgado, N. Martín, A. Sperlich et al. Electronic structure of fullerene heterodimer in bulk-heterojunction blends. *Advanced Energy Materials*, **4**, 7 (2014). doi: [10.1002/aenm.201301517](https://doi.org/10.1002/aenm.201301517).

Bibliography

- [201] J. D. Lin, O. V. Mikhnenko, T. S. van der Poll, G. C. Bazan and T.-Q. Nguyen. Temperature dependence of exciton diffusion in a small-molecule organic semiconductor processed with and without additive. *Advanced Materials*, **27**, 15, 2528 (2015). doi: [10.1002/adma.201404590](https://doi.org/10.1002/adma.201404590).
- [202] Y. Zhang, T. P. Basel, B. R. Gautam, X. Yang, D. J. Mascaro, F. Liu and Z. V. Vardeny. Spin-enhanced organic bulk heterojunction photovoltaic solar cells. *Nature Communications*, **3**, 1043 (2012). doi: [10.1038/ncomms2057](https://doi.org/10.1038/ncomms2057).
- [203] S. Singh, Y. Zhang and Z. V. Vardeny. Effect of spin $\frac{1}{2}$ radicals on the ultrafast photoexcitation dynamics in RR-P3HT/PCBM blends for photovoltaic applications. *Synthetic Metals*, **160**, 3-4, 311 (2010). doi: [10.1016/j.synthmet.2009.07.061](https://doi.org/10.1016/j.synthmet.2009.07.061).
- [204] Y. Zhang, G. Hukic-Markosian, D. Mascaro and Z. V. Vardeny. Enhanced performance of p3ht/pcbm bulk heterojunction photovoltaic devices by adding spin $1/2$ radicals. *Synthetic Metals*, **160**, 3, 262 (2010). doi: [10.1016/j.synthmet.2009.10.005](https://doi.org/10.1016/j.synthmet.2009.10.005).
- [205] Y. Zhang, B. R. Gautam, T. P. Basel, D. J. Mascaro and Z. V. Vardeny. Organic bulk heterojunction solar cells enhanced by spin interaction. *Synthetic Metals*, **173**, 2 (2013). doi: [10.1016/j.synthmet.2012.12.035](https://doi.org/10.1016/j.synthmet.2012.12.035).
- [206] S. Singh and Z. V. Vardeny. Ultrafast Transient Spectroscopy of Polymer/Fullerene Blends for Organic Photovoltaic Applications. *Materials*, **6**, 3, 897 (2013). doi: [10.3390/ma6030897](https://doi.org/10.3390/ma6030897).
- [207] A. A. Bakulin, A. Rao, V. G. Pavelyev, P. H. M. van Loosdrecht, M. S. Pshenichnikov, D. Niedzialek, J. Cornil, D. Beljonne and R. H. Friend. The Role of Driving Energy and Delocalized States for Charge Separation in Organic Semiconductors. *Science*, **9** (2012). doi: [10.1126/science.1217745](https://doi.org/10.1126/science.1217745).
- [208] J. Behrends, A. Sperlich, A. Schnegg, T. Biskup, C. Teutloff, K. Lips, V. Dyakonov and R. Bittl. Direct detection of photoinduced charge transfer complexes in polymer fullerene blends. *Physical Review B*, **85**, 12 (2012). doi: [10.1103/PhysRevB.85.125206](https://doi.org/10.1103/PhysRevB.85.125206).
- [209] Y. Yao, J. Hou, Z. Xu, G. Li, Y. Yang et al. Effects of solvent mixtures on the nanoscale phase separation in polymer solar cells. *Advanced Functional Materials*, **18**, 12, 1783 (2008). doi: [10.1002/adfm.200701459](https://doi.org/10.1002/adfm.200701459).

- [210] M. D. Perez, C. Borek, S. R. Forrest and M. E. Thompson. Molecular and morphological influences on the open circuit voltages of organic photovoltaic devices. *Journal of the American Chemical Society*, **131**, 26, 9281 (2009). doi: [10.1021/ja9007722](https://doi.org/10.1021/ja9007722).
- [211] C.-P. Chen, S.-H. Chan, T.-C. Chao, C. Ting and B.-T. Ko. Low-bandgap poly (thiophene-phenylene-thiophene) derivatives with broaden absorption spectra for use in high-performance bulk-heterojunction polymer solar cells. *Journal of the American Chemical Society*, **130**, 38, 12828 (2008). doi: [10.1021/ja801877k](https://doi.org/10.1021/ja801877k).
- [212] R. B. Ross, C. M. Cardona, D. M. Guldi, S. G. Sankaranarayanan, M. O. Reese, N. Kopidakis, J. Peet, B. Walker, G. C. Bazan, E. Van Keuren, B. C. Holloway and M. Drees. Endohedral fullerenes for organic photovoltaic devices. *Nature Materials*, **8**, 3, 208 (2009). doi: [10.1038/nmat2379](https://doi.org/10.1038/nmat2379).
- [213] Y. He, H.-Y. Chen, J. Hou and Y. Li. Indene- c60 bisadduct: a new acceptor for high-performance polymer solar cells. *Journal of the American Chemical Society*, **132**, 4, 1377 (2010). doi: [10.1021/ja908602j](https://doi.org/10.1021/ja908602j).
- [214] S. H. Park, A. Roy, S. Beaupre, S. Cho, N. Coates, J. S. Moon, D. Moses, M. Leclerc, K. Lee and A. J. Heeger. Bulk heterojunction solar cells with internal quantum efficiency approaching 100%. *Nature photonics*, **3**, 5, 297 (2009). doi: [10.1038/nphoton.2009.69](https://doi.org/10.1038/nphoton.2009.69).
- [215] A. Baumann, J. Lorrmann, D. Rauh, C. Deibel and V. Dyakonov. A New Approach for Probing the Mobility and Lifetime of Photogenerated Charge Carriers in Organic Solar Cells Under Real Operating Conditions. *Advanced Materials*, n/a–n/a (2012). doi: [10.1002/adma.201200874](https://doi.org/10.1002/adma.201200874).
- [216] K. Goushi, K. Yoshida, K. Sato and C. Adachi. Organic light-emitting diodes employing efficient reverse intersystem crossing for triplet-to-singlet state conversion. *Nature Photonics*, **6**, 4, 253 (2012). doi: [10.1038/nphoton.2012.31](https://doi.org/10.1038/nphoton.2012.31).
- [217] F. Zhang, Z. Zhuo, J. Zhang, X. Wang, X. Xu, Z. Wang, Y. Xin, J. Wang, J. Wang, W. Tang, Z. Xu and Y. Wang. Influence of PC60BM or PC70BM as electron acceptor on the performance of polymer solar cells. *Solar Energy Materials and Solar Cells*, **97**, C, 71 (2012). doi: [10.1016/j.solmat.2011.09.006](https://doi.org/10.1016/j.solmat.2011.09.006).
- [218] M. Baldo, M. Thompson and S. Forrest. High-efficiency fluorescent organic light-emitting devices using a phosphorescent sensitizer. *Nature*, **403**, 6771, 750 (2000). doi: [10.1038/35001541](https://doi.org/10.1038/35001541).

Bibliography

- [219] Z. Xiong, D. Wu, Z. V. Vardeny and J. Shi. Giant magnetoresistance in organic spin-valves. *Nature*, **427**, 6977, 821 (2004). doi: [10.1038/nature02325](https://doi.org/10.1038/nature02325).
- [220] B. Hu, L. Yan and M. Shao. Magnetic-field effects in organic semiconducting materials and devices. *Advanced Materials*, **21**, 14-15, 1500 (2009). doi: [10.1002/adma.200802386](https://doi.org/10.1002/adma.200802386).
- [221] A. Mozer, N. Sariciftci, L. Lutsen, D. Vanderzande, R. Österbacka, M. Westerling and G. Juška. Charge transport and recombination in bulk heterojunction solar cells studied by the photoinduced charge extraction in linearly increasing voltage technique. *Applied Physics Letters*, **86**, 11, 112104 (2005). doi: [10.1063/1.1882753](https://doi.org/10.1063/1.1882753).
- [222] W. Baker, T. Keevers, J. M. Lupton, D. McCamey and C. Boehme. Slow hopping and spin dephasing of coulombically bound polaron pairs in an organic semiconductor at room temperature. *Physical review letters*, **108**, 26, 267601 (2012).
- [223] A. J. Kupijai, K. M. Behringer, F. G. Schaebler, N. E. Galfe, M. Corazza, S. A. Gevorgyan, F. C. Krebs, M. Stutzmann and M. S. Brandt. Bipolar polaron pair recombination in polymer/fullerene solar cells. *Physical Review B*, **92**, 24, 245203 (2015). doi: [10.1103/PhysRevB.92.245203](https://doi.org/10.1103/PhysRevB.92.245203).
- [224] J. Behrends, A. Schnegg, K. Lips, E. Thomsen, A. Pandey, I. Samuel and D. Keeble. Bipolaron Formation in Organic Solar Cells Observed by Pulsed Electrically Detected Magnetic Resonance. *Physical Review Letters*, **105**, 17, 176601 (2010). doi: [10.1103/PhysRevLett.105.176601](https://doi.org/10.1103/PhysRevLett.105.176601).
- [225] J. Behrends. Spin-dependent Transport and Recombination in Solar Cells studied by Pulsed Electrically Detected Magnetic Resonance. Ph.D. thesis (2010).
- [226] R. Vranich, B. Henderson and M. Pepper. Spin-dependent pair generation at si/sio₂ interfaces. *Applied physics letters*, **53**, 14, 1299 (1988). doi: [10.1063/1.100450](https://doi.org/10.1063/1.100450).
- [227] A. Kadashchuk, V. I. Arkhipov, C.-H. Kim, J. Shinar, D.-W. Lee, Y.-R. Hong, J.-I. Jin, P. Heremans and H. Bässler. Localized trions in conjugated polymers. *Phys. Rev. B*, **76**, 235205 (2007). doi: [10.1103/PhysRevB.76.235205](https://doi.org/10.1103/PhysRevB.76.235205).
- [228] K. Tvingstedt, O. Malinkiewicz, A. Baumann, C. Deibel, H. J. Snaith, V. Dyakonov and H. J. Bolink. Radiative efficiency of lead iodide based perovskite solar cells. *Scientific reports*, **4** (2014). doi: [10.1038/srep06071](https://doi.org/10.1038/srep06071).

- [229] M. A. Baldo, D. O'Brien, Y. You, A. Shoustikov, S. Sibley, M. Thompson and S. Forrest. Highly efficient phosphorescent emission from organic electroluminescent devices. *Nature*, **395**, 6698, 151 (1998). doi: [10.1038/25954](https://doi.org/10.1038/25954).
- [230] M. Wohlgenannt, K. Tandon, S. Mazumdar, S. Ramasesha and Z. V. Vardeny. Formation cross-sections of singlet and triplet excitons in pi-conjugated polymers. *Nature*, **409**, 25, 494 (2001). doi: [10.1038/35054025](https://doi.org/10.1038/35054025).
- [231] H. Uoyama, K. Goushi, K. Shizu, H. Nomura and C. Adachi. Highly efficient organic light-emitting diodes from delayed fluorescence. *Nature*, **492**, 7428, 234 (2012). doi: [10.1038/nature11687](https://doi.org/10.1038/nature11687).
- [232] C. Adachi. Third-generation organic electroluminescence materials. *Japanese Journal of Applied Physics*, **53**, 6, 060101 (2014).
- [233] F. B. Dias, K. N. Bourdakos, V. Jankus, K. C. Moss, K. T. Kamtekar, V. Bhalla, J. Santos, M. R. Bryce and A. P. Monkman. Triplet harvesting with 100% efficiency by way of thermally activated delayed fluorescence in charge transfer oled emitters. *Advanced Materials*, **25**, 27, 3707 (2013). doi: [10.1002/adma.201300753](https://doi.org/10.1002/adma.201300753).
- [234] K. Goushi, K. Yoshida, K. Sato and C. Adachi. Organic light-emitting diodes employing efficient reverse intersystem crossing for triplet-to-singlet state conversion. *Nature Photonics*, **6**, 4, 253 (2012). doi: [10.1038/nphoton.2012.31](https://doi.org/10.1038/nphoton.2012.31).
- [235] Y.-S. Park, K.-H. Kim and J.-J. Kim. Efficient triplet harvesting by fluorescent molecules through exciplexes for high efficiency organic light-emitting diodes. *Applied Physics Letters*, **102**, 15, 153306 (2013). doi: [10.1063/1.4802716](https://doi.org/10.1063/1.4802716).
- [236] T. Zhang, B. Chu, W. Li, Z. Su, Q. M. Peng, B. Zhao, Y. Luo, F. Jin, X. Yan, Y. Gao et al. Efficient triplet application in exciplex delayed-fluorescence oleds using a reverse intersystem crossing mechanism based on a δ es-t of around zero. *ACS applied materials & interfaces*, **6**, 15, 11907 (2014). doi: [10.1021/am501164s](https://doi.org/10.1021/am501164s).
- [237] D. Graves, V. Jankus, F. B. Dias and A. Monkman. Photophysical investigation of the thermally activated delayed emission from films of m-mtdata: Pbd exciplex. *Advanced Functional Materials*, **24**, 16, 2343 (2014). doi: [10.1002/adfm.201303389](https://doi.org/10.1002/adfm.201303389).
- [238] A. Michaleviciute, E. Gurskyte, D. Y. Volyniuk, V. V. Cherpak, G. Sini, P. Y. Stakhira and J. V. Grazulevicius. Star-shaped carbazole derivatives for bilayer white organic light-emitting diodes combining emission from both excitons and ex-

Bibliography

- ciplexes. *The Journal of Physical Chemistry C*, **116**, 39, 20769 (2012). doi: [10.1021/jp306824u](https://doi.org/10.1021/jp306824u).
- [239] V. Cherpak, P. Stakhira, B. Minaev, G. Baryshnikov, E. Stromylo, I. Helzhynskyy, M. Chapran, D. Volyniuk, Z. Hotra, A. Dabulienė et al. Mixing of phosphorescent and exciplex emission in efficient organic electroluminescent devices. *ACS applied materials & interfaces*, **7**, 2, 1219 (2015). doi: [10.1021/am507050g](https://doi.org/10.1021/am507050g).
- [240] M. Chapran, K. Ivaniuk, P. Stakhira, V. Cherpak, Z. Hotra, D. Volyniuk, A. Michaleviciute, A. Tomkeviciene, L. Voznyak and J. Grazulevicius. Essential electro-optical differences of exciplex type oleds based on a starburst carbazole derivative prepared by layer-by-layer and codeposition processes. *Synthetic Metals*, **209**, 173 (2015). doi: [10.1016/j.synthmet.2015.07.020](https://doi.org/10.1016/j.synthmet.2015.07.020).
- [241] W.-Y. Hung, G.-C. Fang, Y.-C. Chang, T.-Y. Kuo, P.-T. Chou, S.-W. Lin and K.-T. Wong. Highly efficient bilayer interface exciplex for yellow organic light-emitting diode. *ACS applied materials & interfaces*, **5**, 15, 6826 (2013). doi: [10.1021/am402032z](https://doi.org/10.1021/am402032z).
- [242] X. Xing, L. Zhong, L. Zhang, Z. Chen, B. Qu, E. Chen, L. Xiao and Q. Gong. Essential differences of organic films at the molecular level via vacuum deposition and solution processes for organic light-emitting diodes. *The Journal of Physical Chemistry C*, **117**, 48, 25405 (2013). doi: [10.1021/jp410547w](https://doi.org/10.1021/jp410547w).
- [243] Y. Ling, Y. Lei, Q. Zhang, L. Chen, Q. Song and Z. Xiong. Large magneto-conductance and magneto-electroluminescence in exciplex-based organic light-emitting diodes at room temperature. *Applied Physics Letters*, **107**, 21, 213301 (2015). doi: [10.1063/1.4936205](https://doi.org/10.1063/1.4936205).
- [244] T. Basel, D. Sun, S. Baniya, R. McLaughlin, H. Choi, O. Kwon and Z. V. Vardeny. Magnetic field enhancement of organic light-emitting diodes based on electron donor–acceptor exciplex. *Advanced Electronic Materials* (2015). doi: [10.1002/aelm.201500248](https://doi.org/10.1002/aelm.201500248).
- [245] P. Deotare, W. Chang, E. Hontz, D. Congreve, L. Shi, P. Reuswig, B. Modtland, M. Bahlke, C. Lee, A. Willard et al. Nanoscale transport of charge-transfer states in organic donor-acceptor blends. *Nature materials*, **14**, 11, 1130 (2015). doi: [10.1038/nmat4424](https://doi.org/10.1038/nmat4424).
- [246] Q. Peng, A. Li, Y. Fan, P. Chen and F. Li. Studying the influence of triplet deactivation on the singlet–triplet inter-conversion in intra-molecular charge-transfer

- fluorescence-based oleds by magneto-electroluminescence. *Journal of Materials Chemistry C*, **2**, 31, 6264 (2014). doi: [10.1039/C4TC00885E](https://doi.org/10.1039/C4TC00885E).
- [247] G. Méhes, H. Nomura, Q. Zhang, T. Nakagawa and C. Adachi. Enhanced electroluminescence efficiency in a spiro-acridine derivative through thermally activated delayed fluorescence. *Angewandte Chemie International Edition*, **51**, 45, 11311 (2012). doi: [10.1002/anie.201206289](https://doi.org/10.1002/anie.201206289).
- [248] V. Jankus, M. Aydemir, F. B. Dias and A. P. Monkman. Generating light from upper excited triplet states: A contribution to the indirect singlet yield of a polymer oled, helping to exceed the 25% singlet exciton limit. *Advanced Science*, **3**, 1 (2016). doi: [10.1002/advs.201500221](https://doi.org/10.1002/advs.201500221).

A. Publications and Conference Contributions

Publications in peer-reviewed journals

Spins in Organic Semiconductors

1. J.M. Cho, D.S. Kim, S. Bae, S.-J. Moon, W.S. Shin, D.H. Kim, S.H. Kim, A. Sperlich, S. V \ddot{a} th, V. Dyakonov and J.-K. Lee. Light-induced electron spin resonance study of galvinoxyl-doped P3HT/PCBM bulk heterojunctions *Organic Electronics*, **27**, 119 (2015).
2. H. Kraus, M.C. Heiber, S. V \ddot{a} th, J. Kern, C. Deibel, A. Sperlich and V. Dyakonov. Analysis of Triplet Exciton Loss Pathways in PTB7:PC₇₀BM Bulk Heterojunction Solar Cells *Sci. Rep.*, **6**, 29158 (2016).
3. A. Sperlich, S. V \ddot{a} th and V. Dyakonov. Charge Transfer in Polymer:PC₆₀BM:PC₇₀BM Ternary Blends: Where is the Electron Going?
submitted
4. S. V \ddot{a} th, A. Baumann, A. F \ddot{o} rtig, A. Sperlich, V. Dyakonov, M. Ivanovic, H. Peisert, T. Chass \acute{e} and C. Deibel. Detection of Residual Iodine in PTB7:PCBM Blends due to the Additive DIO
in preparation
5. S. V \ddot{a} th, K. Tvingstedt, A. Baumann, M.C. Heiber, A. Sperlich, J.A. Love, T.-Q. Nguyen and V. Dyakonov. The Role of Triplet Excitons in Highly Efficient Solar Cells Based on the Soluble Small Molecule p-DTS(FBTTh₂)₂
submitted
6. S. V \ddot{a} th, K. Tvingstedt, M. Auth, A. Sperlich, V. Cherpak and V. Dyakonov. The Role of Spin States in Thermally Activated Delayed Fluorescence Organic Light Emitting Diodes
submitted

A. Publications and Conference Contributions

Defects in Silicon Carbide

7. D. Riedel, F. Fuchs, H. Kraus, S. V_äth, A. Sperlich, V. Dyakonov, A. A. Soltamova, P. G. Baranov, V. A. Ilyin and G. V. Astakhov. Resonant addressing and manipulation of silicon vacancy qubits in silicon carbide *Phys. Rev. Lett.*, **109**, 22, 226402 (2012).
8. F. Fuchs, V.A. Soltamov, S. V_äth, P. G. Baranov, E.N. Mokhov, G. V. Astakhov and V. Dyakonov. Silicon carbide light-emitting diode as a prospective room temperature source for single photons *Sci. Rep.*, **3**, 1637 (2013).
9. H. Kraus, V.A. Soltamov, D. Riedel, S. V_äth, F. Fuchs, A. Sperlich, P. G. Baranov, V. Dyakonov, and G. V. Astakhov. Room temperature quantum microwave emitters based on spin defects in silicon carbide *Nat. Physics*, **10**, 157 (2014).

Perovskite Solar Cells

10. A. Baumann, K. Tvingstedt, M.C. Heiber, S. V_äth, C. Momblona, H.J. Bolink, V. Dyakonov. Persistent Photovoltage in Methylammonium Lead Iodide Perovskite Solar Cells *APL Mater.*, **2**, 081501, (2014).
11. A. Baumann, S. V_äth, P. Rieder, M.C. Heiber, K. Tvingstedt, V. Dyakonov. Identification of Trap States in Perovskite Solar Cells *J. Phys. Chem. Lett.*, **6**, 2350, (2015).

Contributed Talks

1. DPG Frühjahrstagung 2013 in Regensburg. S. V_äth, D. Riedel, H. Kraus, F. Fuchs, A. Sperlich, V. Dyakonov, V. Soltamov, V. Ilyin, P. Baranov and G. Astakhov. Photo-induced microwave emission of silicon vacancy defects in silicon carbide.
2. DPG Frühjahrstagung 2014 in Dresden. S. V_äth, A. Baumann, A. Sperlich, C. Deibel, M. Ivanovic, H. Peisert, T. Chassé and V. Dyakonov. The role of processing additives in Organic Solar Cells after the preparation process.
3. DPG Frühjahrstagung 2015 in Berlin. S. V_äth, H. Kraus, A. Baumann, K. Tvingstedt, A. Sperlich, V. Dyakonov, J.A. Love and T.-Q. Nguyen. Triplet Exciton Formation in High-Efficiency Donor-Acceptor Photovoltaic Blends.
4. DPG Frühjahrstagung 2015 in Berlin. P. Rieder, M. Fischer, S. V_äth, A. Baumann, K. Tvingstedt and V. Dyakonov. Preparation and characterization of methylammonium lead halide perovskite solar cells in planar-type configuration.

5. MRS Spring Meeting 2015 in San Francisco, CA. S. V \ddot{a} th, H. Kraus, A. Baumann, K. Tvingstedt, A. Sperlich, V. Dyakonov, J.A. Love and T.-Q. Nguyen. Triplet Exciton Formation in High-Efficiency Donor-Acceptor Photovoltaic Blends.
6. DPG Fr \ddot{u} hjahrstagung 2016 in Regensburg. S. V \ddot{a} th, A. Sperlich, A. Baumann and V. Dyakonov. Quantifying Spin-Dependent Recombination in Organic Bulk Heterojunction Solar Cells

Conference Posters

1. DPG Fr \ddot{u} hjahrstagung 2012 in Dresden S. V \ddot{a} th, H. Kraus, A. Sperlich, K. Topczak, M. Zerson, R. Magerle, C. Deibel and V. Dyakonov. Morphology and electronic triplet states of regioregular P3HT ultrathin films.
2. GdCh FGMR 37th Annual Meeting 2015 in Darmstadt. S. V \ddot{a} th, K. Tvingstedt, A. Baumann, A. Sperlich, J.A. Love, T.-Q. Nguyen and V. Dyakonov. Triplet Exciton Formation in High-Efficiency Donor-Acceptor Photovoltaic Blends.

B. Danksagung

An dieser Stelle möchte ich mich bei all denjenigen bedanken, die mich während meiner Promotionszeit begleitet und unterstützt haben, was maßgeblich zu dem erfolgreichen Gelingen beigetragen hat.

Zuerst geht ein besonderer Dank an meinen Betreuer Prof. Vladimir Dyakonov für sein unerschütterliches Vertrauen in meine Fähigkeiten, welches mir ermöglichte weitestgehend selbstverantwortlich zu arbeiten. Andererseits stand seine Tür jederzeit offen für Fragen und Probleme.

Desweiteren bin ich meinen Kollegen Dr. Andreas Sperlich, der während dieser Arbeit zu meinem Gruppenleiter wurde, zu besonderem Dank verpflichtet. Neben seinen überragenden fachlichen Kenntnissen war vor allem sein labview Geschick von entscheidender Bedeutung. Außerdem wäre diese Arbeit ohne die großartigen Vorarbeiten beim Aufbau des Spektrometers von ihm und Dr. Hannes Kraus niemals möglich gewesen.

Ein besonderes Dankeschön muss auch der Deutschen Bundesstiftung Umwelt für die Förderung meiner Arbeit gelten. Aber auch die Durchführung der jährlichen Stipendiaten Seminare ist außergewöhnlich. Durch die Diskussionen mit fachfremden Wissenschaftlern wurden meine Fähigkeiten Dinge zu erklären auf harte Proben gestellt.

Allen Menschen gilt Dank, die meinen Computerfrust in Raum E13 ertragen haben. Insbesondere die alte "Stammbesetzung" Julia Kern, Andreas Zusan und Jasmin hat lange Zeit für ein super Arbeitsklima gesorgt (außer Jasmin für kurze Zeit). Ihr seid von Kollegen zu echten Freunden geworden.

Herzlichen Dank auch an die Insassen des Postdoc Büros E07 Dr. Andreas Baumann und Dr. Kristofer Tvingstedt, die immer auf Augenhöhe mit mir diskutiert haben. Sei es über unerklärliches Verhalten von Perovskiten oder, ungleich wichtiger, über Fußball. Ich hoffe ihr werdet in Zukunft nicht von Fahrrad fahrenden Physikern überrannt!

Vielen Dank auch an André Thiem-Riebe, der mir stets dabei geholfen hat technische Probleme fachmännisch und nicht wie Mcgyver zu lösen, Valentin Baianov, der eine unendlich scheinende Sorgfalt mit Lasersystemen an den Tag legt und Diep Phan,

B. Danksagung

die mir im Dschungel der Bürokratie immer den Weg zur nächsten Machete gezeigt hat.

Besonders gefreut habe ich mich stets auf Kaffeepausen mit Franziska Fuchs, die im Laufe der Zeit von einer langhaarigen Physikerin zu einer kurzhaarigen Freundin wurde.

Vielen Dank auch an die Jungs und Mädels der Siliziumkarbid Gruppe um Georgy Astakhov, Dmitrij Simin, Hannes und Franzi, bei der ich einige Zeit das Vergnügen hatte gutartige, anorganische Systeme zu untersuchen.

Ohne die Unterstützung von WMF1000S weiß ich nicht in welchem Zustand diese Arbeit heute wäre.

Danke schön auch an die vielen Bachelor- und Masteranden, mit denen ich das Vergnügen hatte zu arbeiten: Mathias Fischer, David Kiermasch, Marvin Grüne, Philipp Rieder, Melina Armer, Michael Auth, Lukas Hörlin und alle, die ich jetzt vergessen habe. Es war mir eine Ehre und ich freue mich, dass sich einige jetzt auf den gleichen Weg machen.

Nicht zuletzt ein großes Dankeschön der gesamten EP6. In all ihren verschiedenen Besetzungen war es immer eine reine Freude hier zu arbeiten, wobei es mir so gut wie nie wie Arbeit vorkam.

Zu guter Letzt, aber wahrscheinlich am aller wichtigsten muss ich meiner Familie danken. Zuerst natürlich meinen Eltern, Gabi und Jürgen, die nicht nur mein Studium finanziert haben, sondern auf die ich mich jederzeit zu 100% verlassen kann. Desweiteren meinen Großeltern, die wohl nie genau verstehen werden, was ich eigentlich gemacht habe, deshalb aber nur umso stolzer auf mich sind. Und natürlich meiner Schwester Moni, deren Freundschaft man sich nicht aussuchen kann, ich es aber trotzdem machen würde. Am wichtigsten jedoch ist mir der Dank an meine Frau Kathi, die jederzeit verständnisvoll war wenn ich genervt nach Hause kam oder länger im Labor saß.

Acknowledgment

Die Arbeit an der Universität Würzburg wurde durch die Deutsche Forschungsgemeinschaft (DFG) über die Schwerpunktprogramme SPP 1355 “Elementary Processes in Organic Photovoltaics” und SPP1601 “New Frontiers in Sensitivity for EPR Spectroscopy: From Biological Cells to Nano Materials” unterstützt.

Meine Arbeit wurde durch das Promotionsstipendienprogramm der Deutschen Bundesstiftung Umwelt (DBU) unterstützt (AZ20012/194).